<div align="center">

METALS
AND SUPERCONDUCTORS

Thermodynamic and Kinetic Properties of an Icosahedral Quasicrystalline Phase in the Al–Pd–Tc System

</div>

<div align="center">

**M. N. Mikheeva, G. Kh. Panova, A. A. Teplov, M. N. Khlopkin,
N. A. Chernoplekov, and A. A. Shikov**

Russian Research Center Kurchatov Institute, pl. Kurchatova 1, Moscow, 123182 Russia

e-mail: khlopkin@isssph.kiae.ru

Received April 26, 2000

</div>

Abstract—The properties of a quasicrystalline phase in the Al–Pd–Tc system are studied for the first time. X-ray investigations demonstrate that the quasicrystalline phase in the $Al_{70}Pd_{21}Tc_9$ alloy has a face-centered icosahedral quasi-lattice with parameter $a = 6.514$ Å. Annealing experiments have revealed that this icosahedral phase is thermodynamically stable. The heat capacity of an $Al_{70}Pd_{21}Tc_9$ sample is measured in the temperature range 3–30 K. The electrical resistivity and magnetic susceptibility are determined in the temperature range 2–300 K. The electrical resistivity is found to be high (600 $\mu\Omega$ cm at room temperature), which is typical of quasicrystals. The temperature coefficient of electrical resistivity is small and positive at temperatures above 50 K and negative at temperatures below 50 K. The magnetic susceptibility has a weakly paramagnetic character. The coefficient of linear contribution to heat capacity ($\gamma = 0.24$ mJ/(g-atom K^2)) and the Debye characteristic temperature ($\Theta = 410$ K) are determined. The origin of the specific features in the vibrational spectrum of the quasicrystals is discussed. © *2000 MAIK "Nauka/Interperiodica"*.

1. INTRODUCTION

It is well known that quasicrystals belong to a special class of solids lacking the periodic order inherent in usual crystal systems. However, unlike amorphous materials, quasicrystals are not disordered systems. Quasicrystals are characterized by a specific long-range order—the so-called "quasi-periodic" order. The long-range noncrystalline orientational order (for example, the long-range order that corresponds to a fivefold rotational symmetry, as is the case in icosahedral quasicrystals) was revealed by electron diffraction and x-ray diffraction analyses [1].

The first quasicrystalline materials (aluminum-enriched transition metal alloys with an icosahedral structure) were thermodynamically unstable. Subsequently, stable icosahedral quasicrystals were obtained in the Al–Cu–Li, Al–Cu–Fe–TM (*TM* = Fe, Ru, and Os), Mg–Zn–Ga, Mg–Zn–*R* (*R* = Y, Dy, Tb, Ho, and Er), and Al–Pd–*TM* (*TM* = Mn and Re) systems [2–7].

Investigation into the ternary Al–Pd–*TM* systems (where *TM* = Mn or Re) showed that the icosahedral phase is observed for compositions in which the ratio between components is close to 7 : 2 : 1. In Group VII of the periodic table, technetium is placed between manganese and rhenium. This gives grounds to assume that the quasicrystalline icosahedral phase also exists in the Al–Pd–Tc system. However, until recently, information on the Al–Pd–Tc system was unavailable. This was primarily due to the fact that technetium has no stable isotopes and is of limited occurrence. Moreover, experimenting on this element requires the observance

of radiation safety rules. Attempts to produce the $Al_{70}Pd_{20}Tc_{10}$ quasicrystalline alloy have failed [8].

The quasicrystalline icosahedral phase in the Al–Pd–Tc system was first prepared in our previous work [9] by the conventional solidification technique.

The aim of the present work was to investigate experimentally the thermodynamic and transport properties of this phase.

2. SAMPLE PREPARATION AND STRUCTURAL INVESTIGATIONS

An ingot of the $Al_{70}Pd_{21}Tc_9$ alloy was produced by melting the initial high-purity metals: Al (99.999%), Pd (99.99%), and Tc (99.98%). The melting was carried out in an electric arc furnace with a water-cooled copper bottom. Permanent tungsten electrodes were used. In order to ensure alloy homogeneity, a workpiece was turned over then remelted; this process was repeated four times. The workpiece thus prepared was annealed at a temperature of 940°C for 3 days under vacuum and then was quenched in water. The sample was light gray in color with a metallic luster. A small bar 1.65 × 1.7 × 5.35 mm in size was cut from the workpiece; moreover, a powder suitable for the structural investigation was also prepared from the same workpiece. The procedure of sample preparation was described in detail in [9].

The structure of the alloy prepared was investigated by x-ray powder diffraction on a Philips ADP-10 x-ray diffractometer (CuK_α radiation, graphite monochromator) intended for measurements of radioactive samples.
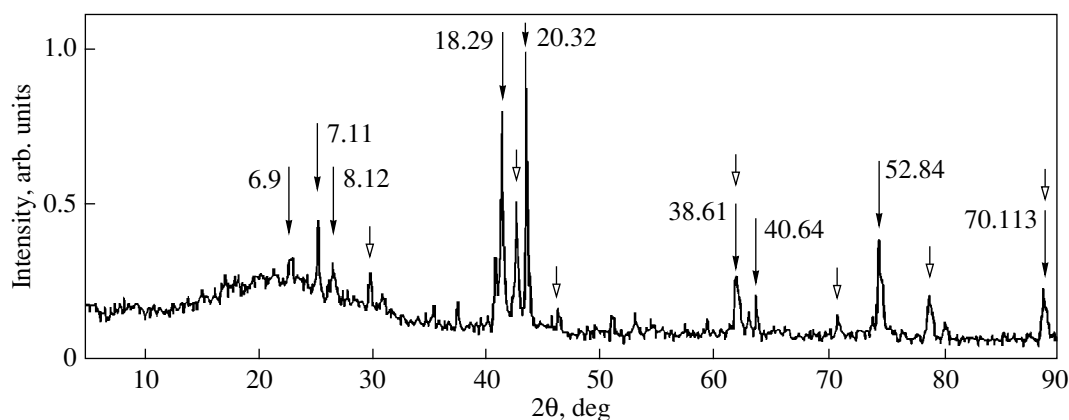
Fig. 1. X-ray diffraction pattern of the Al–Pd–Tc powder. Dark arrows show the peaks attributed to the face-centered icosahedral structure. Light arrows indicate the peaks assigned to the hexagonal compound Al_3Pd_2. Indices of the icosahedral phase are discussed in the text.

Figure 1 displays the x-ray diffraction pattern of an annealed sample of the $Al_{70}Pd_{21}Tc_9$ alloy. This pattern is identical to the x-ray diffraction patterns of the Al–Pd–Mn and Al–Pd–Re quasicrystalline face-centered icosahedral phases. As can be seen, the diffraction pattern exhibits additional peaks, which are not attributed to the quasicrystalline face-centered icosahedral phase and, most likely, correspond to the Al_3Pd_2 compound involved in the form of an impurity phase. Furthermore, a halo assigned to the varnish coating of the sample is observed in the diffraction pattern in the range $2\theta = 18°$–$30°$.

The peaks shown in Fig. 1 that correspond to the quasicrystalline phase are marked by arrows with two

indices, N and M, according to the Cahn scheme [10]. It should be noted that the presence of the (7, 11) peak confirms the fact that our quasicrystalline phase is the face-centered icosahedral phase. This structure can be considered a six-dimensional superstructure in a primitive hypercubic lattice in real space with the six-dimensional lattice parameter a_P, which is half as much as the parameter a_F of the face-centered lattice [2]. In the diffraction patterns experimentally obtained for the face-centered icosahedral phases, the reflections associated with the superstructural ordering ($N = 4n + 3$, where n is the integer) are often very weak compared to the reflections of the primitive lattice. Correspondingly, these reflections are usually indexed using the indices of the primitive lattice with the lattice parameter $a_P = a_F/2$.

For the icosahedral peaks, the wavevector magnitude is given by the relationship

$$Q_{par} = \frac{2\pi}{a_P}\sqrt{\frac{N + M\tau}{2 + \tau}}, \qquad (1)$$

where a_P is the quasi-lattice parameter and $\tau = (\sqrt{5} - 1)/2$ is the golden section.

Figure 2 shows the wavevector Q, which was determined for each x-ray diffraction peak indexed in the icosahedral phase, as a function of the product $Q_{par}a_P$ calculated by formula (1). The dependence $Q(Q_{par}a_P)$ for all the indexed icosahedral reflections is depicted in Fig. 2 together with the straight line describing this dependence. The mean absolute deviation of peak positions (3×10^{-3} Å) is considerably less than the full mean width at half-maximum (2×10^{-2} Å), which is a weighty argument in support of the applicability of our indexing procedure described above.

The quasi-lattice parameter a_P can be determined, with a high accuracy, from analysis of the x-ray powder diffraction patterns at large angles with respect to the
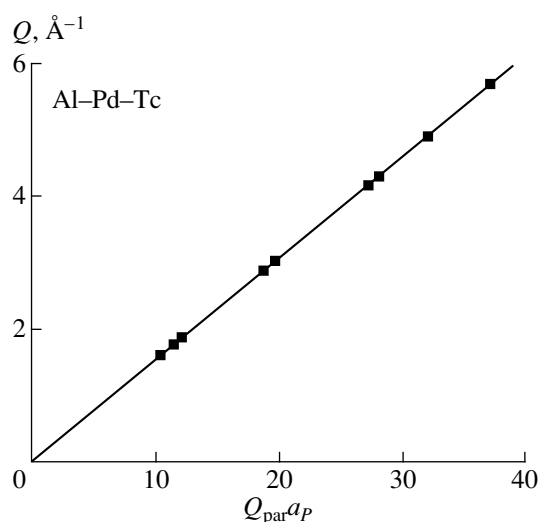

Fig. 2. Wavevector Q for each x-ray diffraction peak attributed to the face-centered icosahedral phase as a function of the product $Q_{par}a_P$ calculated for the icosahedral structure. Wavevector Q for each peak was determined using the weighted mean wavelength of the K_α doublet.

incident x-ray beam. This is explained by the fact that the large Bragg angles are very sensitive to small variations in the quasi-lattice parameter, as is evident from the expression for the derivative of the quasi-lattice parameter a_P with respect to the Bragg angle θ:

$$da_P/d\theta = -a_P \cot\theta .$$

Averaging of the data on $Q_{par}a_P/Q$ over the diffraction angle range $63° < 2\theta < 90°$, which involves three reflections, gives the quasi-lattice parameter $a_P = 6.514 \pm 0.004$ Å. This value is very close to the quasi-lattice parameter $a_P = 6.451$ Å for the Al–Pd–Mn icosahedral quasicrystal [11].

It should be noted that certain x-ray powder diffraction peaks, which cannot be indexed in the icosahedral structure, are most probably attributed to the Al_3Pd_2 compound. This compound crystallizes in a hexagonal structure of the Al_3Ni_2 type with the unit cell parameters $a = 4.217$ Å and $c = 5.166$ Å (Fig. 1).

A cast sample of $Al_{70}Pd_{21}Tc_9$ contained a mixture of the face-centered icosahedral phase with one or more other phases. After the annealing under vacuum at 940°C for 3 days, a considerable part of the sample transformed into the icosahedral phase. This gives grounds to assume that the icosahedral phase of alloys in this system is stable.

If the assumption is made that the impurity phase is a metallic phase whose electronic heat capacity and electrical resistivity are typical of metals, it is possible to estimate qualitatively the fraction of the impurity phase in the given sample. According to the estimate made from the electronic contribution to the heat capacity, the fraction of the impurity metallic crystalline phase in the studied sample is less than 15% and, hence, the fraction of the quasicrystalline phase is more than 85%.

3. INVESTIGATIONS OF ELECTRICAL RESISTIVITY, MAGNETIC SUSCEPTIBILITY, AND HEAT CAPACITY

The temperature dependence of the dc electrical resistivity was measured in a separate experiment by the standard four-point probe method with the use of pressed contacts.

The magnetic susceptibility was determined on an instrument for measurements of the differential magnetic susceptibility in magnetic fields of ~1 Oe with a sensitivity of 10^{-10} A m^2 in the temperature range 4–350 K. The instrument is based on the devised technique of double synchronous detection [12]. This technique makes it possible to measure the absolute magnetic susceptibility of small samples with a weight of the order of several tens of milligrams and a specific magnetic susceptibility of 10^{-7} emu/g, to differentiate the diamagnetic and paramagnetic signals, and to determine the zero position with an accuracy of ~10^{-10} A m^2.
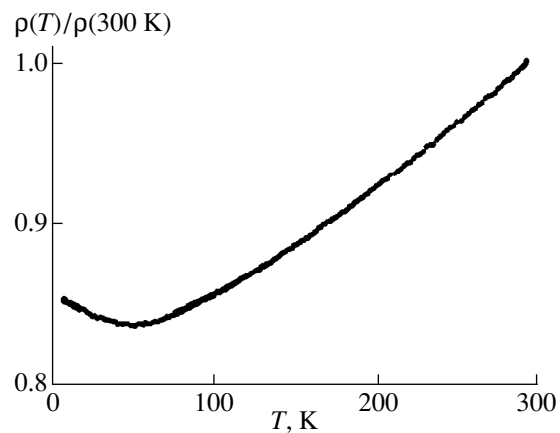
$\rho(T)/\rho(300\ K)$

Fig. 3. Temperature dependence of the electrical resistivity of the Al–Pd–Tc quasicrystalline sample in the temperature range 2–300 K.

The heat capacity of the sample was measured by the adiabatic technique with pulsed heat input [13]. The sample weight was 52 mg, and the experimental error was equal to about 10% in the temperature range 3–6 K and less than 5% in the range 6–30 K.

The experimental data on the heat capacity, magnetic susceptibility, and electrical resistivity of the Al–Pd–Tc quasicrystalline sample are presented in Figs. 3–6 and the table.

Figure 3 displays the temperature dependence of the electrical resistivity for the Al–Pd–Tc sample in the temperature range 2–300 K. This dependence exhibits a minimum at $T = 50$ K. The electrical resistivity at

Molar heat capacities C_p at constant pressure for the $Al_{70}Pd_{21}Tc_9$ quasicrystal as a function of temperature T (1 g-atom = 49.96 g)

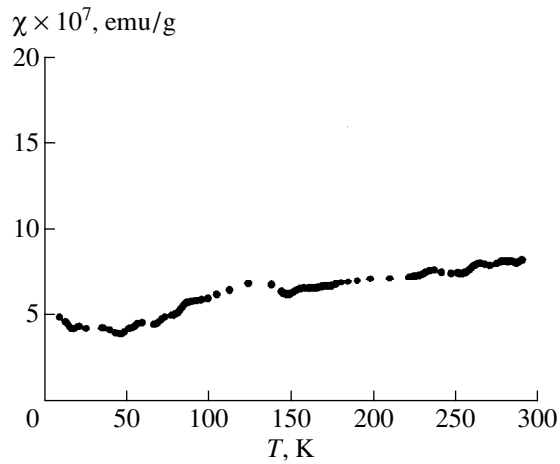| T, K	C_p, mJ/(g-atom K)	T, K	C_p, mJ/(g-atom K)
3	1.57	17	178
4	2.81	18	217
5	4.71	19	260
6	7.45	20	310
7	11.3	21	366
8	16.4	22	428
9	23.2	23	496
10	31.8	24	571
11	42.8	25	652
12	56.4	26	737
13	73.0	27	828
14	93.0	28	921
15	117	29	1017
16	145	30	1113

Fig. 4. Temperature dependence of the magnetic susceptibility of the Al–Pd–Tc quasicrystalline sample in the temperature range 4–300 K. The vertical size of points corresponds to the accuracy in the determination of χ.

300 K has a high value (600 $\mu\Omega$ cm), which is typical of quasicrystals.

The temperature coefficient of electrical resistivity is small and negative over a wide range of temperatures above 50 K. The magnitude of this coefficient does not exceed 8×10^{-4} K^{-1} in the range 50–300 K. At temperatures below 50 K, the temperature coefficient of electrical resistivity is negative.

A comparison of the experimental temperature dependences of the electrical resistivity for the Al–Pd–Tc sample and other quasicrystalline compounds shows that, in the above temperature range, the temperature coefficients of electrical resistivity can be positive and negative. Moreover, there are quasicrystalline systems,

in particular, Al$_{86}$Co$_{14}$, for which the temperature dependence of the electrical resistivity also exhibits a minimum in the low-temperature range [14].

Nonetheless, when analyzing the possible reasons for the positive temperature coefficient of electrical resistivity, the influence of the Al$_3$Pd$_2$ impurity phase, whose additional peaks are observed in the x-ray powder diffraction pattern (Fig. 1), must not be ruled out.

The high electrical resistivity of the sample suggests that the impurity metallic phase does not form a continuous region, and, consequently, its fraction in the sample volume is below the percolation limit.

The temperature dependence of the magnetic susceptibility of the Al–Pd–Tc quasicrystalline sample in the temperature range 4–300 K is shown in Fig. 4. In the temperature range covered, the magnetic susceptibility is extremely small and positive, which indicates its paramagnetic nature. As follows from the experimental data, a decrease in the temperature is accompanied by a decrease in the magnetic susceptibility with a temperature coefficient of $\sim 1.3 \times 10^{-7}$ emu/(g K).

The heat capacity of the sample in the temperature range 3–10 K is displayed in Fig. 5 in the C/T–T^2 coordinates. In these coordinates, the temperature dependence of the heat capacity is close to a straight line, which corresponds to the law typical of metals: $C = \gamma T + \beta T^3$.

The coefficients γ and β determined by the least-squares technique and the low-temperature value of the Debye characteristic temperature Θ, which is related to the β coefficient by the relationship $\beta = 12\pi^4 R/(5\Theta^3)$ (where R is the gas constant), are as follows: $\gamma = 0.24$ mJ/(g-atom K^2), $\beta = 0.029$ mJ/(g-atom K^4), and $\Theta = 410$ K. The term linear in temperature corresponds to the electronic contribution to the heat capacity, and
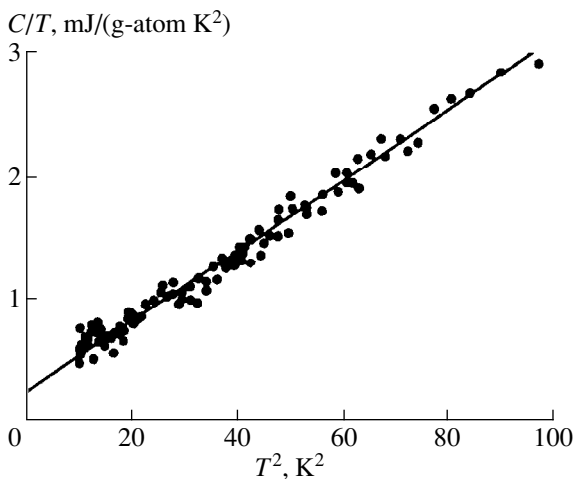

Fig. 5. Temperature dependence of the heat capacity of the Al–Pd–Tc quasicrystalline sample in the temperature range 3–10 K in the C/T–T^2 coordinates.
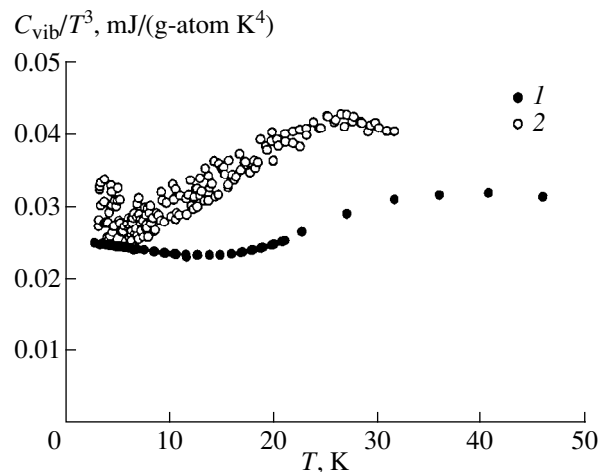

Fig. 6. Temperature dependences of the vibrational heat capacity in the C_{vib}/T^3–T coordinates: (*1*) Al$_{70}$Pd$_{21}$Tc$_9$ quasicrystal (this work) and (*2*) aluminum [17, 18].

the term cubic with respect to the temperature is determined by the vibrational contribution to the heat capacity. Note that the γ coefficient of the term linear with respect to temperature is substantially smaller than that for usual metals, which suggests a low density of states at the Fermi level. Vaks *et al.* [15] noted that it is this low density of states at the Fermi level which favors a decrease in the energy of the system and can be responsible for the stabilization of the quasicrystalline phase with the icosahedral symmetry.

The content of an impurity metallic phase in the sample can be evaluated from the coefficient γ of the term linear in temperature ($\gamma = 0.24$ mJ/(g-atom K^2)). By assuming that the term (linear with respect to temperature) in the heat capacity of the studied sample is completely determined by the impurity phase, which is characterized by the γ_i coefficient of the linear term, and the linear term for the quasicrystalline phase is appreciably less, the upper limit of the fraction η of this impurity metallic phase can be estimated from the formula $\eta = \gamma_i/\gamma$. Setting $\gamma_i = 1.6$ mJ/(g-atom K^2), which is close to the coefficients characteristic of simple metals, we obtain the estimate of the impurity phase fraction $\eta < 15\%$.

The data obtained enable us to separate the vibrational contribution from the measured heat capacity in the studied temperature range and to draw inferences about the character of the energy dependence of the density of vibrational states. For this purpose, it is expedient to plot the vibrational component of the heat capacity $C_{vib} = C - \gamma T$ in the C_{vib}/T^3 vs. T coordinates, because detailed analysis performed by Junod *et al.* [16] showed that the C_{vib}/T^3 quantity is the approximate representation of the function $\omega^2 g(\omega)$ at $\hbar\omega = 4.93 k_B T$, where k_B and $\hbar$ are the Boltzmann and Planck constants, respectively.

Figure 6 shows the temperature dependences of the vibrational heat capacity for the studied Al–Pd–Tc system and pure aluminum [17, 18] in the C_{vib}/T^3–T coordinates in the temperature range 3–30 K. The temperature dependence of C_{vib}/T^3 for the Al–Pd–Tc sample passes through a broad maximum at $T \approx 26$ K, which indicates the intense low-frequency mode at the energy $\hbar\omega \approx 12$ meV in the vibrational spectrum. This low-frequency mode makes an additional contribution to the vibrational energy of the $Al_{70}Pd_{21}Tc_9$ quasicrystalline phase in the low-frequency range and, hence, the corresponding contribution to the vibrational heat capacity in the low-temperature range. Maxima in the dependences of C_{vib}/T^3 on T were also observed for the Al–Cu–Co and Al–Pd–Re icosahedral quasicrystals [19, 20].

4. DISCUSSION

Let us compare the vibrational heat capacities of pure aluminum and a quasicrystalline system consist-

ing of aluminum to the extent of 70%. Since 30% of aluminum atoms in the studied system are replaced by palladium and technetium atoms whose mass is almost four times larger, the mean atomic mass m in the $Al_{70}Pd_{21}Tc_9$ system is equal to 50 amu, which is nearly twice as large as the atomic mass of aluminum [10]. The vibrational heat capacity C_{vib} at low temperatures is determined by the mean sound velocity, which, in turn, substantially depends on the mean atomic mass: $C_{vib}(T/\Theta)^3 \sim T^3(m/k)^{3/2}$. Here, k is the effective force constant, which is proportional to the corresponding elastic modulus. It would be reasonable to expect that the low-temperature heat capacity of the quasicrystal should exceed the heat capacity of pure aluminum by several times due to the twofold increase in the mean atomic mass. However, the increase observed in the heat capacity both in the studied system and other aluminum-based quasicrystals is not so large. As can be seen from Fig. 6, at equal temperatures, the heat capacity of the quasicrystal in the low-temperature range differs from that of aluminum by no more than 50%.

Syrykh *et al.* [21] revealed that substitution of particular atoms for other atoms in actual systems can lead to a substantial change in the force interaction between atoms, including the matrix atoms, which results in the renormalization of the phonon spectrum of the matrix. The electronic subsystem plays a significant role in the renormalization of the phonon spectrum. Gomersall and Gyorffy [22] theoretically treated the renormalization of the phonon spectrum upon the electron–phonon interaction and derived the relationship

$$\langle \omega^2 \rangle \cong \langle \Omega^2 \rangle_0 - \frac{4}{5} E_F N(E_F) \frac{N(E_F)\langle I^2 \rangle}{M}, \qquad (2)$$

where $\langle \omega^2 \rangle$ is the mean-square frequency of the phonon spectrum renormalized by the electron–phonon interaction, $\langle \Omega^2 \rangle_0$ is the mean-square frequency of the bare phonon spectrum, E_F is the Fermi energy, $N(E_F)$ is the density of states at the Fermi level, $\langle I^2 \rangle$ is the matrix element of the electron–phonon interaction, and M is the atomic mass.

With the known relationship (see, for example, [23]) which relates the matrix element of the electron–phonon interaction to the electron–phonon coupling constant λ, that is,

$$\lambda = \frac{N(E_F)\langle I^2 \rangle}{M\langle \omega^2 \rangle},$$

expression (2) can be rearranged to give

$$\langle \Omega^2 \rangle_0 = \langle \omega^2 \rangle \left(1 + \frac{4}{5} E_F N(E_F)\lambda \right) \approx \langle \omega^2 \rangle \left(1 + \frac{6n\lambda}{5} \right).$$

In the right-hand side of the equality, we used the formula valid for the free-electron model

$$E_F N(E_F) = 3n/2,$$

where n is the number of valence electrons of the metal.

It is seen that, within the free-electron model, which is applicable to pure aluminum, the renormalizing factor involves only two parameters, namely, the number of valence electrons and the electron–phonon coupling constant. These parameters are known. The number of valence electrons n is equal to 3 (reasoning from the valence), and the electron–phonon coupling constant $\lambda = 0.38$ was estimated in [23] from the superconducting properties according to the McMillan equation. The estimates made for the renormalization of the phonon spectrum of aluminum by using relationship (2) demonstrate that the electron–phonon interaction in aluminum considerably (by a factor of almost 1.5) decreases the frequency of the phonon spectrum. In quasicrystals, the density of states at the Fermi level is appreciably less. This density in our system is almost six times less than that in aluminum, for which $\gamma = 1.35$ mJ/(g-atom K^2). Therefore, in the quasicrystal, the effect of the phonon frequency renormalization by the electron–phonon interaction is substantially weaker. Consequently, it is believed that a change in the heat capacity of the quasicrystal due to an increase in the mean atomic mass, to a large extent, is compensated by the effect of the spectrum renormalization upon the electron–phonon interaction.

Now, we consider the possible reasons for the appearance of the intense low-frequency mode in the vibrational spectrum, which manifests itself as a maximum in the temperature dependence of C_{vib}/T^3.

It is known [24] that the vibrational spectrum of crystalline systems with heavy impurity atoms exhibits a resonance feature associated with the so-called quasi-local vibrations, which were predicted in [25] and revealed experimentally in [26, 27]. More recently, similar features in the vibrational spectra were also observed for disordered amorphous systems [28]. Zhernov and Augst [29] carried out detailed numerical calculations of the contribution from the quasi-local vibrations to the heat capacity of systems with different ratios between the masses of the components. However, in the case of a heavy impurity in a light matrix, there are simple relationships for the quasi-local frequency and the change in the heat capacity [22]:

$$\frac{\omega_R^2}{\omega_D^2} \approx \frac{1}{3}\frac{M}{M_d - 0.6M}, \tag{3}$$

$$\frac{\Delta C_{vib}}{C_{vib}} = 0.091\eta\left(\frac{\omega_D}{\omega_R}\right)^3, \tag{4}$$

where ω_R is the frequency of quasi-local vibrations, ω_D is the characteristic (Debye) frequency of the initial material (matrix), M is the mass of the matrix atom, M_d is the mass of a heavy impurity atom ($M_d \gg M$), η is the concentration of heavy impurity atoms, C_{vib} is the vibrational heat capacity of the initial material, and ΔC_{vib} is the additional contribution to the vibrational heat capacity from the heavy impurity atoms.

The frequency of the quasi-local mode $\hbar\omega_R$ was evaluated from relationship (3) with the atomic mass of aluminum (as the mass of the matrix atom), the atomic mass of palladium (as the mass of an impurity atom), and the experimental Debye frequency ($\Theta = 410$ K): $\hbar\omega_R = 136$ K $= 12$ meV, which is in good agreement with the experimental data. Moreover, according to relationship (4), the height of the maximum in the temperature dependence of C_{vib}/T^3 at a heavy atom concentration of 30% was estimated at about 100%, which also agrees with the experiment.

However, it should be noted that the quasi-local vibrations are not the sole possible reason for the appearance of the maximum in the temperature dependence of C_{vib}/T^3. Similar maxima are observed for usual metals, specifically for aluminum, due to sound velocity dispersion. Consequently, the dispersion can also be responsible for the observed nonmonotonic temperature dependence of C_{vib}/T^3 for quasicrystals. Unfortunately, no investigations of the sound velocity dispersion in the $Al_{70}Pd_{21}Tc_9$ quasicrystals were carried out.

Furthermore, according to the model described in [30], the appearance of resonance low-frequency vibrational modes is due to fluctuations of the density and the force constants in systems without translational symmetry. In the framework of this model, the low-frequency mode also takes place. However, the exact expressions that relate the characteristics of the low-frequency mode to the controllable parameters of the system are absent.

Thus, in the quasicrystals based on the aluminum–transition metal alloys, the effect of quasi-local modes is most likely responsible for the appearance of the low-frequency vibrational mode with the energy $\hbar\omega \sim 10$–15 meV, which shows itself as a maximum in the temperature dependence of C_{vib}/T^3 in the temperature range 20–30 K. At the same time, the possibility of manifesting the effects associated with the sound velocity dispersion and specific features of the quasicrystalline state due to the absence of translational symmetry must not be ruled out.

5. CONCLUSION

In this work, we investigated the properties of the $Al_{70}Pd_{21}Tc_9$ quasicrystalline phase, which has an icosahedral face-centered quasicrystalline lattice with the parameter $a = 6.514 \pm 0.004$ Å.

The electrical resistivity of the studied system proved to be rather high (600 $\mu\Omega$ cm at 300 K), which is characteristic of the quasicrystals. The temperature

dependence of the resistivity $\rho(T)/\rho(300\ \text{K})$ exhibits a minimum at $T = 50$ K. The positive temperature coefficient of electrical resistivity does not exceed $8 \times 10^{-4}\ \text{K}^{-1}$ in the temperature range 50–300 K, and the negative temperature coefficient of resistivity at temperatures below 50 K is of the order of $5 \times 10^{-4}\ \text{K}^{-1}$.

The experimental data on the magnetic susceptibility suggest a weak paramagnetic interaction in the quasicrystalline system under consideration.

The magnitude of the coefficient of the linear (in temperature) contribution to the heat capacity of the $Al_{70}Pd_{21}Tc_9$ quasicrystal indicates the low density of states at the Fermi level, which agrees with the data for other quasicrystalline materials. The Debye characteristic temperature Θ is equal to 410 K. This value falls in the range of the Θ temperatures typical of the stable quasicrystals. The temperature dependence of C_{vib}/T^3 for Al–Pd–Tc passes through a broad maximum at $T \sim 26$ K, which suggests the presence of an intense low-frequency mode with energy $\hbar\omega \sim 12$ meV in the vibrational spectrum.

ACKNOWLEDGMENTS

REFERENCES

1. D. Shechtman, I. Blech, D. Gratias, and J. W. Cahn, Phys. Rev. Lett. **53**, 1951 (1984).

2. S. Ebalard and F. Spaepen, J. Mater. Res. **4**, 39 (1989).

3. W. Ohashi and F. Spaepen, Nature **330** (6148), 555 (1987).

4. A. P. Tsai, A. Inoue, and T. Masumoto, Jpn. J. Appl. Phys. **27**, L1587 (1988).

5. A. P. Tsai, A. Inoue, Y. Yokoyama, and T. Masumoto, Philos. Mag. Lett. **61**, 9 (1990).

6. A. P. Tsai, A. Inoue, and T. Masumoto, Philos. Mag. Lett. **62**, 95 (1990).

7. C. Beeli, H.-U. Nissen, and J. Robadey, Philos. Mag. Lett. **63**, 87 (1991).

8. N. S. Athanasiou, Mod. Phys. Lett. B **11**, 367 (1997).

9. M. N. Mikheeva, A. A. Teplov, K. G. Bukov, *et al.*, Philos. Mag. Lett. (2000) (in press).

10. J. W. Cahn, D. Shechtman, and D. Gratias, J. Mater. Res. **1**, 13 (1986).

11. C. Bellic, Ph. D. Thesis, ETH-Zurich (1992).

12. A. A. Nikonov, Prib. Tekh. Éksp., No. 6, 168 (1995).

13. M. N. Khlopkin, N. A. Chernoplekov, and P. A. Cheremnykh, Preprint No. 3549/10, IAÉ (Kurchatov Institute of Atomic Energy, Moscow, 1982).

14. A. M. Bratkovskiĭ, Yu. A. Danilov, and G. I. Kuznetsov, Fiz. Met. Metalloved. **68**, 1045 (1989).

15. V. G. Vaks, V. V. Kamyshenko, and G. D. Samolyuk, Phys. Lett. A **132** (2–3), 131 (1988).

16. A. Junod, T. Jarlborg, and J. Muller, Phys. Rev. B **27** (3), 1568 (1983).

17. W. T. Berg, Phys. Rev. **167**, 583 (1968).

18. W. F. Giaugue and P. F. Meads, J. Am. Chem. Soc. **63** (7), 1897 (1941).

19. M. A. Chernikov, A. Bianchi, E. Felder, *et al.*, Europhys. Lett. **35** (6), 431 (1996).

20. K. Edagawa, M. A. Chernikov, A. Bianchi, *et al.*, Phys. Rev. Lett. **77** (6), 1071 (1996).

21. G. F. Syrykh, M. G. Zemlyanov, N. A. Chernoplekov, and B. I. Savel'ev, Zh. Éksp. Teor. Fiz. **81** (1), 308 (1981) [Sov. Phys. JETP **54**, 165 (1981)].

22. L. G. Gomersall and B. L. Gyorffy, Phys. Rev. Lett. **33** (21), 1286 (1974).

23. W. L. McMillan, Phys. Rev. B **1** (2), 331 (1968).

24. A. P. Zhernov, N. A. Chernoplekov, and É. Mrozan, *Metals with Nonmagnetic Impurity Atoms* (Énergoatomizdat, Moscow, 1992).

25. Yu. M. Kagan and Ya. A. Ioselevskiĭ, Zh. Éksp. Teor. Fiz. **44** (1), 284 (1963) [Sov. Phys. JETP **17**, 195 (1963)].

26. N. A. Chernoplekov and M. G. Zemlyanov, Zh. Éksp. Teor. Fiz. **49** (2), 449 (1965) [Sov. Phys. JETP **22**, 315 (1965)].

27. G. Kh. Panova and B. N. Samoĭlov, Zh. Éksp. Teor. Fiz. **49** (2), 456 (1965) [Sov. Phys. JETP **22**, 320 (1965)].

28. G. Kh. Panova, A. A. Shikov, N. A. Chernoplekov, *et al.*, Zh. Éksp. Teor. Fiz. **90** (4), 1351 (1986) [Sov. Phys. JETP **63**, 791 (1986)].

29. A. P. Zhernov and G. R. Augst, Fiz. Tverd. Tela (Leningrad) **9** (8), 2196 (1967) [Sov. Phys. Solid State **9**, 1724 (1967)].

30. V. M. Manichev and E. A. Gusev, Fiz. Tverd. Tela (St. Petersburg) **41** (3), 372 (1999) [Phys. Solid State **41**, 334 (1999)].

Translated by O. Borovik-Romanova

METALS
AND SUPERCONDUCTORS

The Influence of the Metalloid Species on the Electronic Structure of Disordered Transition-Metal–Metalloid Alloys

D. A. Korolev, V. Ya. Bayankin, and E. P. Elsukov

Physicotechnical Institute, Ural Division, Russian Academy of Sciences, ul. Kirova 132, Izhevsk, 426000 Russia
e-mail: uufti@fti.udmurtia.su
Received April 24, 2000; in final form, May 29, 2000

Abstract—The results of x-ray emission investigations of the electronic structure of Fe–Si and Fe–P disordered alloys are presented. Relying on the analysis of the spectrum parameters and data available in the literature, a qualitative model of the electronic-structure formation in disordered Fe–P alloys is proposed. The model allows one to account for the concentration dependence of the average magnetic moment per iron atom in the disordered systems investigated. © *2000 MAIK "Nauka/Interperiodica".*

Disordered alloys prepared by various techniques represent a new state of solid substances, different from ordered crystal materials. Many disordered systems have no simple crystalline analogs, and their composition can be varied continuously within a single-phase state. This makes it possible to obtain homogeneous alloys and investigate their electronic structure without facing complications caused by structural phase transitions.

The alloys of the transition-metal–metalloid type represent one of the most important groups of disordered materials. An unresolved problem is the influence of the metalloid species on the formation of the valence band in disordered alloys. The aim of this work is to investigate the formation of the electronic structure of Fe–Si and Fe–P disordered alloys.

1. EXPERIMENT

Microcrystalline powders of $Fe_{1-x}Si_x$ ($x = 6$–50 at. %) alloys and a binary amorphous alloy of the eutectic composition $Fe_{80}P_{20}$ were chosen as the objects for the investigations of the influence of the metalloid species on the formation of the electronic structure of disordered transition-metal–metalloid alloys.

The Fe–Si alloys were prepared from high-purity components (99.99% Fe, 99.99% Si) in a vacuum induction furnace in an argon atmosphere. Homogenization of the ingots was fulfilled in a vacuum of 10^{-4} Pa at a $T = 1423$ K for six hours. The ingots were ground up in a "Pulverizette-5" planetary ball mill designed to produce disordered powders. The grinding was carried out in an argon atmosphere. The average size of the powder grains was 2 μm.

An amorphous binary alloy of $Fe_{80}P_{20}$ was produced by quenching from a melt. The thickness of the amorphous ribbon was 12 to 14 μm, which corresponds to a melt cooling rate of about 10^6 K/s.

X-ray analysis was used for the structure and single-phase condition testing. According to the x-ray analysis, the $Fe_{80}P_{20}$ alloy was amorphous. The produced microcrystalline powders of Fe–Si alloys have a disordered BCC structure at Si concentrations up to 33 at. %; a disordered hexagonal structure was observed at higher silicon concentrations.

X-ray emission spectroscopy was used for the electronic-structure investigations, which permits one to set apart the contributions from the partial densities of the states of each component of the alloy to the valence band.

X-ray fluorescence spectra $Si(P) K_{\beta_1}$ and $Fe L_{\alpha_{1,2}}$ of the $Fe_{1-x}Si_x$ and $Fe_{80}P_{20}$ alloys and of intermetallic Fe_3P, as well as of pure silicon, iron, and red phosphorus, were obtained with an "SARF-1" x-ray spectrometer, which provides fluorescence measurements.

The inaccuracy in the determination of the point energy position in the spectra was ±0.2 and ±0.1 eV for $Si(P) K_{\beta_1}$ and $Fe L_{\alpha_{1,2}}$, respectively. The spread of the intensity values was no more than six percent. The spectra measured were processed in the standard way (correction of inaccuracies due to the apparatus and the signal internal level width, background subtraction, normalization, and smoothing).

An analysis of the $Si(P) K_{\beta_1}$ and $Fe L_{\alpha_{1,2}}$ spectra associated with the $Si(P)$ (3p–1s) and Fe (3d4s–2p) transitions allows one to judge the density distribution of the 3p and 3d electrons of $Si(P)$ and Fe, respectively, in the valence band of the alloys.

2. EXPERIMENTAL RESULTS AND DISCUSSION

The main features of all the measured x-ray emission spectra of the $Fe_{80}P_{20}$ and $Fe_{1-x}Si_x$ disordered alloys (Figs. 1, 2) are (1) a shift in the intensity maxima

of the $P(Si)K_{\beta_1}$ and $FeL_{\alpha_{1,2}}$ bands to lower energies compared with the spectra of the pure elements and (2) a shoulder on the high-energy side of the $P(Si)K_{\beta_1}$-band due to the interaction of the P(Si) 3p and Fe 3d electrons. The latter feature is also present in the spectra of intermetallic Fe_3P (Fig. 1).

Earlier investigations of ordered transition-metal (TM) silicides showed that the TM–Si chemical bond has a covalent–metal character and the strengthening of the covalent component takes place in the series TM_3Si, TM_5Si_3, TMSi, and $TMSi_2$ [1].

The influence of the metalloid species on the structure of the x-ray emission VK_{β_5} bands in ordered V–sp-element compounds was studied in considerable detail [2]. It was shown that the VK_{β_5} spectrum of these compounds consists of three bands, and the subbands associated fundamentally with the 3d states of V and the np states of the sp element were separated [3]. The disposition of these subbands relative to each other depends on the type of atoms of the sp element and its position in the periodic table. For example, as the atomic number increases within the period (from Al to Si, from Ga to Ge, and from Sn to Sb), an increase in the spacing between these spectral subbands is observed.

The regularities observed in the variations of the spectrum parameters are also characteristic of the compounds of V and Ti with C, N, and O [4, 5], as well as of alloys based on Cr [6] and Mn [7].

Comparing the main thermodynamic characteristics [8] of different compounds of the transition metals with sp elements (see table), a clear tendency can be seen. This tendency consists in an increase in $|\Delta G|$ and $|\Delta H|$ with an increase in the sp-element atomic number on going along the period, which indicates the strengthening of the chemical interaction between the alloy components. At the same time, the spacing between the spectral subbands associated fundamentally with the d states of the transition metal and the p states of the metalloid increases [2–7]. Therefore, the spacing between the subbands in the spectrum correlates with the stability of these compounds.

In contrast to the intermetallic compounds, the disordering in Fe–Si and Fe–P alloys results in the formation of the p zone possessed by the sp element, because the appearance of two metalloid atoms that are the nearest neighbors of each other is more probable in this case. This causes a redistribution of the intensities in the low-energy region of the x-ray emission SiK_{β_1} bands [9]. In particular, the intensity of the 3d-like band in the x-ray emission SiK_{β_1} spectra decreases at the order–disorder transition [10].

It was pointed out in a number of publications [11–14] that the two subbands in the valence spectrum of the metalloids in the amorphous alloys of the $TM_{80}X_{20}$
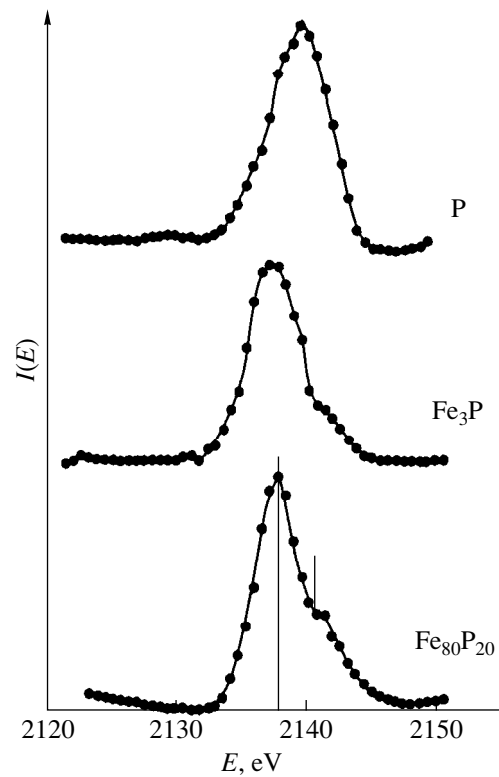

Fig. 1. X-ray emission PK_{β_1} bands of an $Fe_{80}P_{20}$ amorphous alloy, an Fe_3P intermetallic compound, and red phosphorus.
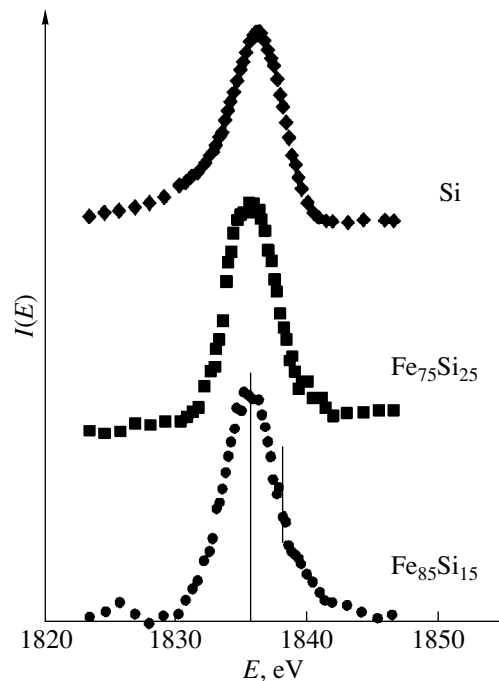

Fig. 2. X-ray emission SiK_{β_1} bands of disordered $Fe_{85}Si_{15}$ and $Fe_{75}Si_{25}$ alloys and pure silicon.

Main thermodynamic constants of several compounds of transition metals with *sp* elements [8]

Compound	ΔH^0_{298}, cal/mol	ΔG^0_{298}, cal/mol	Compound	ΔH^0_{298}, cal/mol	ΔG^0_{298}, cal/mol
$VC_{0.88}$	−24.1		Fe_3Si	−22.4	
VN	−51.9	−45.7	Fe_3P	−40	
VO	−100	−93.5	FeS_2	−42.4	−36.2
MnC	−17.0		MnSi	−17.0	
MnN	−46.1		MnP	−23.0	
MnO_2	−124.4	−111.3	MnS	−49.0	−46.9
Ni_3C	9.0	7.6	Ni_3Si	−35.5	
Ni_3N	0.2		Ni_3P	−53.0	
NiO	−57.3	−50.6	Ni_3S_2	−47.5	

type (*TM* is a transition metal, *X* is a metalloid) stem from the hybridization of the *Xnp* and *TM3d* states. The contribution of the *Xnp* states predominates at the band bottom, while the *TM3d* states dominate in the high-energy region.

A comparison of the K_{β_1} bands of Si and P in the corresponding $Fe_{85}Si_{15}$ and $Fe_{80}P_{20}$ alloys (Figs. 1, 2) shows that, due to more *p* electrons participating in the chemical interaction, the hybridization effect in an $Fe_{80}P_{20}$ amorphous alloy is more pronounced than in an $Fe_{85}Si_{15}$ alloy. The energy distance between the main spectrum maximum and the 3*d*-like band in the PK_{β_1} spectrum of an $Fe_{80}P_{20}$ alloy (2.8 eV) is observed to be greater than the similar characteristic of the SiK_{β_1} band of the Fe–Si disordered alloys (2.6 eV).

From the data available in the literature [15, 16] and the results of this paper, it follows that an increase in the energy separation of the subbands in the x-ray emission K_{β_1} spectra of the metalloids takes place in the sequence Fe–Al (2.5 eV) [15] ⟶ Fe–Si (2.6 eV) ⟶ Fe–P (2.8 eV) ⟶ Fe–S (3.3 eV) [16]. Therefore, in terms of the approach proposed in this paper, an increase in the chemical interaction of the alloy components is observed in this sequence.

According to a qualitative model of the electronic-structure formation in $Fe_{1-x}Si_x$ and $Fe_{1-x}Sn_x$ disordered alloys [17], the formation of the covalent bonds with some shift of the electron density from the atom of the *sp* element (Si, Sn) to the Fe atom, with the active participation of the 3*d* electrons of the Fe atom, occurs at the concentrations $x > 10$–12 at. % Si and $x > 25$–30 at. % Sn, respectively. Obviously, due to an extra *p* electron possessed by an isolated phosphorus atom, the formation of such bonds should occur at a concentrations of P less than that of Si and Sn. This statement is supported by the behavior of the average Fe atom magnetic moment. Its value begins to decrease at a phosphorus concentrations of ~6 at. % for Fe–P disordered alloys [18].

It should be noted that, at the same metalloid concentration (for example, ~20 at. %) in Fe–Si and Fe–P disordered alloys, the average magnetic moment per Fe atom ($\overline{m}_{Fe}$) decreases in going from Fe–Si (1.8 μ_B) to Fe–P (1.65 μ_B). Therefore, as the hybridization character of the 3*d* electrons of the Fe atom and the 3*p* electrons of the metalloid (Si, P) changes, redistribution of the electron density occurs, resulting in a decrease in the average magnetic moment per Fe atom [18, 19].

Thus, an increase in the energy separation between the subbands in the x-ray emission spectra with a decrease in the main thermodynamic characteristics (ΔH^0_{298}, ΔG^0_{298}) is observed in the present work, which indicates that one goes to a compound with higher stability. On the basis of this correlation, it has been suggested that the chemical interaction in Fe–P disordered alloys is stronger than in Fe–Si alloys.

ACKNOWLEDGMENTS

REFERENCES

1. E. I. Gladyshevskiĭ, Yu. K. Gorelenko, I. D. Shcherba, and V. I. Yarovets, Metallofizika **31** (1), 63 (1995).

2. É. Z. Kurmaev, S. A. Nemnonov, V. P. Belash, and Yu. V. Efimov, Fiz. Met. Metalloved. **33** (3), 578 (1972).

3. S. A. Nemnonov, É. Z. Kurmaev, V. I. Minin, *et al.*, Fiz. Met. Metalloved. **30** (3), 569 (1970).

4. É. Z. Kurmaev, S. A. Nemnonov, A. Z. Men'shikov, and G. P. Shveĭkin, Izv. Akad. Nauk SSSR, Ser. Fiz. **31** (6), 996 (1967).

5. S. A. Nemnonov and É. Z. Kurmaev, Fiz. Met. Metalloved. **27** (5), 816 (1969).

6. E. Z. Kurmaev, V. P. Belash, S. A. Nemnonov, and A. S. Shulakov, Phys. Status Solidi B **61**, 365 (1974).

7. L. D. Finkel'shteĭn and S. A. Nemnonov, Fiz. Met. Metalloved. **32** (3), 662 (1971).

8. M. Kh. Karapet'yants and M. L. Karapet'yants, *Basic Thermodynamic Constants of Inorganic and Organic Matters* (Khimiya, Moscow, 1968).

9. V. I. Anisimov, A. V. Postnikov, É. Z. Kurmaev, and G. Wikh, Fiz. Met. Metalloved. **62** (4), 730 (1986).

10. E. P. Elsukov, V. P. Churakov, G. N. Konygin, and V. Ya. Bayankin, Metally, No. 1, 172 (1991).

11. É. Z. Kurmaev, V. M. Cherkashenko, and L. D. Finkel'shteĭn, *X-ray Spectra of Solids* (Nauka, Moscow, 1989).

12. V. Ya. Bayankin, V. I. Lad'yanov, V. A. Trapeznikov, and V. P. Churakov, Fiz. Met. Metalloved. **82** (1), 85 (1996).

13. K. Tanaka, M. Yoshino, and K. Suzuki, J. Phys. Soc. Jpn. **51** (12), 3882 (1982).

14. E. Belin, C. Bonnelle, S. Zuckerman, and F. Machizaud, J. Phys. F **14**, 625 (1984).

15. V. G. Zyryanov, V. I. Minin, S. A. Nemnonov, and M. F. Sorokina, Fiz. Met. Metalloved. **31** (2), 335 (1971).

16. S. A. Nemnonov, S. S. Mikhaĭlova, L. D. Finkel'shteĭn, *et al.*, Available from VINITI, No. 2695 (1974).

17. E. P. Elsukov, D. A. Korolev, O. M. Kanunnikova, *et al.*, Fiz. Met. Metalloved. **89** (3), 39 (2000).

18. E. P. Elsukov, Fiz. Met. Metalloved. **76** (5), 5 (1993).

19. E. P. Yelsukov, E. V. Voronina, G. N. Konygin, *et al.*, J. Magn. Magn. Mater. **166**, 334 (1997).

Translated by N. Kovaleva

METALS
AND SUPERCONDUCTORS

On the Specific Features and Transformation of the Band Structure of Mercury-Based HTSC Compounds

M. V. Elizarova, A. O. Lukin, and V. É. Gasumyants

St. Petersburg State Technical University, ul. Politechnicheskaya 29, St. Petersburg, 195251 Russia
e-mail: marina@twonet.stu.neva.ru
Received April 18, 2000

Abstract—A systematic analysis of the temperature dependences of the thermopower $S(T)$ for different phases of the $HgBa_2Ca_{n-1}Cu_nO_{2n+2+\delta}$ family ($n = 1, 2, 3$) at different doping levels is performed in the framework of a narrow-band phenomenological model. Quantitative estimates of the main parameters of the band responsible for conduction in the normal phase of $HgBa_2Ca_{n-1}Cu_nO_{2n+2+\delta}$ are given for optimally doped samples. The character of the variation in these parameters with an increasing number n of the copper–oxygen layers is discussed. A trend toward broadening of the conduction band with increasing n is revealed, which can be due to the increase of the density-of-states (DOS) peak near the Fermi level with an increasing number of the CuO_2 layers responsible for the formation of the conduction band. It is found that an increase in the number n leads to an increase in the fraction of localized carriers in the band owing to a more defective structure observed in the more complex phases of $HgBa_2Ca_{n-1}Cu_nO_{2n+2+\delta}$. The variations in the band-structure parameters in going from under- to overdoped compositions in the $HgBa_2Ca_{n-1}Cu_nO_{2n+2+\delta}$ family are also discussed. © *2000 MAIK "Nauka/Interperiodica".*

1. INTRODUCTION

The discovery of high-temperature superconductivity was followed by finding superconducting systems based on yttrium, bismuth, thallium, neodymium, mercury, and other elements, adding up to more than 50 various families of high-temperature superconductors (HTSCs). A record-high temperature of the superconducting transition T_c (about 130 and 160 K under atmospheric [1] and elevated pressure [2–4], respectively) was found in samples of the mercury-based $HgBa_2Ca_{n-1}Cu_nO_{2n+2+\delta}$ system for $n = 3$. Studies of the crystal structure and superconducting properties of $HgBa_2Ca_{n-1}Cu_nO_{2n+2+\delta}$ for different n made it possible to elucidate the dependence of T_c on the number of copper–oxygen layers [5, 6] and the oxygen content [7] in these compounds. Some works dealt with the transport properties of the $HgBa_2Ca_{n-1}Cu_nO_{2n+2+\delta}$ system, including the temperature dependences of the electrical resistivity [8–11] and the thermopower [8–12]. However, despite a fairly large body of experimental data available, their analysis is made difficult by the complexity of the crystal structure of mercury-based superconductors and the high defect concentration, specifically in phases with $n > 1$. As a result, the authors of [8–12], for instance, restricted themselves primarily to a discussion of the general character of the $S(T)$ dependences and to a purely qualitative analysis of the effect of doping on the magnitude of the thermopower.

At the same time, the family of mercury-based HTSCs is a very interesting subject for investigation, because the $HgBa_2Ca_{n-1}Cu_nO_{2n+2+\delta}$ system allows the realization of various oxygen saturation regimes and, of particularly importance, permits the obtainment of compositions with excess oxygen [8, 12], which is extremely difficult to achieve, for instance, in the $YBa_2Cu_3O_y$ system. Moreover, a comparative study of a series of the $HgBa_2Ca_{n-1}Cu_nO_{2n+2+\delta}$ solid solutions with different n offers the possibility of following the change in the properties of the material with an increasing number of the copper–oxygen layers. This can provide important information on the nature of the band responsible for the conduction and on the relation of the characteristics of the charge carrier system in the normal phase with the superconducting properties of a given compound.

It is apparently the complexity of the mercury-based superconductors that accounts for the extreme paucity of available theoretical band-structure calculations for this system. In this connection, phenomenological models have a serious advantage. One of them, which permits one to obtain information on the band structure from the temperature dependences of the transport coefficients, is the narrow-band model [13]. As was repeatedly shown earlier, this model provides a means for determining the main parameters of the band responsible for conduction in the normal phase and of following their variation as the yttrium- [13–15] and bismuth-based [16, 17] superconducting systems deviate from the stoichiometric composition. The most informative of the transport coefficients is the thermopower S. The purpose of this work was to check the applicability of the narrow-band model to mercury-based HTSCs and to analyze, in terms of this model, the

experimental dependences $S(T)$ obtained for the $HgBa_2CuO_{4+\delta}$, $HgBa_2CaCu_2O_{6+\delta}$, and $HgBa_2Ca_2Cu_3O_{8+\delta}$ phases with different oxygen contents in order to estimate the band structure parameters for the above phases, as well as to study their transformation under the variation of both the number of the copper–oxygen layers and the oxygen content.

2. STARTING DATA

The band structure parameters of mercury-based superconductors were analyzed on the basis of the available experimental data on the temperature dependences of the thermopower for the following phases: $HgBa_2CuO_{4+\delta}$ (abbreviated as Hg-1201) [8, 12], $HgBa_2CaCu_2O_{6+\delta}$ (Hg-1212) [9, 12], and $HgBa_2Ca_2Cu_3O_{8+\delta}$ (Hg-1223) [10–12]. All samples were prepared by the standard solid-phase method from the corresponding oxides. Different oxygen saturations of the samples were achieved by employing different regimes of the final annealing. The Hg-1212 and Hg-1223 samples studied in [12] were synthesized at a pressure of 3 kbar and the Hg-1201 samples were synthesized at atmospheric pressure. Then, the samples of all three phases were annealed at different partial oxygen pressures (from 10^{-7} to 2×10^2 atm) in the temperature range 260–450°C. In [8], the Hg-1201 samples were annealed in an oxygen flow at 300 and 500°C for different times (from 1 to 40 h). The Hg-1212 samples studied in [9] were subjected to a final annealing in an oxygen flow at 200°C for 10 and 35 h. In [10], the samples of the Hg-1223 phase were annealed at 400–500°C for 24–124 h. In all cases, the single-phase state of the samples and their crystal structure were tested by neutron diffraction and x-ray powder diffraction analyses.

3. SPECIFIC FEATURES IN THE TEMPERATURE DEPENDENCES OF THE THERMOPOWER OF MERCURY-BASED HTSCS

Figure 1 shows typical temperature dependences of the thermopower in samples of the mercury-based HTSC system for the Hg-1201, Hg-1212, and Hg-1223 phases doped to a level optimal for their superconducting properties. It is seen that the $S(T)$ dependences obtained for close-to-optimally doped samples of each phase are typical of all chainless HTSCs [18]. The temperature dependences of the thermopower exhibit a clearly pronounced maximum at a temperature above the superconducting transition and a linear portion above this maximum, extending to $T = 300$ K, where S decreases with an increase in temperature. As the oxygen content in samples of each phase increases, the thermopower decreases in magnitude. As a result, the thermopower at room temperature, S_{300}, becomes negative for some compositions. The thermopower S_{300} for optimally doped samples of the Hg-1201 and Hg-1212 phases is ±1 μV/K and –0.5 to +2 μV/K, respectively.
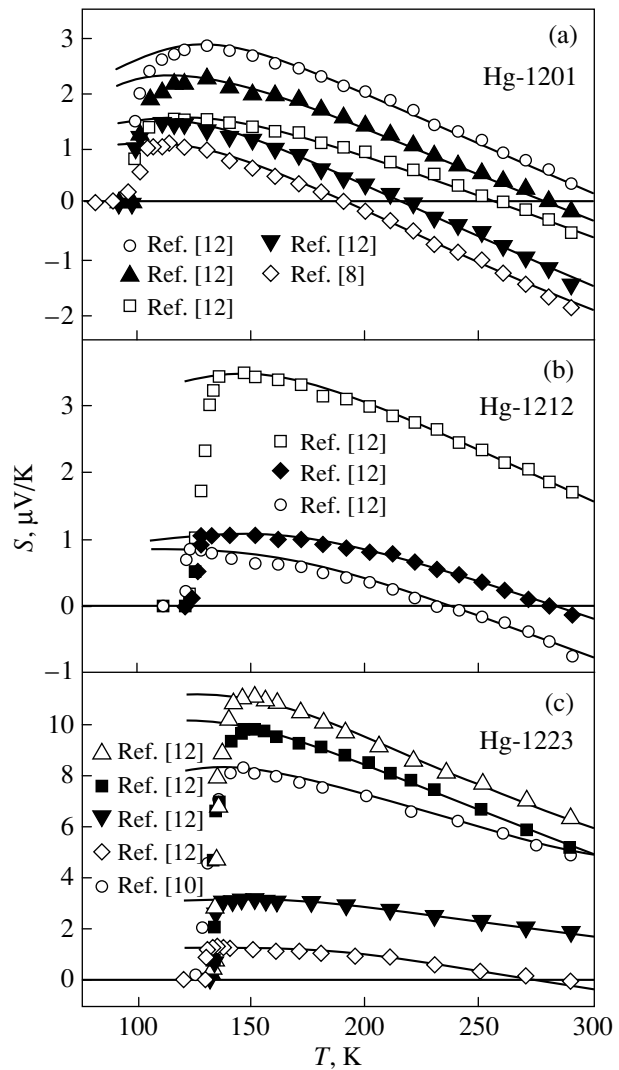

Fig. 1. Temperature dependences of the thermopower of optimally doped compositions of the (a) Hg-1201, (b) Hg-1212, and (c) Hg-1223 phases. Different symbols correspond to the optimally doped samples at different oxygen contents (the oxygen content increases with a decrease in the magnitude of the thermopower). Solid lines are the dependences calculated in terms of the narrow-band model.

The range of variation in the absolute values of S for the Hg-1223 phase is somewhat broader than that for the above two phases, and S_{300} varies from 0 to 8 μV/K. As is seen from Fig. 1a, T_c for the Hg-1201 phase with a close-to-optimum oxygen content varies within the narrow range 95–98 K. For the Hg-1212 and Hg-1223 phases, the critical temperature is $T_c \approx 120$ and ≈ 135 K, respectively (Figs. 1b, 1c).

Figures 2a and 2b display typical dependences $S(T)$ for samples of each phase in the case of oxygen deficiency (underdoped samples) and oxygen excess (overdoped samples). The only exception is the overdoped Hg-1223 phase, because information on the details of the preparation of these samples is lacking. Unfortu-
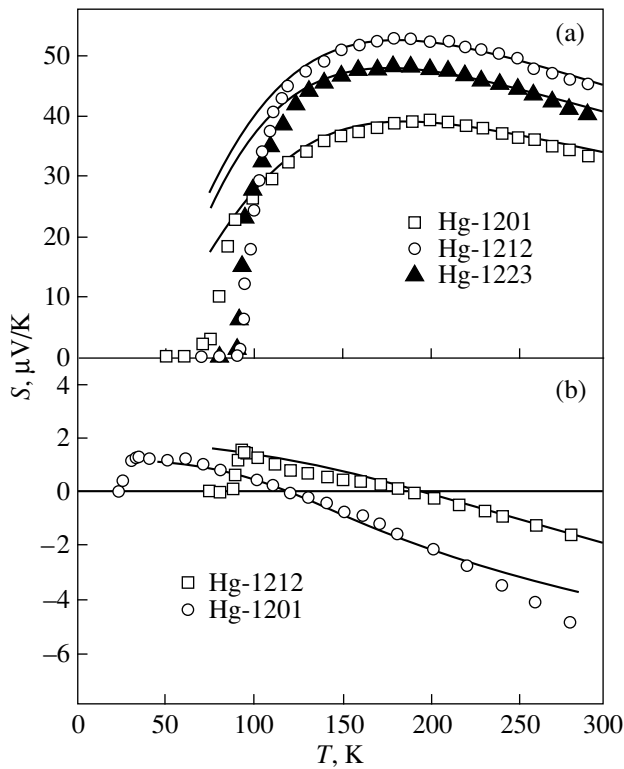
Fig. 2. Temperature dependences of the thermopower of the mercury-based system for different deviations from the stoichiometric composition [12]: (a) underdoped (Hg-1201, Hg-1212, and Hg-1223) and (b) overdoped (Hg-1201 and Hg-1212) samples (different symbols). Solid lines are the dependences calculated in terms of the narrow-band model.

nately, the papers used by us in the analysis, rather than quoting the value of the oxygen index for the samples studied, specify only the direction of its variation from one sample to another. For this reason, we will discuss below only the general trends in the variation of the band structure parameters for under- and overdoped phases of the mercury-based HTSCs.

The absolute values of the thermopower for underdoped samples of each phase are higher than those for the optimally oxygen-doped compositions. An increase in the doping level leads to a progressive increase in the thermopower S_{300} from 10 to 50 μV/K for the Hg-1201 and Hg-1212 phases and from 25 to 40 μV/K for the Hg-1223 phase. The maximum in the temperature dependences of the thermopower in this case becomes more diffuse and shifts toward higher temperatures. Note that a similar transformation of the $S(T)$ dependences is observed upon going over from the optimally doped to underdoped samples of bismuth-based superconductors [16, 18]. As the material becomes underdoped, the magnitude of T_c decreases for all phases of the mercury-based system.

The temperature dependences of the thermopower for overdoped samples of Hg-1201 and Hg-1212 exhibit negative or close-to-zero absolute values $S_{300} =$

$-(2–6)$ μV/K. The maximum in the $S(T)$ dependences becomes narrower, and as the oxygen content increases still more (the heavily overdoped regime), it disappears altogether. The magnitude of the thermopower decreases monotonically with a decrease in temperature in the range of negative S. We have not been able to find any literature data on the $S(T)$ dependences for overdoped samples of the Hg-1223 phase. In overdoped Hg-1201 and Hg-1212 samples, T_c also decreases.

Summing up, note the main features observed in the temperature dependences of the thermopower of the mercury-based system. The $S(T)$ dependences for samples of the Hg-1201, Hg-1212, and Hg-1223 phases are qualitatively similar to those measured for other chainless HTSC systems. The room-temperature values of the thermopower S_{300} range from dozens of μV/K for underdoped compositions to a few μV/K for optimally doped samples, and S_{300} becomes negative for overdoped compositions. A gradual increase in the oxygen content (from underdoped $\longrightarrow$ optimally doped $\longrightarrow$ overdoped compositions) brings about a transformation of the temperature dependences of the thermopower, so that the maximum of $S(T)$ becomes narrower and the values of S_{300}, as well as those of S at the maximum of the $S(T)$ curve, decrease with an increase in the oxygen content.

We present below an analysis of the experimental data in terms of the narrow-band model. We are first going to consider the $S(T)$ dependences for compositions with a close-to-optimum oxygen content [8–10, 12] and use the results of the analysis for all the above phases to determine the main band-structure parameters. Then, we will examine the character of the band-structure transformation in going from optimally doped to underdoped and overdoped compositions.

4. ANALYSIS OF EXPERIMENTAL DATA

The narrow-band model used here to analyze the temperature dependences of the thermopower for the Hg-1201, Hg-1212, and Hg-1223 mercury-based superconductors was described in detail in [13]. This model is based on the assumption that the band structure of HTSC materials contains a narrow density-of-states (DOS) peak, whose existence accounts for the main features of carrier transfer in the normal phase. One of the possible reasons for the formation of such a narrow peak could be the Van Hove singularity in the electron energy spectrum [19–21]. It was shown earlier [13] that if the condition of a narrow conduction band is satisfied, the actual form of the dispersion relation and of the energy dependence of the relaxation time are inessential. This permits one to approximate the DOS function $D(E)$ and the differential conductivity $\sigma(E)$ in the calculation of the temperature dependences of the chemical potential μ and the transport coefficients by

rectangles. In this approximation, the $S(T)$ dependence can be represented in the form [13]

$$
S = -\frac{k_B}{e}\left\{ \frac{W_\sigma^*}{\sinh W_\sigma^*}\left[\exp(-\mu^*) + \cosh W_\sigma^* \right.\right.
$$

$$
\left. -\frac{1}{W_\sigma^*}(\cosh\mu^* + \cosh W_\sigma^*) \right. \tag{1}
$$

$$
\left.\left. \times \ln\frac{\exp(\mu^*) + \exp(W_\sigma^*)}{\exp(\mu^*) + \exp(-W_\sigma^*)} \right] - \mu^* \right\},
$$

$$
\mu^* \equiv \frac{\mu}{k_B T} = \ln\frac{\sinh(FW_D^*)}{\sinh((1-F)W_D^*)}, \tag{2}
$$

where $W_D^* \equiv W_D/2k_B T$ and $W_\sigma^* \equiv W_\sigma/2k_B T$. Thus, the $S(T)$ dependence can be described using three model parameters: W_D is the total effective bandwidth; W_σ is the bandwidth associated with conduction (the $C \equiv W_\sigma/W_D$ ratio characterizes the degree of carrier localization); and F is the degree of band filling by electrons, which is equal to the ratio of the number of electrons to the total number of states in the band. By properly varying their values so as to obtain the best fit of the calculated data to the experimental temperature dependence of the thermopower, one can determine the model parameters for each sample studied and follow the transformation of these parameters for various deviations from stoichiometry [13–17].

The pattern of the $S(T)$ dependences for mercury-based HTSCs, as well as the results obtained earlier for the bismuth-based HTSC system [16, 17], indicate that, in order to analyze the behavior of the thermopower in the $HgBa_2Ca_{n-1}Cu_nO_{2n+2+\delta}$ system, one has to invoke the assumption of a weak asymmetry of the conduction band. The simplest way to take this band asymmetry into account is to introduce a certain distance bW_D (where b is the asymmetry parameter) between the centers of the rectangles approximating the $D(E)$ and $\sigma(E)$ functions [13, 16, 17]. In this case, expression (1) remains valid if μ^* calculated by formula (2) is replaced with $(\mu^*)' = \mu^* - bW_D/k_B T$.

At the first stage, we analyzed experimental data on the thermopower for close-to-optimally doped samples of the Hg-1201, Hg-1212, and Hg-1223 phases. It should be noted that in the framework of the symmetric narrow-band model, the set of the model parameters for a specific sample is determined unambiguously from the $S(T)$ dependence [13]. The introduction of the fourth parameter, i.e., the parameter b accounting for the degree of band asymmetry, extends the range of variations in the other parameters, which can make their determination ambiguous. To find the extent of this ambiguity, the band structure parameters were calculated repeatedly for each experimental dependence $S(T)$, with C or b fixed. This allowed one to determine

the possible range of variations in these parameters, which was found to be 0.3–0.5 for the C parameter and –(0.02–0.05) for parameter b. Note that, in the former case, this range is in accord with the results obtained earlier for yttrium-based [13–15] and bismuth-based [16, 17] HTSCs for a close-to-optimum doping level and the asymmetry parameters are close in magnitude to those for the bismuth-based HTSCs [16, 17]. These results were then used to carry out calculations for each sample with the aim of obtaining all possible sets of model parameters that would satisfactorily describe the experimental dependences $S(T)$ for this sample. To illustrate the fit of the calculated dependences $S(T)$ to the experiment, Fig. 1 presents calculated curves for some samples of each phase to be compared with the experimental data. Thus, the possible range of variations in each of the four parameters was determined for each given sample. The results of these calculations are listed in Table 1. Therefore, the width of the possible range of variations in the model parameters can be considered an error in the determination of their values, which arises upon the inclusion of the conduction-band asymmetry.

One of the main goals of this work was to estimate the main band-structure parameters of mercury-based superconductors as a whole and to reveal the differences between the simplest and more complex phases. To accomplish this, we had to analyze the most complete possible set of experimental data obtained on different samples of each of the phases (Hg-1201, Hg-1212, and Hg-1223). Thus, the second stage of our analysis consisted in generalizing the results obtained for specific samples, i.e., in determining the range of variations in the band-structure parameters characteristic of each optimally doped $HgBa_2Ca_{n-1}Cu_nO_{2n+2+\delta}$ phase. The results thus obtained are presented in Table 2. For each of the Hg-1201, Hg-1212, and Hg-1223 phases, we determined the range of possible values of all four band-structure parameters, namely, the effective bandwidth, the band filling, the degree of localization of the states, and the band asymmetry. It should be pointed out that the ranges of variations in F, W_D, C, and b (Table 2) characterize primarily not the errors in the calculations but rather the ranges of possible values of the band-structure parameters for each phase, which are associated with a generalization of the results obtained in an analysis of data on a large set of samples.

5. BAND-STRUCTURE TRANSFORMATION OF MERCURY-BASED HTSCs WITH AN INCREASING NUMBER OF COPPER–OXYGEN LAYERS

We now turn to the discussion and interpretation of the results obtained. As is seen from Table 2, there is a trend to a gradual broadening of the band in going from the simple Hg-1201 phase to the more complex ones, Hg-1212 and Hg-1223. Indeed, the effective bandwidth

Table 1. Band structure parameters calculated for different optimally doped samples of the Hg-1201, Hg-1212, and Hg-1223 phases within the narrow-band model

Reference	F	W_D, meV	C	b
		Hg-1201 phase		
[12]	0.475–0.487	80–135	0.34–0.45	−0.024…−0.030
	0.474–0.488	70–135	0.31–0.63	−0.021…−0.029
	0.473–0.487	85–135	0.31–0.51	−0.018…−0.020
	0.473–0.486	70–120	0.30–0.59	−0.020…−0.032
[8]	0.452–0.485	70–133	0.38–0.69	−0.024…−0.050
		Hg-1212 phase		
[12]	0.474–0.489	100–190	0.28–0.44	−0.021…−0.022
	0.471–0.486	110–190	0.25–0.55	−0.017…−0.021
	0.471–0.488	95–145	0.26–0.41	−0.015…−0.024
[9]	0.481–0.496	90–155	0.35–0.41	−0.032…−0.050
	0.423–0.493	90–135	0.31–0.54	−0.038…−0.051
	0.470–0.496	90–160	0.32–0.42	−0.024…−0.040
		Hg-1223 phase		
[12]	0.466–0.488	100–155	0.26–0.34	−0.042…−0.050
	0.466–0.485	95–150	0.28–0.41	−0.048…−0.050
	0.474–0.494	95–185	0.20–0.31	−0.015…−0.018
	0.462–0.487	95–175	0.22–0.42	−0.016…−0.040
[10]	0.469–0.494	95–180	0.36–0.50	−0.029…−0.045
	0.479–0.494	95–160	0.28–0.48	−0.022…−0.032
	0.471–0.496	100–205	0.21–0.50	−0.026…−0.041
	0.468–0.496	95–210	0.27–0.41	−0.040…−0.050
	0.471–0.503	95–175	0.22–0.47	−0.040…−0.050

in samples of the Hg-1201 phase varies from 70 to 135 meV, whereas for Hg-1212 and Hg-1223, this range is W_D = 90–190 and 95–210 meV, respectively. Note that an increase in the number of the copper–oxygen layers brings about not only a shift of the W_D range toward larger values, but its slight broadening as well. The width of the range of band filling by electrons, F, practically does not change as one transfers from the simpler Hg-1201 phase to more complex ones. The band asymmetry is small for all phases and amounts to 2–5% of the bandwidth. As regards the degree of localization of the states, it is the smallest for the simplest phase Hg-1201 (the largest ratio of the range of delo-

Table 2. Ranges of band-structure parameter variation for different optimally doped phases of the mercury-based system

Phase	F	W_D, meV	C	b
Hg-1201	0.45–0.49	70–135	0.3–0.7	−0.02…−0.05
Hg-1212	0.46–0.495	90–190	0.25–0.55	−0.02…−0.05
Hg-1223	0.45–0.5	95–210	0.2–0.5	−0.02…−0.05

calized states to the total bandwidth is $C \equiv W_\sigma/W_D$) and increases slightly for the more complex phases.

Let us discuss these trends in the character of the band-structure transformation with increasing n in their relation to the superconducting properties of the $HgBa_2Ca_{n-1}Cu_nO_{2n+2+\delta}$ system.

As is well known from experiments, the value of T_c for $HgBa_2Ca_{n-1}Cu_nO_{2n+2+\delta}$ increases gradually with an increasing number of the copper–oxygen layers for $n < 4$ [22]. It has been established that it is the presence of the CuO_2 layers that is crucial for the onset of high-temperature superconductivity; i.e., these layers form the band responsible both for the superconducting properties of the HTSCs and for the conductivity of these compounds in the normal phase. We believe that both these points agree well with our results of the analysis of the thermopower. As was already mentioned, we revealed a trend toward a gradual increase in the conduction-band width with an increasing number n. The existence of this trend can be considered to be due to the fact that an increase in the number of the copper–oxygen layers responsible for the formation of a narrow conduction band brings about an increase in the total number of states in the band, i.e., an increase in the

DOS peak on the whole and, in particular, in its broadening. In this case, the improvement of the superconducting properties in the $HgBa_2Ca_{n-1}Cu_nO_{2n+2+\delta}$ system with increasing n can be caused by an increase in the magnitude of the DOS function at the Fermi level $D(E_F)$. A similar broadening of the conduction band with an increasing number of copper–oxygen layers, which was accompanied by an improvement of the superconducting properties, was also observed in [16] for bismuth-based HTSCs upon going from the Bi-2212 to Bi-2223 phase.

On the other hand, the overall complication of the structure with an increase in the number of copper–oxygen layers renders the Hg-1223 system potentially more defective than Hg-1212 and Hg-1201. As was noted in [23], this affects the W_D range characteristic of these phases. Indeed, our calculations showed that the W_D range for the simplest phase Hg-1201 is somewhat narrower than that for the Hg-1212 and Hg-1223 phases. We believe that the broadening of this range, specifically the elevation of its upper boundary, is caused by the effect of the disorder introduced into the system by phase inhomogeneities and various structural defects, whose formation becomes enhanced substantially with increasing n. Additional evidence for an increase in the concentration of defects in more complex phases of the compound is provided by our calculations of the degree of localization, which slightly increases when going over from Hg-1201 to Hg-1212 and, further, to Hg-1223 (the C parameter decreases, as is seen from Table 2). However, the broadening of the band and an increase in the number of localized states at its edges as a result of the disordering, which occur in accordance with the Anderson model, are minor, while negative, factors for the superconducting properties. As a result, although a structure imperfection can bring about a decrease in $D(E_F)$ because of the band broadening and, hence, a drop of the T_c temperature, an increase in the number of the copper–oxygen layers in more complex phases provides a noticeable general growth of the DOS peak and, hence, an improvement in the superconducting properties.

Note that the band filling F in optimally doped samples varies within the same range for all three phases (Table 2). This implies that the ratio of the number of electrons to the total number of states in the band remains unchanged with increasing n; i.e., an increase in the number of states in the band is accompanied by an increase in the number of free carriers.

Thus, the results obtained give grounds to maintain that the narrow-band model is applicable to optimally doped mercury-based HTSCs and offers the possibility of estimating the band-structure parameters for samples of different phases and of analyzing the trends in their changes with an increasing number of copper–oxygen layers.

6. TRANSFORMATION OF THE $HgBa_2Ca_{n-1}Cu_nO_{2n+2+\delta}$ BAND STRUCTURE WITH OXYGEN NONSTOICHIOMETRY

The next step of our work consisted in analyzing the transformation of the $HgBa_2Ca_{n-1}Cu_nO_{2n+2+\delta}$ band-structure upon going to nonoptimally doped compositions of Hg-1201, Hg-1212, and Hg-1223. For this purpose, we used the above approach to analyze the available experimental data on the temperature dependences of the thermopower for the underdoped [8, 12] and overdoped [8, 12] samples of different phases. As is seen from Fig. 2, in this case, the experimental and calculated dependences $S(T)$ are in good agreement. The results of the calculations performed for each of the compositions studied are listed in Tables 3 and 4. Note that because of the difficulties encountered in preparing samples of the Hg-1223 phase, particularly of those with an oxygen nonstoichiometry, experimental data on the transport properties of these samples are extremely scarce. Treatment and analysis of the data obtained on single samples and presented in [12] cannot provide reliable information on the band structure of this phase. For this reason, we cannot estimate the probable ranges of the band-structure parameters for Hg-1223 samples deviating strongly from stoichiometry. Nevertheless, it was found that all the trends in the variation of the band-structure parameters with an increasing number of copper–oxygen layers, which were revealed for optimally doped samples, remain valid for the overdoped and underdoped compositions as well.

Consider the character of the band-structure transformation of the Hg-1201 and Hg-1212 phases under variation of the doping level. As follows from our calculations, an increase in the oxygen content throughout the range covered brings about a decrease in the band filling by electrons, which reflects the acceptor nature of the additional oxygen anions doped into the system. The overlap of the ranges of variations in F (and the other parameters too) in various regimes is readily accounted for if one takes into account that the division into the underdoped, overdoped, and optimally doped ranges is fairly conventional. As a result, marginal samples can belong to either one or the other composition. Note that as the oxygen content in each of the mercury-based HTSC compositions increases, the degree of the conduction-band asymmetry remains practically unchanged and does not exceed 5%.

As one goes over from the optimally doped to underdoped compositions, the band responsible for conduction broadens substantially. Indeed, for an optimally doped Hg-1201 phase, the W_D values range from 70 to 135 meV, whereas the conduction-band width in the underdoped Hg-1201 increases gradually to $W_D = 240$–360 meV for the largest deviation from the optimally doped composition. A similar trend to a broadening of the conduction band for underdoped compositions is observed in the Hg-1212 phase as well (see

Table 3. Band structure parameters calculated for different underdoped samples of the Hg-1201, Hg-1212, and Hg-1223 phases within the narrow-band model

Reference	F	W_D, meV	C	b
		Hg-1201 phase		
[8]	0.471–0.483	155–245	0.25–0.35	−0.027…−0.031
[12]	0.492–0.492	140–235	0.18–0.31	−0.024…−0.034
	0.500–0.525	195–310	0.15–0.26	−0.021…−0.049
	0.530–0.558	245–360	0.16–0.23	−0.022…−0.039
		Hg-1212 phase		
[12]	0.493–0.506	155–240	0.18–0.33	−0.016…−0.027
	0.500–0.537	170–295	0.17–0.28	−0.017…−0.026
	0.502–0.548	175–340	0.16–0.28	−0.018…−0.035
	0.515–0.547	210–380	0.17–0.27	−0.013…−0.048
		Hg-1223 phase		
[12]	0.496–0.510	160–370	0.22–0.26	−0.016…−0.032
	0.508–0.529	160–260	0.18–0.24	−0.020…−0.035

Note: The samples of each phase are placed in the order of decreasing oxygen content.

Table 4. Band structure parameters calculated for overdoped samples of the Hg-1201 and Hg-1212 phases within the narrow-band model

Reference	F	W_D, meV	C	b
		Hg-1201 phase		
[12]	0.459–0.473	79–100	0.27–0.49	−0.033…−0.044
	0.465–0.476	55–80	0.21–0.35	−0.032…−0.036
[8]	0.464–0.470	60–70	0.34–0.47	−0.030…−0.038
		Hg-1212 phase		
[12]	0.470–0.477	72–115	0.40–0.63	−0.031…−0.036
	0.472–0.483	66–110	0.21–0.45	−0.021…−0.028

Note: The samples of each phase are placed in the order of increasing oxygen content.

Table 3). Note also that the degree of localization of states with an increase in the oxygen deficiency reveals a weak trend to an increase (the C parameter decreases) for both phases. Thus, the band-structure transformation in underdoped phases of the $HgBa_2Ca_{n-1}Cu_nO_{2n+2+\delta}$ system is similar in character to that observed earlier for $YBa_2Cu_3O_y$ with an increase in the oxygen deficiency or under nonisovalent doping (i.e., when going from close-to-stoichiometric to underdoped compositions) [13–15] and for $Bi_2Sr_2CaCu_2O_y$, when calcium is partially replaced by trivalent rare-earth elements [16, 17]. In our opinion, this implies that the mechanism of the band-structure transformation in underdoped compositions of the mercury-based HTSC family is the same as in the yttrium- and bismuth-based HTSCs. In particular, a decrease in the oxygen content brings about lattice disordering, which results, in accordance with the Anderson model, in a broadening of the conduction band and is accom-

panied by localization of states at its edges. The band broadening entails a decrease in the DOS function at the Fermi level, which, in turn, leads to a decrease in T_c.

An analysis of the experimental data on overdoped compositions does not yield reliable information on the character of the band-structure transformation, which is a result of the paucity of these data. Nevertheless, a trend was found of only a slight change and, possibly, even of some decrease in the conduction-band width with an increase in the oxygen content above the stoichiometric value and some increase in the degree of localization of states for the Hg-1201 and Hg-1212 phases (Table 4). Hence, introduction of excess oxygen into the system is not as disordering a factor as is an increasing oxygen deficiency. However, overdoped mercury-based HTSC compositions also exhibit a decrease in T_c. This means that the mechanism of the effect of excess oxygen on the band structure of the mercury-based HTSC system and the reasons for the
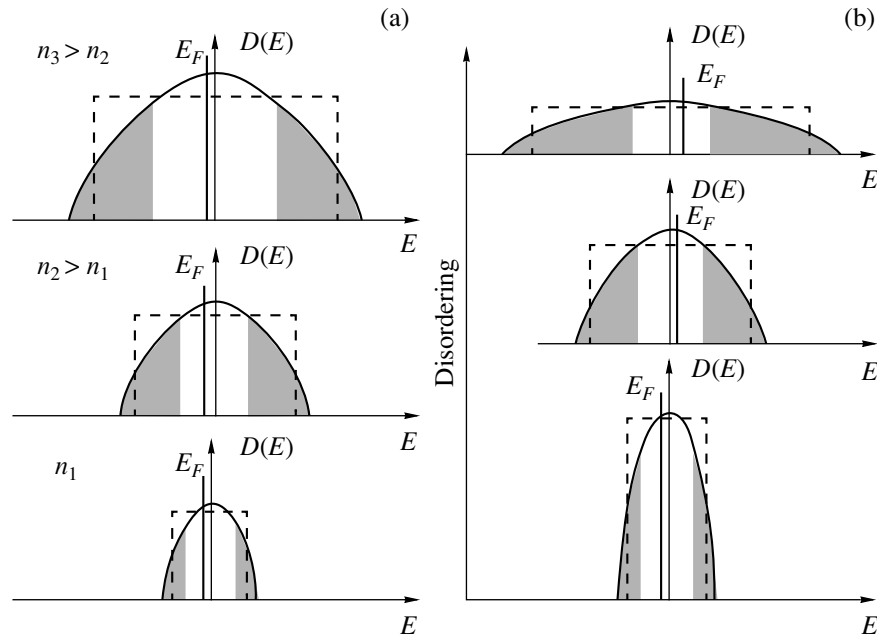
Fig. 3. Mechanisms of band-structure modification in $HgBa_2Ca_{n-1}Cu_nO_{2n+2+\delta}$: (a) band broadening and an increase in the DOS peak with an increasing number of copper–oxygen layers n and (b) band broadening and a decrease in the DOS peak with increasing disorder (increased concentration of structural defects). The shaded regions correspond to localized states at the conduction-band edges, and the rectangles show the approximation used to calculate the thermopower in terms of the narrow-band model.

suppression of superconductivity in this case differ radically from those in the underdoped regime. It should be pointed out that the complexity of the system under study, the lack of reliable information on the crystal-structure transformation of mercury-based HTSCs in the case of a large oxygen excess, and the scarce data available on the behavior of the thermopower in overdoped compositions impede analysis of the data obtained and hamper their generalization. The mechanism by which superconductivity is suppressed in overdoped compositions of mercury-based HTSCs is undoubtedly an extremely interesting issue, which should be a subject of further studies.

In conclusion, let us compare the effects of two different mechanisms of band-structure transformation in $HgBa_2Ca_{n-1}Cu_nO_{2n+2+\delta}$ compounds, which act on the superconducting properties of the mercury-based HTSC family. On the one hand, an increase in the number of copper–oxygen layers results, as was already mentioned, in a growth of the DOS peak as a whole (Fig. 3a). For the value $F \approx 0.5$, which varies only weakly in optimally doped phases with different n, this effect causes an increase in $D(E_F)$, thus providing an increase in T_c with increasing n. On the other hand, the doping-induced lattice disorder in each phase, as well as the increase in the defect concentration when going over from Hg-1201 to Hg-1212 and, finally, to Hg-1223, entails a broadening of the band and an increase in the localization of states at its edges by the Anderson mechanism (Fig. 3b). For the phases with larger n, the

action of this effect on the decrease in $D(E_F)$ becomes smaller compared to the first mechanism. As a result, despite the relative drop of $D(E_F)$ associated with a more defective structure in the more complex phases, the T_c temperature increases. When going from optimally doped to underdoped compositions within each phase, this mechanism becomes dominant and causes suppression of the superconducting properties with an increasing doping level.

Thus, a systematic analysis of the temperature dependences of the thermopower in the $HgBa_2Ca_{n-1}Cu_nO_{2n+2+\delta}$ system ($n = 1, 2, 3$) within the framework of the narrow-band model has yielded the following main results and conclusions:

(1) The narrow-band model is applicable to mercury-based high-temperature superconductors and permits determination of the main band-structure parameters for optimally doped samples of the $HgBa_2Ca_{n-1}Cu_nO_{2n+2+\delta}$ phases ($n = 1, 2, 3$); it also allows one to reveal trends in their variation in going over from underdoped to overdoped compositions.

(2) The total effective width of the band responsible for conduction in optimally doped mercury-based HTSCs varies from 70 to 200 meV, and the band is close to half-filling by electrons. Mercury-based HTSCs are characterized also by a slightly asymmetric conduction band.

(3) A comparative study of the Hg-1201, Hg-1212, and Hg-1223 phases has revealed a trend to a gradual broadening of the conduction band with an increase in

the number of the copper–oxygen layers. This is possibly due to an increase in the DOS peak as a result of a larger number of the copper–oxygen layers involved in its formation.

(4) The probable higher defect concentration of the more complex Hg-1212 and Hg-1223 phases, as compared to Hg-1201, manifests itself in a broadening of the range of variations in the band parameters characteristic of these phases and brings about an increase in the localization of states with an increasing number of the copper–oxygen layers.

(5) The transition to underdoped compositions is accompanied by a broadening of the conduction band and an increase in the fraction of localized states at its edges, which are caused by the Anderson mechanism of localization of states due to structural disordering. The band broadening results in a drop of the DOS function at the Fermi level, which may be the reason for the suppression of superconductivity in underdoped compositions.

REFERENCES

1. A. Schilling, M. Cantoni, J. D. Guo, and H. R. Ott, Nature **363** (6424), 56 (1993).
2. C. W. Chu, L. Gao, F. Chen, *et al.*, Nature **365** (6444), 323 (1993).
3. L. Gao, Philos. Mag. Lett. **68** (6), 345 (1993).
4. L. Gao, Y. Y. Xue, F. Chen, *et al.*, Phys. Rev. B **50** (6), 4260 (1994).
5. X. Zhou, M. Cardona, C. W. Chu, *et al.*, Phys. Rev. B **54** (9), 6137 (1996).
6. B. A. Scott, E. Y. Suard, C. C. Tsuei, *et al.*, Physica C (Amsterdam) **230** (3–4), 239 (1994).
7. Q. Xiong, Y. Y. Xue, Y. Cao, *et al.*, Phys. Rev. B **50** (14), 10346 (1994).
8. C. K. Subramaniam, M. Paranthaman, and A. B. Kaiser, Physica C (Amsterdam) **222** (1–2), 47 (1994).
9. Y. T. Ren, J. Clayhold, F. Chen, *et al.*, Physica C (Amsterdam) **217** (1–2), 6 (1993).
10. C. K. Subramaniam, M. Paranthaman, and A. B. Kaiser, Phys. Rev. B **51** (2), 1330 (1995).
11. A. Carrington, D. Colson, Y. Dumont, *et al.*, Physica C (Amsterdam) **234** (1–2), 1 (1994).
12. F. Chen, Q. Xiong, Y. Y. Xue, *et al.*, Preprint No. 96 : 006 (Texas Center for Superconductivity, 1996).
13. V. E. Gasumyants, V. I. Kaidanov, and E. V. Vladimirskaya, Physica C (Amsterdam) **248** (2–3), 255 (1995).
14. V. É. Gasumyants, E. V. Vladimirskaya, M. V. Elizarova, and I. B. Patrina, Fiz. Tverd. Tela (St. Petersburg) **41** (3), 389 (1999) [Phys. Solid State **41**, 350 (1999)].
15. M. V. Elizarova and V. É. Gasumyants, Fiz. Tverd. Tela (St. Petersburg) **41** (8), 1363 (1999) [Phys. Solid State **41**, 1248 (1999)].
16. N. V. Ageev, V. É. Gasumyants, and V. I. Kaĭdanov, Fiz. Tverd. Tela (St. Petersburg) **37** (7), 2152 (1995) [Phys. Solid State **37**, 1171 (1995)].
17. V. E. Gasumyants, N. V. Ageev, E. V. Vladimirskaya, *et al.*, Phys. Rev. B **53** (2), 905 (1996).
18. A. B. Kaiser and C. Ucher, in *Studies of High Temperature Superconductors,* Ed. by A. V. Narlikar (Nova Science, New York, 1991), Vol. 7 (and references therein).
19. F. Chen, Z. J. Huang, R. L. Meng, *et al.*, Phys. Rev. B **48** (21), 16047 (1993).
20. D. L. Novikov, O. N. Mryasov, and A. J. Freeman, Physica C (Amsterdam) **219** (1–2), 246 (1994).
21. D. L. Novikov, O. N. Mryasov, and A. J. Freeman, Physica C (Amsterdam) **222** (1–2), 38 (1994).
22. C. W. Chu, Preprint No. 96 : 011 (Texas Center for Superconductivity, 1996).
23. J. D. Jorgensen, D. G. Hinks, O. Chmaissem, *et al.*, in *Proceedings of the First Polish–US Conference on High Temperature Superconductivity* (Springer-Verlag, New York, 1996).

Translated by G. Skrebtsov

<div align="center">

**SEMICONDUCTORS
AND DIELECTRICS**

Charge Transfer in TlFeS$_2$ and TlFeSe$_2$

S. N. Mustafaeva, É. M. Kerimova, and A. I. Dzhabbarly

Institute of Physics, Academy of Sciences of Azerbaijan, pr. Narimanova 33, Baku, 370143 Azerbaijan

Received March 13, 2000

</div>

Abstract—The temperature dependences of the conductivity and the thermoelectric coefficient in TlFeS$_2$ and TlFeSe$_2$ samples have been investigated in the temperature range 85–400 K. The variable-range hopping conduction has been established. It is found that the density of localized states N_F near the Fermi level is 1.7×10^{18} and 3.3×10^{18} eV^{-1} cm^{-3}, and the average hopping length R is 109 and 104 Å for TlFeS$_2$ and TlFeSe$_2$, respectively. The non-Arrhenius (activationless) behavior of the hopping conductivity is established in the temperature region $T < 200$ K for TlFeS$_2$ and $T < 250$ K for TlFeSe$_2$. © *2000 MAIK "Nauka/Interperiodica"*.

The triple compounds TlFeS$_2$ and TlFeSe$_2$ belong to the semiconductor group that has magnetic properties. Only limited data on the chemical characteristics of their crystals are available in the literature [1, 2], and their physical properties are poorly understood. The only exception is reference [3], which presents the results of electrical and magnetic measurements of TlFeSe$_2$ single crystals. The activation energy of the intrinsic conductivity of the TlFeSe$_2$ crystals was determined to be 0.68 eV from the conductivity temperature dependence in the temperature range 290 to 670 K. The measurements of the magnetic susceptibility of TlFeSe$_2$ single crystals were also carried out in the temperature range 4.2 to 295 K, which provided evidence that TlFeSe$_2$ is a quasi-one-dimensional antiferromagnet [3].

The present work is aimed at the study of the conductivity temperature dependences of TlFeS$_2$ and TlFeSe$_2$ crystals (in the temperature range 85 to 400 K), the conductivity mechanism, and the thermoelectric properties of these compounds.

The regimes of the synthesis of the TlFeSe$_2$ compound and its single-crystal growth are described in [3] in detail. We synthesized the TlFeS$_2$ compound by fusion of the high-purity components (Tl, Fe, and S) taken in the stoichiometric composition in evacuated (up to 10^{-2} Pa) quartz ampoules. In the process of the synthesis, starting from 400–450°C, a violent reaction of the components was observed. The ampoule with the substance was rotated around its axis and gradually introduced with a rate of 1.5–3.0 cm/h into the hotter furnace zone over 7–8 h; then, after keeping it at a temperature of 750°C for about 1–2 h, it was cooled slowly, over 5–6 h, to room temperature. The TlFeS$_2$ compound synthesized by this process was single-phase, fairly soft, and of a black color and, according to differential thermal analysis, melted at 720°C.

Single crystals of the TlFeS$_2$ compound were grown by the modified Bridgman–Stockbarger method. The grown ingots of TlFeS$_2$, as well as of TlFeSe$_2$, consisted of long extrathin fibers oriented along the ampoule and formed a monolithic crystal of the compound. The massive single crystals could be easily broken up into single-crystal fibers. TlFeS$_2$ and TlFeSe$_2$ crystals were soft and plastic; they were representatives of chain one-dimensional crystals.

The structural investigations showed that the crystals of TlFeS$_2$ had a chain structure with the following crystal lattice parameters: $a = 11.643$, $b = 5.306$, and $c = 6.802$ Å; $\beta = 116.75°$; and the space group $c2/m$. TlFeSe$_2$, as was shown in [3], crystallizes in the monoclinic crystal system with the following elementary-cell parameters: $a = 12.02$, $b = 5.50$, and $c = 7.13$ Å; and $\beta = 118.52°$.

For electrical measurements, the samples were prepared in the form of a parallelepiped, with dimensions $12.5 \times 5.0 \times 1.3$ mm, by pressing the crystal fibers of TlFeS$_2$ and TlFeSe$_2$. The samples were then annealed at 450 K. The ohmic contacts were made by electrolytic copper deposition. The electrical conductivity (σ) and thermoelectrical coefficient (α) of the TlFeS$_2$ and TlFeSe$_2$ samples were measured by the four-probe technique with a precision of one percent in the temperature range 85 to 400 K.

We present the results of investigations of the charge transport in TlFeS$_2$ in a direct electric field at the temperatures 189–298 K. The typical temperature dependence of the conductivity of the TlFeS$_2$ samples is shown in Fig. 1. The high-temperature branch of this dependence has an exponential character with a slope of 0.33 eV in the temperature range 235 to 298 K. After the exponential falloff, the conductivity is characterized by a monotonically decreasing activation energy with decreasing temperature. This is evidence that in TlFeS$_2$ samples at the temperatures $T < 235$ K, the
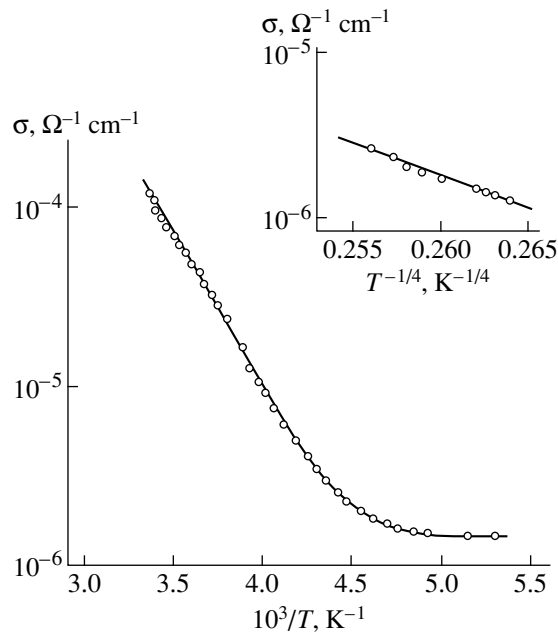
Fig. 1. Temperature dependence of the conductivity of a TlFeS$_2$ sample in the Arrhenius and Mott coordinates (the inset in the upper right corner).
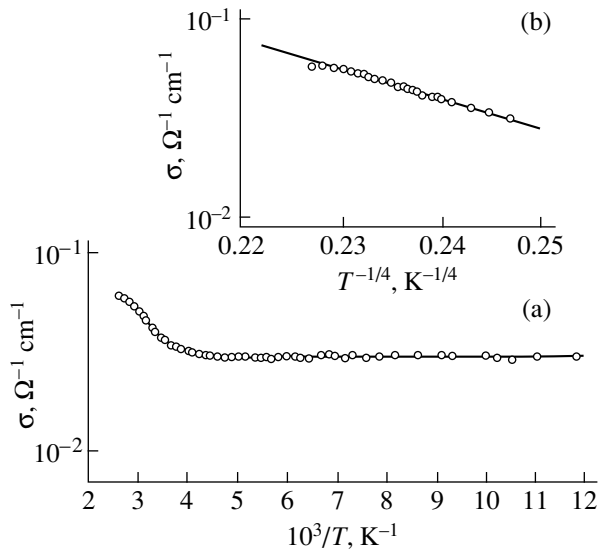

Fig. 2. The dependence of σ versus (a) $10^3/T$ and (b) $T^{-1/4}$ for TlFeSe$_2$.

charge transfer proceeds via variable-range hopping conduction over the states in a narrow energy band (ΔE) near the Fermi level [4]. This type of conductivity is described by the formula [4]

$$\sigma \sim \exp[-(T_0/T)^{1/4}], \qquad (1)$$

where

$$T_0 = \frac{16}{kN_F a^3}; \qquad (2)$$

k is the Boltzmann constant, N_F is the density of localized states near the Fermi level, and a is the localization radius.

The experimental data on the conductivity σ for a TlFeS$_2$ sample at $T < 235$ K are represented in the Mott coordinates, logσ versus $T^{-1/4}$, in the inset of Fig. 1. The experimental points fit the straight line in these coordinates, the slope of the dependence obtained being $T_0 = 4 \times 10^7$ K. Knowing T_0 and using formula (2), we have estimated the density of the localized states near the Fermi level, $N_F = 1.7 \times 10^{18}$ eV^{-1} cm^{-3}. The value $a = 14$ Å was taken for the localization radius, as in binary sulfides of group III elements [5]. The relatively high value obtained for N_F suggests that the TlFeS$_2$ samples investigated are similar in their energy structure to amorphous semiconductors. The presence of strongly deformed, and even broken, chemical bonds, which show the acceptor properties, is characteristic of an amorphous state. The role of these defects is particularly large in crystals with a layered or chain structure; the high density of states near the Fermi level is due to the presence of such defects. The pressing of the crystal fibers during our preparation of the sample increased the disorder in the samples, which, in turn, resulted in a considerable concentration of localized electronic states. In other words, the TlFeS$_2$(Se$_2$) samples we prepared for the electrical measurements were composed of short-range order regions joined together in a disorderly way. The presence of defect centers with a high concentration causes appreciable conduction over the localized states in the band gap even at relatively high temperatures.

Using the formula

$$R = \frac{3}{8}a\left(\frac{T_0}{T}\right)^{1/4}, \qquad (3)$$

we determined the hopping lengths in TlFeS$_2$ at different temperatures: $R = 107$ Å at $T = 230$ K and $R = 111$ Å at $T = 203$ K. The average hopping length is 109 Å in this temperature range, and the R/a ratio is equal to 8; that is, the average hopping length significantly exceeds the average distance between the localization centers of the charge carriers.

Charge carriers hopping from one localization center to another absorb phonons in the temperature range 200–235 K considered above. The activation energy, which decreases monotonically as the temperature decreases, is due to the energy spread of the localized states. A temperature decrease leads to an increase in the probability of a charge carrier hopping to centers that are more distant in space, but closer in energy. This is the reason why the hopping activation energy

decreases and the hopping length increases as the temperature decreases. Finally, the moment arrives when the conductivity is independent of the temperature; in this case, charge carrier hopping occurs with the emission of phonons [6]. As follows from our experimental results, the conductivity of TlFeS$_2$ does not depend on temperature at $T < 200$ K.

The conductivity that is independent of temperature could be due to tunnel transitions of the charge carriers from the localized states to the conduction band in a strong electric field. In our case, we have relatively low electric fields, $F < 10^2$ V/cm, that are far away from the breakdown field. Our experimental data allow us to assert that the non-Arrhenius behavior of the conductivity in TlFeS$_2$ samples at $T < 200$ K is due to the localized charge carriers; that is, the conductivity is essentially the hopping conductivity associated with charge carrier hopping with the emission of phonons.

Analogous tendencies were experimentally discovered in TlFeSe$_2$ samples. In contrast to TlFeS$_2$, the samples of TlFeSe$_2$ had a low resistivity; for example, at $T = 298$ K, it was 25 Ω cm, whereas the resistivity of TlFeS$_2$ was $\rho = 8 \times 10^3$ Ω cm at the same temperature. The curve $\log \sigma$ versus $10^3/T$ (Fig. 2a) for the TlFeSe$_2$ sample had no constant activation energy, but monotonically sloped downward as the temperature decreased (the activation energy was about 0.05 eV). However, these experimental points fit one straight line in the coordinates $\log \sigma$ versus $T^{-1/4}$ (Fig. 2b), with a slope of $T_0 = 1.4 \times 10^6$ K, well. The density of the localized states near the Fermi level was $N_F = 3.3 \times 10^{18}$ eV^{-1} cm^{-3} in the TlFeSe$_2$ samples (the localization radius was taken to be $a = 34$ Å, as in gallium selenide [7]). The average hopping length in TlFeSe$_2$ was 104 Å.

By using the formula [4]

$$\Delta E = \frac{3}{2\pi R^3 N_F}, \qquad (4)$$

we estimated the spreading of the trapping states near the Fermi level, $\Delta E = 0.13$ eV, in TlFeSe$_2$ samples.

The conductivity was practically independent of temperature in the temperature range 85 to 250 K. The temperature-independent conductivity observed in TlFeSe$_2$ (as well as in TlFeS$_2$) is simply the activationless hopping conductivity.
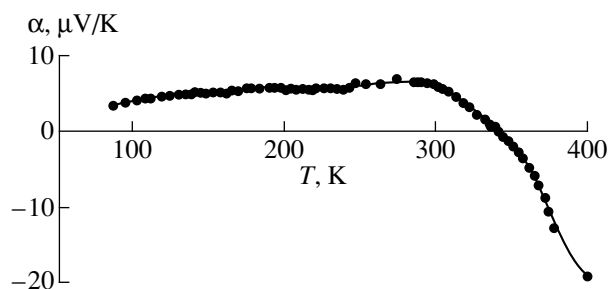

Fig. 3. The temperature dependence of the thermoelectrical coefficient in a TlFeSe$_2$ sample.

Thus, we have studied the charge transfer processes in TlFeS$_2$ and TlFeSe$_2$ samples in a wide temperature range. The experimental data obtained by us suggest that variable-range hopping conduction takes place in these crystals, which becomes activationless as the temperature decreases further.

The temperature dependence of the thermoelectrical coefficient in the TlFeSe$_2$ sample is presented in Fig. 3. The thermoelectrical coefficient slightly rises with increasing temperature, reaches its maximum value at $T = 290$ K, and then decreases to zero at $T = 340$ K; thereafter, the sign of α is reversed. At $T = 400$ K, we have $\alpha = -20$ μV/K.

REFERENCES

1. A. Kutoglu, Naturwissenchaften B **61** (3), 125 (1974).
2. K. Klepp and H. Boller, Monatsh. Chem. B **110** (5), 1045 (1979).
3. É. M. Kerimova, F. M. Seidov, S. N. Mustafaeva, and S. S. Abdinbekov, Neorg. Mater. **35** (2), 157 (1999).
4. N. F. Mott and E. A. Davis, *Electronic Processes in Non-Crystalline Materials* (Oxford Univ. Press, Oxford, 1971; Mir, Moscow, 1974).
5. V. Augelli, C. Manfredotti, R. Murri, *et al.*, Nuovo Cimento **38** (2), 327 (1977).
6. B. I. Shklovskiĭ, Fiz. Tekh. Poluprovodn. (Leningrad) **6** (12), 2335 (1972) [Sov. Phys. Semicond. **6**, 1964 (1972)].
7. S. N. Mustafaeva, Neorg. Mater. **30** (5), 619 (1994).

Translated by N. Kovaleva

SEMICONDUCTORS
AND DIELECTRICS

Combined Photoreflectance/Photoluminescence Studies of the Electronic Properties of Semiconductor Surfaces

R. V. Kuz'menko*, A. V. Ganzha*, É. P. Domashevskaya*, S. Hildebrandt**, and J. Schreiber**

*Voronezh State University, Universitetskaya pl. 1, Voronezh, 394693 Russia
**Fachbereich Physik der Martin-Luther-Universität Halle-Wittenberg, Halle/Saale, D-06108 Deutschland
Received March 23, 2000

Abstract—A technique involving combined photoreflectance/photoluminescence measurements is proposed to study the electronic properties of semiconductor surfaces. The efficiency of the technique is illustrated by a study of the growth and degradation of the luminescence signal from selenium-passivated GaAs substrates under CW laser excitation. © *2000 MAIK "Nauka/Interperiodica"*.

Miniaturization of optoelectronic semiconductor structures makes the monitoring of electronic surface properties an urgent problem. Efforts in this area are presently focused primarily on reducing the density of the semiconductor surface electronic states [1]. The surface quality must be probed by high-precision non-destructive measurement techniques capable of determining the nature and density of the surface states.

The standard phenomenological model employed to describe the electronic properties of a free or passivated semiconductor surface is based on the density-of-surface-states distribution function $N_{SS}(E)$ in the band gap. These states trap majority carriers from the bulk of the semiconductor, which results in the creation of a depleted near-surface region (space charge region) and of a surface electric field with a strength F decaying in the space charge region and, as a consequence, in the semiconductor band bending $e\varphi$ [2].

Laser excitation with photon energies in excess of the semiconductor band gap generates nonequilibrium carriers of both signs. The number of created carriers depends on the distance from the surface z (the semiconductor surface is at $z = 0$) and is proportional to $I_0 \exp(-\alpha z)$, where α is the absorption coefficient for the exciting light. Recombination of excess carriers may occur radiatively (luminescence) and in a nonradiative manner. Nonradiative recombination at the semiconductor surface, which involves surface states, is described through the surface recombination velocity v_S. In the absence of nonradiative recombination, $v_S = 0$, and in the case where recombination in the near-surface region proceeds nonradiatively, $v_S \longrightarrow \infty$ [3].

Photoluminescence excitation spectroscopy (PES), which is based on the measurement of the integrated photoluminescence-signal intensity near the fundamental absorption edge, has recently attracted considerable attention due to its extremely high sensitivity to the state of the semiconductor surface [3–8]. The intensity of the integrated luminescence signal can be used to determine the surface recombination velocity from the expression [9]

$$I \sim \eta \frac{1}{1-\alpha^2 L^2}\left(\Phi(\alpha) - \frac{\alpha L + v_S/v_D}{1 + v_S/v_D}\Phi\left(\frac{1}{L}\right)\right), \quad (1)$$

where η is the internal quantum efficiency, L is the diffusion length of the minority carriers, v_D is the diffusion velocity of the minority carriers, and Φ is a function introduced in [9] to describe the diffusion contribution from the bulk of the semiconductor. As follows from the Shockley–Read–Hall recombination model, the surface recombination velocity is directly proportional to the density of recombination-active states. Thus, by measuring the absolute value of the integrated photoluminescence signal, one can obtain information on the density of recombination-active surface states. Measurement of the time dependence of the integrated luminescence signal was used to study photostimulated reactions on the GaAs surface [4–6].

Photoreflectance spectroscopy, which is a modification of electroreflectance spectroscopy, is at present one of the most precise methods for determining of the surface electric field or the surface potential of a semiconductor sample [10]. This method is based on a periodic electrical modulation of the reflectance signal from the near-surface region of a semiconductor through modulation of the intrinsic surface electric field, which is achieved by illuminating the surface by laser light with a photon energy in excess of the band gap. Because of the very strong broadening effects in the region of high-energy transitions, the most useful information is contained in photomodulation spectra obtained near the fundamental absorption edge, E_0.

Photoreflectance spectroscopy operates with spectral structures of two types [11]. At moderate fields,

where the electrooptical energy

$$\hbar\Omega = \left[\frac{e^2 F^2 \hbar^2}{8\mu_\parallel}\right]^{1/3} \qquad (2)$$

($\mu_\parallel$ is the reduced effective electron–hole mass in the direction of the electric field and e is the electronic charge) exceeds the phenomenological spectral-broadening energy Γ of the interband transition, the spectral structure consists of a main peak near the transition energy and Franz–Keldysh high-energy oscillations (Fig. 1). In the low-field case, where the $\hbar\Omega < \Gamma$ condition is satisfied, the spectral structure represents a resonance line with two extrema of opposite sign.

As shown in the photoreflection theory, when photoreflectance spectra are measured near the E_0 interband transition for a three-dimensional critical point, the Franz–Keldysh oscillations can be described by the approximate asymptotic relation [12, 13]

$$\frac{\Delta R}{R}(E) = \frac{1}{E - E_0}\frac{1}{E^2}\exp\left(-\frac{\sqrt{E - E_0}\Gamma}{\hbar\Omega^{3/2}}\right)$$
$$\times \cos\left[\frac{2}{3}\left(\frac{E - E_0}{\hbar\Omega}\right)^{3/2} + \Theta_0\right]. \qquad (3)$$

Thus, the period of the Franz–Keldysh oscillations can be used to determine the electrooptic energy and, if $\mu_\parallel$ is known, the surface electric field. Knowing this and the equilibrium carrier concentration n, one can use the relation

$$\varphi = \frac{\varepsilon\varepsilon_0 F^2}{2en} = \frac{Q_{SS}^2}{2\varepsilon\varepsilon_0 en} \qquad (4)$$

to determine the surface potential φ and the density of charged surface states Q_{SS} [2].

Thus, by measuring a photoreflectance spectrum and an integrated photoluminescence signal in the same region of the semiconductor surface, one can obtain information both on the strength of the surface electric field and on the surface recombination velocity, i.e., estimate the density of both electrically and recombination-active surface states. This would provide a relatively accurate determination of the electronic properties of the surface. A further advantage of the proposed combined method consists in that these studies can be performed on the setup already described in detail in [14].

This paper illustrates combined photoreflectance and photoluminescence measurements in a specific example of a study of the stability of a passivated GaAs surface.

The samples studied were fabricated at the Voronezh Technological Academy. They were n-GaAs(100) substrates annealed in Se or Se + As vapor at a temperature of 660–680 K for 5–45 min. The Se vapor pressure was maintained during annealing within the 0.1–1 Pa interval. Subjecting a GaAs substrate to a
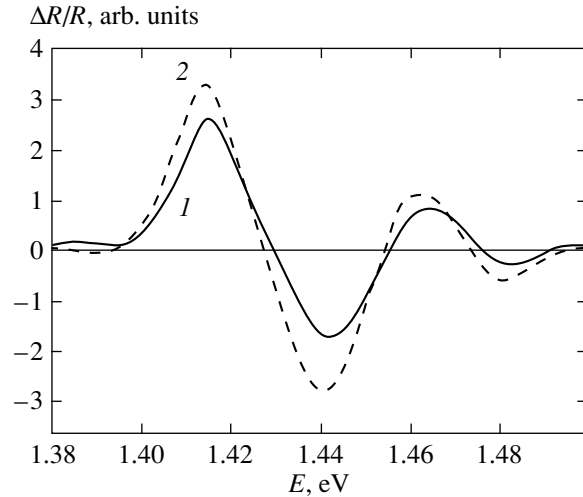
$\Delta R/R$, arb. units

Fig. 1. Experimental E_0 photoreflectance spectra obtained on Se-passivated GaAs samples. The difference between the Franz–Keldysh oscillation periods implies different surface electric fields: $F_1 = 3.19 \times 10^6$ V/m, $F_2 = 2.91 \times 10^6$ V/m.

chalcogen-containing medium at the above temperatures initiates the reaction of heterovalent substitution and the formation of a pseudoamorphous Ga_2Se_3 layer on the sample surface. It was established that the density of surface states on the $Ga_2Se_3/GaAs$ interface is lower than that of a naturally oxidized surface [1, 15, 16]. However, the stability of the effect achieved was not studied. Because it is known from the literature that CW laser illumination of a GaAs surface stimulates the processes of desorption, reoxidation, and defect generation [3–8], it can be suggested that PES would be an efficient tool to probe the stability of surface passivation.

All measurements were carried out in air at room temperature on the setup described in [14] by the following technique. Modulated laser light (He–Ne laser, $\lambda = 632.8$ nm) is focused on a 0.1×0.1 mm area on the sample surface, and the GaAs E_0 photoreflectance spectrum is measured (the pseudoamorphous Ga_2Se_3 layer is transparent at $\lambda = 632.8$ nm). Because high laser-excitation densities are capable of initiating photostimulated reactions at the GaAs surface, the photoreflectance spectra were obtained at those laser excitation densities at which no noticeable change in the integrated luminescence signal occurred during the measurement time. After the measurement of the photoreflectance spectrum, the laser power density is increased, modulation of the laser light is removed, and the dependence of the photoluminescence signal intensity on time, $I^{PL}(t)$, is measured. After a certain time, determined in each particular case by the actual pattern of the observed integrated luminescence-signal evolution, the PL measurement is terminated, the laser excitation density is reduced, and the photoreflectance spectrum is measured again at the low laser-excitation
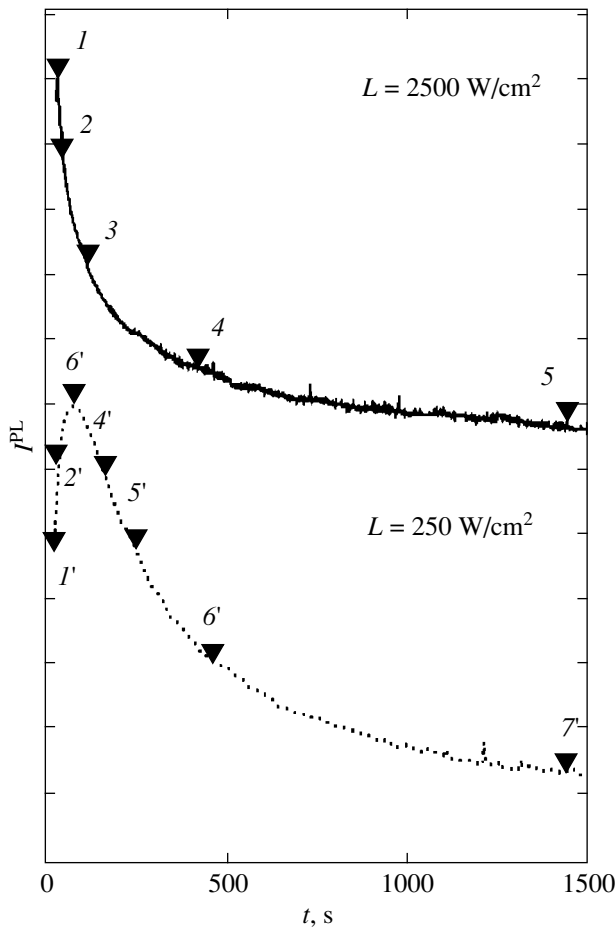
Fig. 2. Results of a correlated photoreflectance/photoluminescence study performed at a laser excitation density $L = 2500$ (top) and 250 W/cm^2 (bottom). The electric fields F, 10^6 V/m: (*1*) 3.01, (*2*) 2.90, (*3–5*) 2.89; (*1'*) 3.12, (*2'*) 3.04, (*3'*) 2.99, (*4'*) 2.97, and (*5'–7'*) 2.95.

density. Having obtained the photoreflectance spectrum, the laser power density is brought back to the preceding level, it is checked for breaks in the integrated photoluminescence (IPL) intensity curve, and the measurement of the $I^{PL}(t)$ dependence is resumed.

It was empirically found that the laser excitation density $L \sim 1$ mW/cm^2 does not cause any noticeable change in the IPL signal of the samples studied over several hours. By contrast, for $L > 100$ W/cm^2, the signal is observed to change already after a few seconds. It is these values of L that were chosen for measurements of the photoreflectance and IPL. The $I^{PL}(t)$ measurement time was 1500 s. The time spent to take one photoreflectance spectrum was 600 s.

Figure 2 illustrates a combined photoreflectance/photoluminescence study typical of the samples used. As seen from the upper curve of Fig. 2, at excitation densities $L \sim 2500$ W/cm^2, one observes only a decay (degradation) of the signal, which exemplifies

the first type of photoluminescence intensity dependence on time.

A tenfold decrease in the excitation density changes the pattern of the relation in the initial phase. As is evident from the lower curve of Fig. 2, in the initial phase, one now observes growth of the signal, which is followed, on reaching a maximum value, by a decay similar to that observed in relations of the first type.

Further decrease in the laser power density stretches the growing part of the curve in time, so that only a slow growth of the PES signal becomes evident at laser excitation densities $L \sim 1$ W/cm^2.

Mathematical modeling of the observed $I^{PL}(t)$ relations showed that curves of the first type are fitted well by one decaying exponential, while those of the second type are described by a superposition of one growing and one decaying exponential:

$$I^{PL}(t) = I^{PL}(t = \infty)\left[C + A\exp\left(-\frac{t}{t_1}\right) - B\exp\left(-\frac{t}{t_2}\right)\right], \quad (5)$$

where t_1 and t_2 are the rate constants of the processes initiated by the laser excitation.

Our calculations show that the time constant t_2 of the growing exponential is substantially smaller than that of the decaying one, t_1. Growth of the excitation density brings about a decrease in both constants, with the difference between the two increasing. For instance, for a laser excitation density $L = 100$ W/cm^2, the time constants averaged over ten samples are $t_1 = 420$ s and $t_2 = 280$ s; for $L = 500$ W/cm^2, we have $t_1 = 150$ s and $t_2 = 10$ s; and for $L = 2500$ W/cm^2, $t_1 = 30$ s. These figures suggest that even an $I^{PL}(t)$ relation of the first type has its growing portion, but it is not seen because of the relatively large instrument resolution time (0.4 s).

Quantitative analysis of photoreflectance spectra obtained before the initiation of photostimulated reactions yields the following averaged parameters: $F \approx 3 \times 10^6$ V/m, $e\varphi \approx 0.3$ eV, and $Q_{SS}/e \approx 2 \times 10^{11}$ cm^{-2}. The photoreflectance measurements made in the course of the PES studies are shown graphically in Fig. 2. As seen from the upper curve, in the initial part of this descending curve, the surface electric field decreases; however, a short time thereafter, saturation is obtained. The lower curve reveals that the decay in the electric field is associated with the growing component. Thus, photoreflectance measurements provide unambiguous supportive evidence for the presence of a growing component with a short time constant in IPL time relations of the first type as well.

The observed IPL relations can be interpreted in terms of a model assuming photoinduced chemical reactions near the semiconductor surface to proceed simultaneously with the generation of "nonradiative" defects in the near-surface region of the GaAs substrate. The generation of nonradiative defects in the

near-surface region of GaAs under laser irradiation was reported in [3, 8].

We believe that the surface of the samples studied is nonuniform and possesses regions both of stable passivation, where heterovalent substitution has come to an end, and of incomplete passivation. A passivated region can be associated with the lowest density of states, while a region with incomplete passivation has an enhanced Se-induced density of states, which is superimposed on the intrinsic semiconductor-surface states. The existence of regions with different surface-state densities is confirmed by measurements of photoreflectance spectra obtained with a high surface resolution (10×10 μm) in different surface areas of a passivated substrate. These studies showed that the magnitude of the surface electric field depends strongly on the actual point of measurement. This effect is not observed on an untreated substrate.

The laser-induced conversion of incomplete to stable passivation results in a decrease in the surface recombination velocity, which brings about a growth in the luminescence intensity; by contrast, generation of nonradiative defects in the near-surface region entails signal degradation. That the generation of nonradiative defects occurs not on the surface itself but rather in the near-surface region of a semiconductor is supported by the absence of any change in the surface electric field within the degradation part of the relation, whereas the conversion of incomplete to stable passivation is characterized by a changing surface electric field. The latter observation suggests that the states forming in the course of the transition from incomplete to stable passivation should either be created within the band-gap regions close to the band edges or destroy the midgap states.

Thus, study of the stability of the selenium-passivated GaAs surface has shown that combined photoreflectance/photoluminescence measurements are an efficient method for probing the electronic properties of a semiconductor surface. Direct measurements have established that the process responsible for the degradation of the photoluminescence signal is the generation of nonradiative defects in the near-surface region of the semiconductor, while the growth of the photoluminescence signal can be accounted for by the photostimulated reactions in the vicinity of the passivated surface.

REFERENCES

1. B. I. Sysoev, V. F. Antyukhin, V. D. Strygin, and V. N. Morgunov, Zh. Tekh. Fiz. **56**, 913 (1986) [Sov. Phys. Tech. Phys. **31**, 554 (1986)].
2. R. B. Darling, Phys. Rev. B **43**, 4071 (1991).
3. M. Y. A. Raja, S. R. J. Brueck, M. Osinski, and J. McInerney, Appl. Phys. Lett. **52**, 625 (1988).
4. T. Suzuki and M. Ogawa, Appl. Phys. Lett. **31**, 473 (1977).
5. N. M. Haegel and A. Winnacker, Appl. Phys. A **A42**, 233 (1987).
6. D. Guidotti, E. Hasan, H.-J. Hovel, and M. Albert, Appl. Phys. Lett. **50**, 912 (1987).
7. J. Ogawa, K. Tamamura, K. Akimoto, and Y. Mory, Appl. Phys. Lett. **51**, 1949 (1987).
8. D. Guidotti, E. Hasan, H.-J. Hovel, and M. Albert, Nuovo Cimento **11**, 583 (1989).
9. W. Hergert, S. Hildebrandt, and L. Pasemann, Phys. Status Solidi A **102**, 819 (1987).
10. N. Bottka, D. K. Gaskill, R. S. Sillmon, *et al.*, J. Electron. Mater. **17**, 161 (1988).
11. D. E. Aspnes, Surf. Sci. **37**, 418 (1973).
12. D. E. Aspnes, Phys. Rev. B **10**, 4228 (1974).
13. D. E. Aspnes and A. A. Studna, Phys. Rev. B **7**, 4605 (1973).
14. J. Schreiber, S. Hildebrandt, W. Kircher, and T. Richter, Mater. Sci. Eng., B **9**, 31 (1991).
15. B. I. Sysoev, N. N. Bezryadin, G. I. Kotov, and V. D. Strygin, Fiz. Tekh. Poluprovodn. (St. Petersburg) **27**, 131 (1993) [Semiconductors **27**, 69 (1993)].
16. N. N. Bezryadin, É. P. Domashevskaya, I. N. Arsent'ev, *et al.*, Fiz. Tekh. Poluprovodn. (St. Petersburg) **33**, 719 (1999) [Semiconductors **33**, 665 (1999)].

Translated by G. Skrebtsov

SEMICONDUCTORS
AND DIELECTRICS

X-ray Measurement of a Microdistortion Tensor and Its Application in an Analysis of the Dislocation Structure of Thick GaN Layers Obtained by Hydrochloride Gaseous-Phase Epitaxy

V. V. Ratnikov, R. N. Kyutt, and T. V. Shubina

Ioffe Physicotechnical Institute, Russian Academy of Sciences, Politekhnicheskaya ul. 26, St. Petersburg, 194021 Russia

Submitted April 27, 2000

Abstract—The method of two- and three-crystal x-ray diffractometry (TCD) is used for studying the dislocation structure of thick GaN layers grown by chloride gaseous-phase epitaxy (CGE) on sapphire, as well as on a thin GaN layer, which is grown by the metalloorganic synthesis (MOS) method. Five components of the microdistortion tensor $\langle \varepsilon_{ij} \rangle$ and the sizes of the coherent scattering regions along the sample surface and along the normal to it are obtained from the measurements of diffracted intensity in the Bragg and Laue geometries. These quantities are used to analyze the type and geometry of the dislocation arrangement and to calculate the density of the main types of dislocations. The density of the vertical screw dislocations, as well as of the edge dislocations, decreases (by a factor of 1.5 to 3) during growth on a thin GaN layer. The diffraction parameters of the thick layer on the MOS-GaN substrate suggest that it has a monocrystalline structure with inclusions of microcrystalline regions. © 2000 MAIK "Nauka/Interperiodica".

The large difference between the lattice constants and the temperature expansion coefficients of layers and of sapphire substrates normally used for their growth is a serious problem in the epitaxial growth of GaN. As a result, the samples are bent and various defects are generated, which deteriorates the optoelectronic characteristics of the layers. This problem could be solved, for example, by using the homoepitaxial growth of GaN, but crystals and layers of GaN are seldom used as substrates. Another promising approach is to obtain thick GaN layers grown by the chloride gaseous-phase epitaxy (CGE) [1–4], which can be used for the subsequent growth of heterostructures. It was proved recently that the application of MOS of GaN thin layers (on sapphire) as substrates for the subsequent growth of GaN by CGE can noticeably improve the quality of their structure [5].

Defects in GaN layers are studied by using various methods including photo- and cathodoluminescence, transmission electron microscopy (TEM), atomic force microscopy, the Raman method, and x-ray diffractometry [1–6]. According to the obtained data, layers are characterized by a high defect density near the interface between the layer and the substrate, which decreases in the direction to the surface. The change in the size of microblocks in the layers with increasing distance from the interface is also determined. Along with vertical screw and edge dislocations, dislocations of a mixed type are also present, although the number of former dislocations is much larger [4].

Among the methods listed above, x-ray diffractometry is the only nondestructive method which provides information about a large volume of the layer all at once. As a rule, measurements of the symmetric diffraction in Bragg's geometry are used for this purpose. In the framework of the mosaic model, dispersion of the *c* axis of microcrystallites [henceforth called coherent scattering regions (CSRs)] leads to broadening of the rocking curve in the direction of the normal to the diffraction vector due to mosaic spread (tilt), which is the same for any reflex used, while the so-called size effect depends on the diffraction angle in view of the limitations on the CSR size. Such a behavior of the symmetric diffraction curves is widely used for analyzing the defect structure of nitrides. Metzger *et al.* [7] indicated the limitations of such an analysis and proposed that the results of measurement of asymmetric Bragg reflections also be used. However, the measurement of asymmetric reflections in Bragg's geometry is ineffective in our opinion since the broadening of the asymmetric reflection contains (in general) a complex combination of contributions from microrotations and microdeformations of the crystal planes parallel and normal to the surface, as well as from broadening due to the limited size of the CSRs along and at right angles to the sample surface. Additional simulation of the relation between the different contributions to the halfwidths being measured, which is required in this case, complicates the analysis of the defected structure. In addition, the conventional mosaic model disregards structural defects and the related lattice deformation in the CSRs themselves.

In this paper, we use a complex approach based on the x-ray measurement of the microdistortion tensor for GaN layers obtained by the CGE method, which allows us to avoid the disadvantages mentioned above. Microdistortions due to displacement fields around structural defects modify the shape of a reciprocal lattice (RL) site causing its broadening and, hence, the broadening of the corresponding diffraction curve [8, 9]. We include in our analysis defect-induced microdistortions of crystal planes in micrograins and show how to obtain the microdistortion tensor and the CSR size along and at right angles to the sample surface from diffraction curves by using only two scanning modes [θ and (θ–2θ)] and two (Bragg and Laue) geometries of symmetric diffraction. We carry out a simple analysis of the relation between the microdistortion tensor being measured and the type and geometry of the arrangement of dislocations in GaN. The potentialities of the proposed analysis are demonstrated by comparing the structural quality of thick CGE layers of GaN grown on sapphire and on thin GaN substrates by the MOS technique.

1. X-RAY DIFFRACTION AND CRYSTAL LATTICE MICRODISTORTION IN NITRIDES

The different influences of the tilt and the size effect on the broadening of Brag's rocking curves in the case of a mosaic structure of crystals are usually analyzed by using the method proposed by Williamson and Hall [10]. Presuming a linear superposition of the contributions, we construct the dependences

$$\omega_\theta(\sin\theta/\lambda) = f(\sin\theta/\lambda) \qquad (1)$$

and

$$\omega_{\theta-2\theta}(\cos\theta/\lambda) = f(\sin\theta/\lambda), \qquad (2)$$

where ω_θ and $\omega_{\theta-2\theta}$ are the angular width at half the reflection intensity peak for θ and θ–2θ scanning and θ and λ are Bragg's angle and the wavelength of x-rays, respectively. The slope given by Eq. (1) is used to determine the contribution of microdisorientations ω_{tlt} to the broadening. The slope of the dependence in Eq. (2) gives the values of microstrain ε_c along the c axis. The sizes of the CSR along the surface (τ_x) and along the normal to it (τ_z) are estimated from intercepts cut by the dependences in Eqs. (1) and (2) on the y axis.

Recently, we proposed [9] a new approach for characterizing the structural perfection of strongly mismatched epitaxial layers, which is based on x-ray measurement of the microdistortion tensor components $\langle\varepsilon_{ij}\rangle$ that are standard deviations of the average distortion components. In view of the isotropy of the (0001) plane in hexagonal GaN, the microdistortion tensor is composed of just five independent components. However, the broadening of the symmetric θ and (θ–2θ) reflections, each of which is related only to a single component of $\langle\varepsilon_{ij}\rangle$, is also determined by the dimensions of the CSR along the surface τ_x and along the normal to it τ_z.

In order to separate the contributions from the components of the $\langle\varepsilon_{ij}\rangle$ tensor and the CSR, we propose that the measurements of the diffracted intensity in the Laue symmetric (transmission) geometry be used along with the Bragg reflection geometry. In this case, Bragg's three-crystal θ curve contains information on ε_{zx} and τ_z, while the (θ–2θ) curve carries information on ε_{zz} and τ_x. In the Laue geometry, ε_{xz} and τ_z are obtained from the θ curve, while ε_{xx} and τ_x are obtained from the (θ–2θ) curve. Thus, the application of two scanning modes in the two symmetric diffraction geometries makes it possible to measure each component of the microdistortion tensor without making additional assumptions concerning their relation in the half-widths being measured.

It was mentioned above that only the tilt and the size effect are normally used for analyzing the structure of strongly mismatched epitaxial layers in the mosaic model. However, our measurements of the Laue diffraction revealed a difference in the broadening of the Bragg (B) and Laue (L) θ curves of reflection (taking into account the size effect), which means that the mosaic model is not quite adequate. While analyzing the measured half-widths, we must obviously take into consideration the contribution from individual defects in microblocks. This is also important to do in view of advances in obtaining less defected (almost monocrystalline) nitride layers. Consequently, for θ scanning we can write

$$(\omega_\theta^{B(L)})^2 = (\omega_{\tau x(\tau z)}^{B(L)})^2 + (\omega_{tlt}^{B(L)})^2 + (\omega_\varphi^{B(L)})^2, \qquad (3)$$

where the term $\omega_{\tau x(\tau z)}^{B(L)} \sim \lambda/(\tau_{x(z)}\sin\theta)$ is associated with the size effect along the diffracting planes. The contribution of $\omega_{tlt}^{B(L)}$ is determined by the mosaic spread disordering of the CSR, does not depend on Bragg's angle θ, and is the same in the measurements of the Bragg and Laue diffraction ($\omega_{tlt}^B = \omega_{tlt}^L$). The contribution $\omega_\varphi^{B(L)} \sim \langle\varepsilon_{zx(xz)}\rangle$ is proportional to the shear component of the microdistortion tensor and originates from microdisorientation of the diffracting planes near defects in the CSR.

The broadening of the (θ–2θ) curve is determined by only two components:

$$(\omega_{\theta-2\theta}^{B(L)})^2 = (\omega_{\tau z(\tau x)}^{B(L)})^2 + (\omega_\varepsilon^{B(L)})^2, \qquad (4)$$

where $\omega_{\tau z(\tau x)}^{B(L)} \sim \lambda/(\tau_{z(x)}\cos\theta)$ is associated with the size effect along the normal to the diffracting planes, while $\omega_\varepsilon^{B(L)} \sim \langle\varepsilon_{zz(xx)}\rangle\tan\theta$ is proportional to the diagonal tensor component and is determined by microdeformations of the diffracting planes.

The contributions to the broadening of θ and (θ–2θ) reflections in the Bragg, as well as Laue, geometry are

summed up according to a quadratic law since the reflection curves have a Gaussian shape (see [9]).

In order to characterize completely the structural perfection of nitrides, the measurements of the broadening of the θ and (θ–2θ) symmetric reflection are insufficient since the rotation of the CSR in the plane of the layers and the microtwists (twt) of local crystal regions near defects around the normal to the surface also take place. Srikant *et al.* [11] demonstrated recently that the correct value of the twist component ω_{twt} can be determined from the dependence of the half-widths ω_{OOP} for a series of symmetric Bragg's reflections of the ($101l$) type on the angle ξ formed by these out-of-plane (OOP) planes with the basal (0001) plane rather than from the conventionally used ϕ scanning [7, 12] or from the measurements of grazing Bragg diffraction (GBD) [13]. The half-width measured in the case of ϕ scanning contains both tilt and twist contributions, and the GBD method, which is correct from the methodological point of view, provides information only on a very thin (~100 nm) surface layer. As the value of ξ increases, the effect of tilt on ω_{OOP} decreases with a simultaneous increase in the twist component and, hence, the measurement of ω_{OOP} as a function of ξ and the extrapolation of the dependence $\omega_{OOP} = f(\xi)$ to $\xi = 90°$ gives the value of ω_{twt}. The value of ω_{twt} measured by the OOP method is connected with the microdistortion tensor components:

$$(\omega_{twt}) = \langle\varepsilon_{xx}\rangle^2 + \langle\varepsilon_{xy}\rangle^2. \tag{5}$$

2. MICRODISTORTION TENSOR AND DISLOCATIONS IN GaN

Apart from the dispersion of the c axis of microblocks and the presence of small-angle boundaries formed by horizontal edge dislocations in the layers, which is associated with the dispersion, the main defects in the layers are vertical screw and edge dislocations (see, for example, [5–7, 9]). In our analysis of the dislocation structure of the layers, we used the relation between the components of $\langle\varepsilon_{ij}\rangle$ with the geometry and type of dislocations in GaN. For example, a vertical screw dislocation with the Burgers vector parallel to the normal to the surface makes contributions only to the $\langle\varepsilon_{zx}\rangle$ component, while a vertical edge dislocation with the Burgers vector parallel to the surface makes contributions both to $\langle\varepsilon_{xx}\rangle$ (L) and to $\langle\varepsilon_{xy}\rangle$ (B). A similar form of the dependence for the main types of dislocations in the geometry of their arrangement in GaN is illustrated in Fig. 1. The recording geometry (B or L) determines the mutual orientation of the normal **n** to the surface and the diffraction vector **H**. The density ρ_{vs} of the vertical screw dislocations can be estimated from $\langle\varepsilon_{zx}\rangle$ using the expression from [14] modified by us:

$$\rho_{vs} = \langle\varepsilon_{zx}\rangle^2 / 0.92 b_{vs}^2, \tag{6}$$

where $\mathbf{b}_{vs}$ is the Burgers vector of a screw dislocation (0.5186 nm in GaN). The density of randomly distributed vertical edge dislocations ρ_{ve} can also be determined using expression (6) in which $\langle\varepsilon_{zx}\rangle$ is replaced by $\langle\varepsilon_{xy}\rangle$ and b_{vs} by $b_{ve} = 0.3185$ nm.

When vertical edge dislocations form small-angle boundaries, their density is given by [14]

$$\rho_{ve}^{lab} = \langle\varepsilon_{xy}\rangle^2 / (2.1 b_{ve}\tau_x), \tag{7}$$

where τ_x is the separation between these boundaries along the surface.

3. EXPERIMENT

Thick (25 μm) GaN layers investigated by us were grown at 1090°C by the CGE method described earlier [3]. The samples were grown on the (0001) sapphire without a buffer (A206) and on a thin GaN layer (U296). A thin (2.5 μm) MOS-GaN layer (ATX5), which was used as a substrate, was also grown on the (0001) sapphire. Its structural parameters were also studied in order to estimate the initial conditions for growing the thick layer.

X-ray diffraction measurements of layers were made on a two-crystal, as well as three-crystal, diffractometer in the Bragg (Cu$K_{\alpha1}$) and Laue (Mo$K_{\alpha1}$) geometries. The three-crystal diffractometer was used for measuring the θ and (θ–2θ) scanning curves for the following reflections of the GaN layers (Fig. 2): symmetric 0002 and 0004 reflections in the Bragg geometry and symmetric $10\bar{1}0$ and $20\bar{2}0$ reflections in the Laue geometry (the layer at the x-ray exit).

Two-crystal curves were measured with a widely open detector window for asymmetric reflections in the Bragg geometry for the glancing angle of incidence ($11\bar{2}4$) and reflection ($11\bar{2}\bar{4}$) of the x-ray (the normal to the sample surface lies in the plane of scattering), symmetric reflections of the $10\bar{1}l$ type in the Bragg geometry from planes forming angles from 17° to 75°, respectively, with the (0001) surface (the normal to the sample surface lies outside the scattering plane).

Perfect Ge(220) crystals with a resolution not worse than 15″ were used as the monochromator and the analyzer. The dispersion in the x-ray optical scheme was taken into account while processing the diffraction curves.

4. DISCUSSION OF RESULTS

The half-widths of the diffraction curves of the samples are presented in Table 1. The correction for macrotwist of the samples (~5″ for the A206 sample having the maximum curvature) was taken into account while processing the experimental data according to [15]. For all the samples, the following features of the measured half-widths were observed: (i) $\omega_\theta \gg \omega_{\theta-2\theta}$, which indi-
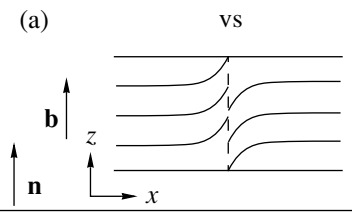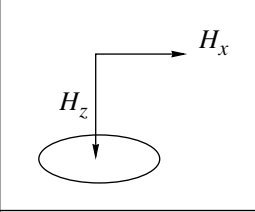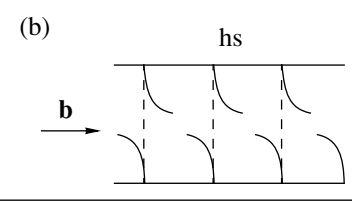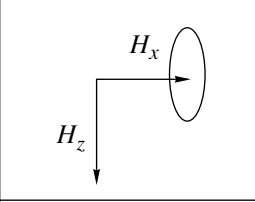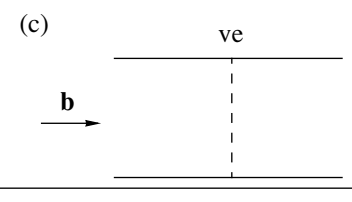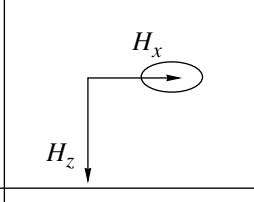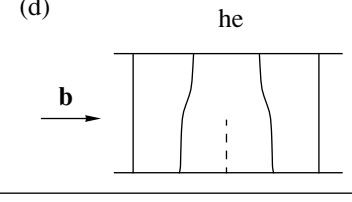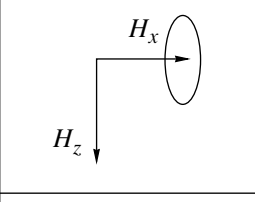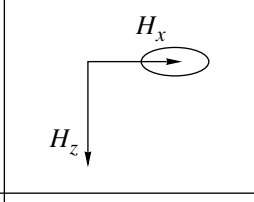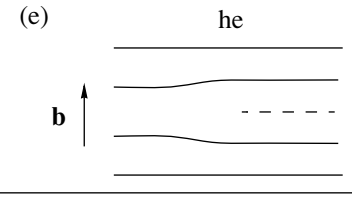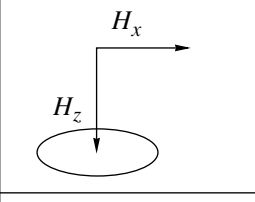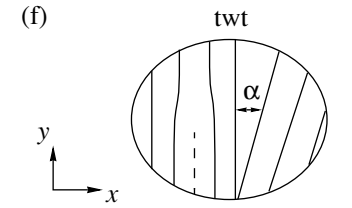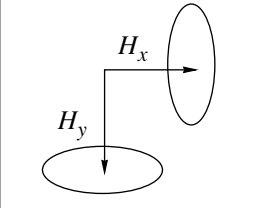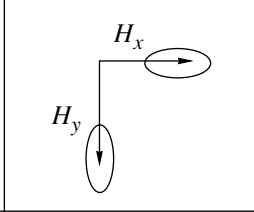
Real space	$\langle \varepsilon_{ij} \rangle$	Reciprocal space	
		θ-scan	θ-2θ-scan
(a) vs	$\langle \varepsilon_{zx} \rangle$	H_x, H_z	
(b) hs	$\langle \varepsilon_{xz} \rangle$	H_x, H_z	
(c) ve	$\langle \varepsilon_{xx} \rangle$		H_x, H_z
(d) he	$\langle \varepsilon_{xz} \rangle$ $\langle \varepsilon_{xx} \rangle$	H_x, H_z	H_x, H_z
(e) he	$\langle \varepsilon_{zx} \rangle$ $\langle \varepsilon_{zz} \rangle$	H_x, H_z	H_x, H_z
(f) twt	$\langle \varepsilon_{xy} \rangle$ $\langle \varepsilon_{xx} \rangle$	H_x, H_y	H_x, H_y

Fig. 1. Relation between the microdistortion tensor components $\langle \varepsilon_{ij} \rangle$ and the shape of reciprocal lattice sites for (a–e) various types and geometries of the arrangement of dislocations and (f) crystal lattice rotations in the plane of the layer: vs denotes vertical screw; hs, horizontal screw; ve, vertical edge; and he, horizontal edge dislocations; twt stands for twist; **b** is the Burgers vector; **H** is the diffraction vector; and **n** is the normal to the surface.
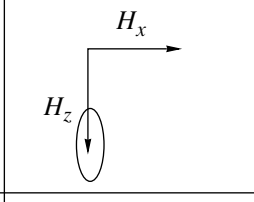
cates a strong anisotropy of diffraction scattering (the shape of a site in the reciprocal shape); (ii) $\omega_\theta^{0002} > \omega_\theta^{0004}$, which indicates the presence of a size effect in the measured half-widths; (iii) $\omega_{\theta-2\theta} \sim \tan\theta$, which indicates that the broadening of the (θ–2θ) curves is mainly determined by microdeformations of the compression–extension type; (iv) $\omega^{11\bar{2}4} < \omega^{11\bar{2}\bar{4}}$ and $\omega^{11\bar{2}4} < \omega^{0002}$, which means that a reciprocal lattice site is
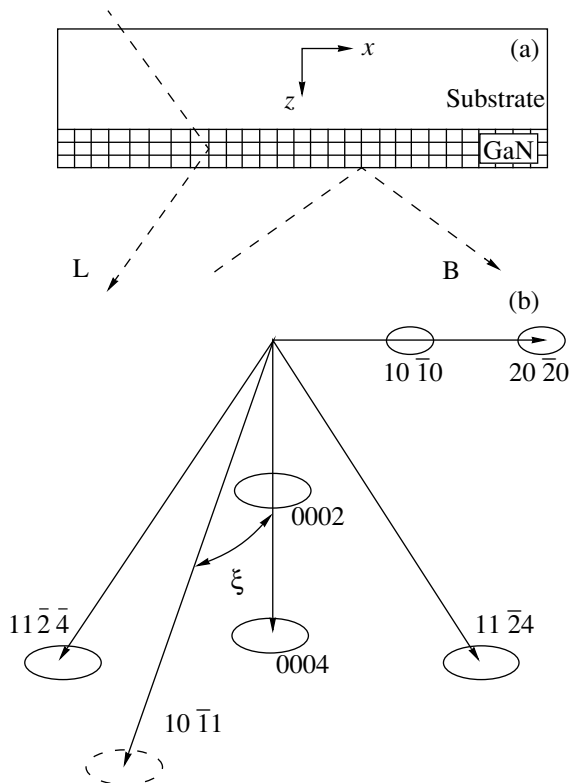
Fig. 2. (a) Bragg (B) and Laue (L) geometries of x-ray diffraction measurements in GaN and (b) mutual arrangement and shape of reciprocal lattice sites of the reflections used for GaN layers.

extended not along the diffraction vector, but along the surface (or occupies an intermediate position between them); and (v) $\omega_\theta^{0002} > \omega_\theta^{10\bar{1}0}$.

If the layers are composed only of CSRs free of defects and characterized by a certain tilt, we should expect that ω_θ^{0002} is equal to $\omega_\theta^{10\bar{1}0}$. Item (v) rules out this assumption. If we consider that the size effect is insignificant ($\omega_\theta^{0004, 20\bar{2}0} / \omega_\theta^{0002, 10\bar{1}0} \geq 0.9$) and the effect of horizontal edge (mismatching) dislocations on $\omega_\theta^{10\bar{1}0}$ can be neglected, we can assume that $\omega_\theta^{10\bar{1}0} \cong \omega_{\text{tlt}}$. In

this case, the difference between ω_θ^{0002} and $\omega_\theta^{10\bar{1}0}$ indicates that ω_θ^{0002} also contains a contribution from defects, the displacements from which have a nonzero component along the diffraction vector. In the analysis of broadening of x-ray reflections that will be carried out here, we proceed from the assumption that the broadening of θ curves are determined, in addition to the size effect associated with a limited size of CSR, by two disorientation components. The first is determined by the angular rotation of the CSR (so-called tilt corresponding to the second term in formula (3)) and does not depend on the chosen reflection and the recording geometry. The reason behind the mosaic spread (tilt) in the case of nitrides is the strong mismatching of the parameters of the layer and substrate lattices and the three-dimensional growth associated with it. The second component is due to defects in the microblocks themselves, which are mainly grown-in vertical screw and edge dislocations (the third term in formula (3)).

The microdistortion tensor components obtained from experimental half-widths by using formulas (1)–(5) are presented in Table 2.

The layers under investigation are characterized by the following general regularities in the behavior of $\langle \varepsilon_{ij} \rangle$ components: (i) $\langle \varepsilon_{zx} \rangle > \langle \varepsilon_{xz} \rangle$ (i.e., the microdisorientations of the planes parallel to the surface are larger than for planes perpendicular to the surface); (ii) $\langle \varepsilon_{xx} \rangle > \langle \varepsilon_{zz} \rangle$, which corresponds to a higher level of microdeformation of planes perpendicular to the surface in comparison with planes parallel to the surface.

Additionally, the components for thick GaN grown on a sapphire by the CGE technique differ significantly from those for a thin GaN layer grown by the MOS method.

4.1. Undoped MOS GaN (ATX5) and a Thick Layer (U296) on It

Table 2 shows that $\langle \varepsilon_{zx} \rangle > \langle \varepsilon_{xz} \rangle$ for both samples. The values of $\langle \varepsilon_{zx} \rangle$ and $\langle \varepsilon_{xz} \rangle$ presented in Table 2 also include the tilt of CSR, which is the same for both geometries of diffraction, $\omega_\varphi^B = \omega_\varphi^L$. Consequently, the difference between $\langle \varepsilon_{zx} \rangle$ and $\langle \varepsilon_{xz} \rangle$ is due only to the type and geometry of the arrangement of defects (dislocations) in the

Table 1. Angular half-widths for GaN layers (in seconds of arc)

Sample	ω_{twt}	$11\bar{2}4/11\bar{2}\bar{4}$	Bragg				Laue			
			θ 0002	θ–2θ 0002	θ 0004	θ–2θ 0004	θ $10\bar{1}0$	θ–2θ $10\bar{1}0$	θ $20\bar{2}0$	θ–2θ $20\bar{2}0$
A206	1400	560/920	591	42	535	90	525	44	510	85
ATX5	862	257/590	414	26	390	67	184	42	180	75
U296	675	153/261	215	17	200	69	62	22	75	42

microblocks themselves. According to Fig. 1, only vertical screw dislocations make a contribution to $\langle\varepsilon_{zx}\rangle$ and do not affect $\langle\varepsilon_{xz}\rangle$, while vertical edge dislocations do not affect any component of the tensor. In other words, the difference in the components for the two geometries of diffraction makes it possible to calculate the density of the vertical screw dislocations ρ_{vs}. At the same time, the difference in the absolute values of $\langle\varepsilon_{zx}\rangle$ and $\langle\varepsilon_{xz}\rangle$ for thin MOS GaN and a thick layer on it can be due either to a decrease in the density of the vertical screw dislocations in a growing thick layer (because of their bending into the plane of the layer and the formation of dislocation half-loops) or to a separation of the region of the layer under investigation from a strongly defective interface. Thus, the values of $\delta^2 = \langle\varepsilon_{zx}\rangle^2 - \langle\varepsilon_{xz}\rangle^2$ and not of $\langle\varepsilon_{zx}\rangle$ must be used for calculating ρ_{vs} by using relation (6).

It follows from Table 1 that $\langle\varepsilon_{zz}\rangle$ is determined only by horizontal edge dislocations. Since the value of $\langle\varepsilon_{zz}\rangle$ is practically the same in the MOS-GaN substrate and in the thick layer on it, the density of this type of dislocation (or defects with analogous displacement fields) does not change in the case of the CGE growth of GaN.

The value of $\langle\varepsilon_{xx}\rangle$ depends on the presence of vertical, as well as horizontal, edge (misfit) dislocations in the layers, and a decrease in $\langle\varepsilon_{xx}\rangle$ to almost half the initial value upon a transition to the thick layer indicates a decrease in the density of such dislocations. Since misfit dislocations are located predominantly at the interface, the decrease in $\langle\varepsilon_{xx}\rangle$ can be due to the loss of their influence on the diffraction curve for the thick sample. However, the fact that $\langle\varepsilon_{xy}\rangle$ also decreases by one-fourth indicates a simultaneous decrease in the density ρ_{ve} of the vertical edge dislocations (annihilation of dislocations and their bending to the basal plane). The values of ρ_{ve} calculated by formula (6) using $\langle\varepsilon_{xy}\rangle$ are presented in Table 2. The same table contains the value of the density ρ_{ve}^{lab} of vertical edge dislocations (forming small-angle boundaries), which can be obtained from $\langle\varepsilon_{xy}\rangle$ and the values of the lateral size τ_x of the CSR given by Eq. (7). The value of ρ_{ve}^{lab} is three orders of magnitude lower than ρ_{ve}. The values of ρ_{ve} obtained by us from $\langle\varepsilon_{xy}\rangle$ and $\langle\varepsilon_{xx}\rangle$ (in analogy with [16]) indicate the preferred location of vertical edge dislocations in the grains themselves rather than on the grain boundaries.

The difference between the values of ρ_{ve} obtained from our measurements and by the TEM method [5] is worth noting. Since $\rho_{ve} \sim \omega_{OOP}^2$, the possible presence of stacking faults in the layers may lead to an additional broadening of ω_{OOP} that is not associated with the presence of dislocations and, hence, to an exaggerated estimate of ρ_{ve}. However, this correction cannot eliminate the difference between our data and the TEM data. The latter data should be estimated critically from the view-

Table 2. Microdistortion tensor components $\langle\varepsilon_{ij}\rangle$, size τ_i of CSR, and dislocation densities ρ in GaN layers

Components	A206	ATX5	U296
$\langle\varepsilon_{zz}\rangle$, 10^{-4}	2.29	2.36	2.59
$\langle\varepsilon_{zx}\rangle$, 10^{-4}	12.50	9.24	4.71
$\langle\varepsilon_{xx}\rangle$, 10^{-4}	7.57	6.74	3.75
$\langle\varepsilon_{xz}\rangle$, 10^{-4}	12.20	4.32	1.90
$\langle\varepsilon_{xy}\rangle$, 10^{-4}	67.40	41.25	32.52
τ_x (μm)	0.68	1.00	1.61
τ_z (μm)	0.40	1.29	$\gg 1$
ρ_{vs}, 10^8 cm^{-2}	0.30	2.70	0.75
ρ_{ve}, 10^{10} cm^{-2}	4.87	1.83	1.13
ρ_{ve}^{cl}, 10^7 cm^{-2}	1.01	0.25	0.10

point of the improvement in the statistics of processed images, as well as of the completeness of elucidation of all dislocations.

Summarizing the results obtained for these two samples, we note a decrease in the density of dislocations in CGE GaN by a factor of 1.5–3 as compared to the MOS-GaN substrate along with a simultaneous increase in the size of the CSRs. The extremely low value of the half-width of the θ-TCD reflection curve in the Laue geometry (62″), which was not observed earlier for nitrides, allows us to assume that the thick CGE layer of GaN is monocrystalline with inclusions of an insignificant amount of microcrystalline regions.

4.2. The Thick CGE Layer of GaN (A206) on Sapphire

For this layer, the value of $\langle\varepsilon_{zx}\rangle$ is close to $\langle\varepsilon_{xz}\rangle$, which complicates an analysis of the dislocation structure since the contributions cannot be separated by the method used earlier because of the tilt and dislocations. The fact that the half-widths of all (except $11\bar{2}\bar{4}$) θ curves of diffraction are close indicates that the tilt contribution is mainly responsible for the broadening of the diffraction curve in this case. If we assume, as before, that $\omega_{tlt} \cong \omega_\theta^{10\bar{1}0}$, the calculation gives $\rho_{vs} = 0.25 \times 10^8$ cm^{-2}, which is smaller than for a thin MOS-GaN layer and the CGE GaN on it. At the same time, all angular half-widths are larger in the case when the thick layer grows on sapphire without a buffer. This means that the tilt contribution to $\omega_\theta^{10\bar{1}0}$ and the influence of defects on this half-width are overestimated. A more detailed analysis of this layer requires the construction of a map illustrating the distribution of the diffracted intensity in the reciprocal space and a detailed analysis of the dislocation structure on the basis of this map, similar to that carried out in [17].

The densities of vertical randomly distributed edge dislocations calculated from $\langle\varepsilon_{xy}\rangle$ in accordance with Eqs. (6) and (7) for the model of dislocations forming small-angle boundaries are given in Table 2. Their value in this layer is four times higher (for random dislocations) than that for a thick CGE layer on a MOS-GaN substrate and an order of magnitude higher for the model of the formation of small-angle boundaries from vertical edge dislocations.

Thus, we have carried out a complex x-ray diffraction analysis of the dislocation structure of thick CGE layers of GaN on sapphire, as well as on a thin MOS-GaN layer used as a substrate.

We used the approach proposed by us earlier and associated with the x-ray diffraction measurement of the microdistortion tensor and analysis of the defective structure of epitaxial layers, which is carried out on its basis. Use was made of optimal x-ray layouts for detecting the diffracted intensity and the relation between its angular distribution and the type and position of defects in the layers.

The disadvantages of the mosaic model applied for analyzing the dislocation structure of nitrides are demonstrated. It is proposed that apart from the contributions associated with the tilt and size effect, the component associated with defects in the CSR (micrograins) can be singled out and investigated in an analysis of x-ray reflection broadening.

The asymmetric shape of the reciprocal-lattice site is typical of all samples. The shape varies from that extended along the normal to the diffraction vector for the A206 sample (due to the predominance of the tilt effect) to that extended along the sample surface (due to anisotropy in the size of the CSRs, as well as in the deformation fields of defects in them).

The defect structure of all the layers under investigation is characterized by the presence of a large number of vertical screw and edge dislocations in it (the number of the latter dislocations is two orders of magnitude larger). It was found that the density of vertical screw dislocations in a thick CGE-GaN layer is smaller than in a MOS-GaN substrate used for its growth by a factor of 2.5. The density of vertical edge dislocations in the thick layer on a GaN substrate is one-fourth of its value in a thick layer grown directly on sapphire. The extremely low value of the half-width of the θ TCD reflection curve in the Laue geometry (62″) allows us to treat the thick layer as monocrystalline with inclusions of an insignificant number of microcrystalline regions.

REFERENCES

1. R. J. Molnar, W. Gotz, L. T. Romano, and N. M. Johnson, J. Cryst. Growth **178**, 147 (1997).
2. L. T. Romano, B. S. Krusor, and R. J. Molnar, Appl. Phys. Lett. **71**, 2283 (1997).
3. H. Siegle, A. Hoffman, L. Eckey, *et al.*, Appl. Phys. Lett. **71**, 2490 (1997).
4. Y. Golan, X. H. Wu, J. S. Speck, *et al.*, Appl. Phys. Lett. **73**, 3090 (1998).
5. T. Pashkova, S. Tungasmita, E. Valcheva, *et al.*, Mater. Res. Soc. Symp. Proc. (2000) (in press).
6. E. M. Goldys, T. Pashkova, I. G. Ivanov, *et al.*, Appl. Phys. Lett. **73**, 3583 (1998).
7. T. Metzger, R. Hopler, E. Born, *et al.*, Philos. Mag. A **77**, 1013 (1998).
8. R. N. Kyutt and T. S. Argunova, Nuovo Cimento D **19**, 267 (1997).
9. R. N. Kyutt, V. V. Ratnikov, G. N. Mosina, and M. P. Shcheglov, Fiz. Tverd. Tela (St. Petersburg) **41** (1), 30 (1999) [Phys. Solid State **41**, 25 (1999)].
10. G. K. Williamson and W. H. Hall, Acta Metall. **1**, 22 (1953).
11. V. Srikant, J. S. Speck, and D. R. Clarke, J. Appl. Phys. **82** (9), 4286 (1997).
12. M. C. Lee, H.-C. Lin, Y.-C. Pan, *et al.*, Appl. Phys. Lett. **73**, 2606 (1998).
13. K. Kobayashi, A. Yamaguchi, S. Kimura, *et al.*, Jpn. J. Appl. Phys., Part 2 **38**, L611 (1999).
14. C. O. Dunn and E. F. Koch, Acta Metall. **5**, 548 (1957).
15. J. E. Ayers, J. Cryst. Growth **135**, 71 (1994).
16. P. F. Fewster, J. Appl. Crystallogr. **22**, 64 (1989).
17. P. F. Fewster, in *Proceedings of the International School of Crystallography: 23rd Course, X-ray and Neutron Dynamical Diffraction: Theory and Applications, Erice, Italy, 1996*, p. 287.

Translated by N. Wadhwa

Resonant Phonon Scattering due to Crystal-Field-Split Paramagnetic Levels of Pr Ions in PrTe$_{1.46}$

R. G. Mitarov*, L. S. Parfen'eva**, V. V. Popov**, and I. A. Smirnov**

*Dagestan State Technical University, Makhachkala, 367015 Russia

**Ioffe Physicotechnical Institute, Russian Academy of Sciences, Politekhnicheskaya ul. 26, St. Petersburg, 194021 Russia

e-mail: Igor.Smirnov@shuvpop.ioffe.rssi.ru

Received May 5, 2000

Abstract—The lattice heat conductivity κ_{ph} of PrTe$_{1.46}$ and LaTe$_{1.46}$ has been measured within the 2- to 100-K interval. The quantity $-\Delta\kappa_{res}(T)$, the decrease in the heat conductivity caused by resonant phonon scattering due to crystal-field-split paramagnetic levels of Pr, was derived from experimental data using the relation $-\Delta\kappa_{res}(T) = \kappa_{ph(PrTe_{1.46})}(T) - \kappa_{ph(LaTe_{1.46})}(T)$. The energy of the first split paramagnetic level of Pr, Δ_1 was calculated from the $\Delta\kappa_{res}(T)$ relation for $T < T_{res}$. It was found that Δ_1 depends on the nature of the nearest neighbor environment of Pr ions in the lattice. The temperature dependence $\Delta\kappa_{res}(T)$ has been determined to be $\Delta\kappa_{res}(T)$ ($\Delta\kappa_{res} \sim T^{-0.5}$) for $T > T_{res}$. © 2000 MAIK "Nauka/Interperiodica".

INTRODUCTION

A large number of publications deal with phonon scattering due to crystal-field-split paramagnetic levels of rare-earth (RE) ions in solids (see, e.g., monographs and reviews [1–5]).

The cases were considered where the RE ions were impurities [4, 6, 7] (low RE concentration) or main components of a compound (large RE concentration). Situations were discussed where the RE ions were distributed over the lattice in an ordered or disordered manner [4, 5, 8–10] or entered glass compositions [5, 11]. The latter cases related to heavily defective materials.

We were prompted to reconsider the effect of phonon scattering due to RE paramagnetic levels by the unusual behavior of the lattice heat conductivity (κ_{ph}) of YbInCu$_4$ and YbAgCu$_4$.[1] We suggested that the behavior of κ_{ph} in these compounds could be related to the above-mentioned effect. YbInCu$_4$ and YbAgCu$_4$ belong to moderately defective materials, on which phonon scattering due to crystal-field-split paramagnetic levels of RE ions was not investigated within a broad temperature range.

The model compound PrTe$_{1.46}$ can also be classed among the moderately defective materials.

In this work, we have attempted to study the effect of phonon scattering from RE ions on κ_{ph} in moderately

defective materials and to see whether some new specific features would appear in the effect.

Prior to considering our experimental data on the heat conductivity of PrTe$_{1.46}$, let us recall the essence of the effect of phonon scattering from RE ions and characterize the subject of the study.

The inner $4f$ shells of paramagnetic RE ions are only partially filled. Their orbital (L), spin (S), and total (J) angular momenta are nonzero. A free RE ion with an angular momentum J is in a state which is $(2J + 1)$-fold degenerate with respect to the J direction. The electric field of the crystal lattice lifts the degeneracy, so that a system of levels appears in place of one. Lattice vibrations can cause transitions of an ion from one level to another and vary the orientation of J in the process. This results in phonon absorption and, as a consequence, in a decrease in κ_{ph}. The $4f$ shells lie deep within an atom, and, therefore, the lattice crystal field splits their levels by a small amount (~100 K or less). The effect of a decrease in κ_{ph} due to phonon scattering from paramagnetic RE ions can be visualized by means of the diagrams presented in Figs. 1a and 1b. Consider a two-level system (Fig. 1a) and the thermal-phonon energy distribution function (Planck's function, Fig. 1b). A scattering event occurs with the absorption of a phonon of energy $\hbar\omega = \Delta$ (Fig. 1a). In this process, phonons with energies within a narrow interval (hatched in Fig. 1b) do not take part in heat transport, which reduces κ_{ph} by an amount labeled here by $\Delta\kappa_{res}$. Theoretical calculations [4, 12] of the temperature dependence of $\Delta\kappa_{res}$ are presented in graphical form in Fig. 1c. The temperature of the maximum of $\Delta\kappa_{res}$ is

---

[1] The results of heat conductivity measurements on YbInCu$_4$ and YbAgCu$_4$ and their theoretical interpretation are being prepared for publication.
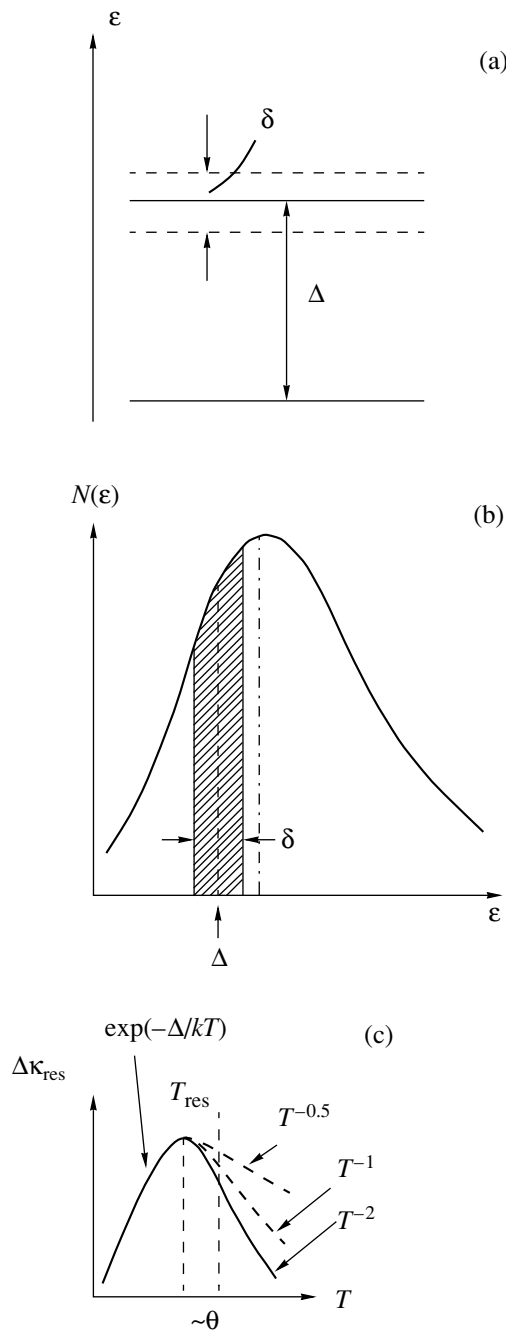
Fig. 1. (a) Energy level diagram of a two-level system, where δ is the temperature-induced level broadening ($\delta \sim \sqrt{T}$ [3, 4, 11]) and Δ is the splitting energy; (b) thermal-phonon energy distribution function; and (c) schematic representation of the temperature dependence of $\Delta\kappa_{res}$ [3, 4, 11]. See text for explanation of the $\Delta\kappa_{res}$ temperature dependences. Θ is the Debye temperature.

For $T > T_{res}$ and $T > \Theta$ (Θ is the Debye temperature), the pattern of the temperature dependence of $\Delta\kappa_{res}$ is determined by the concentration of the paramagnetic ions and by their ordered or disordered arrangement in the lattice. As long as the concentration of paramagnetic ions is low (i.e., they can be considered as an impurity), we have

$$\Delta\kappa_{res} \sim T^{-2}. \tag{1}$$

For high concentrations of paramagnetic ions, where they are the main components of a compound and are positioned in an ordered or disordered manner on the lattice (in the latter case, the phonon–phonon scattering is assumed to be weaker than the phonon–impurity one), one can write

$$\Delta\kappa_{res} \sim T^{-0.5}. \tag{2}$$

For large concentrations and disordered arrangements of paramagnetic ions and under the assumption that the phonon–phonon scattering is stronger than the phonon–impurity scattering, we have

$$\Delta\kappa_{res} \sim T^{-1}. \tag{3}$$

Temperature dependences of the type in Eqs. (1)–(3) were observed experimentally for a number of materials with RE ions [3–5].[2]

We chose $PrTe_{1.46}$ to study resonant phonon scattering due to crystal-field-split paramagnetic levels of RE ions in moderately defective materials. The composition corresponding to the formula $PrTe_{1.46}$ is an "inner" member of the $Pr_{3-y}V_yTe_4$ system, where V_y are cation vacancies. All compositions of the system have a cubic lattice of the type γ-Th_3P_4. The extreme compounds of the above system are Pr_3Te_4 ($PrTe_{1.333}$) and Pr_2Te_3 ($PrTe_{1.5}$). $PrTe_{1.333}$ and $PrTe_{1.5}$ differ from one another only in the concentrations of the vacancies (y varies within the range $0 \leq y \leq 0.333$) and carriers [$n = n_0(1 - 3y)$, where n_0 is the carrier concentration in $PrTe_{1.333}$] [13, 14]. Passing from $PrTe_{1.333}$ to $PrTe_{1.45}$, the vacancy concentration increases from 0 to $\sim 10^{21}$ cm^{-3} and n decreases from $\sim 10^{21}$ cm^{-3} to 0.[3]

Thus, the $PrTe_{1.46}$ composition chosen by us has a sufficiently high Pr vacancy concentration and a low carrier concentration.

The purpose of this work was to isolate and analyze $\Delta\kappa_{res}$ for $PrTe_{1.46}$. To isolate $\Delta\kappa_{res}$, we made use of an experimental method presented in [3]. By this method, $-\Delta\kappa_{res}$ was determined as the difference between the heat conductivities κ_{ph} of crystals containing paramagnetic RE ions and of those which had the same RE concentration but zero L or J angular momenta. We took

denoted by T_{res}. For $T < T_{res}$, we have $\Delta\kappa_{res} \sim e^{-\Delta/kT}$. The dominant contribution to $\Delta\kappa_{res}$ is due, as a rule, to the first split-off level Δ_1, so that, when treating our experimental data, we can accept $\Delta = \Delta_1$.

[2] It should be pointed out that relations of the type $\Delta\kappa_{res} \sim T^{-n}$ were experimentally observed to persist for $T > T_{res}$ to temperatures substantially lower than Θ.

[3] A similar behavior is observed in the Ln_2X_3–Ln_3X_4 systems with a lattice of the γ-Th_3P_4 type, where Ln is a RE element and X stands for S, Se, and Te.

$LaTe_{1.46}$ as the reference material (for La^{3+}, we have $J = 0$); in such a material, phonons do not scatter from paramagnetic ions. If we make the reasonable assumption that the phonon–phonon and phonon–impurity scattering in $PrTe_{1.46}$ and $LaTe_{1.46}$ are close in strength, the quantity $\Delta\kappa_{res}$ for $PrTe_{1.46}$ can be derived as

$$-\Delta\kappa = -\Delta\kappa_{res} = \kappa_{ph}(PrTe_{1.46}) - \kappa_{ph}(LaTe_{1.46}). \quad (4)$$

EXPERIMENTAL

The $LaTe_{1.46}$ and $PrTe_{1.46}$ compounds were prepared from elemental substances by the technique described in [15]. Polycrystalline samples were obtained by RF melting in sealed molybdenum crucibles. After melting, the ingots were annealed at a temperature of ~1200°C. The homogeneity of the samples was checked by thermopower measurements, and the phase composition was judged by x-ray diffraction. All samples had a distinct Th_3P_4-type lattice. The composition of the samples was determined by two-component chemical analysis [16].

The heat conductivity of $LaTe_{1.46}$ and $PrTe_{1.46}$ was measured in the 2- to 100-K range by the absolute method of steady-state linear heat flux.

RESULTS AND DISCUSSION

Measurements are presented in Fig. 2. Because the electronic heat conductivity component was small, it can be accepted that the measured κ is equal to κ_{ph} for both samples. For $LaTe_{1.46}$, in which phonons do not scatter from paramagnetic ions, we have $\kappa_{ph} \sim T^{1.5}$ at low temperatures and $\kappa_{ph} \sim T^{-0.4}$ in the high-temperature domain. Interestingly, a similar behavior of κ_{ph} is also observed in $LuInCu_4$ and $LuAgCu_4$ [17, 18], which can likewise be placed in the class of moderately defective materials and in which, as in $LaTe_{1.46}$, there is no phonon scattering from paramagnetic ions.

Figure 3 presents the quantity $\Delta\kappa$ calculated from Eq. (4), which may be considered equal to $\Delta\kappa_{res}$. The bell-shaped $\Delta\kappa_{res}(T)$ dependence obtained by us experimentally is similar to the relation predicted theoretically in [3–5] (see Fig. 1c).

We first consider the region of temperatures $T < T_{res}$. As is evident from Fig. 3, this region exhibits two resonant temperatures, T_1 and T_2. At T_2, there is a clearly pronounced maximum, while at T_1, only a weak shoulder is seen.

Figure 4 compares our earlier data on $\Delta\kappa(T) = \Delta\kappa_{res}(T)$ for $PrTe_{1.46}$ (Fig. 3) and the Schottky component of heat capacity, $C_{Sch}(T)$ [13], obtained for the $PrTe_{1.47}$ composition. The T_2 maximum in $\Delta\kappa_{res}(T)$ coincides with the first maximum in $C_{Sch}(T)$. The $C_{Sch}(T)$ curve does not exhibit any anomalies corresponding to the maximum at T_1.
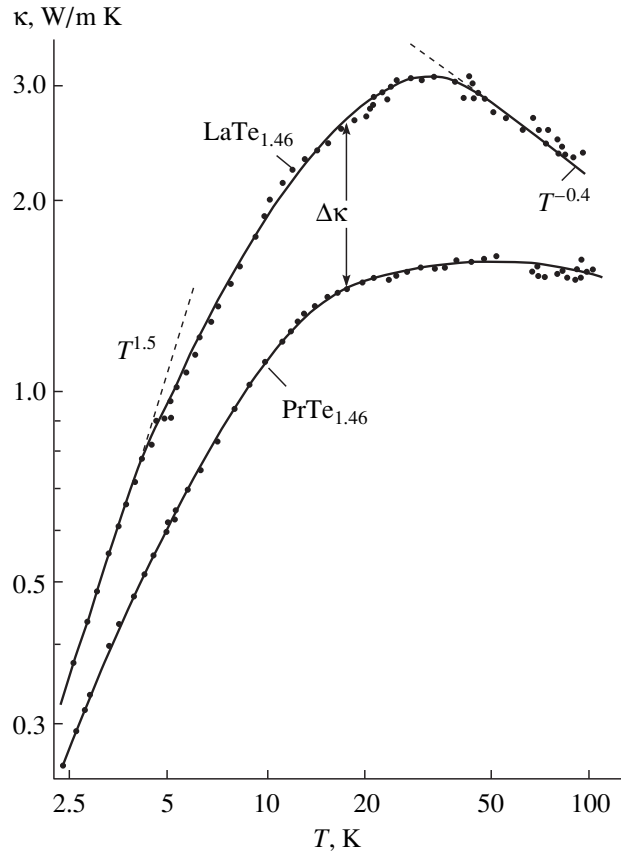
Fig. 2. Temperature dependence of the experimentally measured heat conductivity of $PrTe_{1.46}$ and $LaTe_{1.46}$: $\kappa = \kappa_{ph}$ and $-\Delta\kappa = \kappa_{ph}(PrTe_{1.46}) - \kappa_{ph}(LaTe_{1.46})$.
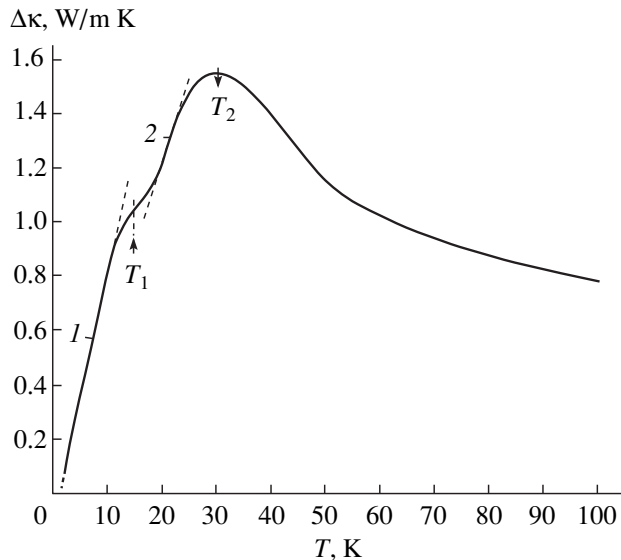

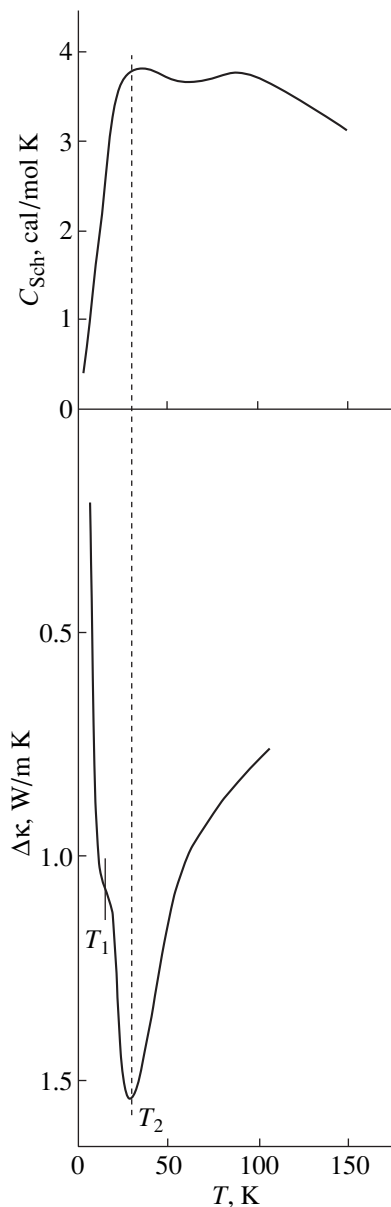**Fig. 3.** Temperature dependence of $\Delta\kappa$ for $PrTe_{1.46}$: $\Delta\kappa = \Delta\kappa_{res}$.

Fig. 4. Temperature dependences of C_{Sch} for PrTe$_{1.47}$ [13] and of $\Delta\kappa = \Delta\kappa_{res}$ for PrTe$_{1.46}$ (this experiment).
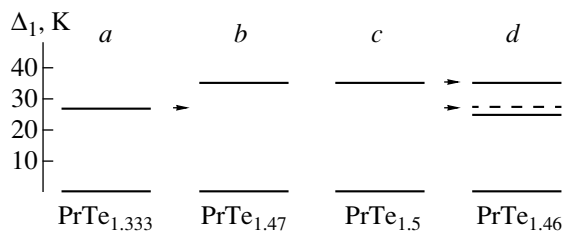

Fig. 5. Energies of the first split-off level Δ_1 of the Pr ion in the crystal field of the PrTe$_x$ lattice derived for different x: (*a*) 1.333, (*b*) 1.47, (*c*) 1.5, and (*d*) 1.46. The figures (*a*, *b*, *c*) were derived from experimental data for C_{Sch} [13, 17], and (*d*) are the results of this experiment. The dashed line in (*d*) identifies the values of Δ_1 obtained in [13, 17] for PrTe$_{1.333}$.

Let us turn back to the analysis of $\Delta\kappa_{res}(T)$. As already pointed out, for $T < T_{res}$, we have $\Delta\kappa_{res} \sim e^{-\Delta_1/kT}$. We succeeded in estimating the values of Δ_1 for regions *1* and *2* (Fig. 3) from the $\log(\Delta\kappa) = f(1000/T)$ relation; they were found to be 24 and 36 K, respectively.

The crystal-field-split Pr levels in PrTe$_{1.333}$, PrTe$_{1.47}$, and PrTe$_{1.5}$ were derived from an analysis of the Schottky component of the heat capacity C_{sch} [13, 19]. The energies for the first split level Δ_1 (obtained by a theoretical treatment of experimental C_{sch} curves) were found to be 27.5, 35.1, and 36.2 K, respectively. These results are presented in Fig. 5 together with data obtained for PrTe$_{1.46}$. Note an interesting feature. The values of Δ_1 obtained by us for PrTe$_{1.46}$ within region *2* are close to those obtained in [13] for PrTe$_{1.5}$ and PrTe$_{1.47}$, while in region *1* they are close to the corresponding figures for PrTe$_{1.333}$. We are going to suggest at least a qualitative interpretation of the above results.

All Pr ions in the PrTe$_{1.333}$ lattice (denoted by Pr1) have the same environment, which entails the same splitting (Δ_1') of their paramagnetic levels (scheme *A* in Fig. 6a). As already pointed out, we shall be interested only in the position of the first split-off level. For PrTe$_{1.333}$, $\Delta_1' = 27.5$ K [13]. As one passes from PrTe$_{1.333}$ to PrTe$_{1.5}$, cation vacancies are created in the lattice, so that the Pr ions may now have different environments. Part of the Pr ions, more specifically, Pr1, have the same environment as in PrTe$_{1.333}$, and, hence, for these ions, $\Delta_1' \sim 27.5$ K (scheme *A* in Fig. 6b), while others (denoted by Pr2) are surrounded by Pr vacancies V_{Pr} in addition to Pr1 ions. In this case, the Pr2 ions will be characterized by another energy, Δ_1'' (Fig. 6b, scheme *B*). A fairly large number of praseodymium ions in PrTe$_{1.5}$, the marginal and most heavily defective compound in the Pr$_{3-y}V_y$Te$_4$ system, can be placed in the Pr2 category. According to [13], for these ions, $\Delta_1 = \Delta_1'' = 36.2$ K. PrTe$_{1.46}$ is an intermediate case (it lies between PrTe$_{1.333}$ and PrTe$_{1.5}$). It may be conjectured that it contains small regions ("islands") with a Pr environment similar to that in PrTe$_{1.333}$ (Figs. 6a, 6b, scheme *A*) and larger regions where Pr has an environment similar to that in PrTe$_{1.5}$ (scheme *B* in Fig. 6). Figure 6c suggests a possible division of PrTe$_{1.46}$ into regions *A* and *B*. Thus, the above reasoning provides a qualitative explanation of the fact that PrTe$_{1.46}$ has two levels with energies of ~24 and 36 K. It remains unclear, however, why this effect was not observed in C_{Sch} [13].

Consider now the $T > T_{res}$ interval in the $\Delta\kappa_{res}(T)$ curve of Fig. 3. Theory suggests that $\Delta\kappa_{res}(T)$ can have different temperature dependences in this temperature region [3–5, 12]. In defective samples (at high RE concentrations, the case where these ions are dominant
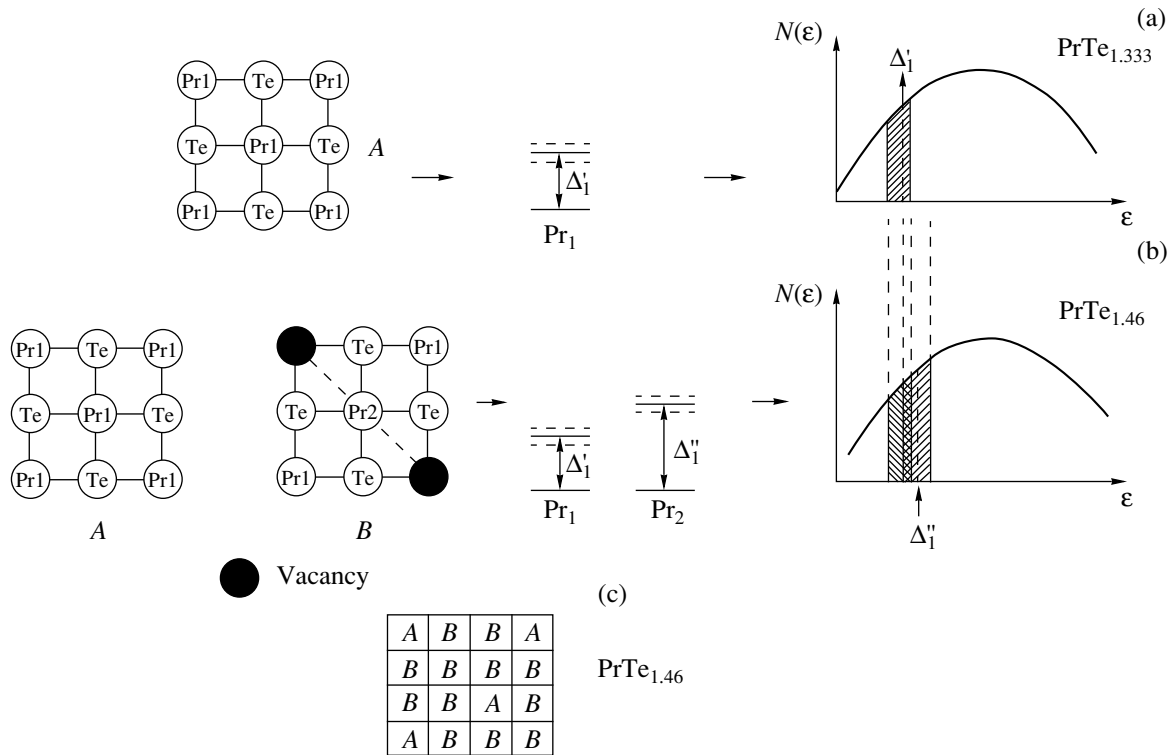
Fig. 6. Schematic illustrating the effect of PrTe$_{1.46}$ crystal-lattice defectiveness on $\Delta\kappa_{res}$. See text for explanation of the data in (a–c).
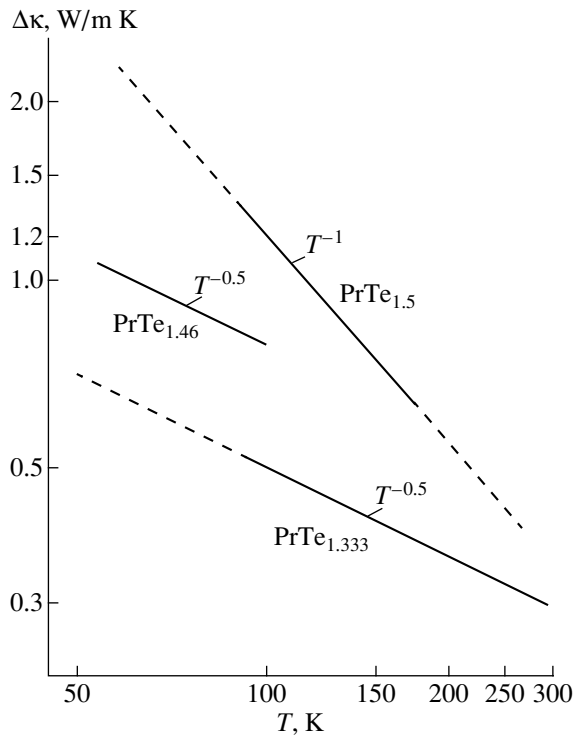
Fig. 7. Temperature dependences of $\Delta\kappa = \Delta\kappa_{res}$ for PrTe$_x$. The data for $x = 1.333$ and 1.5 was taken from [3, 4, 11] and for $x = 1.46$, from this experiment.

components of a compound), $\Delta\kappa_{res}$ scales with temperature as either $T^{-0.5}$ or T^{-1}, depending on the actual defect arrangement in the lattice [3–5, 12] (see Introduction). Based on the data presented in Fig. 3 for PrTe$_{1.46}$, we obtained a relation $\Delta\kappa_{res} \sim T^{-0.5}$, which is plotted in Fig. 7 together with the published data for PrTe$_{1.333}$ and PrTe$_{1.5}$ [3, 4]. As seen from the figure, $\Delta\kappa_{res}$ has a different magnitude for defective and defect-free samples.

As a result of the presence in defective samples of Pr1 and Pr2 ions having different environments in the lattice and, hence, different splittings of the praseodymium paramagnetic levels, the Δ'_1 and Δ''_1 levels (which form bands because of thermal broadening) can merge to produce broad continuous resonant bands (Fig. 6b), which may extend over a sizable part of the phonon spectrum. As a consequence, $\Delta\kappa_{res}$ of PrTe$_{1.333}$ can be substantially smaller than its value observed in defective compositions [4, 12] (Fig. 7).

In closing, we present the T_{res} dependence on Δ_1 in graphical form for a number of materials studied by us earlier [3–5] and for PrTe$_{1.46}$ measured in this work (Fig. 8). The results obtained on all materials fall close to a common straight line.
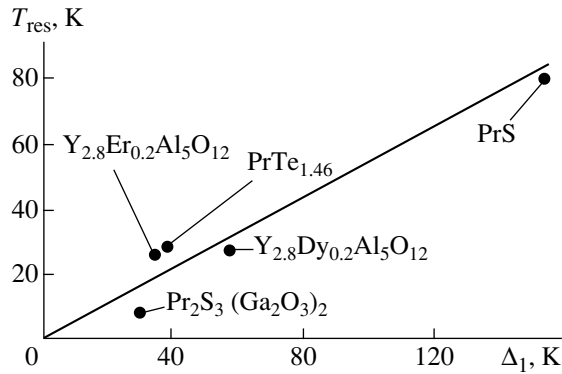
Fig. 8. T_{res} vs. Δ_1 plot for a number of studied materials. The data for $Y_{2.8}Er_{0.2}Al_5O_{12}$, $Y_{2.8}Dy_{0.2}Al_5O_{12}$, and PrS taken from [4, 5]; for the $Pr_2S_3(Ga_2O_3)_2$ glass, from [5]; and for $PrTe_{1.46}$, from this experiment.

CONCLUSIONS

Thus, our experimental study can be summed up as follows:

1. We have measured κ_{ph} for $PrTe_{1.46}$ and $LaTe_{1.46}$. We determined $\Delta\kappa_{res}(T)$, the decrease in the heat conductivity caused by resonant scattering of phonons due to crystal-field-split paramagnetic levels of Pr.

2. An analysis of the $\Delta\kappa_{res}(T)$ relation has yielded the following:

(a) The value of Δ_1 for the first crystal-field-split-off Pr paramagnetic level for $T < T_{res}$. It was found that Δ_1 in a moderately defective material has a specific feature. This quantity depends on the nature of the nearest Pr environment. It is assumed that a sample contains islands, where the nearest neighbors of Pr are similar Pr ions, within the main bulk of material in which Pr vacancies may occupy the place of the nearest Pr neighbors.

(b) The temperature dependence $\Delta\kappa_{res}(T)$ for the $T > T_{res}$ region ($\Delta\kappa_{res} \sim T^{-0.5}$).

REFERENCES

1. V. S. Oskotskiĭ and I. A. Smirnov, *Defects in Crystals and Thermal Conductivity* (Nauka, Leningrad, 1972).

2. R. Berman, *Thermal Conduction in Solids* (Clarendon Press, Oxford, 1976; Mir, Moscow, 1979).

3. I. A. Smirnov, V. S. Oskotskiĭ, and L. S. Parfen'eva, in *Topical Problems of Physics and Chemistry of Rare-Earth Semiconductors. Thematic Collection* (Inst. Fiz. Dagestan. Filiala Akad. Nauk SSSR, Makhachkala, 1988), p. 4.

4. I. A. Smirnov, V. S. Oskotskii, and L. S. Parfen'eva, High Temp.-High Pressures **21**, 237 (1989).

5. I. A. Smirnov and V. S. Oskotskii, *Handbook on the Physics and Chemistry of Rare Earths,* Ed. by K. A. Gshneidner, Jr. and L. Eyring (North-Holland, Amsterdam, 1993), Vol. 16, p. 107.

6. L. N. Vasil'ev, I. Dzhabbarov, V. S. Oskotskiĭ, *et al.*, Fiz. Tverd. Tela (Leningrad) **26** (9), 2710 (1984) [Sov. Phys. Solid State **26**, 1641 (1984)].

7. L. N. Vasil'ev, I. Dzhabbarov, L. S. Parfen'eva, *et al.*, High Temp.-High Pressures **16**, 45 (1984).

8. L. N. Vasil'ev, T. I. Komarova, L. S. Parfen'eva, and I. A. Smirnov, Fiz. Tverd. Tela (Leningrad) **20** (4), 1077 (1978) [Sov. Phys. Solid State **20**, 622 (1978)].

9. S. M. Luguev, T. I. Komarova, V. N. Bystrova, and I. A. Smirnov, Izv. Akad. Nauk SSSR, Neorg. Mater. **14** (1), 46 (1978).

10. G. A. Slack and D. W. Oliver, Phys. Rev. B **4**, 592 (1971).

11. I. A. Smirnov, V. S. Oskotskii, and L. S. Parfen'eva, J. Less-Common Met. **111**, 353 (1985).

12. S. M. Luguev, V. S. Oskotskiĭ, V. M. Sergeeva, and I. A. Smirnov, Fiz. Tverd. Tela (Leningrad) **17** (9), 2697 (1975) [Sov. Phys. Solid State **17**, 1791 (1975)].

13. R. G. Mitarov, V. V. Tikhonov, L. N. Vasil'ev, *et al.*, Phys. Status Solidi A **30**, 457 (1975).

14. A. V. Golubkov, E. V. Goncharova, V. P. Zhuze, G. M. Loginov, V. M. Sergeeva, and I. A. Smirnov, *Physical Properties of Rare-Earth Chalcogenides* (Nauka, Leningrad, 1973).

15. A. V. Golubkov, T. B. Zhukova, and V. M. Sergeeva, Izv. Akad. Nauk SSSR, Neorg. Mater. **2**, 77 (1966).

16. S. M. Luguev, V. S. Oskotskiĭ, L. N. Vasil'ev, *et al.*, Fiz. Tverd. Tela (Leningrad) **17** (11), 3229 (1975) [Sov. Phys. Solid State **17**, 2126 (1975)].

17. A. V. Golubkov, L. S. Parfen'eva, I. A. Smirnov, *et al.*, Fiz. Tverd. Tela (St. Petersburg) **42** (8), 1357 (2000) [Phys. Solid State **42**, 1394 (2000)].

18. A. V. Golubkov, L. S. Parfen'eva, I. A. Smirnov, *et al.*, Fiz. Tverd. Tela (St. Petersburg) **42** (11), 1938 (2000) [Phys. Solid State **42**, 1990 (2000)].

19. R. G. Mitarov, V. V. Tikhonov, L. N. Vasil'ev, *et al.*, Fiz. Tverd. Tela (Leningrad) **17** (2), 496 (1975) [Sov. Phys. Solid State **17**, 310 (1975)].

Translated by G. Skrebtsov

DEFECTS, DISLOCATIONS, AND PHYSICS OF STRENGTH

Local Vibrations in FCC Crystals with Two-Parametric Substitutional Impurities

I. A. Gospodarev*, A. V. Grishaev**, E. S. Syrkin*, and S. B. Feodos'ev*

*Verkin Institute of Low-Temperature Physics and Engineering, National Academy of Sciences of Ukraine, Kharkov, 61164 Ukraine
e-mail: syrkin@ilt.kharkov.ua
**Kharkov State Polytechnical University, ul. Frunze 21, Kharkov, 31002 Ukraine
Received December 29, 1999; in final form, April 21, 2000

Abstract—The threshold parameters of defects (the mass defect and the relative change in the force constants) are determined at which local vibrations start to occur in an fcc crystal with substitutional impurities. The characteristics of local vibrations are investigated, and the influence of the defect parameters on the frequency of local vibrations and their decay rate with distance from the impurity atom is analyzed. The frequencies and the intensities of local vibrations are calculated for the nearest neighboring atoms of an impurity, which, combined with the impurity atom, form a defect cluster. © 2000 MAIK "Nauka/Interperiodica".

INTRODUCTION

One of the principal trends in modern solid-state physics is the study of the properties of so-called zero-dimensional systems, which are virtually isolated atoms or small atomic clusters. Such systems show a surprising behavior; for example, an exotic phenomenon, which is referred to as a "quenching mirage" [1], was observed in a system consisting of an isolated magnetic atom and a nonmagnetic metallic matrix. The characteristics of individual atoms are investigated experimentally, for example, with the help of a scanning tunneling microscope [2] or by microcontact microscopy [3], which opens the way to the controlled synthesis of systems with desired acoustic, optical, mechanical, and other properties (see, e.g., [4]).

For this reason, an investigation of vibrational characteristics of individual, both guest and host, atoms in a crystal lattice is also a topical and urgent problem. The groundwork laid by Lifshitz and the papers of those who adhere to his theories for study into the atomic dynamics of imperfect crystals and disordered systems [5–7] have enabled relevant predictions to be made; in particular, the local vibrational modes with frequencies lying either beyond [8] or within [9] a band of the continuous vibration spectrum of a perfect crystal can exist near a defect. In the physical mechanics of crystal lattices, however, an individual atom is considered as a point oscillator, which is a source of spherical waves. To treat its oscillations in terms of the traditional classification based on an expansion in plane waves is a highly complicated problem. In the case of perfect crystal structures with a simple lattice, the difficulties can be obviated by calculating the characteristics of the crystal as a whole. However, for a lattice with a multiatomic unit cell or for a crystal with defects, the problem has to be solved by atomic-dynamics methods, which leads, within the traditional classification of vibrations, to highly cumbersome expressions, which are very difficult to analyze even in the case of relatively simple systems (see, e.g., [10–14]). Clearly, such is not the case for one-dimensional systems, in which the "plane" and "spherical" waves are the same.

For this reason, no consistent theoretical description has yet been given of many interesting phenomena closely related to the wavefront curvature of elastic waves in the vicinity of a defect. In particular, the conditions for the formation of local vibrational modes that can be split off from the upper boundary of the continuous vibration spectrum in the presence of light or strongly bound impurity atoms in the lattice have not been analyzed and the characteristics of these modes have not been determined.

Determining the maximum number of such vibrational modes existing in a specific lattice-plus-impurity system and calculating the threshold values of the defect parameters (the mass of the impurity atom and the force constants characterizing its interaction with the nearest neighboring atoms) and the fundamental characteristics (the frequency and the dependence of the vibration amplitude on the distance from the impurity) for each of these modes make up an important and pressing problem in atomic dynamics. Its solution provides a way to experimentally determine the force interaction of an impurity atom with the host lattice and is also of technological interest, for example, in developing systems with given resonance properties.

In this paper, we solve this problem for the case of a substitutional impurity in an fcc lattice in which the forces acting between nearest neighboring atoms are central. This model is fairly simple and characterized

by a small number of parameters. At the same time, it is fairly realistic and closely approximates some actual structures. Therefore, this model would be expected to describe qualitatively and, in some instances, quantitatively the behavior of specific systems. The effect of static stresses and weak dilatation in the vicinity of the defect on the results obtained is discussed in the last section.

1. FORMULATION OF THE PROBLEM

As in the theory of lattice dynamics, we represent a crystal lattice as a periodic array of point particles interacting with each other. Their interaction is described by a potential $\varphi_{\mathbf{r}, \mathbf{r'}}$, where $\mathbf{r}$ and $\mathbf{r'}$ are the position vectors of the interacting atoms. For most crystals, this potential cannot be assumed to be pairwise, $\varphi_{\mathbf{r}, \mathbf{r'}} \neq \varphi(\mathbf{r} - \mathbf{r'})$, because it depends on the positions of other atoms. However, for many close-packed crystal lattices, especially for fcc crystals of inert gases (see, e.g., [15]) and some metals (see, e.g., [12]), the pairwise isotropic potential approximation is reasonable, $\varphi_{\mathbf{r}, \mathbf{r'}} = \varphi(|\mathbf{r} - \mathbf{r'}|)$.

Harmonic vibrations of a crystal lattice are described by the Hamiltonian

$$\hat{\mathscr{H}} = \sum_{\mathbf{R}} \frac{\hat{\mathbf{p}}^2(\mathbf{R})}{2m(\mathbf{R})} + \frac{1}{2} \sum_{\mathbf{R} \neq \mathbf{R'}} \hat{\Phi}(\mathbf{R}, \mathbf{R'})\mathbf{u}(\mathbf{R})\mathbf{u}(\mathbf{R'}), \quad (1)$$

where $\mathbf{R}$ and $\mathbf{u}(\mathbf{R})$ are the position vector of an atom in equilibrium (lattice site) and the atomic displacement vector from this equilibrium position, respectively [$\mathbf{r} \equiv \mathbf{R} + \mathbf{u}(\mathbf{R})$]; $\hat{\mathbf{p}}(\mathbf{R})$ and $m(\mathbf{R})$ are the momentum operator and the mass of an atom at the site $\mathbf{R}$, respectively; and $\hat{\Phi}(\mathbf{R}, \mathbf{R'})$ is the force-constant matrix, whose elements are $\Phi_{ik}(\mathbf{R}, \mathbf{R'}) = \partial^2 U/\partial u_i(\mathbf{R})\partial u_k(\mathbf{R'})|_{\mathbf{u} = 0}$, with $U = \frac{1}{2} \sum_{\mathbf{R} \neq \mathbf{R'}} \varphi_{\mathbf{r}\mathbf{r'}}$ being the potential energy of the lattice.

In the case where the interatomic interaction is characterized by an isotropic pairwise potential, we have (see, e.g., [16, 17])

$$\Phi_{ik}(\mathbf{R}, \mathbf{R'}) = (\delta_{\mathbf{R}\mathbf{R'}} - 1)\left[\alpha_{\mathbf{R}\mathbf{R'}}\frac{(X_i - X_i')(X_k - X_k')}{|\mathbf{R} - \mathbf{R'}|^2}\right.$$
$$\left. + \beta_{\mathbf{R}\mathbf{R'}}\delta_{ik}\right] + \delta_{\mathbf{R}\mathbf{R'}}\sum_{\Delta \neq 0}\left[\alpha_{\mathbf{R}\mathbf{R} - \Delta}\frac{\Delta_i\Delta_k}{\Delta^2} + \beta_{\mathbf{R}\mathbf{R} - \Delta}\delta_{ik}\right], \quad (2)$$

where $\Delta \equiv \mathbf{R} - \mathbf{R'}$, $\Delta \equiv |\Delta|$, and

$$\beta_{\mathbf{R}\mathbf{R'}} \equiv \beta_{\mathbf{R}\mathbf{R} - \Delta} \equiv \frac{1}{\Delta}\frac{\partial\varphi_{\mathbf{R}\mathbf{R'}}}{\partial\Delta},$$

$$\alpha_{\mathbf{R}\mathbf{R'}} \equiv \alpha_{\mathbf{R}\mathbf{R} - \Delta} \equiv \frac{\partial^2\varphi_{\mathbf{R}\mathbf{R'}}}{\partial\Delta^2} - \beta_{\mathbf{R}\mathbf{R} - \Delta},$$

$$\varphi_{\mathbf{R}\mathbf{R'}} = \varphi_{\mathbf{R}\mathbf{R} - \Delta}(\Delta) \equiv \varphi_{\mathbf{r}, \mathbf{r'}}|_{\mathbf{u} = 0}.$$

It is obvious that if an atom interacts not only with its nearest neighbors but also with other atoms of the lattice, then the parameter β, characterizing the internal stresses in the lattice, will be nonzero. In the case of an infinite crystal, the presence of such stresses is consistent with the equilibrium condition $\partial U/\partial u_i(\mathbf{R}) = 0$. However, the formation of a free surface, a vacancy, or some other defect in the crystal will have to be accompanied by a relaxation of the force constants near this defect. If only nearest neighboring atoms interact with each other, it is reasonable to assume that the lattice is unstressed; that is, the equilibrium interatomic distances are determined by the pairwise potential, which remains a central force potential. Thus, in Eq. (2), we have

$$\beta_{\mathbf{R}\mathbf{R'}} = \frac{1}{\Delta}\frac{\partial\varphi_{\mathbf{R}\mathbf{R} - \Delta}}{\partial\Delta} \equiv 0,$$

$$\alpha_{\mathbf{R} - \Delta} \equiv \frac{\partial^2\varphi_{\mathbf{R}\mathbf{R} - \Delta}}{\partial\Delta^2} = \frac{\lambda_m}{8}(1 + \eta\delta_{\mathbf{R}0}). \quad (3)$$

Here, the impurity atom is assumed to be at the origin of the coordinates, $\lambda_m/8$ is the force constant of the perfect lattice (λ_m is the square of the maximum frequency of the continuous vibration spectrum), and $\alpha_{0\Delta} = (\lambda_m/8)(1 + \eta)$. The atomic masses at lattice sites are

$$m(\mathbf{R}) = m(1 + \varepsilon\delta_{\mathbf{R}0}), \quad (4)$$

where m is the mass of an atom in the perfect crystal. This description is referred to as two-parametric, because the impurity atom differs from the host atom in mass and single force constant (parameters ε and η).

This model adequately describes, for example, perfect crystals of inert gases Ar, Kr, and Xe [15, 18]. If the impurity is not isotopic, the condition $\beta = 0$ corresponds to the case where the equilibrium interatomic distances for the host–host and impurity–host interaction potentials are equal, which is a very restrictive assumption. However, the unstressed-lattice model with nearest neighbor interaction, in which the force constant characterizing the interaction of the impurity with its nearest neighbors is considered as an adjustable parameter, is proven adequate in many cases [18, 19].

Harmonic vibrations of the crystal lattice are conveniently described by introducing an operator $\hat{\mathscr{L}}$ defined by the expression

$$\mathscr{L}_{ik}(\mathbf{r}, \mathbf{r'}) = \frac{\Phi_{ik}(\mathbf{r}, \mathbf{r'})}{\sqrt{m(\mathbf{r})m(\mathbf{r'})}}. \quad (5)$$

Let $\hat{\mathscr{L}}_0(\mathbf{r}, \mathbf{r'})$ be the operator corresponding to the perfect lattice and $\hat{\mathscr{L}}(\mathbf{r}, \mathbf{r'}, \varepsilon, \eta) \equiv \hat{\mathscr{L}}_0(\mathbf{r}, \mathbf{r'}) + \hat{\Lambda}(\mathbf{r}, \mathbf{r'}, \varepsilon, \eta)$ be the operator characterizing the lattice with a two-parametric substitutional impurity. Combining Eqs. (3)–(5), we find that the perturbation operator rep-

resenting the effect of the impurity on the phonon spectrum of the unstressed fcc lattice has the form

$$
\Lambda_{ik}(\mathbf{r}, \mathbf{r}', \varepsilon, \eta) = \delta_{\mathbf{r}, \mathbf{r}'}\delta_{ik}\left(\frac{\lambda_m}{2}\frac{-\varepsilon + \eta}{1 + \varepsilon}\delta_{\mathbf{r}0} + \frac{\lambda_m}{8}\eta\delta_{\mathbf{r}\Delta}\right)
$$
$$
+ \frac{\lambda_m}{8}(\delta_{\mathbf{r}, \mathbf{r}'-\Delta} + \delta_{\mathbf{r}-\Delta, \mathbf{r}'})\left(\frac{1 + \eta}{\sqrt{1 + \varepsilon}} - 1\right)\frac{\Delta_i\Delta_k}{\Delta^2}. \tag{6}
$$

In the model under discussion, the operator representing the perturbation of the phonon spectrum caused by the impurity can be written as a sum of independent degenerate perturbation operators whose rank is not higher than two [5, 18]. The perturbed spectrum and the additive thermodynamic characteristics of such a system have already been calculated very accurately, the accuracy being limited only by the accuracy of determining the spectrum of the unperturbed system [18, 20]. These calculations were performed in the framework of Lifshitz' theory of regular degenerate perturbation operators by using the Jacobian matrix ($\mathscr{J}$-matrix) method developed by Peresada [20, 21]. The lattice periodicity, broken down by the defect, is not involved explicitly in this method; therefore, it is applicable to both perfect structures and structures with defects. Moreover, the operators ($\mathscr{J}$ matrices), in terms of which vibrations of a system are described in this method, have a nondegenerate spectrum, which allows one to avoid many computational difficulties.

The $\mathscr{J}$-matrix method is described in detail in [20–22] (see also [23, 24]). However, there is no detailed description of its current application to phonon systems. For this reason, Appendix 1 presents the fundamentals of this method, which is necessary in understanding the nomenclature used in this paper.

2. LOCAL VIBRATIONAL MODES OF AN UNSTRESSED FCC CRYSTAL WITH A SUBSTITUTIONAL IMPURITY

In the system under discussion, the operator given by Eq. (6) is degenerate not only in the site representation, but also in the displacement space H, in which the vectors $\mathbf{h} \in H$ are linear combinations of quantities $|\mathbf{r}_s|\mathbf{u}_s$, i.e., the displacements $\mathbf{u}_s$ of an atom at site s from its equilibrium position $\mathbf{r}_s$. The five eigenvectors of this operator that correspond to nonzero eigenvalues (see, e.g., [18, 19]) belong to five different irreducible representations, respectively, of the point symmetry group O_h: τ_-^5, τ_+^1, τ_+^3, τ_+^4, and τ_-^4 (in the notation of [25]). These wavevectors are presented in Appendix 2 and depicted in Fig. 1.

Using these eigenvectors, which are displacements of the atoms of the "defect cluster" comprising the impurity and its nearest host neighbors, one can (see Appendix 1) separate five subspaces of space H, which are invariant under both operators $\hat{\mathscr{L}}_0 (\mathbf{r}, \mathbf{r}')$ and

$\hat{\Lambda} (\mathbf{r}, \mathbf{r}', \varepsilon, \eta)$ (cyclic subspaces). The perturbation introduced into the lattice vibration spectrum by the two-parametric substitutional impurity involves only these mutually orthogonal subspaces. In each of these subspaces $H^h \subset H$, the operators $\hat{\mathscr{L}}_0$, $\hat{\Lambda}$, and $\hat{\mathscr{L}}$ induce operators $\hat{\mathscr{L}}_0^{(h)}$, $\hat{\Lambda}^{(h)}$, and $\hat{\mathscr{L}}^{(h)}$, respectively, which have a simple spectrum and which are represented [in terms of the basis set obtained by the orthonormalization defined by Eq. (A1.1)] by tridiagonal J matrices.

The impurity atom itself is displaced only in the $H^{(\tau_-^5)}$ subspace, and its perturbation of the phonon spectrum depends on the mass defect ε. The operator $\hat{\Lambda}^{(\tau_-^5)}$ is a degenerate operator of the second rank and is represented by the matrix

$$
\Lambda_{ik}^{(\tau_-^5)} = \frac{\lambda_m}{8}\begin{bmatrix} 4\dfrac{-\varepsilon + \eta}{1 + \varepsilon} & 2\left(\dfrac{1 + \eta}{\sqrt{1 + \varepsilon}} - 1\right) \\ 2\left(\dfrac{1 + \eta}{\sqrt{1 + \varepsilon}} - 1\right) & \eta \end{bmatrix}. \tag{7}
$$

In the other four cyclic subspaces, the impurity is at rest at the origin of the coordinates. The operators induced in these four subspaces by the operator defined in Eq. (6) do not depend on the mass defect ε and are perturbation operators of the first rank:

$$
\Lambda_{ik}^{(\tau_+^1)} = \Lambda_{ik}^{(\tau_+^3)} = \Lambda_{ik}^{(\tau_-^4)} = \Lambda_{ik}^{(\tau_+^4)} = \eta\frac{\lambda_m}{8}\delta_{i0}\delta_{k0}. \tag{8}
$$

Because the spectra of the operators $\hat{\mathscr{L}}^{(h)}$ are simple and the zeros of the polynomials $\mathscr{P}_n(\lambda)$ and $\mathscr{P}_{n+1}(\lambda)$ in Eq. (A1.3) alternate with one another (see, e.g., [26]), only one local mode can occur in each of the five cyclic subspaces. Therefore, the two-parametric impurity can give rise to at most five local vibrational modes in the nonstressed fcc lattice. Let us determine the threshold values of the defect parameters ε and η for the occurrence of the local modes. As in the case of exactly soluble models (see, e.g., [27–30]), we can calculate the corresponding Green's functions from Eqs. (A1.2–A1.7), using the $\mathscr{J}$-matrix elements of the operators $\hat{\mathscr{L}}^{(h)} = \hat{\mathscr{L}}_0^{(h)} + \hat{\Lambda}^{(h)}$, and find the poles of these functions, which determine the frequencies of the local modes and, hence, the conditions for their occurrence. (Note that, formally, the degeneracy of the perturbation operator is not essential in this method.) However, in the case under study, the analytic approximation to these functions is not an exact solution (this is always the case for systems in dimensions higher than unity because of the presence of van Hove singularities in the phonon density of states). For this reason, the method involving the degeneracy of the perturbation operators $\hat{\Lambda}^{(h)}$ is more appropriate.
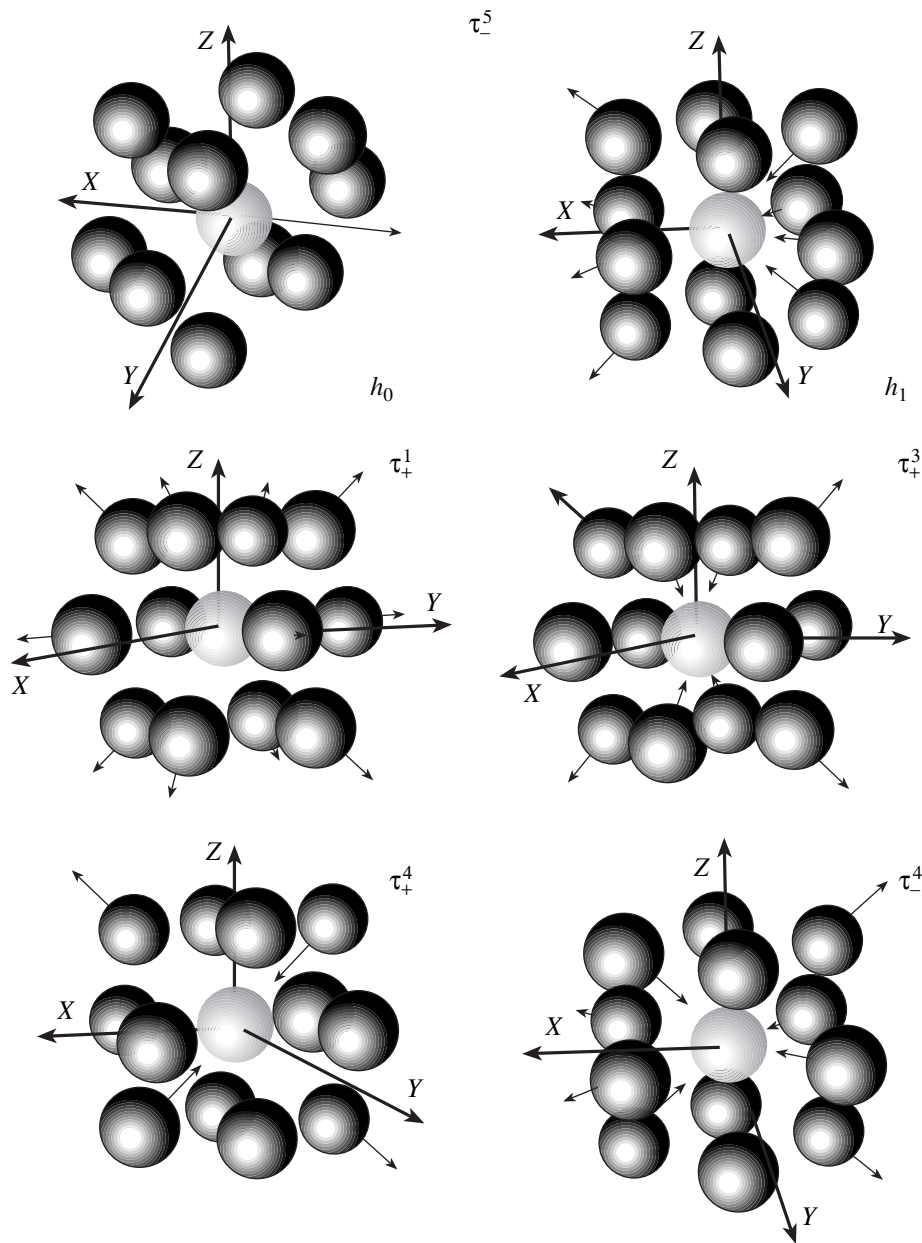
Fig. 1. Eigenvectors of the operator $\hat{\Lambda}$ in the displacement space.

If the spectrum of the operator corresponding to the perfect lattice has no discrete frequencies, the change produced by the degenerate perturbation operator in an additive vibrational characteristic $\mathcal{F}$ can be written in the form [31]

$$\Delta \mathcal{F} = \mathrm{Tr}\{F(\hat{\mathcal{L}}_0 + \hat{\Lambda}) - F(\hat{\mathcal{L}}_0)\}$$
$$= \sum_{\mathbf{h}} \left\{ \int_0^{\lambda_m} \frac{d\mathcal{F}(\lambda)}{d\lambda} \xi^{(h)}(\lambda) d\lambda + [\mathcal{F}(\lambda_l^{(h)}) - \mathcal{F}(\lambda_m)] \right\}, \quad (9)$$

where $\mathcal{F}(\lambda)$ is a function of the frequency, the form of which depends on the characteristic being calculated

and, as a rule, is known with certainty [if $\mathcal{F}(\lambda) \equiv 1$, then $\mathcal{F}$ is the number of independent vibrational modes in the continuous spectrum], and $\xi^{(h)}(\lambda)$ is a spectral-shift function in the cyclic subspace $H^{(h)}$. This function is continuous in the interval $[0, \lambda_m]$, and its derivative $d\xi^{(h)}(\lambda)/d\lambda = \Delta(1/\pi)\mathrm{Im}\,\mathrm{Sp}\,\mathcal{G}^{(h)}$ characterizes the change produced by the degenerate operator $\hat{\Lambda}^{(h)}$ in the continuous spectrum of the operator $\hat{\mathcal{L}}_0^{(h)}$. It should be noted that Eq. (9) is valid only if $\xi^{(h)}(0) = 0$. If the spectrum of the perturbed operator has no local modes (λ_l is the square of the local frequency), then all terms which are

not integrals are also absent in Eq. (9). Owing to the fact that the spectrum of the operators $\hat{\mathcal{L}}^{(h)}$ is simple, the $\mathcal{J}$-matrix method gives the following fairly simple equation for the spectral-shift function [20]:

$$\pi \cot \pi \xi(\lambda) = \frac{S(\lambda, \varepsilon, \mu) + \Psi(\lambda)}{\rho(\lambda)}, \qquad (10)$$

where $\rho(\lambda)$ is the spectral density for the perfect crystal, the quantity

$$\Psi(\lambda) = f \frac{\rho(\mu)}{\mu - \lambda} d\mu = -\mathrm{Re}\,\mathcal{G}_{00}(\lambda)$$

is also a function of the defect parameters, and the quantity $\mathcal{S}(\lambda, \varepsilon, \mu)$ can be written in the form

$$\mathcal{S}(\lambda, \varepsilon, \eta) = \frac{1 + \sum_{\sigma}^{r} \Gamma_{\sigma}(\lambda, \varepsilon, \eta) \mathcal{Q}(\lambda)}{\sum_{\sigma}^{r} \Gamma_{\sigma}(\lambda, \varepsilon, \eta) \mathcal{P}(\lambda)},$$

$$\Gamma_{\sigma}(\lambda, \varepsilon, \eta) = \Lambda_{\sigma, \sigma-1}(\varepsilon, \eta) \tilde{\mathcal{P}}_{\sigma-1}(\lambda, \varepsilon, \eta) \qquad (11)$$

$$+ \Lambda_{\sigma, \sigma}(\varepsilon, \eta) \tilde{\mathcal{P}}_{\sigma}(\lambda, \varepsilon, \eta)$$

$$+ \Lambda_{\sigma, \sigma+1}(\varepsilon, \eta) \tilde{\mathcal{P}}_{\sigma+1}(\lambda, \varepsilon, \eta).$$

Here, r is the rank of the degenerate operator $\tilde{\Lambda}$, that is, the number of eigenfunctions corresponding to nonzero eigenvalues, and $\mathcal{P}_{\sigma}(\lambda)$, $\mathcal{Q}_{\sigma}(\lambda)$, and $\tilde{P}_{\sigma}(\lambda, \varepsilon, \eta)$ are the polynomials given by Eq. (A1.3), constructed using the J matrices of the nonperturbed and perturbed operators, respectively.

For each of the cyclic subspaces, the change caused by the degenerate perturbation operator in the number of states of the continuous spectrum [equal to $\xi^{(h)}(\lambda_m)$ if $\mathcal{F}(\lambda) \equiv 1$, as seen from Eq. (9)] is zero if local modes do not occur but is equal to -1 if one local mode is split off. In a three-dimensional crystal, we have $\rho^{(i)}(0) = \rho^{(i)}(\lambda_m) = 0$ for all cyclic subspaces. Therefore, when $\xi^{(h)}(\lambda_m) = -1$, we obtain from Eq. (10) the inequality

$$\mathcal{S}(\lambda_m, \varepsilon, \eta) + \Psi(\lambda_m) < 0, \qquad (12)$$

from which one can derive the conditions for the occurrence of local vibrational modes in each of the cyclic subspaces. In the case under study, the quantity $\mathcal{S}(\lambda, \varepsilon, \mu)$ in the subspace $H^{(\tau_-^5)}$ has the form

$$\mathcal{S}^{(\tau_-^5)}(\lambda, \varepsilon, \eta) = \frac{2\eta\lambda(1 + \varepsilon) + \lambda_m(1 + \eta)}{\lambda[2\lambda(1 + \varepsilon) - \varepsilon\lambda_m(1 + \eta)]}. \qquad (13)$$

In the other subspaces, where the impurity atom is at rest, the rank of the perturbation operator is equal to unity and its single nonzero matrix element is the same

for the four cyclic subspaces,

$$\Lambda_{00}^{(\tau_+^1)} = \Lambda_{00}^{(\tau_+^3)} = \Lambda_{00}^{(\tau_+^4)} = \Lambda_{00}^{(\tau_-^4)} = \frac{\lambda_m}{8}\eta, \qquad (14)$$

and is naturally independent of ε. A local mode occurs in the subspace $H^{(\tau_-^5)}$ when

$$\eta > \eta_*^{(\tau_-^5)} = \frac{1 - \varepsilon \Psi^{(\tau_-^5)}(\lambda_m)}{-3 - 2\varepsilon - (2 + \varepsilon) \Psi^{(\tau_-^5)}(\lambda_m)} \qquad (15)$$

and in the other subspaces when

$$\eta > \eta_*^{(h)} = -\frac{8}{\Psi^{(h)}(\lambda_m)}. \qquad (16)$$

As the rank of the $\mathcal{J}$ matrix increases, the quantities $\Psi^{(h)}(\lambda_m)$ rapidly approach their limiting values in all subspaces (see Table 1):

$$\eta_*^{(\tau_-^5)} \approx \frac{1 + 4\varepsilon}{5 + 2\varepsilon} \quad \eta_*^{(\tau_+^1)} \approx 2.094; \quad \eta_*^{(\tau_+^3)} \approx 3.347;$$

$$\eta_*^{(\tau_+^4)} \approx 2.720; \quad \eta_*^{(\tau_-^4)} \approx 3.653. \qquad (17)$$

The $\eta_*^{(\tau_-^5)}(\varepsilon)$ dependence is plotted in Figs. 2a and 2b (curve *1*; local modes exist above this curve). This curve approaches the line $\eta = 2$ (dashed line *1'*) as $\varepsilon \longrightarrow \infty$; therefore, at $\eta > 2$, the local mode exists for any (as large as one likes) mass of the impurity atom.

The threshold magnitudes $\eta_*^{(i)}$ of the interatomic interaction above which a local mode exists in the corresponding subspace are indicated in Fig. 2a by hori-

Table 1. Evolution of the values of $\Psi^{(h)}(\lambda_m)$ with increasing rank of the $\mathcal{J}$-matrix $\Psi^{(h)}(\lambda)$

| n	τ_-^5	τ_+^1	τ_+^3	τ_+^4	τ_-^4
1	4.0000	4.5714	2.4615	3.2000	2.2857
2	4.6667	4.0585	2.7574	3.3542	2.3416
3	3.8048	3.9078	2.4235	3.0339	2.2180
4	4.0904	3.8729	2.4258	2.9558	2.2011
5	4.2304	3.8578	2.4222	3.0032	2.1946
6	4.0845	3.8460	2.4139	2.9691	2.1933
8	4.2074	3.8331	2.4157	2.9580	2.1914
10	4.1457	3.8284	2.3968	2.9440	2.1905
12	4.0471	3.8253	2.3968	2.9453	2.1904
16	4.0736	3.8232	2.3940	2.9417	2.1902
20	4.1425	3.8224	2.3947	2.9424	2.1902
24	4.0903	3.8220	2.3938	2.9416	2.1902
30	4.0868	3.8216	2.3934	2.9411	2.1902
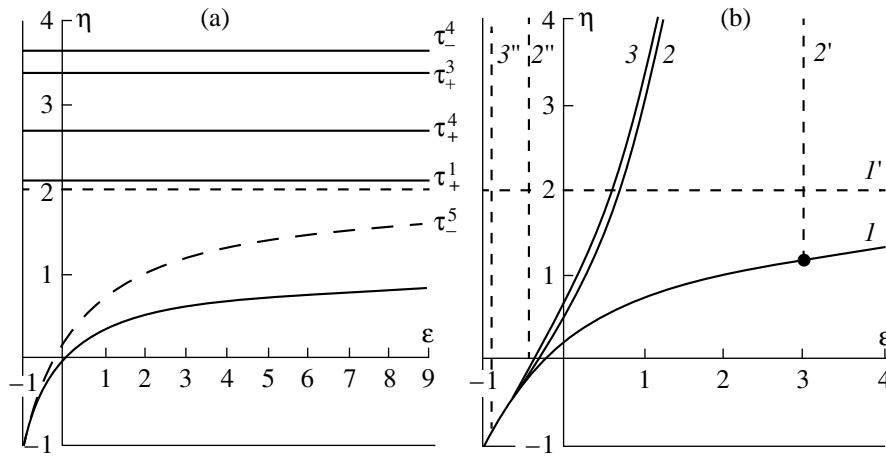
Fig. 2. (a) Threshold values of the defect parameters for the occurrence of local vibrational modes in the various cyclic subspaces of an fcc crystal with a two-parametric substitutional impurity, and (b) the local-vibration mode intensity distribution among the impurity and its first coordination shell in the cyclic subspace τ_-^5 generated by the displacements of the impurity atom.

zontal lines. At $\eta < \eta_*^{(\tau_-^5)}(\varepsilon)$, there are no local vibrational modes. When $\eta \in [\eta_*^{(\tau_-^5)}(\varepsilon), \eta_*^{(\tau_+^1)}]$, there is one local mode in the system. The number of local modes is two at $\eta \in [\eta_*^{(\tau_+^1)}, \eta_*^{(\tau_+^4)}]$, three at $\eta \in [\eta_*^{(\tau_+^4)}, \eta_*^{(\tau_+^3)}]$, four at $\eta \in [\eta_*^{(\tau_+^3)}, \eta_*^{(\tau_-^4)}]$, and five at $\eta > \eta_*^{(\tau_-^4)}$. The impurity atom itself is involved in local vibrations only in one local mode, namely, at the frequency $\omega_l^{(\tau_-^5)} \equiv \sqrt{\lambda_l^{(\tau_-^5)}}$. In the other local modes, only the impurity's neighbors oscillate, whereas the impurity atom itself is at rest.

In the cyclic subspace $H^{(\tau_-^5)}$, the perturbation operator $\hat{\Lambda}$ is a degenerate operator of the second rank; therefore, the intensity of local vibrations with the frequency $\omega_l^{(\tau_-^5)}$ of the impurity's nearest neighbors may be higher than that of the impurity itself. Such a situation was analyzed in [32] for the case of a two-parametric impurity in a linear chain. The results of similar analysis of the model considered in this paper are presented in Fig. 2b. Curve *2* corresponds to $\mathcal{P}_1^2(\lambda_l) = 1$, while curve *3* corresponds to $\mu_0 = 1/2$. Therefore, the intensity of local-mode oscillations of the impurity atom is higher than that of all host atoms taken together in the defect parameter range to the left of curve *3* and is higher than that of the host atoms in the first coordination shell (i.e., of the other atoms of the defect cluster) in the range to the left of curve *2*. The vertical dashed lines *2″* and *3″* correspond to the points of intersection of curves *2* and *3*, respectively, with curve *1*. To

the left of these dashed lines (at $\varepsilon < -0.41$ and -0.89, respectively), the inequalities $\mathcal{P}_1^2(\lambda_l) < 1$ and $\mu_0 > 1/2$ are true for any value of the parameter η. The vertical dashed line *2′* is the common asymptote ($\varepsilon = 3$) of curves *2* and *3* as $\eta \longrightarrow \infty$. Therefore, at $\varepsilon > 3$, the intensity of local-mode oscillations of the nearest host neighbors of the impurity is higher than that of the impurity itself for any value of η.

The fact that curves *2* and *3* are close to each other and have a common asymptote as $\eta \longrightarrow \infty$ suggests that the local vibrational mode in the cyclic subspace $H^{(\tau_-^5)}$ involves only the defect cluster comprising the impurity and its nearest neighbors.

In the other cyclic subspaces, the operator $\hat{\Lambda}$ is a degenerate operator of the first rank and the quantities $\mathcal{P}_n^2(\lambda_l)$ decay exponentially with increasing n from $n = 1$. However, the intensity of the local vibrational modes in these subspaces can also depend nonmonotonically on the coordination shell, because the projections of atomic displacements onto the vectors $\mathbf{h}_n$ in different shells of neighbors can be different, especially for small values of n (i.e., in the vicinity of the defect cluster). Table 2 lists the intensities of the local-mode oscillations for the first four shells of the neighbors in the case of $\varepsilon = 1/2$ and $\eta = 4$.

It is worth noting that the intensity of oscillations of atoms in the second shell is very low. The reason for this is that the displacements of these atoms have no components along the vectors $\mathbf{h}_1$ (nor along $\mathbf{h}_2$ in the $H^{(\tau_-^5)}$ and $H^{(\tau_+^1)}$ subspaces) and their contribution to the local vibrations is exponentially small, even though they are close to the defect.

Table 2. Intensities of local-mode oscillations of the impurity's neighbors in the first four coordination shells for the defect parameters $\varepsilon = 0.5$ and $\eta = 4.0$

	$\dfrac{\omega_l}{\omega_m}$	μ_0	$\mu(0)$	$\mu(I)$	$\mu(II)$	$\mu(III)$	$\mu(IV)$	$\sum_{Z=0}^{4}\mu(Z)$
τ_-^5	1.5617	0.63249	0.63249	0.36100	7.5×10^{-6}	0.00187	0.001608	0.9993
τ_+^1	1.0909	0.88948	–	0.88951	8.6×10^{-6}	0.00598	0.003703	0.9863
τ_+^3	1.0240	0.69019	–	0.69101	0.00809	0.10803	0.17340	0.9805
τ_+^4	1.0510	0.77309	–	0.83912	0.00057	0.07338	0.07048	0.9836
τ_-^4	1.0149	0.73106	–	0.73192	–	0.05072	–	0.7826

The frequencies and intensities of local vibrations can be determined as the poles and residues at these poles, respectively, of the Green's function (A1.2). Figures 3 and 4 show the dependences of the squared local-mode frequency λ_l (curve *1*), local-mode frequency $\omega_l = \sqrt{\lambda_l}$ (dashed curve *2*), and local-mode intensity μ_l (curve *3*) on the impurity parameters. Figure 3 presents these characteristics for the subspace $H^{(\tau_-^5)}$, where they depend on both the impurity mass and the change in the interatomic interaction. Three cases are covered: an isotopic impurity ($\eta = 0$), an impurity whose mass is equal to that of a host atom ($\varepsilon = 0$), and an impurity whose Einstein frequency is equal to that for the perfect lattice ($\eta = \varepsilon$).

For a light isotopic impurity, the local-mode frequency and intensity increase rapidly with decreasing impurity mass and, when the impurity atom is ten times lighter than a host atom, the parameter μ_l becomes close to unity; that is, the amplitude of local-mode oscillations of all atoms of the lattice, excluding the impurity, is negligible.

At $\varepsilon = 0$, the local vibrational mode occurs when the interaction of the impurity atom with its nearest neighbors is strengthened. Clearly, these vibrations cannot be localized entirely on the impurity; the first shell of its neighbors is certain to be involved. Therefore, the intensity of the local mode cannot be equal to unity. The local-mode frequency increases indefinitely with η,
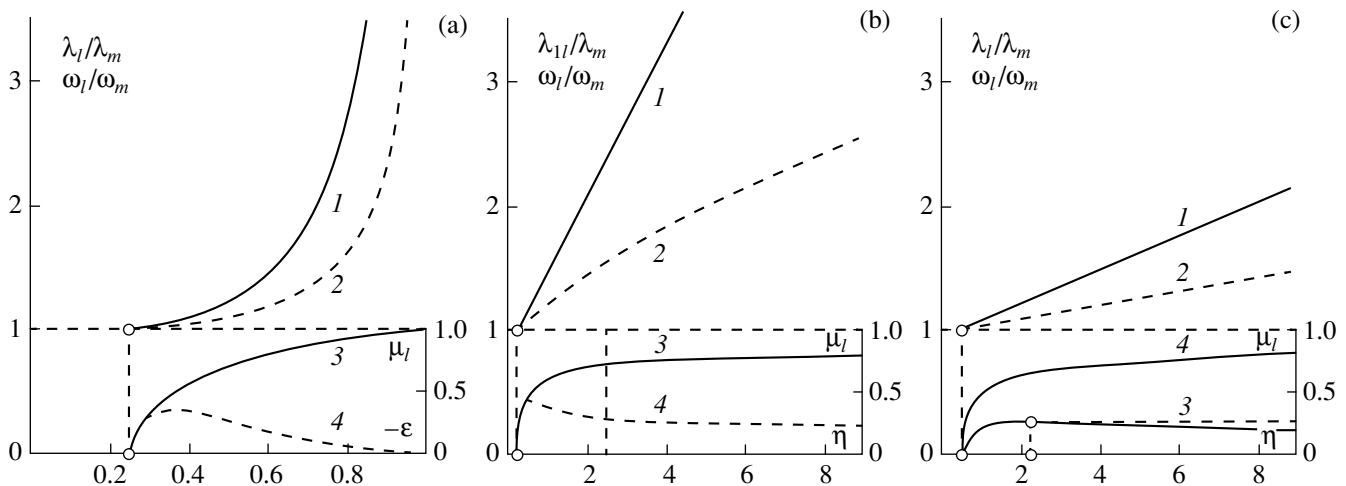
Fig. 3. Dependences on the defect parameters of (*1*) squared frequencies and (*2*) frequencies of local vibrational modes, as well as of the intensities of local-mode oscillations of (*3*) the impurity atom and (*4*) its nearest neighboring atoms in the cyclic subspace τ_-^5 generated by displacements of the impurity atom: (a) $\eta = 0$ (isotopic impurity), (b) $\varepsilon = 0$ (only force constants are changed), and (c) $\eta = \varepsilon$ (the Einstein frequency of the impurity remains unchanged and equal to that of the host atom).
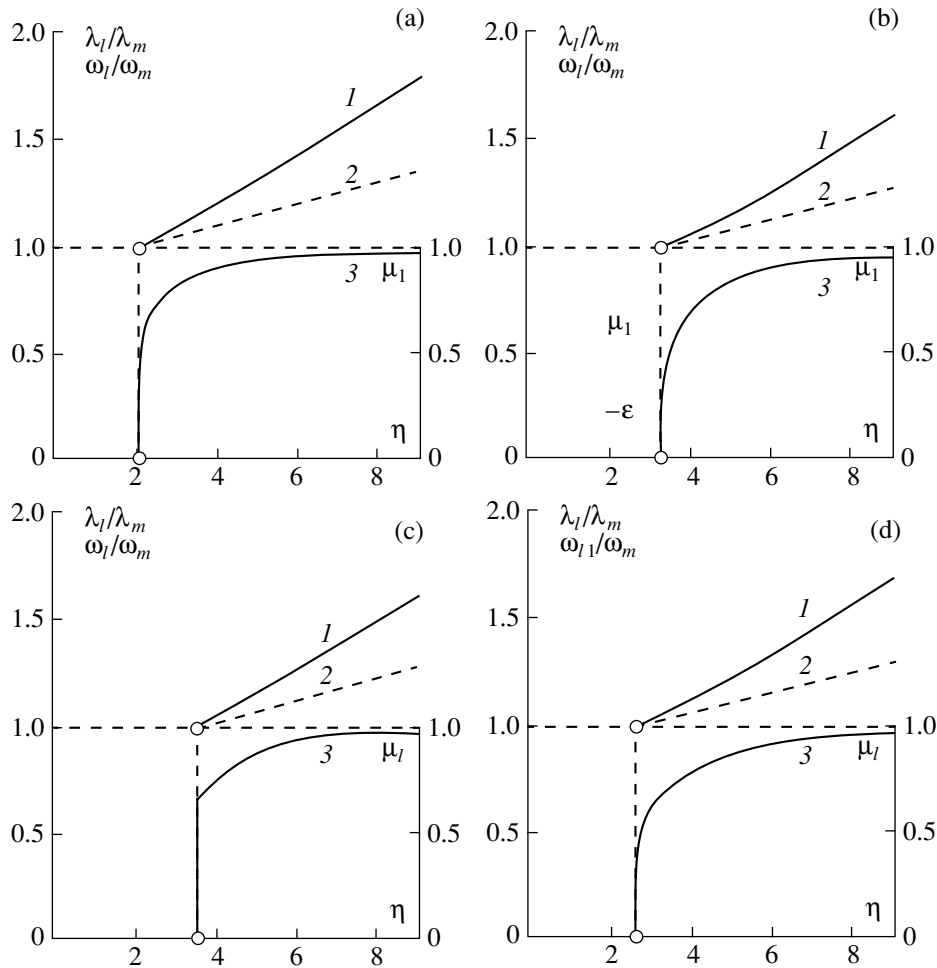
Fig. 4. Dependence on a change in the force constants of (*1*) squared frequencies, (*2*) frequencies, and (*3*) intensities of local vibrational modes in the cyclic subspaces generated by displacements of the impurity's nearest neighboring atoms (the impurity atom itself is at rest): (a) cyclic subspace τ_+^1, (b) τ_+^3, (c) τ_-^4, and (d) τ_+^4.

while μ_l tends to its value μ_l^* for very large η (in the case in question, $\mu_l^* \leq 0.8$).

Finally, at $\varepsilon = \eta$, the local-mode frequency also increases indefinitely with increasing defect parameters, but the increase is slower than in the above two cases; the intensity reaches its maximum $\mu_{l,\,max} \approx 0.2585$ at $\varepsilon = \eta \approx 2.3$ and then slowly decreases to zero. Thus, in this case, the local mode in the $H^{(\tau_-^5)}$ subspace is also not localized on the impurity.

Figure 4 shows the $\lambda_l^{(i)}(\eta)$, $\omega_l^{(i)}(\eta)$, and $\mu_l^{(i)}(\eta)$ dependences for the cyclic subspaces $H^{(\tau_+^1)}$, $H^{(\tau_+^3)}$, $H^{(\tau_+^4)}$, and $H^{(\tau_-^4)}$.

Since the symmetry transformations of the displacements of each of the impurity's nearest neighbors involve all the irreducible representations indicated

above, its oscillation spectrum can have as many as five local-mode frequencies. Figure 5 shows the effect of the parameter η on the functions $\nu^{(i)}(\omega) \equiv 2\omega\rho^{(i)}(\lambda)$, where $\rho^{(i)}(\lambda)$ is the spectral density given by Eq. (A1.8) and is associated with the displacements of an atom of the first coordination shell (at $\mathbf{r} = \boldsymbol{\Delta}$) along three mutually perpendicular directions for the case of a heavy impurity ($\varepsilon = 1/2$).

At $\eta = 1/2$, as seen from Eq. (17), a local vibrational mode appears in the $H^{(\tau_-^5)}$ cyclic space. This is accompanied by the emergence of a square-root-type singularity in the spectral density associated with a displacement of the given atom in the direction $\boldsymbol{\Delta}$ (Fig. 5, curve *1*). The spectral densities associated with the displacements of the given atom along directions perpendicular to the vector $\boldsymbol{\Delta}$ (Fig. 5, curves *2, 3*) are little more than the densities of states of the perfect fcc lattice, represented in all eighteen panels of Fig. 5 by dashed curves.
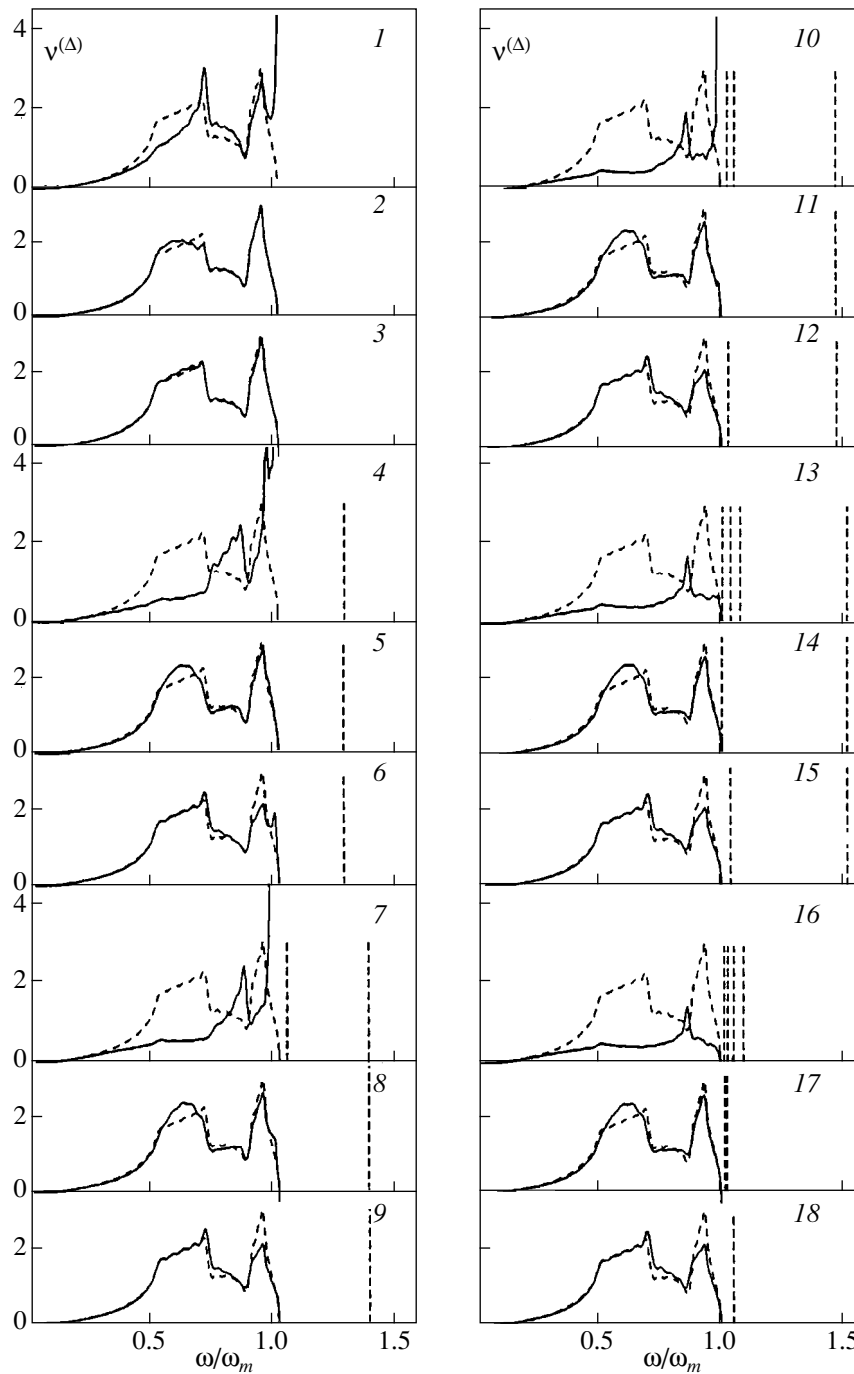
Fig. 5. Effect of strengthening interatomic interaction on spectral densities associated with displacements of a nearest neighboring atom of the heavy impurity ($\varepsilon = 1/2$) along different crystallographic directions.

Curves *4–6* in Fig. 5 correspond to the case of $\eta = \eta_*^{(\tau_+^1)} > \eta_*^{(\tau_-^5)}$, where the local-mode frequency $\omega_l^{(\tau_-^5)} \approx 1.2606\omega_m$ already exists in the vibration spectrum. Further, curves *7–9* correspond to $\eta = \eta_*^{(\tau_+^4)}$; curves *10–12*, to $\eta = \eta_*^{(\tau_+^3)}$; and curves *13–15*, to $\eta = \eta_*^{(\tau_-^4)}$. Accord-

ingly, at $\eta = \eta_*^{(\tau_+^4)}$, there are two local-mode frequencies in the spectrum: $\omega_l^{(\tau_-^5)} \approx 1.3656\omega_m$ and $\omega_l^{(\tau_+^1)} \approx 1.0268\omega_m$. At $\eta = \eta_*^{(\tau_+^3)}$, there are three frequencies: $\omega_l^{(\tau_-^5)} \approx 1.4639\omega_m$, $\omega_l^{(\tau_+^1)} \approx 1.0575\omega_m$, and $\omega_l^{(\tau_+^4)} \approx 1.0221\omega_m$. And at $\eta = \eta_*^{(\tau_-^4)}$, there are four frequencies:

$\omega_l^{(\tau_-^5)} \approx 1.5108\omega_m$, $\omega_l^{(\tau_+^1)} \approx 1.0731\omega_m$, $\omega_l^{(\tau_+^4)} \approx 1.0353\omega_m$, and $\omega_l^{(\tau_+^3)} \approx 1.0008\omega_m$.

Curves *16–18* correspond to the case of $\eta = 4 > \eta_*^{(\tau_+^4)} \equiv \{\eta_*^{(h)}\}_{\max}$, where all possible (five) local-mode frequencies are present in the spectrum: $\omega_l^{(\tau_-^5)} \approx 1.5617\omega_m$, $\omega_l^{(\tau_+^1)} \approx 1.0909\omega_m$, $\omega_l^{(\tau_+^4)} \approx 1.0510\omega_m$, $\omega_l^{(\tau_+^3)} \approx 1.0238\omega_m$, and $\omega_l^{(\tau_-^4)} \approx 1.0146\omega_m$.

There is no oscillation direction for which the oscillation spectrum of a nearest neighbor of the impurity does not contain local-mode frequency $\omega_l^{(\tau_-^5)}$. However, the intensities of oscillations along the vector $\boldsymbol{\Delta}$ and along a direction perpendicular to it are significantly different (the local-mode intensity is given by the difference of the areas under the corresponding solid and dashed curves in Fig. 5). The local-mode frequency $\omega_l^{(\tau_+^1)}$ is present only in oscillations along the vector $\boldsymbol{\Delta}$, the reason for which is easily seen from the form of the generating vector $\mathbf{h}_0^{(\tau_+^1)}$ given by Eq. (A2.1). It should be noted that the local modes existing at a given value of η are observed only in oscillations along the $\boldsymbol{\Delta}$ direction (curves *4, 7, 10, 13, 16*).

The local-mode frequencies $\omega_l^{(\tau_+^3)}$ and $\omega_l^{(\tau_-^4)}$ (when present in the spectrum) are also observed (curves *14, 17*) in oscillations of the $\mathbf{r} = \boldsymbol{\Delta}$ atom along the direction of the vector product $\boldsymbol{\Delta} \times \mathbf{n}$ ($\mathbf{n}$ is a normal to either of the two close-packed planes of the fcc lattice in which the vector $\boldsymbol{\Delta}$ does not lie), while the local-mode frequency $\omega_l^{(\tau_+^4)}$ is also observed in oscillations along the $\boldsymbol{\Delta} \times (\boldsymbol{\Delta} \times \mathbf{n})$ direction (curves *12, 15, 18*).

At the edges of the continuous spectral band in the cyclic subspaces $H^{(\tau_+^1)}$, $H^{(\tau_+^3)}$, and $H^{(\tau_+^4)}$, we have $\rho^{(i)}(\lambda) \sim [\lambda(\lambda_m - \lambda)]^{3/2}$, while $\rho^{(\tau_-^4)}(\lambda) \sim [\lambda(\lambda_m - \lambda)]^{5/2}$ [19, 20], which hampers the calculation of the threshold values of the defect parameters using Eq. (A1.2). Only in the cyclic subspace $H^{(\tau_-^5)}$ (where the generating vector is a one-atomic displacement) is the spectral density proportional to $\sqrt{\lambda(\lambda_m - \lambda)}$ near the end points of the interval $[0, \lambda_m]$. Because the function $\mathrm{Re}\,\mathcal{G}_{00}(\lambda)$ is a polynomial with simple real roots, it is proportional to $\lambda_l \longrightarrow \lambda_m$ when $\lambda_m - \lambda$. Therefore, as seen from Eq. (A1.2), root-type singularities appear in the spectral densities $\rho^{(\tau_-^5)}(\lambda)$, $\rho^{(\tau_+^1)}(\lambda)$, $\rho^{(\tau_+^3)}(\lambda)$, and $\rho^{(\tau_+^4)}(\lambda)$ at the threshold defect parameter values for the occur-

rence of a local mode. In the invariant subspace $H^{(\tau_-^4)}$, no root-type singularity appears in the spectral densities associated with the displacements of the impurity's nearest neighbor (at $\mathbf{r} = \boldsymbol{\Delta}$) along the $\boldsymbol{\Delta}$ direction at the threshold values of the parameter η: $\eta = \eta_*^{(\tau_-^5)}$ (Fig. 5, curve *1*); $\eta = \eta_*^{(\tau_+^1)}$ (curve *4*); $\eta = \eta_*^{(\tau_+^4)}$ (curve *7*); and $\eta = \eta_*^{(\tau_+^3)}$ (curve *10*). Also, a singularity does not occur in the spectral densities associated with the displacements of a nearest impurity neighbor at $\eta = \eta_*^{(\tau_+^4)}$ (curves *13–15*).

3. DISCUSSION OF RESULTS

The model of an unstressed close-packed lattice with a two-parametric substitutional impurity considered in this paper is intermediate between exactly soluble one-dimensional models of systems with defects (see, e.g., [10, 11] and also [27–30]) and real crystals. In contrast to one-dimensional models, the model at hand is fairly realistic and can adequately describe actual systems. At the same time, it can be analyzed relatively correctly; even analytical dependences can be derived in a number of cases.

It should be noted that, in the framework of the traditional classification of vibrations, one cannot make good use of computational methods and present-day computers for solving atomic-dynamics problems, because the natural frequencies have infinitely high degeneracies. Therefore, in order to carry the solution of a problem to its conclusion when studying three-dimensional crystals with defects, most investigators are forced either to use direct computational methods that do not involve any classification of vibrations (e.g., a molecular-dynamics technique) or to oversimplify the model at hand, frequently at the cost of its stability. It is self-evident that only very general features can be described on the basis of oversimplified models of a crystal lattice. Using such a model, quasi-local vibrations were predicted in the low-frequency region of the phonon spectrum and their contribution to low-temperature lattice thermodynamics was determined [9, 33], the qualitative features of the dependence of the phonon spectrum on the concentration of the impurity atoms were elucidated [34], etc. However, a more detailed analysis of the vibrational properties of crystals with defects is impossible to make within such models.

Analyzing the Green's function of an fcc lattice with a two-parametric substitutional impurity, we arrived at the following conclusions.

(1) A two-parametric substitutional impurity in an fcc lattice with nearest neighboring atoms interacting with one another via central forces is a degenerate regular perturbation. It can cause the occurrence of no

more than five local vibrational modes. The spectrum of oscillations of the impurity itself can have only one local-mode frequency; the characteristics of this local mode alone depend on the mass of the impurity atom.

The threshold values of the defect parameters for the occurrence of each of the five local vibrational modes are determined. For these values of the parameters, the corresponding spectral densities associated with the displacements of a nearest neighbor of the impurity along different directions are analyzed.

(2) Beyond the defect cluster, the amplitude of a local vibrational mode decays exponentially with increasing index n of the basis vector $\mathbf{h}_n$ in the classification of vibrations in terms of $\mathscr{J}$ matrices (see Eq. (A1.9)). Because the projections of the displacements of atoms in different coordination shells onto these vectors depend nonmonotonically on the coordination shell, the dependence of the local-mode oscillation amplitude of an atom on its distance from the impurity is also nonmonotonic, especially in the vicinity of the defect cluster. As a rule, the intensity of local-mode oscillations beyond the first four shells of the impurity's neighbors is negligible.

The distribution of the amplitudes of a given local vibration mode within the defect cluster composed of the impurity and its nearest neighbors is calculated numerically as a function of both the mass defect of the impurity and the change in the force constants. It is shown that the amplitude of each of the local vibrational modes (and even the occurrence of the local mode) depends on the relationship between the direction of the oscillations of a given atom and its position with respect to the impurity.

When studying the local vibrations in actual fcc lattices with substitutional impurities, one should take into consideration that, as a rule, an impurity causes elastic stresses. Therefore, even if the interatomic interaction in the host lattice can be assumed to be purely central, the parameter β in Eq. (2) for the matrix of the force constants characterizing the interaction of the impurity with its nearest neighbors will be nonzero. In this case, the operator $\hat{\Lambda}(\mathbf{r}, \mathbf{r'})$ given by Eq. (6) and representing (in the coordinate representation) the perturbation due to the impurity becomes

$$
\begin{aligned}
\Lambda_{ik}(\mathbf{r}, \mathbf{r'}) = {} & \delta_{\mathbf{rr'}}\delta_{ik}\left[\left(\frac{\lambda_m - \varepsilon + \eta}{2\ 1 + \varepsilon} + \beta\right)\delta_{\mathbf{r0}}\right. \\
& + \left(\frac{\lambda_m}{8}\eta + \beta\right)\delta_{\mathbf{r\Delta}}\right] + (\delta_{\mathbf{rr'} - \Delta} + \delta_{\mathbf{r} - \Delta\mathbf{r'}}) \\
& \times \left[\left(\frac{\lambda_m}{8}\frac{1 + \eta}{\sqrt{1 + \varepsilon}} - 1\right)\frac{\Delta_i\Delta_k}{\Delta^2} + \beta\delta_{ik}\right].
\end{aligned} \tag{18}
$$

Its eigenvalues are obtained by adding β to the eigenvalues of the operator in Eq. (6). Therefore, all operators $\hat{\Lambda}^{\mathbf{h}}$ induced by operator (18) in the cyclic sub-

spaces $H^{(\mathbf{h})}$ generated by displacements of the atoms in the first coordination shell are nonzero. In this case, the eigenvalues of operator (18) depend on the change in the central-force constants of the interatomic interaction near the impurity (parameter η) only in the subspaces generated by the vectors given by Eq. (A2.1) and on the impurity mass (parameter ε) only in the subspace $H^{(\tau_-^5)}$ defined in Eq. (A2.1).

Only in the subspaces generated by the vectors $\mathbf{h}$ which transform according to one-dimensional irreducible representations of the O_h group, namely, τ_+^1, τ_+^4, and τ_-^4, and by the two-dimensional representation τ_+^3 realized in the first coordination shell of the fcc lattice by only one basis, does operator (18) induce degenerate operators which are of the first rank. (A group-theoretical analysis of displacements of the impurity's nearest neighboring atoms in the fcc lattice was performed in [19, 20].)

The operators induced by operator (18) are nondegenerate in the other cyclic subspaces. It should be noted that, since the matrix elements a_n and b_n of the $\mathscr{J}$ matrices tend to the limiting values in Eq. (A1.6) with increasing index n, in the classification of vibrations in terms of Eq. (A1.9) there is no fundamental difference between degenerate and nondegenerate perturbation operators that correspond to a defect that does not change the point symmetry group of the crystal. In particular, only one local vibrational mode can occur in each of the cyclic subspaces which transform according to the irreducible representations of group O_h.

In cyclic subspaces generated by vectors other than those presented in Eq. (A2.1), local vibrational modes can occur only for $\beta > 0$. However, it can be shown (see, e.g., [17]) that, when the equilibrium distance for the interaction potential between the impurity atom and a host atom $\tilde{r}_0$ is smaller than that for the interaction potential between host atoms r_0, the impurity is weakly bound to the host lattice. In this case, there can occur only one local vibrational mode, namely, that corresponding to the cyclic subspace $H^{(\tau_-^5)}$ generated by the displacement of the fairly light impurity and presented in Eq. (A2.1). For this mode, the spectral density $\rho^{(\tau_-^5)}(\lambda)$ [17] is localized near the squared Einstein frequency λ_e of the impurity atom, so that the threshold for the occurrence of the local mode corresponds to $\lambda_e \approx \lambda_m$, which agrees with Eq. (17) and Fig. 2 for a light and weakly bound impurity. Note that the range of applicability of the approximation linear in the impurity concentration for calculating vibrational characteristics of such systems is significantly wider in this case (see, e.g., [35, 36]).

The exception to this may be the case where the potential well for the impurity interacting with the host

atoms is many times deeper than that for the host atoms interacting with each other. In this case, additional local vibrational modes can occur. However, such combinations of the host lattice and impurity are seldom encountered. Furthermore, it is unlikely that the impurity concentration will be low in this case; therefore, the impurity atoms, rather than being isolated defects, will form a more complicated structure in combination with the host lattice (an example is the Pd–H system).

If $\tilde{r}_0 > r_0$ and $\beta < 0$, local vibrational modes can occur only in the cyclic subspaces presented in Eq. (A2.1); that is, as in the case of a two-parametric impurity, no more than five local vibrational modes can occur in the system. Direct calculations of the matrix elements of the force interaction using specific (Lennard-Jones, Buckingham, and other) potentials show that in this case, we have $\alpha \gg \beta$ and threshold values of the defect parameters, as well as dependence of the local-mode characteristics on these parameters, which are adequately described by the relations derived for a two-parametric impurity.

The dilatation that may very likely be produced by the impurity atom in this case will not change the results qualitatively if the point symmetry group of the crystal remains unchanged. Naturally, the range of applicability of the approximation linear in the impurity concentration becomes much smaller in this case and is less than one percent.

Thus, we may expect that the basic results obtained in this paper in the two-parametric-impurity approximation will adequately describe the characteristics and the conditions for the occurrence of local vibrational modes in real crystalline systems with impurities. In closing, it is worth remarking that local vibrational modes reveal themselves in optical characteristics. For example, the local modes in the cyclic subspaces $H^{(\tau_-^5)}$ and $H^{(\tau_-^4)}$ should be observed in infrared spectra, while the local modes in cyclic subspaces $H^{(\tau_+^1)}$, $H^{(\tau_+^3)}$, and $H^{(\tau_+^4)}$ should be observed in Raman spectra [37].

APPENDIX 1

FUNDAMENTALS OF THE $\mathcal{J}$-MATRIX METHOD

Let H be the linear space of the atomic displacements of the crystal lattice. Harmonic vibrations of the system can be described with the help of the operator $\hat{\mathcal{L}}$ defined for this space in Eq. (5).

For any vector $\mathbf{h} \in H$, one can construct a cyclic subspace $H^{(\mathbf{h})} \subset H$ invariant under the operator $\hat{\mathcal{L}}$. This subspace is a linear hull spanned by the vectors

$$\{\hat{\mathcal{L}}^n \mathbf{h}\}_{n=0}^{\infty} = \mathbf{h}, \hat{\mathcal{L}}\mathbf{h}, \hat{\mathcal{L}}^2\mathbf{h}, \ldots, \hat{\mathcal{L}}^n\mathbf{h}\ldots \quad (A1.1)$$

In the basis $\{\hat{\mathcal{L}}^n \mathbf{h}_n\}_{n=0}^{\infty}$ obtained by orthonormalizing the vectors in Eq. (A1.1), the operator $\hat{\mathcal{L}}^{(\mathbf{h})}$ induced by the operator $\hat{\mathcal{L}}$ in the subspace $H^{(\mathbf{h})}$ has the form of a Jacobian (tridiagonal) matrix ($\mathcal{J}$ matrix). We denote the diagonal elements of this operator by $a_n^{(\mathbf{h})}$ and the off-diagonal elements by $b_n^{(\mathbf{h})}$, where $n = 1, 2, 3, \ldots$. The index ($\mathbf{h}$) will be dropped when there is no need to indicate the subspace. The operators $\hat{\mathcal{L}}^{(\mathbf{h})}$ have a simple spectrum; their eigenvalues (squared frequencies of free vibrations) are denoted by λ.

The matrix elements of the Green's operator $\hat{\mathcal{G}} = (\lambda \hat{\mathcal{J}} - \hat{\mathcal{L}})^{-1}$ (where $\hat{\mathcal{J}}$ is the unit operator) corresponding to the $\mathcal{J}$ matrix of the operator $\hat{\mathcal{L}}$ can be represented in the form of a continued fraction, and the Green's function $\mathcal{G}_{00}(\lambda)$ can be written as

$$\mathcal{G}_{00}(\lambda) = \frac{\mathcal{G}_n(\lambda) - b_{n-1}\mathcal{G}_{n-1}(\lambda)\mathcal{K}_{\infty}(\lambda)}{\mathcal{P}_n(\lambda) - b_{n-1}\mathcal{P}_{n-1}(\lambda)\mathcal{K}_{\infty}(\lambda)}. \quad (A1.2)$$

Here, $\mathcal{P}_n(x)$ and $\mathcal{G}_n(x)$ are polynomials generated by the $\mathcal{J}$ matrix of the operator $\hat{\mathcal{L}}$; they obey the same recurrence relation

$$\begin{aligned} b_m\{\mathcal{P}, \mathcal{G}\}_{m+1}(x) &= (x - a_m)\{\mathcal{P}, \mathcal{G}\}_m(x) \\ &\quad - b_{m-1}\{\mathcal{P}, \mathcal{G}\}_{m-1}(x), \end{aligned} \quad (A1.3)$$

but are subject to different initial conditions:

$$\mathcal{P}_{-1}(x) \equiv 0, \quad \mathcal{P}_0(x) \equiv 1,$$

$$\mathcal{G}_0(x) \equiv 0, \quad \mathcal{G}_1(x) \equiv \frac{1}{b_0}.$$

The polynomial $\prod_{k=0}^{n-1} b_k$ coincides with the determinant of the $\mathcal{J}$-matrix $\lambda\mathcal{J} - \mathcal{L}_n$ (except for the factor $\mathcal{P}_n(\lambda)$), where $\hat{\mathcal{L}}_n$ is the $\mathcal{J}$ matrix whose elements coincide with those of the operator $\hat{\mathcal{L}}$ (from the first elements to a_{n-1} and b_{n-1} inclusive), while $\hat{\mathcal{G}}_n(\lambda)$ is the minor of the first diagonal element of this matrix. $\mathcal{K}_{n+1}(\lambda)$ is the continued fraction corresponding to the $\mathcal{J}$-matrix $\mathcal{L} - \mathcal{L}_n$.

From the definition of the basis $\{\mathbf{h}\}_{n=0}^{\infty}$ and from the recurrence relation (A1.3), it follows that

$$\mathbf{h}_n = \mathcal{P}_n(\hat{\mathcal{L}})\mathbf{h}_0. \quad (A1.4)$$

Hence, for all eigenvalues λ (lying in the continuous band, as well as the discrete), we have

$$\mathcal{G}_{mn}(\lambda) = \mathcal{P}_m(\lambda)\mathcal{P}_n(\lambda)\mathcal{G}_{00}(\lambda), \quad (A1.5)$$

where $\mathcal{G}_{00}(\lambda)$ is given by Eq. (A1.2). The function $\mathcal{K}_n(\lambda)$ involved in Eq. (A1.2) can be defined in different ways (see, e.g., [20, 22, 29, 38]). Let us consider a simple crystal lattice whose continuous vibration spectrum occupies the interval $[0, \lambda_m]$ and has no gap. It is well known (see, e.g., [20, 21, 23]) that the elements of $\mathcal{J}$ matrices of operators with a spectrum of this type satisfy the limiting relations

$$\lim_{n \to \infty} a_n = a, \quad \lim_{n \to \infty} b_n = b, \quad a = 2b = \frac{\lambda_m}{2}. \quad \text{(A1.6)}$$

The continued fraction corresponding to the $\mathcal{J}$ matrix composed of the elements a and b reduces to the expression

$$\mathcal{K}_\infty(\lambda) = 4\lambda_m^{-2}\{2\lambda - \lambda_m + 2Z(\lambda)\sqrt{\lambda|\lambda - \lambda_m|}\}, \quad \text{(A1.7)}$$

where

$$Z(\lambda) = i\Theta(\lambda)\Theta(\lambda_m - \lambda) - \Theta(\lambda - \lambda_m),$$

with $\Theta(x)$ being the Heaviside theta function. Substituting function (A1.7) for $\mathcal{K}_n(\lambda)$ in Eq. (A1.2), we obtain $\mathcal{G}_{00}(\lambda)$, which is an analytic approximation to the Green's function $\mathcal{G}_{00}(\lambda)$ (that is, this function is approximated by an analytic function).

The function given by Eq. (A1.7) has a nonzero imaginary part in the continuous spectral band, $\lambda \in [0, \lambda_m]$. Therefore, the spectral density $\rho(\lambda)$, defined as (see, e.g., [10]) $\rho(\lambda) = (1/\pi)\lim_{\gamma \to 0} \text{Im}\,\mathcal{G}_{00}(\lambda + i\gamma)$, can be written in the form [22]

$$\rho(\lambda) = \frac{1}{\pi}\text{Im}\,\mathcal{G}_{00}(\lambda)$$
$$= \frac{1}{\pi}\frac{\text{Im}\,\mathcal{K}_\infty(\lambda)}{|\mathcal{P}_n(\lambda) - b_{n-1}\mathcal{P}_{n-1}(\lambda)\mathcal{K}_\infty|^2}. \quad \text{(A1.8)}$$

The function $\rho(\lambda)$ characterizes the frequency distribution of the vibrational modes in the continuous spectral band. The total density of states (the squared-frequency distribution function) is equal to the arithmetic mean of the spectral densities in the subspaces generated by linearly independent displacements $\mathbf{h}^{(i)} \in H$. If all elements b_n are nonzero (and, therefore, the J matrix does not reduce to a block-diagonal form), the function $\mathcal{G}_{00}(\lambda)$ will have no poles in the continuous spectral band, as seen from Eqs. (A1.7) and (A1.8). If there exist poles at $\lambda_l \notin [0, \lambda_m]$, they correspond to the squared frequencies of local vibrational modes, while the residues at these poles determine the intensity (i.e., the relative amplitudes) of the vibrational modes.

The eigenfunction of the operator $\hat{\mathcal{L}}$ corresponding to its eigenvalue λ can be written in the form

$$\chi_\lambda = \sum_n \mathcal{P}_n(\lambda)\mathbf{h}_n. \quad \text{(A1.9)}$$

Since the elements of $\mathcal{J}$ matrices tend to certain limiting values with increasing n [see, e.g., Eq. (A1.6)], the structure of the vibration spectrum will be controlled by their first elements and the singularities of the function in Eq. (A1.9) will be determined fundamentally by its first several terms. Therefore, the distortions of the phonon spectrum caused by a local defect are associated predominantly with the cyclic subspaces generated by the displacements of the impurity atom and its nearest neighbors (more specifically, with the first elements of the corresponding $\mathcal{J}$ matrices). This, along with the nondegeneracy of the spectrum, is the reason why the classification based on the eigenfunctions in Eq. (A1.9) is favored over the traditional classification in terms of plane waves in considering vibrations of systems with defects and complex crystal structures.

APPENDIX 2

EIGENVECTORS CORRESPONDING
TO NONZERO EIGENVALUES
OF THE OPERATOR $\hat{\Lambda}(\mathbf{r}, \mathbf{r}', \varepsilon, \eta)$

$$\mathbf{h}_0^{(\tau_-^5)} = |0|1\rangle,$$

$$\mathbf{h}_0^{(\tau_+^1)} = \frac{1}{2\sqrt{3}}\sum_\Delta \left|\Delta\left|\frac{\Delta}{\Delta}\right\rangle\right.,$$

$$\mathbf{h}_0^{(\tau_+^3)} = \frac{1}{4}\begin{vmatrix} a/2(\ 1 & 0 & 1) \\ a/2(\ 1 & 0 & -1) \\ a/2(-1 & 0 & 1) \\ a/2(-1 & 0 & -1) \\ a/2(\ 0 & 1 & 1) \\ a/2(\ 0 & 1 & -1) \\ a/2(\ 0 & -1 & 1) \\ a/2(\ 0 & -1 & -1) \end{vmatrix}\begin{pmatrix} 1 & 0 & 1 \\ 1 & 0 & -1 \\ -1 & 0 & 1 \\ -1 & 0 & -1 \\ 0 & -1 & -1 \\ 0 & -1 & -1 \\ 0 & 1 & -1 \\ 0 & 1 & 1 \end{pmatrix}, \quad \text{(A2.1)}$$

$$\mathbf{h}_0^{(\tau_+^4)} = \frac{1}{2\sqrt{2}}\begin{vmatrix} a/2(\ 0 & 1 & 1) \\ a/2(\ 0 & 1 & -1) \\ a/2(\ 0 & -1 & 1) \\ a/2(\ 0 & -1 & -1) \end{vmatrix}\begin{pmatrix} 0 & 1 & 1 \\ 0 & -1 & 1 \\ 0 & 1 & -1 \\ 0 & -1 & -1 \end{pmatrix},$$

$$\mathbf{h}_0^{(\tau_-^4)} = \frac{1}{4}\begin{vmatrix} a/2(\ 1 & 1 & 0) \\ a/2(\ 1 & -1 & 0) \\ a/2(-1 & 1 & 0) \\ a/2(-1 & -1 & 0) \\ a/2(\ 1 & 0 & 1) \\ a/2(\ 1 & 0 & -1) \\ a/2(-1 & 0 & 1) \\ a/2(-1 & 0 & -1) \end{vmatrix}\begin{pmatrix} 1 & 1 & 0 \\ 1 & -1 & 0 \\ 1 & -1 & 0 \\ 1 & 1 & 0 \\ -1 & 0 & -1 \\ -1 & 0 & 1 \\ -1 & 0 & 1 \\ -1 & 0 & -1 \end{pmatrix},$$

REFERENCES

1. H. C. Manoharan, C. P. Lutz, and D. M. Eigler, in *Abstracts of the 18th General Conference of the COND, Mat. Division of EPS, Montreux, Switzerland, 2000*, p. 141.

2. V. Madhavan, W. Chen, T. Jamneala, *et al.*, Science **280** (5363), 567 (1998).

3. A. I. Yanson, I. K. Yanson, and J. N. van Ruitenbeek, Nature **400**, 144 (1999).

4. B. M. Smirnov, Usp. Fiz. Nauk **163** (10), 29 (1993) [Phys. Usp. **36**, 933 (1993)]; Usp. Fiz. Nauk **164** (11), 1166 (1994) [Phys. Usp. **37**, 1079 (1994)].

5. I. M. Lifshitz, Nuovo Cimento Suppl. **3**, 716 (1956).

6. I. M. Lifshitz and A. M. Kosevich, Rep. Prog. Phys. **29**, 217 (1966).

7. I. M. Lifshitz, S. A. Gredeskul, and L. A. Pastur, *Introduction to the Theory of Disordered Systems* (Nauka, Moscow, 1982; Wiley, New York, 1988).

8. I. M. Lifshitz, Zh. Éksp. Teor. Fiz. **12**, 117 (1942); **12**, 137 (1942); **12**, 156 (1942); Dokl. Akad. Nauk SSSR **48** (2), 83 (1945).

9. Yu. Kagan and Ya. Iosilevskiĭ, Zh. Éksp. Teor. Fiz. **42** (1), 259 (1962); Zh. Éksp. Teor. Fiz. **44** (1), 284 (1963) [Sov. Phys. JETP **17**, 195 (1963)]; Zh. Éksp. Teor. Fiz. **45** (3), 819 (1963) [Sov. Phys. JETP **18**, 562 (1963)].

10. A. M. Kosevich, *The Theory of Crystal Lattice* (Vishcha Shkola, Kharkov, 1988).

11. A. A. Maradudin, E. W. Montroll, G. N. Weiss, and I. P. Ipatova, *Lattice Dynamics and Models of Interatomic Forces* (Springer-Verlag, Berlin, 1982).

12. G. Leibfried and N. Brauer, *Point Deffects in Metals* (Springer-Verlag, Heidelberg, 1978; Mir, Moscow, 1981).

13. H. Bottger, *Principles of the Theory of Lattice Dynamics* (Physik-Verlag, Weinheim, 1983; Mir, Moscow, 1986).

14. A. P. Zhernov, N. A. Chernoplekov, and É. Mrozan, *Metals with Non-Magnetic Impurity Atoms* (Énergoatomizdat, Moscow, 1992).

15. *Physics of Cryocrystals*, Ed. by V. G. Manzhelii and Yu. A. Freiman (American Inst. of Physics, New York, 1996).

16. J. A. Reissland, *The Physics of Phonons* (Wiley, New York, 1973; Mir, Moscow, 1975).

17. S. B. Feodosyev, I. A. Gospodarev, M. A. Mamalui, and E. S. Syrkin, J. Low Temp. Phys. **111** (3–4), 441 (1998).

18. V. I. Peresada and V. P. Tolstoluzhskiĭ, Fiz. Nizk. Temp. **3** (6), 788 (1977) [Sov. J. Low Temp. Phys. **3**, 383 (1977)].

19. V. I. Peresada and V. P. Tolstoluzhskiĭ, *Effect of Impurity Atoms on the Thermodynamic Properties of the FCC Lattice*, Preprint FTINT Akad. Nauk USSR (Kharkov, 1970).

20. V. I. Peresada, Doctoral Dissertation in Mathematical Physics (FTINT Akad. Nauk USSR, Kharkov, 1972).

21. V. I. Peresada, in *Physics of the Condensed State* (FTINT Akad. Nauk USSR, Kharkov, 1968), p. 172.

22. V. I. Peresada, V. N. Afanas'ev, and V. S. Borovikov, Fiz. Nizk. Temp **1** (4), 461 (1975) [Sov. J. Low Temp. Phys. **1**, 227 (1975)].

23. R. Haydock, in *Solid State Physics*, Ed. by H. Ehrenreich *et al.* (Academic, New York, 1980), Vol. 35, p. 129.

24. M. Lanno and J. Bourgoin, *Point Defects in Semiconductors, Experimental Aspects* (Springer-Verlag, New York, 1981; Mir, Moscow, 1984).

25. O. V. Kovalev, *Irreducible Representations of the Space Groups* (Akad. Nauk USSR, Kiev, 1961; Gordon and Breach, New York, 1965).

26. G. Szego, *Orthogonal Polynomials* (American Mathematical Society, New York, 1959; Fizmatgiz, Moscow, 1962).

27. M. A. Mamaluĭ, E. S. Syrkin, and S. B. Feodos'ev, Fiz. Tverd. Tela (St. Petersburg) **38** (12), 3683 (1996) [Phys. Solid State **38**, 2006 (1996)].

28. E. S. Syrkin and S. B. Feodos'ev, Fiz. Nizk. Temp. **20** (6), 586 (1994) [Low Temp. Phys. **20**, 463 (1994)].

29. M. A. Mamaluĭ, E. S. Syrkin, and S. B. Feodos'ev, Fiz. Nizk. Temp. **24** (8), 773 (1998) [Low Temp. Phys. **24**, 583 (1998)].

30. M. A. Mamaluĭ, E. S. Syrkin, and S. B. Feodos'ev, Fiz. Nizk. Temp. **25** (1), 72 (1999) [Low Temp. Phys. **25**, 55 (1999)].

31. I. M. Lifshitz, Usp. Mat. Nauk **7**, 171 (1952).

32. M. A. Mamaluĭ, E. S. Syrkin, and S. B. Feodos'ev, Fiz. Nizk. Temp. **25** (8–9), 976 (1999) [Low Temp. Phys. **25**, 732 (1999)].

33. A. P. Zhernov and G. R. Augst, Fiz. Tverd. Tela (Leningrad) **9** (9), 2196 (1967) [Sov. Phys. Solid State **9**, 1724 (1967)].

34. M. A. Ivanov, Fiz. Tverd. Tela (Leningrad) **12** (7), 1895 (1970) [Sov. Phys. Solid State **12**, 1508 (1971)].

35. E. S. Syrkin and S. B. Feodos'ev, Fiz. Tverd. Tela (St. Petersburg) **34** (5), 1377 (1992) [Sov. Phys. Solid State **34**, 727 (1992)].

36. M. I. Bagatskiĭ, E. S. Syrkin, and S. B. Feodos'ev, Fiz. Nizk. Temp. **18** (8), 894 (1992) [Sov. J. Low Temp. Phys. **18**, 629 (1992)].

37. H. Poulet and J.-P. Mathieu, *Vibrational Spectra and Symmetry of Crystals* (Gordon and Breach, Paris, 1970; Mir, Moscow, 1973).

38. Yu. Ya. Tomchuk, Author's Abstract of Candidate's Dissertation (Kharkovs. Gos. Univ., Kharkov, 1964).

Translated by Yu. Epifanov

KCl Crystals with a Silver Impurity: From Point Defects to Oriented AgCl Microcrystals in a Crystalline Host

P. G. Baranov, N. G. Romanov, V. A. Khramtsov, A. G. Badalyan, and R. A. Babunts

Ioffe Physicotechnical Institute, Russian Academy of Sciences, Politekhnicheskaya ul. 26, St. Petersburg, 194021 Russia
e-mail: Nikolai.Romanov@pop.ioffe.rssi.ru

Received April 27, 2000

Abstract—This paper presents the first unambiguous optically detected magnetic-resonance (ODMR) evidence that AgCl crystals embedded in the KCl lattice and retaining the host orientation are formed in KCl crystals grown with a 2–3 mol % silver impurity. ODMR spectra were obtained of self-trapped holes, shallow electronic centers, and self-trapped excitons, which are typical of AgCl, and a number of substantially different ODMR spectra were also obtained. The differences between the ODMR spectra observed in samples cleaved from different parts of a KCl : AgCl crystal are probably accounted for by embedded AgCl crystals varying in size from large micro- to nanocrystals. © 2000 MAIK "Nauka/Interperiodica".

Low-dimensional solid-state systems have recently been attracting considerable attention. The fabrication of single and periodically repeating potential wells by combining materials having different band gaps and dimensions providing spatial confinement of electrons and holes permitted the development of new solid-state structures with unique optical and electronic properties. Of particular importance for the physics of low-dimensional structures and the development of new materials are semiconductor nanocrystals embedded in solid-state matrices (usually glasses or organic materials). A number of such systems have been developed in recent years by using a variety of materials and technologies (see, e.g., [1] and references therein).

Recent publications report on the formation of silver halide nanocrystals in alkali halide host crystals [2, 3], in particular, of AgCl in KCl, by growing alkali halide crystals with a large (about 1–3 mol %) concentration of the silver impurity. The band gap of AgCl, which is 3.237 eV [4], is much smaller than that of KCl (≈ 8.7 eV), and, therefore, AgCl nanocrystals may be considered as a quantum-dot system. Silver halides occupy an intermediate position between ionic and semiconductor crystals and exhibit unique properties favoring their wide use in photography [4].

The structure and processes of the formation and recombination of point defects in alkali halide crystals with a silver impurity were extensively studied by optical spectroscopy and magnetic resonance and are presently well known. The introduction of silver in very low concentrations is known to produce in them both single Ag$^+$ impurity ions and pairs of these ions. Irradiation of such crystals with UV or x-ray radiation initiates the formation in the crystals of a number of silver-associated defects, namely, neutral silver atoms in the cation

and anion lattice sites, Ag$^-$ ions in anion positions, Ag^{2+} ions, silver atoms with a closely located anion vacancy (laser-active A_F centers), and Ag$_2^+$ pair defects [5, 6]. Therefore, an investigation of the properties of silver clusters forming in KCl with an increasing impurity concentration is of particular interest.

Another important point is the availability of a wealth of information on bulk AgCl crystals. When irradiated by UV light, electrons are excited from the valence to the conduction band. The hole remaining in the valence band may become self-trapped to form Ag^{2+}, a self-trapped hole (STH). Free electrons can be trapped to produce shallow electron (SE) centers. The capture of an electron by a self-trapped hole gives rise to the formation of a self-trapped exciton (STE), in which the electron occupies a very delocalized $1s$ orbital. The structures of the STH, STE, and shallow electron centers were studied in considerable detail by optical methods and pulsed EPR and ENDOR [7–9]. The STE was shown to consist of a strongly delocalized electron (with a Bohr radius of 15.1 ± 0.6 Å) trapped by a strongly localized STH [8]. The spatial distribution of the wave function of the shallow electron center, which is believed to play an important part in the formation of latent images, was determined. The proposed model of the center assumes the electron to be weakly coupled to two neighboring silver ions occupying a cation site of the AgCl lattice (the so-called split-interstitial silver pair). The wave function of this center is very diffuse [9]. As a result of the Jahn–Teller effect, the STHs (Ag^{2+} centers) have a tetragonal symmetry with the axis aligned with one of the $\langle 100 \rangle$ crystallographic axes. The existence in the bulk AgCl of both strongly localized (STH) and strongly delocalized (STE, SE) centers with
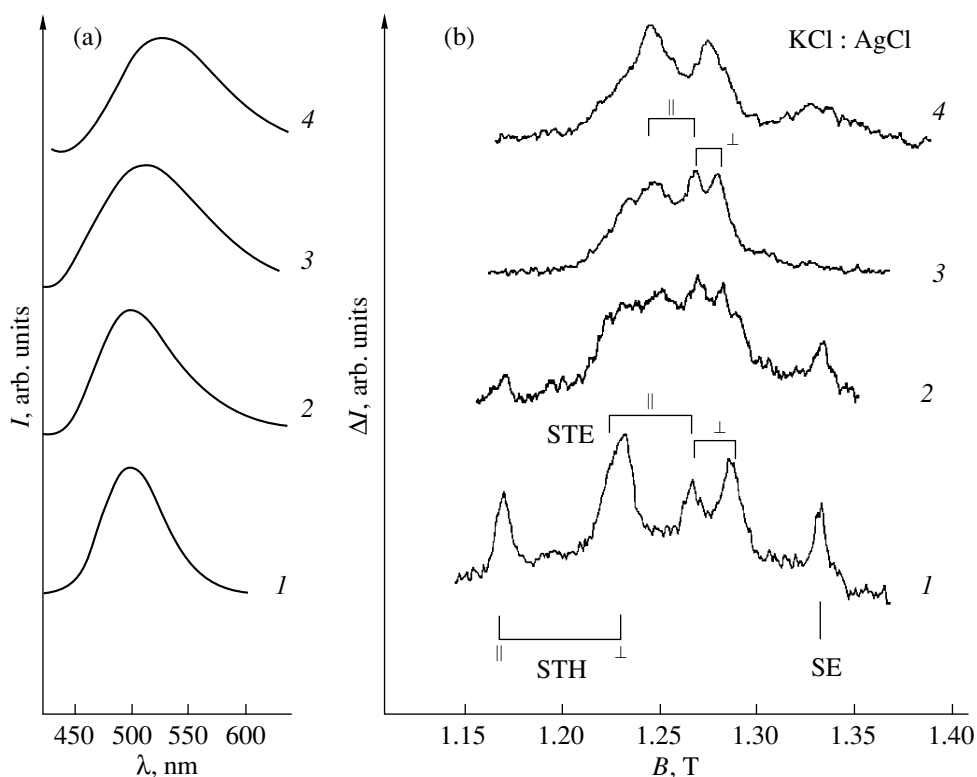
Fig. 1. Spectra of (a) luminescence and (b) ODMR of four samples (*1–4*) cleaved from different parts of a KCl : Ag crystal (2 mol % in the melt) grown with a silver concentration gradient. The ODMR spectra were recorded by monitoring the luminescence intensity under the following conditions: $T = 1.6$ K, $\nu = 35.2$ GHz, $P = 100$ mW, $f_{mod} = 80$ Hz, and $B \parallel$ [001]. Figure 1b (bottom) specifies the positions of the ODMR lines corresponding to self-trapped holes (STH), shallow electron centers (SE), and self-trapped excitons (STE) in bulk AgCl crystals. The signals assigned in [3] to STEs in AgCl nanocrystals are shown in ODMR spectrum *3*. The symbols $\parallel$ and $\perp$ refer to the centers whose axes are parallel and perpendicular to the magnetic field *B*, respectively.

known spatial distributions of the wave functions, as well as the Jahn–Teller effect, makes an investigation of the size quantization phenomena in AgCl-based nanostructures very promising.

This paper reports on an optically detected magnetic-resonance (ODMR) study of self-trapped holes, shallow electron centers, and self-trapped excitons in micro- and nanocrystals of AgCl in KCl : Ag with a silver concentration gradient.

The KCl : AgCl crystals were grown by the Stockbarger method. The silver concentration in the melt was 1–3 mol %. The ODMR at 35 GHz was detected at a temperature of 1.6 K from the luminescence excited by UV light of a deuterium or mercury arc lamp, which was provided by the corresponding filters. The luminescence was analyzed with a monochromator or a set of color filters. The microwave power entering the cavity of the ODMR spectrometer was modulated at a frequency of 80–10000 Hz, and the changes in the luminescence intensity caused by the microwave field were measured with a lock-in amplifier. Samples measuring $2 \times 2 \times 4$ mm were cleaved from different parts of the grown crystal. In contrast to the silver halides, the NaCl-type alkali halide crystals cleave easily along the

{100} planes, which facilitates the sample orientation. For comparison, ODMR spectra were also obtained on bulk AgCl crystals. EPR spectra were studied at temperatures from 4 to 300 K in the *X* range (9.3 GHz) on a JEOL spectrometer.

Figure 1a shows spectra of the luminescence and Fig. 1b ODMR spectra derived from this luminescence for four samples (*1–4*) cleaved from different parts of a KCl : AgCl crystal (2 mol % AgCl in the melt). The luminescence was excited by the light of a deuterium lamp passed through a UFS-1 color filter (250–400 nm). The ODMR spectra were derived from the variation of the luminescence intensity in the 440- to 600-nm interval, with the [001] crystal axis aligned with the magnetic field *B* and the microwave power (100 mW) modulated at 80 Hz. One readily sees that different samples exhibit substantial changes in the spectra of both the luminescence (a broadening and a red shift of the luminescence band) and the ODMR.

Figure 2 presents for comparison ODMR spectra recorded on a bulk AgCl crystal under the same conditions (spectrum *1*) and at a lower microwave power (spectrum *2*). The higher microwave power was used to increase the sensitivity when detecting ODMR in

KCl : AgCl. The ODMR signals belonging to the STHs, SE centers, and STEs are marked by the lines. Because the tetragonal axis of the STH and STE is directed along one of the $\langle 100 \rangle$ crystallographic axes, there are three types of centers. The symbols $\parallel$ and $\perp$ denote the ODMR lines of the centers with the Jahn–Teller distortion axes parallel and perpendicular to the magnetic field B, respectively. The parameters of these ODMR spectra coincide with those well known from numerous publications (see, e.g., [7] and references therein).

The ODMR spectrum of sample *1* in Fig. 1b agrees completely with that observed in bulk AgCl crystals (curve *1* in Fig. 2). It has the same angular dependence and the same parameters, namely, $g_\parallel = 2.14$, $g_\perp = 2.04$ for the STH; $g = 1.88$ for the SE center, and $D = -730$ MHz for the STE. Curve *1* in Fig. 1b shows the ODMR lines associated with the STEs, STHs, and SE centers. This sample, similar to bulk AgCl, also exhibited the so-called nonresonant background due to microwave-heated free carriers, which corresponds to the increase of the luminescence intensity and depends only weakly on the magnetic field. Thus, one can maintain with confidence that fairly large AgCl microcrystals, retaining the properties of the bulk material and oriented in the same direction as the host, form in the KCl crystals.

The ODMR spectrum of sample *3* has lines corresponding to the ODMR signals assigned in [3] to triplet STEs in AgCl nanocrystals. These lines are identified in Fig. 1b for two orientations of the centers' tetragonal axis. The angular dependences of the ODMR signal obtained by rotating the sample in the (100) and (1̄10) planes indicate the existence of an axial symmetry with a $\langle 100 \rangle$-type axis and can be described by a triplet spin Hamiltonian with parameters ($g_\parallel = 1.99$, $g_\perp = 1.96$, $|D| = 335$ MHz) differing substantially from those of the STEs in bulk AgCl. We have succeeded in observing $\Delta m = \pm 2$ forbidden transitions in this sample under the [111] $\parallel B$ orientation, which supports the triplet nature of the spectra. The nonresonant background was practically absent in this crystal. The ODMR spectrum of sample *2* cleaved from an intermediate region of the starting crystal is a superposition of spectra *1* and *3* (curve *2* in Fig. 1b). When studying the luminescence spectra, sample *3* revealed, besides the above-mentioned ODMR lines, additional anisotropic ODMR signals in the 540- to 600-nm wavelength interval, which were similar to the ODMR spectrum of sample *4* (curve *4* in Fig. 1b). This ODMR spectrum exhibits an axial symmetry with a $\langle 100 \rangle$ axis, and its maximum is at 540 nm.

Figure 3 displays the ODMR spectra obtained with spectral resolution on sample *2*. The inset shows the luminescence spectrum specifying the wavelengths at which the ODMR signal was observed. As the measured luminescence wavelength increases from 490 to 540 nm, the STE, STH, and SE signals typical of bulk
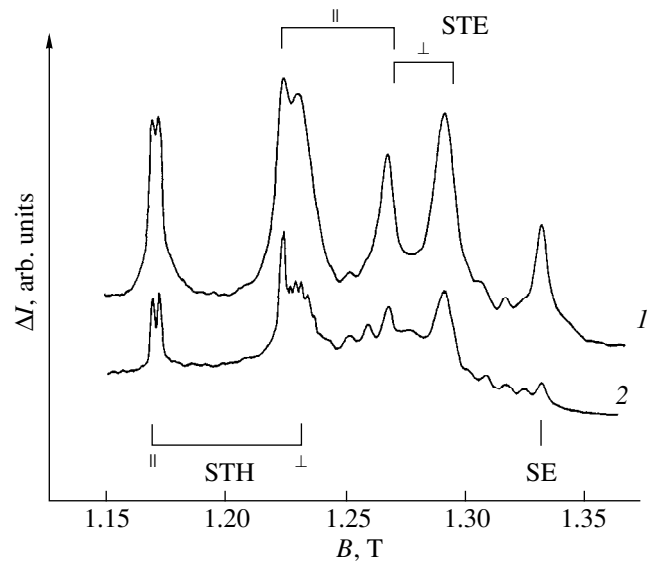

Fig. 2. (*1*) ODMR spectrum of a bulk AgCl crystal obtained from the luminescence intensity under the same conditions as the KCl : AgCl ODMR spectra displayed in Fig. 1, and (*2*) ODMR spectrum obtained at a lower microwave power (−10 dB). The ODMR signals corresponding to the STH, SE, and STE are identified. The symbols $\parallel$ and $\perp$ refer to the centers whose axes are parallel and perpendicular to the magnetic field B, respectively. $T = 1.6$ K, $\nu = 35.2$ GHz, $f_{mod} = 80$ Hz, and $B \parallel [001]$.

AgCl disappear, which indicates a complex structure of the emission band. The luminescence and ODMR spectra of KCl : AgCl change when the samples are kept in the dark at room temperature or subjected to heat treatment. For instance, the ODMR spectrum of sample *3* recorded two months after spectrum *3* (Fig. 1b) is similar to spectrum *4* in Fig. 1b. After quenching this sample from 550°C to room temperature, its ODMR spectrum contained only a broad structureless band.

Because the STE is formed by a strongly delocalized electron captured by a strongly localized STH, the exchange splitting between the lowest triplet and the upper singlet STE states is small. The singlet–triplet splitting can be a measure of the spatial extent of the electron wave function and, hence, can provide information on size-quantization effects in nanocrystals. We have succeeded in observing multiple-quantum transitions involving absorption of up to seven microwave quanta (the effective frequency of $7 \times 35 = 245$ GHz) in ODMR spectra of bulk AgCl crystals, which permitted highly accurate determination of the STE singlet–triplet splitting, $J = -161.0 \pm 0.1$ GHz [10]. Multiquantum transitions in ODMR spectra of KCl : AgCl (sample *1*) were detected only for the triplet state of the STE, with no singlet–triplet transitions observed. This is possibly associated with an increase in the exchange splitting in microcrystals.

The conclusion that the AgCl phase is formed in KCl crystals with a high (2–3 mol %) impurity-silver
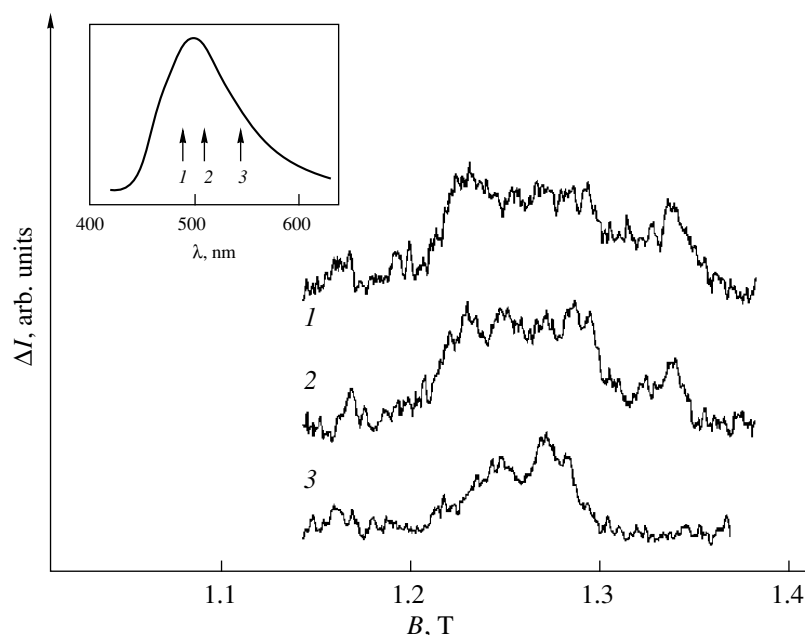
Fig. 3. Luminescence spectrum (inset) and ODMR spectra of KCl : AgCl (sample *2*) measured with the spectral resolution at three wavelengths specified by arrows (*1*, *2*, *3*) in the inset. The conditions of recording are the same as those for the spectra in Fig. 1.

concentration was drawn [2, 3] from a study of optical-absorption and luminescence spectra, as well as from atomic-force microscopy data, which do not provide such direct information on the nature of this phase as EPR is capable of yielding. In the KCl : AgCl samples (2 mol %) studied in [3], the average size of the inclusions visible in photomicrographs and identified with AgCl nanocrystals was about 5–10 nm. The ODMR spectra obtained in that work and attributed to nanocrystals differ substantially from those of bulk AgCl crystals. While this observation is of considerable interest, it cannot serve as a direct proof of the ODMR spectra being produced by AgCl crystals. It cannot be ruled out that the ODMR spectra of KCl : AgCl may contain signals due to point defects associated with the silver. We have succeeded in observing, for the first time in KCl : AgCl crystals, the ODMR spectra of STHs, SE centers, and STEs, which may be considered as signatures of AgCl crystals; thus, the formation of the AgCl crystals embedded in the KCl lattice may be indeed considered as unambiguously proven, which provides supportive evidence for the brilliant idea of the authors of [2, 3]. The differences between the ODMR spectra observed in samples cleaved from different parts of a grown KCl : AgCl crystal are probably due to the variation in the sizes of the embedded AgCl crystals, which range from fairly large microcrystals to nanocrystals. Additional investigation, which is being conducted presently, is necessary to learn the relations governing these changes and their dependence on the AgCl crystal size and external factors. Note the absence of a smooth transition from ODMR spectrum *1* to spectra *3* and *4*

(Fig. 1), which may imply the existence of some threshold effect.

Thus, the investigation of the ODMR of KCl : AgCl crystals grown with a silver concentration gradient has revealed the presence of silver impurity clusters varying in size from point defects (in the form of single silver ions and pairs of them) to microcrystals; these silver impurity clusters retain the main properties of bulk AgCl and have the orientation of the host crystal. In the intermediate concentration region, AgCl nanocrystals are apparently observed, which may be considered as self-organized quantum dots. The KCl : AgCl system provides a unique possibility for studying oriented micro- and nanocrystals in a transparent crystalline matrix. It is important that the properties of bulk AgCl and KCl : Ag materials are well known, thus making possible the application of such an efficient method as the ODMR. Bulk AgCl contains both fairly diffuse objects (STEs and SE centers) and strongly localized Jahn–Teller centers (STHs). This makes an investigation of the size-quantization effects in AgCl micro- and nanocrystals particularly promising.

REFERENCES

1. U. Woggon, Springer Tracts Mod. Phys. **136** (1997).

2. H. Stolz, H. Vogelsang, and W. von der Osten, *Handbook of Optical Properties: Optics of Small Particles, Interfaces, and Surfaces* (CRC Press, Boca Raton, 1997), Vol. II, p. 31.

3. H. Vogelsang, O. Husberg, U. Köhler, *et al.*, Phys. Rev. B **61**, 1847 (2000).

4. H. Kanzaki, Photogr. Sci. Eng. **24**, 219 (1980).

5. N. I. Melnikov, P. G. Baranov, and R. A. Zhitnikov, Phys. Status Solidi B **46**, K73 (1971); **59**, K111 (1973).

6. A. G. Badalyan, P. G. Baranov, and R. A. Zhitnikov, Fiz. Tverd. Tela (Leningrad) **19**, 1847 (1977); **19**, 3575 (1977).

7. O. G. Poluektov, M. C. J. M. Donckers, P. G. Baranov, and J. Schmidt, Phys. Rev. B **47** (16), 10 226 (1993).

8. M. T. Bennebroek, A. Arnold, O. G. Poluektov, *et al.*, Phys. Rev. B **53**, 15 607 (1996).

9. M. T. Bennebroek, A. Arnold, O. G. Poluektov, *et al.*, Phys. Rev. B **54** (16), 11 276 (1996).

10. N. G. Romanov and P. G. Baranov, Semicond. Sci. Technol. **9**, 1080 (1994).

Translated by G. Skrebtsov

DEFECTS, DISLOCATIONS, AND PHYSICS OF STRENGTH

Analysis of the Plasticizing Effect of Hydrogen Dissolved in a Crystal on the Evolution of Plastic Deformation at the Tip of a Crack

D. N. Karpinskiĭ and S. V. Sannikov

Research Institute of Mechanics and Applied Mathematics, Rostov State University, Rostov-on-Don, 344090 Russia
e-mail: karp@math.rsu.ru
Received April 13, 2000

Abstract—The effect of interstitial hydrogen atoms on the evolution of plastic deformation in a crystal at the tip of a tensile crack is estimated taking into account gas exchange at the crack banks. It is found that, for an initial concentration of not less than 10^{-4}, the plasticizing effect of dissolved hydrogen causing a dislocation expulsion is significant and can be responsible (at least, partially) for plasticization. As regards the evolution of the distribution of hydrogen atoms, a monotonic drain of dissolved hydrogen atoms into the hollow of the crack is observed for concentrations below 5×10^{-4}, while at higher concentrations the impurity concentration at the banks of the crack varies periodically: complete drain is replaced by the accumulation of hydrogen corresponding to a "blocking" of the drain by the gas pressure. Numerical calculations are made for an α-Fe crystal. © 2000 MAIK "Nauka/Interperiodica".

Plasticization of materials in the hydrogen medium has been established experimentally in recent years (see, for example, [1–6]). In this connection, it would be interesting to explain this effect from the viewpoint of energy advantage in the interaction of interstitial hydrogen atoms with a dislocation [7]. It is known [1–6] that plasticization processes have the highest intensity in the vicinity of the crack tip. It was pointed out in [7], however, that the main reason behind this effect is not completely clear at present: either the main contribution comes from the mechanism of dislocation expulsion by interstitial hydrogen atoms or the effect of molecular pressure in the hollow of the crack is dominant. The inclusion of this mechanism in an analysis of the evolution of plastic deformation at the crack tip in [8] proved that an insignificant increase in the initial hydrogen concentration in a crystal with a crack leads to a change in the deformation regime from the "passive" mode (migration of point defects weakly affects the deformation conditions) to the "active" mode, for which the gas pressure in the hollow of the crack causes unlimited loading in the model calculations, which corresponds to the growth of the crack in the experiments.

This communication is aimed at analyzing the evolution of plastic deformation at the tip of a crack in a non-hydride-forming crystal under the action of a mechanical tensile stress taking into account the plasticizing effect of hydrogen atoms dissolved in the crystal and gas exchange at the banks of the crack.

The migration of point defects in a loaded sample with cracks and pores has attracted the attention of researchers for a long time (see, for example, the literature cited in [9, 10]). The evolution of the concentra-

tion $c(r, t)$ of interstitial impurity atoms and the relative contributions from dislocation mechanisms to the transport of interstitial impurity atoms were investigated by us earlier in [8], where a crack of length $2l$ located in the cleavage plane (010) (along the negative semiaxis Ox) was studied in an infinitely long crystal with a body-centered cubic (bcc) lattice. A uniform tensile stress $\sigma_{yy}(t) = \sigma'_a(t)$ (mode I), which increased monotonically to a certain value σ_a sufficient for plastic deformation of the crystal but insufficient for the growth of the crack, was applied to the planes $y = \pm\infty$ of the crystal. Prior to loading, interstitial hydrogen atoms were uniformly distributed in the crystal with a concentration c_0.

Analogous to [8–11], we assume that plastic deformation of the bcc crystal is executed through the displacement of perfect dislocations with the Burgers vector $b = \frac{1}{2}\langle 111 \rangle$ along easy slip planes {100}. The {110} planes intersecting the Oxy plane form two families of slip lines on it with uniformly distributed sources of dislocations, emitting rectangular loops which lie in the easy-slip planes. An analysis of the evolution of plastic deformation in the absence of point defects was carried out in [11], in which the plastic shear rate $\dot{\varepsilon}$ at the crack tip was calculated by the formula

$$
\frac{d\varepsilon^j(r, t)}{dt} = \dot{\varepsilon}_0 \exp\left\{ -\frac{U_0\{1 - [\sigma_e^j(r, t)/\tau_0]^{1/2}\}}{k_B T(r, t)} \right\} \quad (1)
$$

$$
\times \operatorname{sgn} \sigma_e^j(r, t),
$$

where T is the temperature; k_B is Boltzmann's constant; $\dot{\varepsilon}_0$, τ_0, and U_0 are constants (U_0 is the activation energy for dislocation slip); and

$$\sigma_e^j(r, t) = \begin{cases} \sigma^j(r, t) - \sigma_s(r, t)\,\mathrm{sgn}\,\sigma^j(r, t) \\ \quad \text{for } |\sigma^j(r, t)| > |\sigma_s(r, t)| \\ 0 \quad \text{for } |\sigma^j(r, t)| < \sigma_s(r, t) \end{cases} \quad (2)$$

is the effective shear stress in the easy-slip planes. In this expression,

$$\sigma^j(r, t) = \sigma_j^c(r, t) + \sigma^l(r, t) \quad (3)$$

is the shear stress characterizing the elastic field in the easy-slip planes near the crack tip and

$$\sigma_s(r, t) = \sigma_0 + \sigma_f(r, t) \quad (4)$$

is the stress hindering the plastic shear due to lattice friction σ_0 and local strain hardening σ_f of the material, which can be calculated by the formula

$$\sigma_f(r, t) = \sigma_1 \left[\sum_{j=1}^{2} |\varepsilon^j(r, t)| \right]^m, \quad (5)$$

where σ_1 and m are constants. In Eq. (3), σ_j^c is defined by the Westergaard formulas for the elastic field component at the crack tip; the quantity

$$\sigma^l(r, t) = \sum_{k=1}^{2} \int_{D_k} \sigma^k(r, r')\Delta\rho_k(r', t)dr' \quad (6)$$

is the stress field created at the crack tip by dislocations slipping over two easy-slip planes; D_k is the plastic region corresponding to each type of slip ($k = 1, 2$); $\sigma^k(r, r')$ is the shear stress in the easy-slip planes in an unbounded elastic medium with a semi-infinite cut, which contains an edge dislocation separated from the tip of the cut by the distance r'; and the density $\Delta\rho_k$ of effective dislocations at the point r' is defined by the formula

$$\Delta\rho_k(r', t) = -\frac{1}{b}\frac{\partial}{\partial\xi_k}\varepsilon^k(r', t). \quad (7)$$

Let us now supplement Eqs. (1)–(7) by modifying Eq. (4) to take into account the plasticizing effect of the dissolved hydrogen on the evolution of dislocation distribution at the crack tip. We replace σ_0 in Eq. (4) by $\sigma_0' = \sigma_0 + \sigma^\tau$, where [7]

$$\sigma^\tau = \frac{2\pi\beta^2 c_0}{3\sqrt{3}r_0 b k_B T}, \quad \beta = \frac{\mu b(1+\nu)}{3\pi(1-\nu)}\delta v. \quad (8)$$

In these expressions, r_0 is the radius of the dislocation core, μ is the shear modulus, ν is the Poisson ratio, and δv is the change in the crystal volume due to mismatch-

ing between the size of the tetrahedral pores and the radius of the hydrogen atom.

In our earlier publications [9, 10], we analyzed three mechanisms of transport of interstitial hydrogen atoms at the crack tip: (1) lattice diffusion, (2) dislocation-induced "sweeping out" of point defects, and (3) the transport of impurity atoms in the cores of dislocations moving in the plastic zone. The results of calculations [9, 10] proved that the first mechanism of transport of interstitial atoms (lattice diffusion) makes the main contribution to the flow of impurity atoms. Henceforth, we will take into account only the first transport mechanism, which is associated with hydrostatic stress in the vicinity of the crack tip, which is created by the crack together with dislocations in the plastic zone. The effect of this transport process on the evolution of plastic deformation at the crack tip will be taken into account by substituting $c(r, t)$ for c_0 in Eq. (8).

Let us now consider the basic equations of mechanical diffusion (see, for example, [12]):

$$\frac{\partial c}{\partial t} = -\nabla J, \quad J = \frac{Dc}{k_B T}\nabla\mu, \quad (9)$$

where D is the diffusion coefficient; for a dilute solution of impurities in the elastic field of stresses, the chemical potential $\mu = k_B T \ln(c/c_0) - V(r, t)$. Here, $V(r, t) = \Delta v \sigma_{ii}$, where Δv is the change in the volume of a unit cell in the crystal lattice due to an interstitial atom contained in it and σ_{ii} is the spherical component of the stress tensor. Considering that $\nabla^2 V = 0$, we obtain from Eq. (9)

$$\frac{\partial c}{\partial t} = D\nabla^2 c(r, t) + \frac{D}{k_B T}\nabla c(r, t)\nabla V(r, t). \quad (10)$$

The initial conditions are chosen in the form $c = c_0$ for $t = 0$, and the boundary conditions for $y = 0$ [13] are

$$-\frac{\partial c}{\partial y} = 0 \text{ for } x > 0;$$

$$D\frac{\partial c}{\partial y} = k_m(c^2 - (\Gamma')^{-1}P(t)) \text{ for } x < 0, \quad (11)$$

where k_m is the mass-exchange constant at the interface between the gaseous and solid phases, $P(t)$ is the gas pressure in the hollow of the crack, Γ' is the modified Henry constant [14]

$$\Gamma'(T) = T(\Delta v)^2 \left(\frac{mT}{2\pi\hbar^2}\right)^{3/2}\exp(\psi_H/T), \quad (12)$$

m is the mass of the molecule, $\hbar$ is Planck's constant, ψ_H is the energy of dissolution spent for dividing a molecule into two atoms and the subsequent implantation of these atoms into the solid solution, and $c = c_0$ for $|r|^2 = x^2 + y^2 \longrightarrow \infty$.

Let us now consider the choice of the boundary conditions for $y = 0$, $x < 0$ in greater detail. We assume that

the gas is ideal; in this case, its pressure $P(t)$ in the crack is given by [6]

$$P(t) = (\sigma_a'(t)/2)\left[\left(\frac{1 + 4\mu k_B TN(t)}{\pi(1-\nu)l^2\sigma_a'^2(t)}\right)^{1/2} - 1\right]. \quad (13)$$

In contrast to [8], we will assume that the gas dissolved in the bulk of the crystal mainly flows into the hollow of the crack through its banks. In this case, the number of hydrogen molecules in the hollow of the crack is $N(t) = \int_0^t J(t')dt'$, where $J(t) = k_m \int_{-\infty}^0 [c^2(x, 0, t) - (\Gamma')^{-1}P(t)]dx$ is the flux of gas atoms through the banks of the crack.

The method for solving Eqs. (1)–(13) involved successive solution of the system of equations (1)–(8) and (10)–(13) at each time step. The method of solution of Eqs. (1)–(8) is similar to that in [11], while the method of solution of Eqs. (10)–(13) is described in [8].

Analysis of the evolution of plastic deformation enabled us to estimate the evolution of the stress intensity factor (SIF) in a loaded crystal. We assumed that the SIF for a crack can be presented in the form [11]

$$K(t) = K^c(t) + K^p(t), \quad (14)$$

Fig. 1. Distributions of the plastic strain $\varepsilon(r)$ (in %) at the crack tip [without taking into account the plasticizing effect of hydrogen (a, c) and taking this effect into consideration (b, d)] after completion of stress relaxation at instants of time (a) $t = 5.15$, (b) 9.18, (c) 5, and (d) 3.94 s for the initial concentration of interstitial hydrogen impurity atoms $c_0 = 10^{-4}$ (a, b) and $c_0 = 5 \times 10^{-4}$ (c, d).

where $K^c(t) = (\sigma_a'(t) + P(t))\sqrt{\pi l}$ is the SIF term for the crack, which does not take into account the effect of plastic deformation on it, whereas $K^p(t)$ is determined exclusively by this effect [11]:

$$K^p(t) = \sum_{k=1}^2 \int_{D_k} \hat{K}^p(z_k')\Delta\rho_k(z', t)dz', \quad (15)$$

where z' is the coordinate in the complex plane.

In the case under investigation, we are using the following formula for $\hat{K}^p = \hat{K}_I^p - i\hat{K}_{II}^p$ [11]:

$$\hat{K}_I^p(z', k) - i\hat{K}_{II}^p(z', k) = A/\sqrt{\pi}[J_1 + iJ_2(-1)^k], \quad (16)$$

where

$$J_1 = -\pi[1/\sqrt{z'} + 3/2\sqrt{z'} - z'/2(z')^{3/2}],$$

$$J_2 = -\pi[1/\sqrt{z'} + 1/2\sqrt{z'} + z'/2(z')^{3/2}].$$

The calculations for a crystal of α-Fe were made for the following values of constants: $2l = 10^{-3}$ m, $\dot{\varepsilon}_0 = 10^{11}$ s^{-1}, $T_0 = 300$ K, $b = 2.48 \times 10^{-4}$ μm, $D = 4.88 \times 10^{-12}$ m^2 s^{-1}, $\psi_H = 48.8$ kJ/mol, $E_B = 0.6$ eV, $k_m = 4.88 \times 10^{-9}$ m s^{-1} [8], $r_0 = 2b$, $\mu = 83$ GPa, $\nu = 0.28$, and $\delta v = 3 \times 10^{-30}$ m^3 [7].

The rate of crystal loading was chosen such that the maximum strain rate in the plastic zone was 0.1 s^{-1}. The stresses created by a crack in the crystal are due to the joint action of the external stress $\sigma_a'(t)$ and the gas pressure $P(t)$ in the hollow of the crack. After the stress $\sigma_a'(t) + P(t)$ attained its upper limit $\sigma_a = 5$ MPa, the value of $\sigma_a'(t)$ remained unchanged and the load on the crystal with a crack increased only as a result of an increase in the gas pressure $P(t)$ caused by the gas flow to the hollow of the crack. The computational process was terminated when the effective stress $\sigma_e^j(r, t)$ in Eq. (2) dropped to zero. The calculations made on the basis of this model proved that, for the initial concentration $c_0 < 10^{-3}$, the pressure $P(t)$ of gaseous hydrogen in the hollow of the crack does not exceed 0.05 MPa by the instant when $\sigma_e^j(r, t)$ relaxes completely. For $c_0 \geq 10^{-3}$, the pressure $P(t)$ is so high that the stress relaxation due to the multiplication and displacement of dislocations in the plastic zone has no time to suppress the increase in $\sigma_e^j(r, t)$ via its components $\sigma_j^c(r, t)$ in Eq. (3) before the plastic zone becomes larger than the computational mesh. In contrast to [9, 10], this model takes into account the "feedback" which ensures the action of plastic deformation on the crack through the filling of its hollow by the gas under the conditions controlled by the same evolution of plastic deformation. A
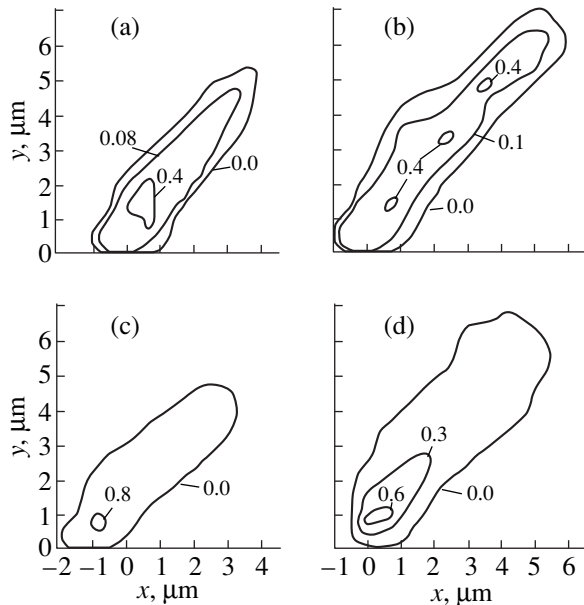
similar feedback was used in [8], but here it is refined by the correction given by Eq. (8).

Let us now consider the features of the plasticizing effect of dissolved hydrogen on the evolution of plastic deformation at the crack tip for $c_0 < 10^{-3}$. It is important to note that the effect of dissolved hydrogen on the evolution of plastic deformation at the crack tip is determined by the combined operation of two mechanisms: (1) an increase in the mobility of dislocations due to the plasticizing effect of dissolved hydrogen, which enhances the evolution of plastic deformation and leads to additional relaxation of stresses at the tip, and (2) a decrease in hydrogen drain to the hollow of the crack due to lattice diffusion, which is caused by a decrease in the hydrostatic component of effective stresses under the influence of the additional relaxation mentioned in item (1).

Figure 1 shows the distribution of plastic deformation at the crack tip for two values of initial concentration c_0 of interstitial hydrogen atoms at the instants of time corresponding to the termination of evolution of plastic deformation. It can be seen from the figures that the size of the plastic zone increases when the correction in Eq. (8) is taken into account (Figs. 1b, 1d) compared to the case when it is disregarded (Figs. 1a, 1c). It is important to note that in both cases the drain of hydrogen to the hollow of the crack is taken into consideration. In other words, the calculations proved that the plasticizing effect of dissolved hydrogen due to expulsion of a dislocation [7] is significant and can be responsible (at least partially) for plasticization [1–6]. It should also be mentioned that the maximum strain in the plastic zone is the same whether or not the hydrogen-induced plasticization is taken into account.

Let us now compare the evolutions of the SIF in a crystal with dissolved gas. Figure 2 shows the time dependences of the SIF in calculations (i) for a brittle crack in a crystal, $K^c(t)$, whose hollow is filled with a gas which is in equilibrium with the dissolved hydrogen; (ii) for a gas-filled crack taking into account the plastic zone, $K^*(t)$, and without taking into account the plasticizing effect of dissolved hydrogen; and (iii) the same as in (ii), but taking into account the plasticization correction given by Eq. (8), $K(t)$. The termination of the curves in Fig. 2 indicates that the stress relaxation at the crack tip is completed. It can be seen from the figure that the time dependence of the SIF for the brittle crack, $K^c(t)$, changes only insignificantly after the external stress attains the value σ_a at the instant $t = 0.78$ s in spite of the continuous drain of hydrogen to the hollow of the crack. The same figure shows that, due to the action of the plasticization correction given by Eq. (8), the value of $K(t)$ is smaller than $K^*(t)$ by almost 10%.

In conclusion, let us briefly mention the results of the analysis of the evolution of concentration of dissolved hydrogen at the tip of the crack. The calculations made for $c_0 < 5 \times 10^{-4}$ demonstrated a monotonic drain of hydrogen to the hollow of the crack, while calcula-
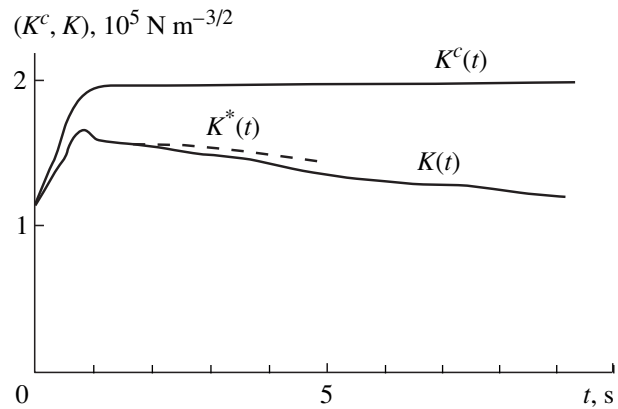

Fig. 2. Time dependence of the stress intensity factors (in $(N\ m^{-3/2})$ (for a tensile crack in a bcc crystal: $K^c(t)$ for a brittle crack in the crystal with the crack hollow filled with a gas in equilibrium with the dissolved hydrogen; $K^*(t)$ for a gas-filled crack taking into account the plastic zone and disregarding the plasticizing effect of dissolved hydrogen (dashed curve); and $K(t)$, which is the same as $K^*(t)$, but takes into account the plasticization correction given by Eq. (8).

tions made for higher concentrations revealed a regime of periodic change in the impurity concentration at the banks of the crack: complete drain is replaced by the accumulation of hydrogen, which corresponds to the blocking of the drain by the gas pressure. It should be noted in connection with this result that Gol'dshteĭn *et al.* [15] assumed in their calculations that the hydrogen concentration at the banks of the crack was constant and equal to zero, but this choice for the boundary condition is not confirmed in the present work.

REFERENCES

1. T. Tabata and H. K. Birnbaum, Scr. Metall. **18**, 231 (1984).

2. I. M. Robertson and H. K. Birnbaum, Acta Metall. **34** (2), 353 (1986).

3. G. M. Bond, I. M. Robertson, and H. K. Birnbaum, Acta Metall. **35** (10), 2289 (1987).

4. D. S. Shin, I. M. Robertson, and H. K. Birnbaum, Acta Metall. **36** (1), 111 (1988).

5. G. M. Bond, I. M. Robertson, and H. K. Birnbaum, Acta Metall. **36** (8), 2193 (1988).

6. L. V. Spivak, M. Ya. Kats, and N. E. Skryabina, Fiz. Met. Metalloved. **6**, 142 (1991).

7. N. M. Vlasov and V. A. Zaznoba, Fiz. Tverd. Tela (St. Petersburg) **41** (3), 451 (1999) [Phys. Solid State **41**, 404 (1999)].

8. D. N. Karpinskiĭ and S. V. Sannikov, Fiz. Met. Metalloved. **85** (2), 121 (1998).

9. D. N. Karpinskiĭ and S. V. Sannikov, Fiz. Tverd. Tela (St. Petersburg) **37** (6), 1713 (1995) [Phys. Solid State **37**, 932 (1995)].

10. D. N. Karpinskiĭ and S. V. Sannikov, Fiz. Tverd. Tela (St. Petersburg) **39** (9), 1580 (1997) [Phys. Solid State **39**, 1407 (1997)].

11. D. N. Karpinskiĭ and S. V. Sannikov, Prikl. Mekh. Tekh. Fiz. **34** (3), 154 (1993).

12. S. D. Gertsriken and I. Ya. Dekhtyar, *Diffusion in Metals and Alloys in Solid Phase* (Fizmatgiz, Moscow, 1960).

13. L. L. Kunin, A. M. Golovin, Yu. N. Surovoĭ, and V. M. Khokhrin, *Problems of Degassing of Metals (Phenomenological Theory)* (Nauka, Moscow, 1972).

14. É. P. Fel'dman, V. M. Yurchenko, V. A. Strel'tsov, and E. V. Volodarskaya, Fiz. Tverd. Tela (St. Petersburg) **34** (2), 616 (1992) [Sov. Phys. Solid State **34**, 330 (1992)].

15. R. V. Gol'dshteĭn, V. M. Entov, and B. R. Pavlovskiĭ, Dokl. Akad. Nauk SSSR **237** (4), 828 (1977) [Sov. Phys. Dokl. **22**, 762 (1977)].

Translated by N. Wadhwa

MAGNETISM
AND FERROELECTRICITY

Crystal Structure and Magnetic State of the $LaMn_{1-x}V_xO_3$ Perovskites

A. E. Teplykh*, A. N. Pirogov*, A. Z. Men'shikov[†]*, and G. V. Bazuev**

* Institute of Metal Physics, Ural Division, Russian Academy of Sciences,
ul. S. Kovalevskoǐ 18, Yekaterinburg, 620219 Russia
** Institute of Solid-State Chemistry, Ural Division, Russian Academy of Sciences,
Pervomaǐskaya ul. 91, Yekaterinburg, 620219 Russia

Received March 29, 2000

Abstract—The crystal structure and the magnetic state of polycrystalline $LaMn_{1-x}V_xO_3$ ($0.1 < x < 0.9$) compounds have been studied by x-ray and neutron diffraction methods, as well as by magnetization and ac susceptibility measurements. It is shown that substitution of vanadium for manganese ions leaves the orthorhombic crystal structure of the compounds (space group *Pnma*) unchanged. The magnetic structure is observed to change from a canted antiferromagnetic ordering (wavevector $\mathbf{k} = [0, 0, 0]$, with the antiferromagnetic moments aligned with the *a* axis and the ferromagnetic component of the magnetic moment parallel to the *b* axis) at vanadium concentrations $x < 0.4$ to a collinear antiferromagnetic ordering (with the magnetic moments parallel to the *b* axis) at $x > 0.8$; at this transition occurs through an intermediate state exhibiting spin-glass properties. © 2000 MAIK "Nauka/Interperiodica".

1. INTRODUCTION

The discovery of the effect of giant magnetoresistance in $La_{2/3}Ca_{1/3}MnO_3$ [1] stimulated renewed interest in studies of the physical properties of manganites with a perovskite structure. Manganites of the type $(R, A)MnO_{3+\delta}$ (R = La, Pr, and Nd; A = Ca, Sr, and Ba) have become a subject of intensive investigation [2–4]. In these compounds, the oxygen nonstoichiometry and the partial substitution of an alkaline- for a rare-earth metal bring about a decrease in the amount of Mn^{3+} ions and an increase in the amount of Mn^{4+} ions. The main regularities governing the changes in the crystal structure and the magnetic state of these manganites upon variations in the Mn^{4+} concentration have already been established.

For instance, the $La_{1-y}Mn_yO_{3+\delta}$ nonstoichiometric manganite is characterized by the presence of vacancies in the cation sublattice [2]. Their concentration and the content of the Mn^{3+} and Mn^{4+} ions are determined by the synthesis conditions and can be estimated from the magnitude of δ by using the relation $1 - y = 3/(3 + \delta)$. The structure obtained at a Mn^{4+} content of less than 10% is orthorhombic with a collinear antiferromagnetic order. In this case, the nearest magnetic moments are ferromagnetically ordered in the $(0\bar{1}0)$ planes and the planes are aligned antiferromagnetically. Within the concentration range 10–14%, canted antiferromagnetism prevails. Manganites with Mn^{4+} concentrations above 14% can have an orthorhombic, rhombohedral,

or cubic lattice with ferromagnetically aligned spins of manganese ions.

However, a complete understanding of the mechanisms responsible for the structural and magnetic phase transitions in manganites also requires knowledge of their behavior under variations in the Mn^{3+} concentration but with a fixed Mn^{4+} content. This can be achieved by a partial replacement of Mn ions in $RMnO_{3+\delta}$ by ions of another trivalent metal. There are only a few publications which report on the investigation of these systems [5, 6].

This paper reports the first investigation of the structural and magnetic states of compounds in the $LaMn_{1-x}V_xO_{3+\delta}$ system by x-ray and neutron diffraction methods, as well as by magnetic measurements. Only extreme compositions have thus far been studied in this system. Unlike lanthanum manganite, the effects associated with oxygen nonstoichiometry of lanthanum orthovanadite are too small to affect the unit cell parameters and volume. According to [7], the orthorhombic perovskite structure is retained at a V^{4+} concentration of no more than 10%. At low temperatures, lanthanum orthovanadite is an antiferromagnet [8–10] in which the nearest-neighbor magnetic moments of the V^{3+} ions are antiferromagnetically aligned in the (010) planes and ferromagnetically ordered in the (100) planes.

Thus, the moments in the extreme compositions of $LaMn_{1-x}V_xO_{3+\delta}$ (at small δ) are antiferromagnetically ordered in opposite directions. This means that an increase in concentration x should bring about a rotation of the antiferromagnetic axis from one direction to

[†] Deceased.

the other. Moreover, substitution should change the relation between the ferromagnetic and antiferromagnetic exchange couplings, which can give rise to the features presented in the magnetic phase diagram.

2. SAMPLES AND EXPERIMENTAL TECHNIQUE

The starting substances for the synthesis were the oxides La_2O_3 (99.9%), MnO_2 (analytical grade), and V_2O_5 (high-purity grade). The lanthanum oxide was preliminarily calcined in air at 1173 K. The manganese oxide was reduced to MnO_2 by calcination in air at 873 K for 8 h, and V_2O_5 was reduced to V_2O_3 by calcining in a hydrogen flow at 1173 K. The $LaMn_{1-x}V_xO_3$ solid solutions with $x = 0.1, 0.2, 0.3, 0.4, 0.5, 0.6, 0.7, 0.8,$ and 0.9 were synthesized in a vacuum furnace at 1473 K and at a residual pressure of 1.3×10^{-3} Pa. The total annealing time was 72 h. After every 24 h of annealing, the samples were ground thoroughly.

X-ray diffraction measurements were carried out on a DRON-2 diffractometer (CuK_α radiation).

The neutron diffraction experiment was performed on a diffractometer mounted in the horizontal channel of an IVV-2M reactor. A monochromatic neutron beam with wavelength $\lambda = 1.805 \times 10^{-1}$ nm was obtained by successive reflection from a strained Ge(111) single crystal and (004) pyrolytic graphite. Measurements were made at temperatures ranging from 4.2 to 293 K. The x-ray and neutron diffraction patterns were processed using the FULLPROPF program [11].

The magnetic properties of the compounds were studied on a vibrating-sample magnetometer in fields of up to 19 kOe in the temperature range from 4.2 to 293 K. The relative error of the magnetization measurements did not exceed 2%. The temperature dependences of the ac susceptibility were measured at a frequency of 1 kHz and a magnetic-field amplitude of ≈ 10 Oe.

3. RESULTS AND DISCUSSION

The x-ray diffraction patterns of all samples were recorded at 293 K in the angular range $10° < 2\Theta < 70°$. The calculations of the diffraction patterns showed that the samples studied have an orthorhombic structure. The unit cell parameters (space group *Pnma*) for all compositions x are given in Table 1. It is readily seen that as the vanadium concentration increases, the a parameter, on the whole, decreases; the b parameter first increases, reaches a maximum of 7.877 Å at $x = 0.5$, and then decreases; and the cell length along the c axis does not change substantially. A comparison of the unit cell parameters in $LaMn_{1-x}V_xO_{3+\delta}$ and in pure $LaMnO_{3+\delta}$ shows that doping with vanadium brings about a noticeable increase in the b parameter.

The lattice parameters obtained in this work for samples of the $LaMn_{1-x}V_xO_{3+\delta}$ system (see Table 1 for the x-ray data obtained at 293 K and Table 2 for the neutron diffraction data taken at 4.2 K) agree satisfactorily with the data available in the literature for extreme compositions [2–5, 10]. However, it should be pointed out that, for all the compounds studied by us, the $b/(a\sqrt{2})$ ratio varies within the range 0.978–0.998, which lies closer to the corresponding value (1.0008) for $LaVO_3$ [9, 10], but somewhat differs from $b/(a\sqrt{2}) \approx 0.95$ for stoichiometric $LaMnO_3$ [2]. It is known that deviation of this ratio from unity is due to orthorhombic distortions in $LaMnO_3$. Hence, substitution of vanadium for manganese results in a decrease in the lattice distortions. This is apparently associated with the fact that such a substitution should reduce the static Jahn–Teller effect characteristic of $LaMnO_3$,

Table 1. Parameters of the $LaMn_{1-x}V_xO_3$ orthorhombic lattice, derived from the profile analysis of x-ray diffraction patterns measured at 293 K

Composition, x	a, Å	b, Å	c, Å	$b/(a\sqrt{2})$	V, Å^3	R, %
0.0 [12]	5.669(1)	7.671(1)	5.523(1)	0.9568	240.188	3.4
0.1	5.661(1)	7.830(1)	5.551(1)	0.9780	246.051	12.8
0.2	5.642(1)	7.859(1)	5.548(1)	0.9849	246.000	6.09
0.3	5.620(1)	7.870(1)	5.559(1)	0.9902	245.871	9.43
0.4	5.617(1)	7.876(1)	5.557(1)	0.9914	245.849	6.71
0.5	5.611(1)	7.877(1)	5.562(1)	0.9927	245.828	5.12
0.6	5.605(1)	7.872(1)	5.562(1)	0.9931	245.410	6.12
0.7	5.589(1)	7.863(1)	5.559(1)	0.9948	244.297	4.61
0.8	5.577(1)	7.857(1)	5.556(1)	0.9962	243.456	5.02
0.9	5.560(1)	7.853(1)	5.553(1)	0.9980	242.598	8.72
1.0 [10]	5.547(4)	7.851(6)	5.553(1)	1.0007	241.830	–

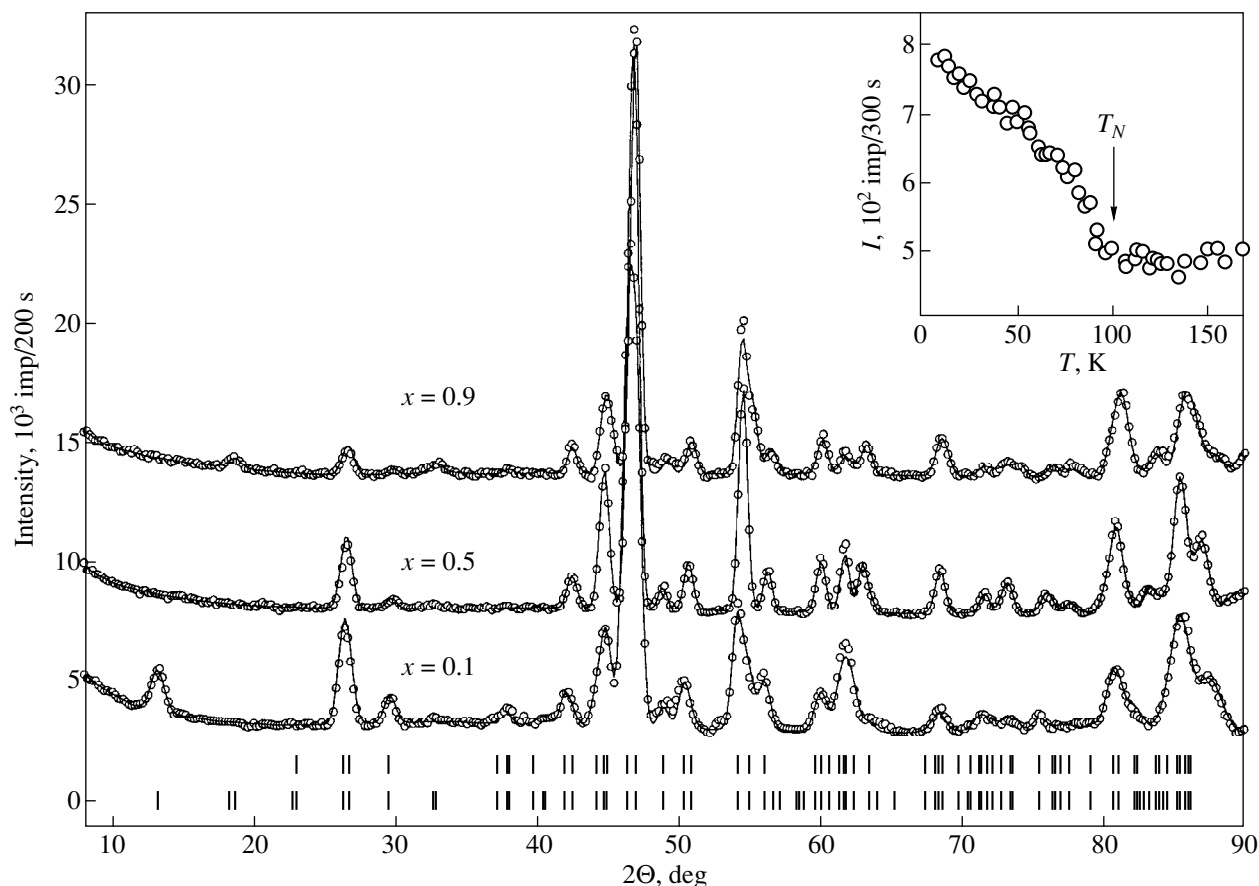Note: The lattice parameters for the extreme compositions are taken from the literature.

Fig. 1. Neutron diffraction patterns of the orthorhombic phase of the $LaMn_{1-x}V_xO_3$ perovskites at 4.2 K for the compositions with $x = 0.1, 0.5,$ and 0.9. Solid lines represent the calculated total intensities (nuclear and magnetic by the proposed models), and open circles are experimental points. Dashes under the diffraction curves specify the angular positions of the nuclear (top) and magnetic (bottom) reflections. The inset displays the temperature dependence of the peak intensity of the $(010)_M$ antiferromagnetic reflection ($2\Theta = 13.2°$) for the composition with $x = 0.1$.

because the number of Jahn–Teller Mn^{3+} ions decreases.

The coordinate parameters and the site occupancies were refined from neutron diffraction measurements. In the orthorhombic lattice (space group *Pnma*), the lanthanum (La) and oxygen (O1) atoms, oxygen (O2), and Mn/V atoms occupy the $4c(x, 1/4, z)$, $8d(x, y, z)$, and $4a(0, 0, 0)$ positions, respectively. The structural parameters derived from the neutron diffraction patterns are listed in Table 2. These values are close to those obtained in [12] for $LaMnO_{3+\delta}$. No data on the coordinate parameters and site occupancies for the other extreme composition of the $LaMn_{1-x}V_xO_{3+\delta}$ system are available in the literature.

As can be seen from Table 2, the oxygen nonstoichiometry in $LaMn_{1-x}V_xO_{3+\delta}$ compounds with $x \leq 0.3$ is $\delta \approx 0.06$, which corresponds to a Mn^{4+} content of about 12%. This concentration of Mn^{4+} ions is observed in lanthanum manganite, whose magnetic moment at low temperatures, in addition to the antiferromagnetic component, has a noticeable ferromagnetic component

[12]. Therefore, it can be assumed that magnetic ordering of this type is realized in the compounds under study at low vanadium concentrations.

In order to elucidate the magnetic structure and the magnetic moments on the Mn and V atoms and to construct the magnetic phase diagram, we carried out neutron diffraction studies and magnetic measurements at temperatures ranging from 4.2 to 293 K.

According to the neutron diffraction patterns obtained at 4.2 K, the samples studied can be divided conventionally into three groups. The neutron diffraction patterns characteristic of each group are displayed in Fig. 1. One group combines compositions with $x = 0.1, 0.2,$ and 0.3. The neutron diffraction patterns of these compositions contain an antiferromagnetic reflection at the angle $2\Theta = 13.2°$. We did not find coherent magnetic scattering in samples of the second group with $0.4 < x < 0.9$. The composition with $x = 0.9$ makes up the third group of samples. The neutron diffraction pattern of this sample exhibits an antiferromagnetic reflection at the angle $2\Theta = 18.5°$. Figure 2 shows fragments of neutron diffraction patterns containing reflec-

Table 2. Structural parameters at 293 K for an isotropic integrated thermal factor of 0.5 Å^{-2}

x	0.1	0.2	0.3	0.4	0.5	0.6	0.7	0.8	0.9
x, La	0.5471(14)	0.5446(04)	0.5418(05)	0.5402(06)	0.5364(04)	0.5365(05)	0.5333(06)	0.5302(08)	0.5301(12)
z, La	0.008(27)	0.0082(08)	0.0060(11)	0.0087(11)	0.0081(08)	0.0056(10)	0.0058(12)	0.0056(15)	0.0041(30)
n, La	0.98(1)	0.99(1)	0.98(1)	1.00(1)	1.00(1)	1.00(1)	0.99(1)	0.99(1)	0.99(1)
x, O1	−0.0148(20)	−0.0168(06)	−0.0163(08)	−0.0162(09)	−0.0157(06)	−0.0172(08)	−0.0169(09)	−0.0170(12)	−0.0157(18)
z, O1	−0.0854(28)	−0.0848(09)	−0.0805(11)	−0.0776(14)	−0.0745(10)	−0.0749(14)	−0.0710(15)	−0.0629(18)	−0.0615(35)
n, O1	1.00	1.00	1.00	1.00	1.00	1.00	1.00	1.00	1.00
x, O2	0.3017(16)	0.2971(04)	0.2950(06)	0.2938(06)	0.2918(04)	0.2934(06)	0.2926(06)	0.2913(08)	0.2874(24)
y, O2	0.0403(13)	0.0409(04)	0.0402(05)	0.0408(06)	0.0416(04)	0.0413(06)	0.0422(06)	0.0432(07)	0.0434(13)
z, O2	0.2137(18)	0.2170(05)	0.2187(6)	0.2151(08)	0.2148(05)	0.2165(06)	0.2176(09)	0.2188(11)	0.2196(13)
n, O2	2.00	2.00	2.00	2.00	2.00	2.00	2.00	2.00	2.00
n, Mn/V	0.98(2)	0.99(1)	0.98(2)	1.00(1)	1.00(1)	1.00(1)	0.99(1)	0.99(1)	0.99(1)
δ	0.067	0.061	0.055	0.00	0.00	0.00	0.027	0.006	0.015
a, Å (4.2 K)	5.656(1)	5.644(1)	5.629(1)	5.621(1)	5.607(1)	5.597(1)	5.985(1)	5.581(1)	5.579(1)
b, Å (4.2 K)	7.827(1)	7.842(1)	7.862(1)	7.870(1)	7.859(1)	7.858(1)	7.855(1)	7.846(1)	7.825(1)
c, Å (4.2 K)	5.544(1)	5.548(1)	5.550(1)	5.554(1)	5.555(1)	5.547(1)	5.550(1)	5.551(1)	5.548(1)
M_x (AF), μ_B	1.7(1)	0.9(1)	0.4(2)	–	–	–	–	–	1.1(2)
M_y (F), μ_B	1.3(1)	1.4(1)	0.6(2)	–	–	–	–	–	
$\langle M \rangle$, μ_B	2.2(1)	1.6(1)	0.7(2)	–	–	–	–	–	1.1(2)
T_N	100(5)	<78	<78						≈120
R_N, %	7.7	4.4	4.2	5.2	3.6	3.8	5.5	5.8	6.1
R_M, %	14.6	21.0	30.0	–	–	–	–	–	30.5

Note: The δ values are given for the experimental values of the site occupancy without regard for error. The magnetic moment projections and the lattice parameters are derived for LaMn$_{1-x}$V$_x$O$_3$ at 4.2 K ($B = 0.1$ Å^{-2}). M_x and M_y are anti- and ferromagnetic projections of the Mn and V magnetic moments, respectively. The parenthetic figures are the standard deviations for the last significant digits.

tions at $2\Theta = 13.2°$ and $18.5°$. It is readily seen that the main antiferromagnetic reflection changes in angular position and intensity with an increase in the vanadium concentration.

As follows from the calculations of the neutron diffraction patterns, the magnetic- and crystal-cell parameters for the compositions with $x = 0.1$–0.3 and 0.9 coincide, which corresponds to the wavevector of the magnetic structure $\mathbf{k} = [0, 0, 0]$. Magnetic symmetry analysis yielded possible magnetic ordering patterns with $\mathbf{k} = [0, 0, 0]$ for the $LaMn_{1-x}V_xO_{3+\delta}$ compounds. The magnetic ions in these compounds occupy only one position, $4a$. For this position, the magnetic representation with $\mathbf{k} = [0, 0, 0]$ has the form [13]

$$d_M = 3\tau_1 + 3\tau_3 + 3\tau_5 + 3\tau_7,$$

where $\tau_1, \ldots, \tau_7$ are irreducible representations of the *Pnma* space group. The basis functions of the irreducible representations belonging to the magnetic representation of the *Pnma* space group are given in Table 1 of our earlier paper [12]. By properly mixing several irreducible representations, one can obtain all lattice-symmetry-allowed magnetic structures.

Neutron diffraction patterns were calculated for various mixing versions. Comparison of the calculated neutron diffraction patterns with those experimentally measured for the compositions with $x = 0.1$–0.3 and 0.9 revealed that the minimum value of the convergence factor R_{mag} is reached under the following conditions. The magnetic structure of the compounds with $x = 0.1$–0.3 is described by a superposition of the recurring representations $\tau_3' + \tau_3$. The τ_3' representation corresponds to antiferromagnetic alignment with the a axis, and the τ_3, to ferromagnetic alignment with the b axis. The ferro- and antiferromagnetic components of the magnetic moment of an ion are given in Table 2. These values relate to a "grey" $3d$ ion occupying the $4a$ position. We readily see that substitution of vanadium for manganese in compositions with $0.1 \leq x \leq 0.3$ results in a fairly drastic decrease in the magnetic moment.

A further increase in the vanadium concentration (up to $x = 0.9$) brings about the disappearance of the ordered magnetic moment. As already pointed out, there is no long-range magnetic order in compounds with $0.4 \leq x \leq 0.8$ for $T \geq 4.2$ K.

For the sample with $x = 0.9$, the R_{mag} factor was found to be the smallest when the magnetic structure was described by the τ_5'' irreducible representation. This representation relates to antiferromagnetic ordering along the b axis. The magnitude of the moment is given in Table 2. Note that, in the composition with $x = 0.9$, not only the orientation of moments with respect to the crystallographic axes but their mutual orientation as well are different from those observed in compositions with $0.1 < x < 0.3$. In the sample with $x = 0.9$, the moments of the nearest neighboring ions are coupled ferromagnetically in the (001)-type planes, and antifer-

Table 3. Characteristics of the $LaMn_{1-x}V_xO_3$ magnetic state, derived from magnetic measurements

x	σ_0, emu/g	μ, μ_B	T_P, K	T_f, K	T_c, K
0.1	19.6(5)	0.9(1)	110	33	100(5)
0.2	16.7(5)	0.7(1)	85	32	65(5)
0.3	9.5(5)	0.4(1)	80	26	30(10)
0.4	–	–	75	25	–
0.5	–	–	65	26	–
0.6	–	–	60	26	–
0.7	–	–	40	28	–
0.8	–	–	0	30	–
0.9	–	–	–125	32	–

romagnetically, between these planes, whereas in compositions with $0.1 < x < 0.3$, we have the reverse situation.

In order to determine the Néel temperature T_N of the sample with $x = 0.1$, we carried out measurements of the peak intensity $I_{(010)}$ of the (010) magnetic reflection (see inset to Fig. 1). It is seen that the reflection disap-
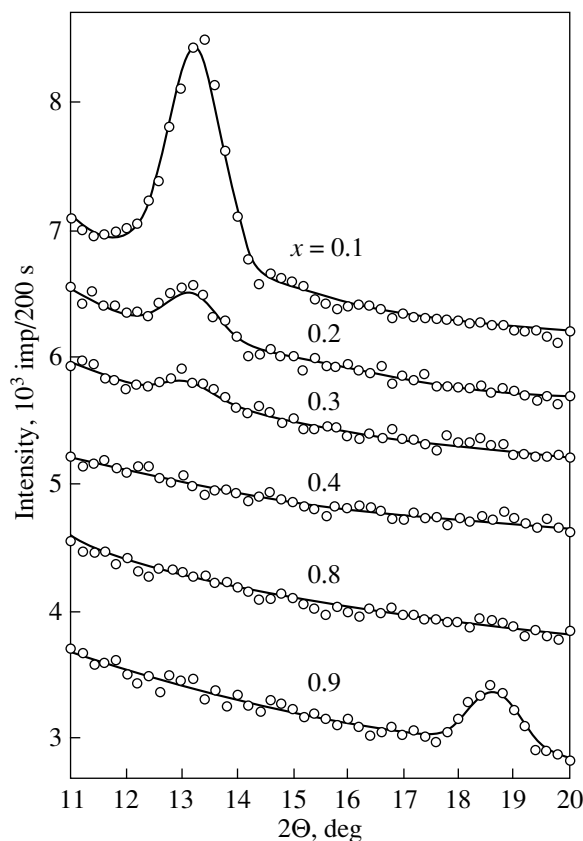

Fig. 2. Fragments of neutron diffraction patterns at 4.2 K for the compositions with $x = 0.1$, 0.2, 0.3, 0.4, 0.8, and 0.9. Open circles are experimental points, and the solid lines represent the calculations within the proposed models.
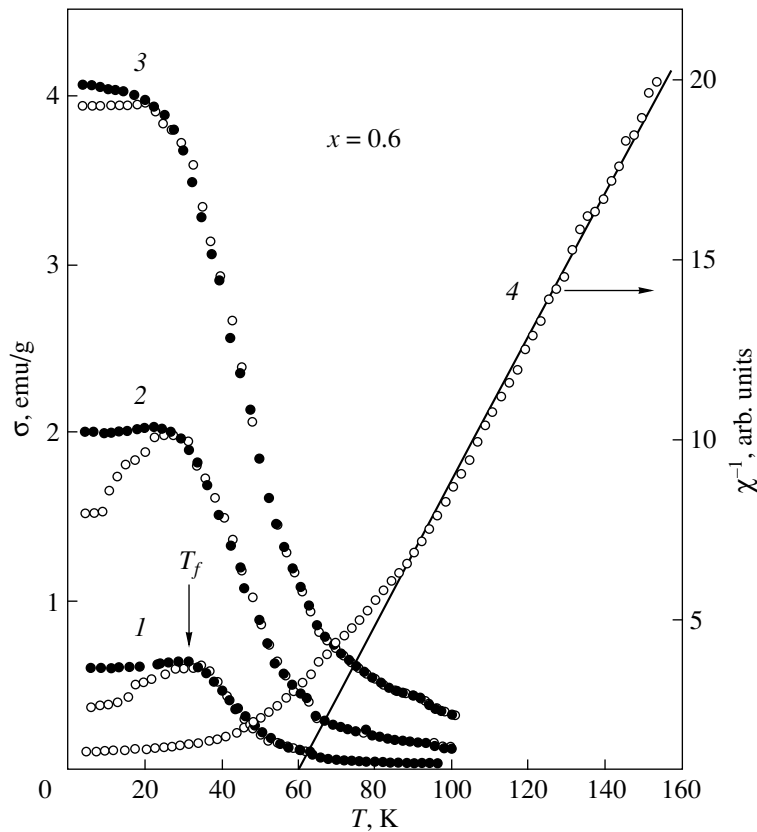
Fig. 3. Temperature dependences of the reversible σ_{FC} (filled circles) and irreversible σ_{ZFC} (open circles) magnetizations of LaMn$_{0.4}$V$_{0.6}$O$_3$ in magnetic fields (kOe): (*1*) 0.3, (*2*) 1.2, and (*3*) 3.0. The arrow identifies the freezing temperature T_f derived from ac susceptibility data. (*4*) Temperature dependence of the inverse susceptibility measured at 16 kOe. The straight line represents the linear extrapolation of the inverse susceptibility to the temperature axis drawn to determine the paramagnetic Curie temperature T_P.

pears at $T_N = (100 \pm 5)$ K. We have not succeeded in measuring the Néel temperature for the compositions with $x = 0.2$ and 0.3 due to the low intensity of the antiferromagnetic reflection. The Néel temperature of ≈ 120 K for the composition with $x = 0.9$ was estimated from the intensities of the antiferromagnetic reflection measured at 4.2 and 78 K.

To obtain information on the magnetic state of LaMn$_{1-x}$V$_x$O$_3$ compounds and to construct the magnetic phase diagram, detailed temperature dependences of the magnetization σ (susceptibility χ) were studied on field-cooled (FC) and zero-field-cooled (ZFC) samples. Figure 3 presents temperature dependences of the magnetization and the static susceptibility for the composition with $x = 0.6$. As is seen, this sample is characterized by an irreversible behavior of the magnetization. Below some temperature T_f, which decreases with increasing field strength, the σ_{ZFC} and σ_{FC} magnetization curves do not coincide. The freezing temperatures T_f derived in the magnetization measurements coincide in the low-field limit with the peak on the temperature dependence of the ac susceptibility. Figure 3 also shows the temperature dependence of the inverse sus-

ceptibility measured in a magnetic field of 16 kOe, whose extrapolation to zero yields the paramagnetic Curie temperature T_P. As follows from the Curie–Weiss law for the temperature dependence of paramagnetic susceptibility, T_P is a parameter determining the dominant role of exchange coupling between magnetically active atoms. Positive paramagnetic Curie points are characteristic of ferromagnetic exchange coupling between spins or magnetic clusters. Zero or negative values of the paramagnetic Curie temperature are typical of systems with no ferromagnetic interactions. Similar temperature dependences of magnetization and susceptibility are observed for all the compounds studied, and Table 3 lists the T_f and T_P temperatures obtained for the compositions investigated. As is seen from the values of T_P, antiferromagnetic interaction in compositions with $x > 0.8$ is dominant.

Figure 4 displays the field dependences of the specific magnetization measured at 4.2 K on ZFC samples of the compounds studied. It is seen that the field dependences of all the compositions, except those with $x = 0.1$ and 0.9, resemble the Langevin-type curves, which are characteristic either of systems with a large anisotropy or of superparamagnets. For $x = 0.1$, the

dependence is closer to the ferromagnetic type, but with a higher susceptibility of the paraprocess. For $x = 0.9$, the magnetization depends linearly on the applied field. Determination of the spontaneous magnetization σ_0 at 4.2 K by linear extrapolation of the magnetization curves to zero field is made difficult because of the absence of a clearly pronounced linear portion in $\sigma(H)$, except for the case of the composition with $x = 0.1$. For this reason, σ_0 was found using a technique similar to the Belov–Arrott thermodynamic coefficient method. To accomplish this, the curves for $\sigma^2 = f(H/\sigma)$ at 4.2 K were plotted for all the compounds studied. Extrapolation to zero field permitted the determination of the spontaneous magnetization σ_0 and the subsequent calculation of the average ferromagnetic moment per "grey" atom occupying a manganese site (Table 3). This approach also makes it possible to determine the critical concentration of disappearance of the ferromagnetic order parameter in the series of the compounds investigated. This concentration can be found by setting the a parameter in the Belov–Arrott equation $a + b\sigma^2 = H/\sigma$ to zero. It was found that for $x < 0.4$, the magnetic ground state of the compounds is characterized by the existence of a ferromagnetic order parameter. The temperature at which the ferromagnetic component transfers to the paramagnetic state, T_c (see Table 3), was determined by the thermodynamic coefficient method, because the temperature dependences of magnetization of these compounds measured in weak fields do not have a step characteristic of the kink method.

As follows from Tables 2 and 3, the compounds with $x < 0.4$ exhibit spontaneous magnetization and the ferromagnetic component of the magnetic moment is comparable in magnitude to the antiferromagnetic component. Because the ferro- and antiferromagnetic alignments for these compositions are described by the same irreducible representation, they are identified by one exchange multiplet. Then, a structure with moments having both ferromagnetic τ_3 and antiferromagnetic τ_3' components will correspond to the ground state of a magnet. Therefore, the magnetic structure of the compositions with $x \leq 0.3$ should be noncollinear, which corresponds to a canted antiferromagnet. It seems all the more probable that the Néel temperature derived from the neutron diffraction data for the composition with $x = 0.1$ coincides, to within the experimental error, with the Curie temperature determined by the magnetic method. It is for this state that the absolute values of the moment $\langle\mu\rangle$ are given in Table 2. The ferromagnetic moments extracted from magnetic measurements (see Table 3) appear to be somewhat underevaluated, possibly because true saturation cannot be achieved in a field of 19 kOe. Recalling that $\langle\mu\rangle$ for LaMnO$_3$ varies from 3.5 to 3.8μ_B, the data of Tables 2 and 3 suggest that substitution of V for Mn ions results in a substantially stronger decrease in the moment on the $3d$ ion than should be expected to result from the
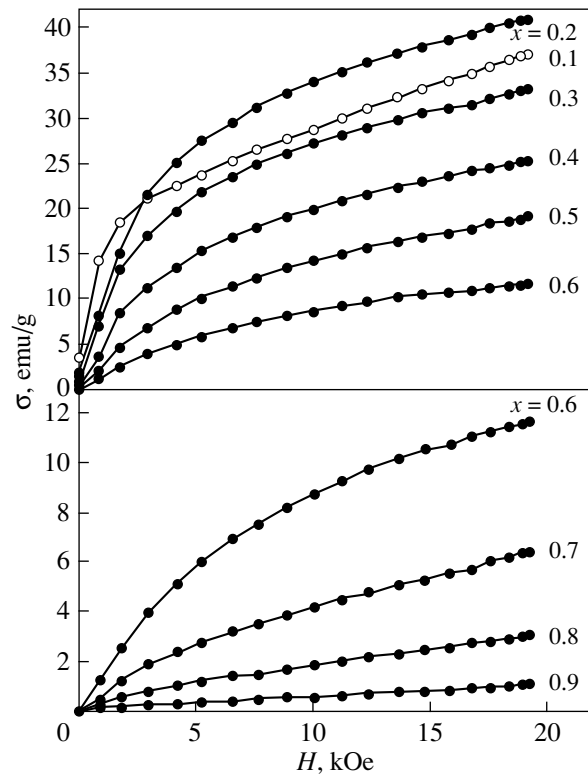

Fig. 4. Magnetization curves for zero-field-cooled samples of the LaMn$_{1-x}$V$_x$O$_3$ compounds with different compositions x at 4.2 K.

dilution of the manganese sublattice alone. The reasons for this may be as follows. As was shown, for instance, in [14], local spin distortions can arise in a canted-spin system. They form clusters around ions, which break the periodicity of the ion distribution over lattice sites. In the case of the LaMn$_{1-x}$V$_x$O$_3$ compounds, vanadium substitutes for manganese in a random manner, which frustrates the Mn ions. The breakdown of the relation between the Mn^{3+}–Mn^{4+} ferromagnetic and Mn^{3+}–Mn^{3+} antiferromagnetic interactions gives rise to a local distortion of the spin structure around the V ion. Moreover, the V^{3+} ion has a magnetic moment whose preferential orientation differs from that of the Mn^{3+} moment, so that the exchange coupling between Mn and V may have opposite signs, depending on the electronic configuration of the ions. This can induce random magnetic fields, which destroy the long-range magnetic order in the matrix more strongly than doping with nonmagnetic ions.

Such systems exhibit properties typical of spin glasses, in particular, the irreversible behavior of the magnetization below the T_f temperature. The magnetic state of compounds with $0.1 \leq x \leq 0.3$ is probably two-phase. One phase supports long-range magnetic order (canted antiferromagnetism), whereas in the other phase, the spin-glass state is realized. We can estimate the sample volume occupied by the former phase by
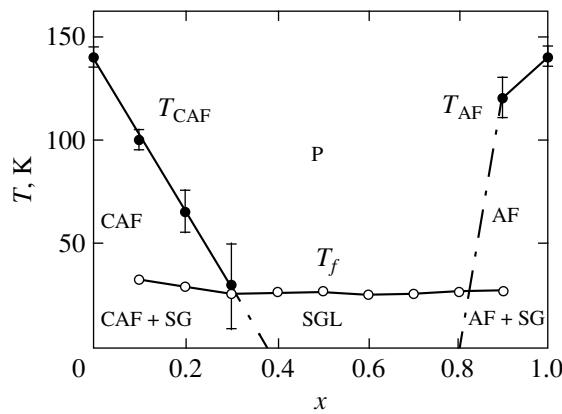
Fig. 5. Magnetic phase diagram of the LaMn$_{1-x}$V$_x$O$_3$ system. Designations: P—paramagnet, CAF—canted antiferromagnet, AF—antiferromagnet, SGL—spin-glass state.

assuming that the moment of the Mn ion is 4μ_B and that the mixing law holds. Then, at 4.2 K, the region with the long-range magnetic order in the sample $x = 0.1$ occupies only about 60% of the sample volume.

Phase segregation, the manner of coexistence of various magnetic phases in perovskites, has recently become a subject of much debate [15]. The basic idea is that manganese ions in different orbital states segregate at different distances. This gives rise to an intrinsic inhomogeneous magnetic ground state in the perovskites, which is strongly affected by an external magnetic field. This description assumes the existence of three magnetic phases, namely, the antiferromagnetic, ferromagnetic, and spin-glass phases, which differ in their lattice parameters and temperature-induced changes. However, the magnitudes of these changes lie beyond the accuracy of our measurements.

The absence of coherent magnetic reflections and magnetic measurements suggest zero spontaneous magnetization in compounds with $0.4 \leq x \leq 0.8$ at 4.2 K. Here, only the short-range order, both antiferromagnetic and ferromagnetic, can exist. The presence of short-range magnetic order regions, which become blocked below T_f, gives rise to a magnetic ground state in the form of a cluster spin glass (see, e.g., [16]).

A further increase in the concentration to $x = 0.9$ initiates long-range magnetic order with an antiferromagnetic alignment similar to that observed earlier in LaVO$_3$ [8, 9]. This is indicated by the linear field dependence of the magnetization and by the magnitude of the paramagnetic Curie temperature. In LaMn$_{0.1}$V$_{0.9}$O$_3$, the magnetic moment of the V ion is 1.2μ_B (if the Mn ions are assumed nonmagnetic), which is close to the value of 1.3μ_B found for LaVO$_3$ [8]. At the same time, the expected spin moment of the V^{3+} ion is 2μ_B. This difference can be explained by the fact that compositions with $x = 0.9$ and 1.0 exhibit regions without long-range magnetic order, which manifest them-

selves in the irreversibility of magnetization below T_f. One also cannot rule out the possibility that antiferromagnetic ordering in these compositions is accompanied by an electronic transition resulting in a noticeable decrease in the localized magnetic moment on the V ions.

Unlike the above case, where the τ_3 and τ_3' representations corresponded to one exchange multiplet, the τ_3 and τ_5 irreducible representations describing the magnetic structures of the extreme compositions with $x = 0.1$ and 0.9 give rise to two discrete multiplets of states degenerate in exchange energy. Therefore, the mixing of these representations will produce not a single-phase state with a noncollinear magnetic structure but rather a state with two phases which have different magnetic structures. In our case, the boundaries separating these phases do not cross; therefore, a magnetic phase transition from one type of the magnetic structure to another occurs not through spin reorientation but via a state with no long-range magnetic order.

In conclusion, we present a magnetic phase diagram (Fig. 5) of the LaMn$_{1-x}$V$_x$O$_3$ orthorhombic perovskites, in which the Néel temperature and the freezing point of the spin-glass state are specified. The T_{CAF} temperature was derived from the data on neutron diffraction and magnetic measurements. The diagram identifies the regions of existence of the long-range magnetic and spin-glass orders, as well as the regions where the magnetic phases coexist.

Thus, we have reported the first investigation of the crystal structure and magnetic ordering in the LaMn$_{1-x}$V$_x$O$_{3+\delta}$ compounds. Oxygen nonstoichiometry is the largest in compounds with $0.1 \leq x \leq 0.3$ and is approximately 0.06. At $T \leq 300$ K, all compounds have an orthorhombic structure with similar parameters $b/\sqrt{2}$ and c, which suggests that the doping of the lanthanum manganite by vanadium reduces orthorhombic distortions. Long-range magnetic order is observed only in compositions with $x \leq 0.3$ and $x = 0.9$. The magnetic structure of the compositions with $x \leq 0.3$ is described by the sum of the irreducible representations $\tau_3' + \tau_3$, which corresponds to a canted antiferromagnetic structure (wavevector $\mathbf{k} = [0, 0, 0]$) with antiferromagnetic moments aligned with the a axis and a ferromagnetic component of the magnetic moment parallel to the b axis. The best description for the composition with $x = 0.9$ is provided by the τ_5'' representation, which corresponds to antiferromagnetic ordering with magnetic moments parallel to the b axis. The compounds in the intermediate composition region with $0.4 < x < 0.9$ reveal an absence of long-range magnetic order at 4.2 K. In this case, the magnetic ground state exhibits properties characteristic of cluster spin glasses.

REFERENCES

1. M. McCormack, S. Jin, T. H. Tiefel, *et al.*, Appl. Phys. Lett. **64**, 3045 (1994).

2. H. C. Nguen and J. B. Goodenough, Phys. Rev. B **52**, 324 (1995); J. Topfer and J. B. Goodenough, Chem. Mater. **9**, 6 (1997).

3. R. Mahendiran, S. K. Tiwary, A. K. Raychaundhuri, and T. V. Ramakrishan, Phys. Rev. B **53** (6), 3348 (1996).

4. F. Moussa, M. Hennion, J. Rodríguez-Carvajal, *et al.*, Phys. Rev. B **54** (21), 15 149 (1996).

5. V. I. Voronin, A. E. Karkin, A. N. Petrov, *et al.*, Physica B (Amsterdam) **234–236**, 710 (1997).

6. B. A. Jacqueline, A. Elemans, B. van der Laar, *et al.*, J. Solid State Chem. **3**, 238 (1971).

7. B. C. Tofield and W. R. Scott, J. Solid State Chem. **10**, 183 (1974).

8. V. G. Zubkov, G. V. Bazuev, V. A. Perelyaev, and G. A. Shveĭkin, Fiz. Tverd. Tela (Leningrad) **15**, 1610 (1973) [Sov. Phys. Solid State **15**, 1078 (1973)].

9. V. G. Zubkov, G. V. Bazuev, and G. P. Shveĭkin, Fiz. Tverd. Tela (Leningrad) **18**, 2002 (1976) [Sov. Phys. Solid State **18**, 1165 (1976)].

10. V. Bazuev and G. P. Shveĭkin, *Complex Oxides of Elements with Incomplete d and f Shells* (Nauka, Moscow, 1985).

11. J. Rodríguez-Carvajal, Physica B (Amsterdam) **192**, 55 (1993).

12. A. N. Pirogov, A. E. Teplykh, V. I. Voronin, *et al.*, Fiz. Tverd. Tela (St. Petersburg) **41**, 103 (1999) [Phys. Solid State **41**, 91 (1999)].

13. Yu. A. Izyumov, V. E. Naĭsh, and R. P. Ozerov, *Neutronography of Magnetics* (Atomizdat, Moscow, 1981).

14. P.-G. de Gennes, Phys. Rev. **118**, 141 (1960).

15. P. G. Radaelli, D. N. Argyriou, J. F. Mitchell, and S.-W. Cheong, in *Conference Programme and Abstracts of the 2nd European Conference on Neutron Scattering, Budapest, 1999*, p. 177.

16. V. S. Dotsenko, Usp. Fiz. Nauk **165** (5), 481 (1995) [Phys. Usp. **38**, 457 (1995)].

Translated by G. Skrebtsov

MAGNETISM
AND FERROELECTRICITY

The Initial Stage in the Nonlinear Motion
of a Domain Wall in Garnet Films

V. A. Bokov*, V. V. Volkov*, N. L. Petrichenko*, and Z. Fraĭt**

*Ioffe Physicotechnical Institute, Russian Academy of Sciences, Politekhnicheskaya ul. 26, St. Petersburg, 194021 Russia
**Institute of Physics, Czech Academy of Sciences, Prague, 18221 Czech Republic
Received April 25, 2000

Abstract—A study of the domain-wall motion in single-crystal garnet films of the YBiFeGa system with a perpendicular magnetic anisotropy, activated by a constant in-plane bias field H_p parallel to the wall plane and a pulsed drive field H_g of an amplitude corresponding to the nonlinear region of the domain-wall velocity vs. the H_g relation is reported. The earlier data suggesting the existence of an initial phase of motion, where the wall is accelerated to a high instantaneous velocity, have been confirmed. The wall behavior in the initial phase has been shown to be affected by the field H_p and the drive-field pulse rise time. A possible mechanism of the wall structure transformation after the application of the H_g pulse is considered. It has been established that the dependence of the wall velocity on H_p in the saturation region disagrees with theory. © 2000 MAIK "Nauka/Interperiodica".

It is known that a domain wall in films with a large perpendicular magnetic anisotropy under drive fields H_g in excess of a certain critical level H_g^c moves with the so-called saturation velocity, which does not depend on H_g. It was also established that, at the initial instants of time immediately after a field pulse application, the domain wall moves with a velocity exceeding the saturation velocity. It was conjectured that in this stage a wall does not contain spin structures such as horizontal Bloch lines (HBL), so its motion can be described in terms of the one-dimensional Walker's model (see, e.g., [1–5]). It was necessary, however, to assume that the wall displacement occurs with losses exceeding those typical of ferromagnetic resonance (FMR) a few times over. At the same time, it was maintained [6, 7] that, on application of a drive field pulse with an amplitude in excess of the field at which steady-state motion breaks down, the domain wall accelerates initially to a high instantaneous velocity. In [7], the wall acceleration was described by the well-known equation of motion with an inertial term. The wall effective mass thus obtained was substantially larger than the Döring mass, which was assigned to a buildup of HBLs in the wall. This approach did not need any assumptions concerning the damping parameter. The measurements in [7] were carried out on one sample at a fixed drive-field pulse rise time, so that the data obtained did not permit any generalizations.

In order to investigate the initial stage of the domain wall motion within the nonlinear region of the drive fields in excess of the critical level H_g^c and to establish the mechanism responsible for the transformation of the wall spin structure, we studied the effect of the H_g pulse rise time on the domain-wall motion. The measurements were performed on two YBiFeGa films with the following characteristics: sample *1* had a thickness of $h = 5.3$ μm, a magnetization $4\pi M = 138$ G, the anisotropy field $H_A = 2570$ Oe, the Bloch wall-thickness parameter $\Delta = 0.28 \times 10^{-5}$ cm, the effective gyromagnetic ratio $\gamma = 1.8 \times 10^7$ Oe^{-1} s^{-1}, and the Gilbert damping parameter $\alpha = 0.0025$ (from FMR data); and sample *2* had $h = 4.6$ μm, $4\pi M = 156$ G, $H_A = 6200$ Oe, $\Delta = 0.2 \times 10^{-5}$ cm, $\gamma = 1.67 \times 10^7$ Oe^{-1} s^{-1}, and $\alpha = 0.002$. The measurements were done on a planar domain wall stabilized by a pulsed gradient field generated by two parallel planar conductors through which a current pulse was passed. The pulse amplitude was large enough to transform the initial labyrinth structure between the conductors into two domains separated by a domain wall parallel to the conductors. One microsecond after the application of the gradient field pulse, when the planar wall has already formed, a pulse of the drive field H_g causing wall motion was applied. The measurements were performed at different field-pulse rise-time constants τ, more specifically at 1, 20, and 35 ns. An in-plane dc bias field H_p was applied parallel to the planar wall. The relations $q(t)$ connecting the wall displacement with time were found for several values of H_p, from 240 to 480 Oe for film *1* and from 400 to 1300 Oe for film *2*, and for different amplitudes of H_g. Visualization was obtained by a high-speed image-recording method, and the ~5-ns pulsed illumination was provided by a Rhodamine 6G dye laser pumped by a pulsed nitrogen laser. A TV camera with a high-sensitivity vidicon served as a receiver, and the images recorded were stored and could be displayed on the
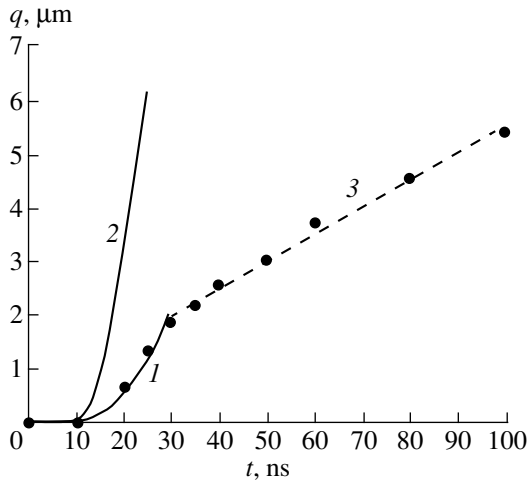
Fig. 1. Domain wall displacement vs. the time reckoned from the instant of the application of the H_g pulse. Sample *1*, $\tau = 1$ ns, $H_g = 45$ Oe, and $H_p = 360$ Oe. The points are experimental; (*1*) approximation by the $q(t)$ function, (*2*) calculation for the $m = m_D$ case, and (*3*) velocity saturation region.
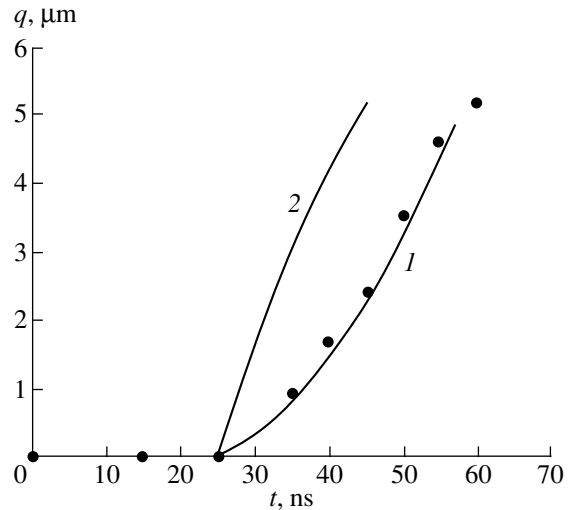

Fig. 2. Domain wall displacement vs. the time reckoned from the H_g pulse application moment. Sample *1*, $\tau = 20$ ns, $H_g = 45$ Oe, and $H_p = 390$ Oe. The points are experimental; (*1*) approximation by the $q(t)$ function and (*2*) calculation for the $\alpha = 0.2$ case.

monitor screen for treatment. The wall displacement was determined by averaging the data obtained in several dozen measurements.

Figures 1 and 2 exemplify the typical $q(t)$ dependences obtained for film *1* with the time constants τ of 1 and 25 ns and an amplitude $H_g = 45$ Oe. One clearly sees an initial delay t' in the wall displacement with respect to the instant of the field pulse application. The length of this delay increases from ~10 ns for $\tau = 1$ ns to ~30 ns for $\tau = 35$ ns. The initial delay is followed by the stage of wall acceleration to a velocity V_m, after which the velocity drops to its saturation value $V_s < V_m$. Qualitatively the same results were obtained for sample *2*. The acceleration phase lasts ~15 ns for $\tau = 1$ ns, and its duration increases to ~30 ns with the time constant τ increasing to 35 ns.

As in [7], when describing the wall motion in acceleration, we limit ourselves to the equation of motion containing an inertial term. Taking into account the initial delay, this equation can be written in the form

$$m\frac{d^2y}{dt^2} + 2M\mu^{-1}\frac{dy}{dt} + 2M\nabla Hy(t)$$
$$= 2MH_g[1 - e^{-(t+t')/\tau}],$$
(1)

where m is the effective wall mass, μ is the mobility, and ∇H is the stabilizing gradient. We do not write out the function $y(t)$ here, which is the solution to this equation, because its explicit form is too cumbersome. We shall approximate the experimental data by the function

$$q(t) = \begin{cases} 0, & \text{for } t \le t' \\ y(t), & \text{for } t' < t \le t''. \end{cases}$$

Here, t'' is the time at which the wall reaches its maximum velocity. The quantities m and t' were used as fitting parameters, and μ was derived from the FMR measurements. It was shown earlier [8] that, in films with a very narrow FMR line, the mobility found from wall dynamics experiments turns out to be a few times smaller than that extracted from the FMR data. In our case, these mobilities differ by a factor two to four; however, one can readily verify that this difference does not affect noticeably the calculated $q(t)$ relation, and, therefore, μ was determined from the FMR data.

In Figs. 1 and 2, the experimental data are fitted by curves *1*. The values of the effective mass found in the H_p interval studied, $m > 10^{-9}$ g/cm², exceed the Döring mass m_D. For instance, for sample *1*, $m_D = (2\pi\Delta\gamma^2)^{-1} = 1.7 \times 10^{-10}$ g/cm², and in the fields H_p employed here, this mass should be less than 10^{-10} g/cm² (see Eq. (16) in [9]). Curve *2* in Fig. 1 shows how the time dependence of the wall displacement would look in the case of $m = m_D$ and for the values of t' and μ corresponding to curve *1*. According to the present notions, the wall mass can be written as [10]

$$m = \frac{\gamma}{2M}\frac{d\overline{\Psi}}{dV_i},$$
(2)

where V_i is the instantaneous wall velocity. A domain wall will possess an anomalously large effective mass if the increase in velocity in the course of its acceleration will be accompanied by a substantial increase in the film-thickness-averaged angle $\overline{\Psi}$ that the magnetization makes with the wall plane. Thus, the data obtained by us in this work and in [7] for films with very low losses permit the conclusion that, when a film

starts to move under a drive field substantially in excess of the breakdown field, HBLs will build up in it at the first instants of time. This is what accounts for the growth of the $\overline{\Psi}$ angle.

The dependence of the duration of the acceleration phase on the field-pulse rise time constant can be explained in the following way. A wall stabilized by a gradient field ∇H and driven by an H_g pulse is acted upon by an effective field

$$H' = H_g[1 - e^{-(t+t')/\tau}] - \nabla H y(t). \qquad (3)$$

This field brings about an increase in the $\overline{\Psi}$ angle, which is described for low losses by the expression

$$\frac{d\overline{\Psi}}{dt} = \gamma H'. \qquad (4)$$

It is possible that the wall accelerates until the angle $\overline{\Psi}$ reaches a certain critical value $\overline{\Psi}'$. After this, one of the HBLs punches through upon reaching the surface and a state of chaos corresponding to the velocity saturation regime sets in. Obviously enough, the time interval during which $\overline{\Psi}$ attains the critical value is given by Eq. (4). If the H_g pulse is step-shaped, the amplitude $H' = H_g$ at the instant of the application of the field, after which, by Eq. (3), H' falls off. At finite values of τ, we always have $H' < H_g$. If one plots $H'(t)$ relations for different τ, it will become evident that, as the pulse rise constant increases, the time required to twist the spins in the wall through the angle $\overline{\Psi}'$ should also increase. If the τ times are large enough, the wall can reach its new equilibrium position where $H' = 0$, while not attaining motion with the saturation velocity.

The wall acceleration stage can apparently be observed only in films with a very low damping parameter α. For comparatively large α, the viscosity effect will prevail. For instance, if sample *1* had a sufficiently large damping parameter, for example, $\alpha = 0.2$, then for the values of *m* and *t'* corresponding to curve *1* in Fig. 2 the solution of Eq. (1) would be represented by curve *2*. Note that the initial portions of the time dependence of the wall translation obtained with drive fields $H_g > H_g^c$ in [1–6] and in other studies where films with large $\alpha \sim 0.1$ were used had the same pattern.

A possible explanation of the initial delay in the wall displacement can be proposed on the basis of the results quoted in [11]. According to the calculations in [11], the first to nucleate in the wall under a high drive field is a single HBL and it appears not near the film surface but rather in the middle (see also [12, 13]). When the Bloch line moves across the film thickness, the wall velocity is given by the relation

$$V_i = \frac{\gamma}{2M} \frac{\partial \sigma}{\partial \overline{\Psi}}, \qquad (5)$$

where σ is the wall energy density. If the HBL is displaced near the film center, σ changes primarily due to the change in the HBL spin energy under the stray field created by charges on the film surface. As is shown by the calculations, this energy and, hence, σ increase very little near the film central plane for a noticeable increase of the $\overline{\Psi}$ angle. Therefore, the wall velocity also grows very little for some time, which is perceived as a delay in the translation. The increase in the delay time *t'* observed to occur with an increasing time constant τ can be explained as due to the fact that, because of the specific character of the dependence of the effective field H' on τ, the twist angle $\overline{\Psi}$ will reach (with increasing τ) the values at which the wall velocity differs noticeably from zero only at later times. Note that an initial delay in the wall displacement was also observed earlier [14, 15] in the translational motion of magnetic bubble domains, but in weak drive fields, of the order of the coercive field, and it was attributed to magnetic aftereffects.

A dc in-plane magnetic field is known to affect substantially the saturation velocity of a domain wall. This effect is dealt with in a number of papers, but their results differ noticeably. For instance, by a simple model [10], in the nonlinear field region, $H_p \gg 8M$, one has

$$V = V_s = \frac{1}{4}\Delta\gamma H_p. \qquad (6)$$

The wall dynamics was considered theoretically for the case of in-plane transverse fields $H_p \gg 4\pi M$, and the conclusion was drawn that the velocity saturation reached by a wall in the presence of a transverse field is caused by a change in the relaxation mechanisms with an increasing drive field [16]. The saturation velocity was obtained as

$$V_s = \frac{\pi}{2}\Delta\gamma H_p. \qquad (7)$$

According to experimental data [17], relation (6) holds in comparatively low drive fields ($H_g < 4M$), while at higher H_g the saturation velocity increases 2π times more rapidly with an increasing field H_p. Such a strong increase in the wall velocity was also observed in [18] for $H_p > 12\pi M$; there, the measurements were performed in the drive fields $H_g > 25M$. These results are at odds with the data quoted in [7, 19]. In particular, the $V_s(H_p)$ relations obtained in [7] with different drive fields ($H_g = 0.5M$ and $6M$) were found to be substantially nonlinear and disagreed with expressions (6) and (7). In view of these contradictions, it appeared reasonable to reconsider the wall motion in the saturation velocity region in the presence of a transverse field and in films with different parameters. In this work, as in [7], the saturation velocity was determined for the linear portion in the $q(t)$ curve, which immediately follows the wall acceleration phase. Figure 3 presents experimental
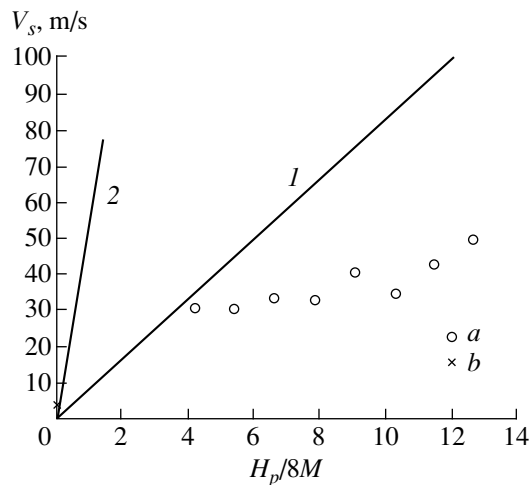
Fig. 3. Saturation velocity vs. dc bias field H_p for film *2*: (a) experimental points, (b) the value of V_s calculated from an expression in [20]; (*1*) calculation using Eq. (6) and (*2*) calculation from expression (7).

data obtained on sample *2* for $4 < H_p/8M < 13$ and $H_g = 60$–85 Oe. Also shown are the relations calculated from Eqs. (6) and (7). The value of V_s calculated using an empirical relation from [20], $V_s = M\Delta\gamma(1 + 6.9\alpha)$, is identified with a cross on the vertical axis. One readily sees that the experimental dependence is not described by expressions (6) and (7), in particular, in the region of the H_p values ($H_p \gg 8M$) where, by [16–18], the linear relation (7) should hold. The data in Fig. 3 qualitatively resemble the relation obtained by us earlier [7]. Our results likewise do not argue for the velocity saturation mechanism proposed in [16].

Thus, we have obtained new data supporting the earlier model of the spin structure transformation of a domain wall in the initial interval of its motion within the velocity saturation region. It has also been shown that the available theory does not provide a correct explanation for the domain wall motion in the velocity saturation region in the presence of a transverse magnetic field.

ACKNOWLEDGMENTS

REFERENCES

1. G. J. Zimmer, L. Gal, and F. B. Humphrey, AIP Conf. Proc. **29**, 85 (1976).

2. G. P. Vella-Coleiro, IEEE Trans. Magn. **13** (5), 1163 (1977).

3. A. M. Balbashov, P. I. Nabokin, A. Ya. Chervonenkis, and A. P. Cherkasov, Fiz. Tverd. Tela (Leningrad) **19** (6), 1881 (1977) [Sov. Phys. Solid State **19**, 1102 (1977)].

4. V. G. Kleparskiĭ and V. V. Randoshkin, Fiz. Tverd. Tela (Leningrad) **21** (2), 416 (1979) [Sov. Phys. Solid State **21**, 247 (1979)].

5. A. G. Shishkov, V. V. Grishachev, E. N. Il'icheva, and Yu. N. Fedyunin, Fiz. Tverd. Tela (Leningrad) **30** (8), 2257 (1988) [Sov. Phys. Solid State **30**, 1303 (1988)].

6. F. H. de Leeuw, J. Appl. Phys. **45** (7), 3106 (1974).

7. V. A. Bokov, V. V. Volkov, A. Maziewski, *et al.*, Fiz. Tverd. Tela (St. Petersburg) **37** (10), 2966 (1995) [Phys. Solid State **37**, 1636 (1995)].

8. V. A. Bokov, V. V. Volkov, N. L. Petrichenko, and M. Maryško, Fiz. Tverd. Tela (St. Petersburg) **39** (7), 1253 (1997) [Phys. Solid State **39**, 1112 (1997)].

9. A. Stankiewicz, A. Maziewski, B. A. Ivanov, and K. A. Safaryan, IEEE Trans. Magn. **30** (2), 878 (1994).

10. A. P. Malozemoff and J. C. Slonczewski, *Magnetic Domain Walls in Bubble Materials* (Academic, New York, 1979), p. 326.

11. T. J. Gallagher and F. B. Humphrey, J. Appl. Phys. **50** (11), 7093 (1979).

12. J. Zebrowski and A. Sukiennicki, J. Appl. Phys. **52** (6), 4176 (1981).

13. A. Sukiennicki and R. A. Kosinski, J. Magn. Magn. Mater. **129** (2/3), 213 (1994).

14. B. Barbara, J. Magnin, and H. Jouve, Appl. Phys. Lett. **31** (2), 133 (1977).

15. S. E. Yurchenko and M. A. Rozenblat, Pis'ma Zh. Tekh. Fiz. **4** (22), 1370 (1978) [Sov. Tech. Phys. Lett. **4**, 552 (1978)].

16. B. A. Ivanov and N. E. Kulagin, Zh. Éksp. Teor. Fiz. **112** (3), 953 (1997) [JETP **85**, 516 (1997)].

17. F. H. de Leeuw, IEEE Trans. Magn. **13** (5), 1172 (1977).

18. V. V. Randoshkin and M. V. Logunov, Fiz. Tverd. Tela (St. Petersburg) **36** (12), 3498 (1994) [Phys. Solid State **36**, 1858 (1994)].

19. K. Vural and F. B. Humphrey, J. Appl. Phys. **50** (5), 3583 (1979).

20. V. V. Volkov, V. A. Bokov, and V. I. Karpovich, Fiz. Tverd. Tela (Leningrad) **24** (8), 2318 (1982) [Sov. Phys. Solid State **24**, 1315 (1982)].

Translated by G. Skrebtsov

MAGNETISM
AND FERROELECTRICITY

The Effect of Off-Center Cu²⁺ Ions on the Phase Transition in Lead Germanate Crystals

M. P. Trubitsyn and V. G. Pozdeev

Dnepropetrovsk State University, pr. Gagarina 72, Dnepropetrovsk 10, 320625 Ukraine
e-mail: trub@ff.dsu.dp.ua
Received March 30, 2000

Abstract—The properties of $Pb_5Ge_3O_{11}$: Cu^{2+} crystals near the temperature of the ferroelectric phase transition are discussed in terms of a phenomenological approach. Assuming a quadratic interaction with the order parameter, the effect of Cu^{2+} is considered a result of static distortions, which result from the off-center position of the copper impurity ions in the lead germanate structure. In this approximation, Cu^{2+} jumps between off-center positions do not affect the dynamic properties of the crystal matrix near T_C. © 2000 MAIK "Nauka/Interperiodica".

1. INTRODUCTION

In recent years, extensive studies have been devoted to phase transitions in real crystal structures containing defects of various types. At the same time, many experimental works whose results are explained as being due to structural imperfections were performed on nominally defect-free crystals. The lack of direct data on the nature and concentration of defect centers makes the proposed interpretation seem unreliable.

The aim of this work was to investigate the dielectric properties and to elucidate the specific features of the phase transition in lead germanate crystals doped with copper ions. The transition in $Pb_5Ge_3O_{11}$ crystals from the high-temperature paraelectric phase (space group C_{3h}^1) to the ferroelectric phase (space group C_3^1) is observed at $T_C = 451$ K and is accompanied by spontaneous polarization along the trigonal polar axis **c** [1–3]. Analysis of the EPR spectra of Cu^{2+} ions showed that impurity ions replace Pb^{2+} ions in the trigonal positions of the $Pb_5Ge_3O_{11}$ structure and occupy three off-center sites in the (**ab**) plane perpendicular to the polar axis [4, 5]. The investigation of the EPR averaging effects and the relaxation maxima in the temperature dependence of the dielectric losses allowed the authors of [5] to infer that thermally activated Cu^{2+} jumps occur between the off-center positions and to determine the activation energy and the natural frequency of the impurity dynamics involved.

Obviously, $Pb_5Ge_3O_{11}$: Cu^{2+} is a promising subject in discussing the role of specific defects, such as off-center impurity ions in crystals with phase transitions. This is supported by the following arguments. First, the results obtained in [4, 5] provide deep insight into the microscopic properties of the Cu^{2+} impurity centers in the crystal structure. Second, lead germanate is a uniaxial ferroelectric, which justifies the applicability of the

mean field approximation within a broad vicinity of T_C. Therefore, we can attempt to reveal the main features of the phase transition in $Pb_5Ge_3O_{11}$: Cu^{2+} at a phenomenological level [6, 7]. Third, we had at our disposal $Pb_5Ge_3O_{11}$ single crystals (nominally pure) with different contents of the Cu^{2+} impurity, namely, 0.1, 0.2, and 0.5 wt %.

2. PERMITTIVITY OF $Pb_5Ge_3O_{11}$: Cu^{2+} CRYSTALS NEAR THE PHASE TRANSITION

In order to obtain information on the effect of off-center copper ions on the properties of lead germanate near the phase transition, we measured the permittivity of the crystals. The results of these measurements are presented in Fig. 1. It is seen that the introduction of a copper impurity leads to a shift of the transition point toward lower temperatures and to a broadening of the ε anomaly. The concentration-induced lowering of T_C indicates that the copper ions are "rigid" defects which stabilize their symmetric environment when cooled below the transition temperature of the ideal structure [8]. The broadening of the thermodynamic anomalies upon the introduction of different impurities is a fairly general phenomenon, which can be associated with a nonuniform distribution of defects over the crystal matrix [7]. To quantify the concentration dependence of the dielectric properties, the experimental data were fitted within the range from $T_C + 5$ K to $T_C + 40$ K by the Curie–Weiss relation $\varepsilon^{-1} = C_{C-W}^{-1}(T - T_C)$. Figure 2 shows the dependence of the displacement of the phase transition temperature, $\Delta T_C = T_C (N = 0) - T_C (N)$, on the dopant content N. The Curie–Weiss constant is practically independent of the copper content and, for all the crystals studied, follows the relation $C_{C-W} = (1.21 \pm 0.02) \times 10^4$ K.

3. PHENOMENOLOGICAL DESCRIPTION OF THE PHASE TRANSITION IN Pb$_5$Ge$_3$O$_{11}$: Cu^{2+}

Let us consider the interval around the transition point for which the approximation of noninteracting defects is valid. In order to relate the state of the system to the microscopic characteristics of Cu^{2+}, we represent the density of the thermodynamic potential $\bar{\phi}$ for a crystal with defects as the sum of the contribution $\phi(\eta)$ from cells with a perfect structure, the contribution ϕ_D from defect cells, and the binding energy ϕ_C for the order parameter η and defects.

In the crystals under study, the Curie–Weiss relation is satisfied and the introduction of Cu^{2+} ions does not result in noticeable changes in the $\varepsilon^{-1}(T)$ dependence (Fig. 1). Therefore, we can neglect the spatial inhomogeneity of the order parameter and represent the $\phi(\eta)$ potential of undistorted cells in the form of the conventional Landau expansion

$$\phi(\eta) = \phi_0 + \frac{1}{2}A\eta^2 + \frac{1}{4}B\eta^4, \qquad (1)$$

where $A = A_0(T - T_C)$, $A_0, B > 0$.

Writing the contribution ϕ_D of defect cells in the exact form would require knowledge of the microscopic reasons for the off-center behavior. However, recalling that Cu^{2+} occupies three off-center positions in the plane perpendicular to the polar axis **c**, we attempt to model the potential relief ϕ_D by going over in the (**ab**) plane to polar coordinates with the origin at the trigonal site of the substituted ion, $x = u\cos\psi$, $y = u\sin\psi$. Taking into account the above notation, the contribution of one defect cell to the thermodynamic potential can be written as

$$\phi_D(u, \psi) = -\frac{1}{2}\alpha u^2 \cos 3\psi + \frac{1}{4}\beta u^4, \qquad (2)$$

where $\alpha, \beta > 0$. The function ϕ_D has a maximum at the trigonal lattice site ($u = 0$). At the angles $\psi_{i0} = 2(i-1)\pi/3$ ($i = 1, 2, 3$), the ϕ_D potential has three minima, which correspond to the equilibrium value of the off-center displacement $u_0 = (\alpha/\beta)^{1/2}$. Information on the relative magnitude of the coefficients in expansion (2) can be obtained from [5], according to which the height of the barrier separating the off-center positions is $W = \alpha^2/(4\beta) \sim 0.24$ eV. In the vicinity of the phase transition, the frequency of the Cu^{2+} jumps between the off-center positions, $\tau^{-1}(T_C) \sim 10^9$–10^{10} Hz [5], considerably exceeds the measuring frequency (1 kHz, Fig. 1). The inclusion of the local dynamics of defect ions results in the time dependence of the polar angle ψ in expansion (2).

Now, we determine the type of interaction between the order parameter η and the coordinates (u, ψ) of the impurity defects. We recall that the off-center position
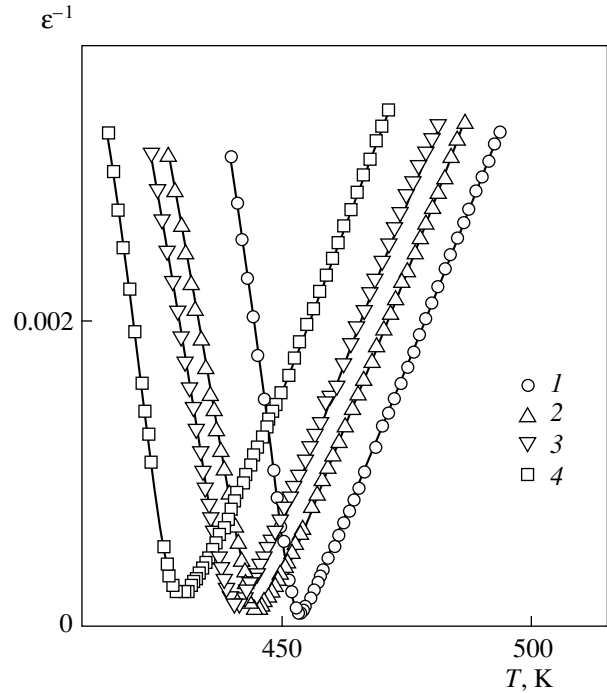

ε^{-1}

Fig. 1, Temperature dependence of the reciprocal permittivity ε^{-1} in the range of the phase transition in Pb$_5$Ge$_3$O$_{11}$ crystals: (*1*) undoped samples and samples doped by (*2*) 0.1, (*3*) 0.2, and (*4*) 0.5 wt % Cu^{2+}. The measurements are made along the polar axis **c** at the frequency $f = 1$ kHz.

of Cu^{2+} in the (**ab**) plane does not violate the mirror plane, which maps $(+\eta)$ into $(-\eta)$. It is obvious that the symmetry of the order parameter contains the axis $C_3 \| \mathbf{c}$, which maps the impurity ion from one off-center position into another. Hence, the interaction energy ϕ_C should be an even function of η and u. According to the symmetry of the lead germanate paraphase and the arrangement of the off-center positions, the lowest order interaction invariant has the form $\eta^2 u^2$. It is essential that this interaction not contain the polar angle ψ and, hence, not depend on the local dynamics of the copper centers.

Taking into account Eqs. (1) and (2) and the type of interaction involved, the density of the thermodynamic potential of a crystal with defects can be written as

$$\bar{\phi}(\eta, u_0) = \phi(\eta) + N\phi_D(u_0, \psi) + N\phi_C(\eta, u_0)$$

$$= \tilde{\phi}_0 + \frac{1}{2}\tilde{A}\eta^2 + \frac{1}{4}B\eta^4. \qquad (3)$$

The last formulation (3) singles out the dependence of $\bar{\phi}$ on η and introduces the notation $\tilde{\phi} + \phi_0 + N\phi_D$ and $\tilde{A} = A + Ngu_0^2$, where $g > 0$ is the coupling parameter.

4. DISCUSSION OF THE RESULTS AND CONCLUSIONS

Consider the effect of the coupling with the order parameter on the state of an impurity ion. As follows from Eq. (3), below T_C, the magnitude of the off-center displacement and the height of the potential barrier separating the Cu^{2+} positions become temperature-dependent:

$$u_0 = \sqrt{\frac{\alpha}{\beta} - \frac{g}{\beta B}A_0(T_C - T)},$$

$$W \cong \frac{\alpha^2}{4\beta} - \frac{\alpha g}{2\beta B}A_0(T_C - T). \quad (4)$$

Expressions (4) show that the state of an impurity ion is sensitive to the static component of the order parameter. Taking into account that the frequency of hopping $(10^9 - 10^{10}$ Hz) between off-center positions near T_C is three orders of magnitude less than the Debye frequency $\Omega \sim 4 \times 10^{12}$ Hz [9], we can assume the effect of higher harmonics of η on the defect time scale to be averaged out to zero. Despite the temperature dependence $W(T)$ predicted by relationships (4), no noticeable changes in the activation energy within the range 100–400 K were observed [5]. Apparently, the error with which the activation energy was derived from the EPR and dielectric spectra in [5] is not exceeded in magnitude by the second term in expressions (4). Note that the binding energy $\phi_C = (1/2)g\eta^2 u_0^2$ in Eq. (3) does not depend on the polar angle ψ and is determined by the static coordinate u_0. In the approximation we are using, the relaxation dynamics of the impurity ions is unaffected by the coordinate of the order parameter η.
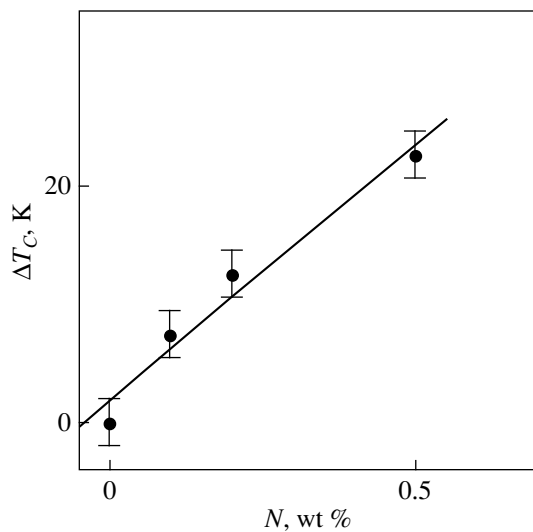

Fig. 2. Dependence of the displacement of the phase transition temperature on the Cu^{2+} content in $Pb_5Ge_3O_{11}$ (derived from dielectric measurements).

and all three minima of the potential of a defect cell remain equivalent.

Analysis of the properties of the crystal matrix makes it evident that the inclusion of the interaction with defects in Eq. (3) results in a renormalization of the expansion coefficient of η^2. The quadratic interaction with the order parameter gives grounds to classify the off-center Cu^{2+} impurity ions in lead germanate among defects of the random local transition temperature type [6, 7]. The displacement of the average phase-transition temperature T_C^D in a crystal containing defects with respect to the T_C point of an impurity-free crystal is proportional to the impurity concentration

$$\Delta T_C = T_C - T_C^D = N\frac{g}{A_0}u_0^2. \quad (5)$$

The influence of copper ions on the dynamic properties of the crystal matrix is limited to an increase in the soft-mode frequency. Defects of the type discussed here do not affect the soft mode damping, and local hopping cannot give rise to a dynamic central-peak component in scattering spectra [10, 11].

The concentration-induced displacement of the transition point ΔT_C (Fig. 2) exhibits a somewhat weaker dependence than predicted by Eq. (5). It should be stressed that the effect of Cu^{2+} ions on the phase transition in lead germanate is discussed here in terms of the copper-center model, which was proposed on the basis of radio spectroscopy data [4, 5]. The anisotropy in the EPR spectra of Cu^{2+} ions does not reveal any distortions along the polar axis which could produce components of a defect of the random-local-field type [6, 7]. Thus, there are no grounds to assume linear interaction between Cu^{2+} defect ions and the order parameter which would result in the features of the dynamic properties and a nonlinear dependence of T_C^D on the concentration N [7, 10–12]. The behavior of the experimental dependence $\Delta T_C(N)$ should be assigned to the scatter in the transition temperatures of the samples prepared from different lead germanate single crystals, which is seen in Fig. 2.

ACKNOWLEDGMENTS

The authors are grateful to V.N. Moiseenko for discussing the results.

REFERENCES

1. S. Nanamatsu, H. Sugiyama, K. Doi, and Y. J. Kondo, J. Phys. Soc. Jpn. **31** (2), 616 (1971).
2. M. I. Kay, R. E. Newnham, and R. W. Wolfe, Ferroelectrics **9**, 1 (1975).
3. A. A. Bush and Yu. N. Venevtsev, *Single Crystals with Ferroelectric and Related Properties in the Pb–O–GeO₂ System and Possible Fields of Their Applications* (NIITÉKhIM, Moscow, 1981).

4. V. A. Vazhenin, A. D. Gorlov, and A. I. Krotkiĭ, Preprint No. 10, IPM (Kiev, 1989), p. 5.

5. M. P. Trubitsyn, S. Waplak, and A. S. Ermakov, Fiz. Tverd. Tela (St. Petersburg) **42** (7), 1303 (2000) [Phys. Solid State **42**, 1341 (2000)].

6. A. P. Levanyuk and A. S. Sigov, Izv. Akad. Nauk SSSR, Ser. Fiz. **49** (2), 219 (1985).

7. A. P. Levanyuk and A. S. Sigov, *Defects and Structural Phase Transitions* (Gordon and Breach, New York, 1988).

8. A. D. Brause and R. A. Cowley, *Structural Phase Transitions* (Taylor and Francis, Philadelphia, 1981; Mir, Moscow, 1984).

9. A. M. Antonenko, Candidate's Dissertation in Mathematical Physics (Dnepropetr. Univ., Dnepropetrovsk, 1980).

10. B. I. Halperin and C. M. Varma, Phys. Rev. B **14** (9), 4030 (1976).

11. K. B. Lyons and P. A. Fleyru, Phys. Rev. B **17** (6), 2403 (1978).

12. B. E. Vugmeĭster and M. D. Glinchuk, Usp. Fiz. Nauk **146** (3), 459 (1985) [Sov. Phys. Usp. **28**, 589 (1985)].

Translated by G. Skrebtsov

Light-Induced Intrinsic Defects in PLZT Ceramics

V. V. Laguta, M. D. Glinchuk, A. M. Slipenyuk, and I. P. Bykov

Institute for Problems of Materials Sciences, National Academy of Sciences of Ukraine, Kiev, 03142 Ukraine;
e-mail: dep4@materials.kiev.ua

Abstract—This paper reports on an EPR study of a ferroelectric, 1.8/65/35, and an antiferroelectric, 2/95/5, of optically transparent $Pb_{1-y}La_yZr_{1-x}Ti_xO_3$ (PLZT) ceramics within a broad temperature range (20–300 K) after illumination at a wavelength of 365–725 nm. Illumination with ultraviolet light, whose photon energy corresponds to the band gap of these materials, at $T < 50$ K creates a number of photoinduced centers: Ti^{3+}, Pb^+, and Pb^{3+}. It is shown that these centers are generated near a lanthanum impurity, which substitutes for both the Pb^{2+} and, partially, Ti^{4+} ions through carrier trapping from the conduction or valence band into lattice sites. The temperature ranges of the stability of these centers are measured, and the position of their local energy levels in the band gap is determined. The most shallow center is Ti^{3+}, with its energy level lying 47 meV below the conduction band bottom. The Pb^{3+} and Pb^+ centers produce deeper local levels and remain stable in the 2/95/5 PLZT ceramics up to room temperature. The migration of localized carriers is studied for both ceramic compositions. It is demonstrated that, under exposure to increased temperature or red light, the electrons ionized into the conduction band from Ti^{3+} are retrapped by the deeper Pb^+ centers, thus hampering the carrier drift in the band and the onset of photoconduction. The part played by localized charges in the electrooptic phenomena occurring in the PLZT ceramics is discussed. © 2000 MAIK "Nauka/Interperiodica".

1. INTRODUCTION

The optically transparent ceramic PLZT belongs to solid solutions of the $PbTiO_3$ ferroelectric and $PbZrO_3$ antiferroelectric doped lightly by La. The introduction of lanthanum into $PbZr_{1-x}Ti_xO_3$ not only increases the density of the hot-pressed ceramic to 99.5%, thus making it optically homogeneous and transparent, but also substantially changes its electrical properties. For instance, at lanthanum concentrations above 8% the permittivity of the 65/35 composition exhibits a noticeable frequency dispersion characteristic of the relaxor systems [1, 2]. A decrease in the grain size and the fragmentation of polar domains upon introduction of La result in a decrease in the coercive field. On the other hand, the fraction of regions adjacent to the domain walls increases and the strength of the nonuniform internal electric fields induced by different-type crystal lattice imperfections, as well as by carriers trapped in defects, also increases substantially. As a result, such a medium becomes extremely sensitive even to weak external factors capable of changing the local electric polarization.

One of these important external factors, which can effectively influence the electric polarization, is optical irradiation. It is the effect of optically induced change in the polar state that underlies many promising applications of the PLZT ceramics. It is intuitively clear that this phenomenon can be associated, in particular, with photocarrier localization at local levels, which entails the creation of regions with a locally uncompensated space charge. This localized carrier usually produces a paramagnetic center, and EPR is the most appropriate method of probing these centers.

Despite the obvious importance of studying photoinduced intrinsic defects, relevant information is scarce. In particular, only two centers, namely, Pb^{3+} and Ti^{3+}, in PLZT of the 7/65/35 and 8/65/35 compositions have been identified to date (see [3–5]). The temperature stability of these centers was studied in our earlier work [5]. However, many issues related to these and to a number of other centers remain unclear.

In this work, we continued the study of light-induced defects in the PLZT ceramics of two different compositions (1.8/65/35 and 2/95/5). In particular, an analysis of the spectrum near the g-factor of 2.0 permitted the isolation of EPR lines belonging to a new electron-type Pb^+ center. It was shown that at an elevated temperature or upon exposure to red light, the electrons ionized from Ti^{3+}, rather than annihilating with the holes, are retrapped by the deeper-lying Pb^+ centers. The positions of the Pb^+, Pb^{3+}, and Ti^{3+} energy levels were determined by deriving the temperature dependence of the probability of localized-carrier thermal ionization from the EPR spectra. A mechanism of photocarrier localization in the PLZT ceramics is proposed, and the role of the localized carriers in the electrooptic phenomena characteristic of this type of the ferroelectric ceramics is discussed.
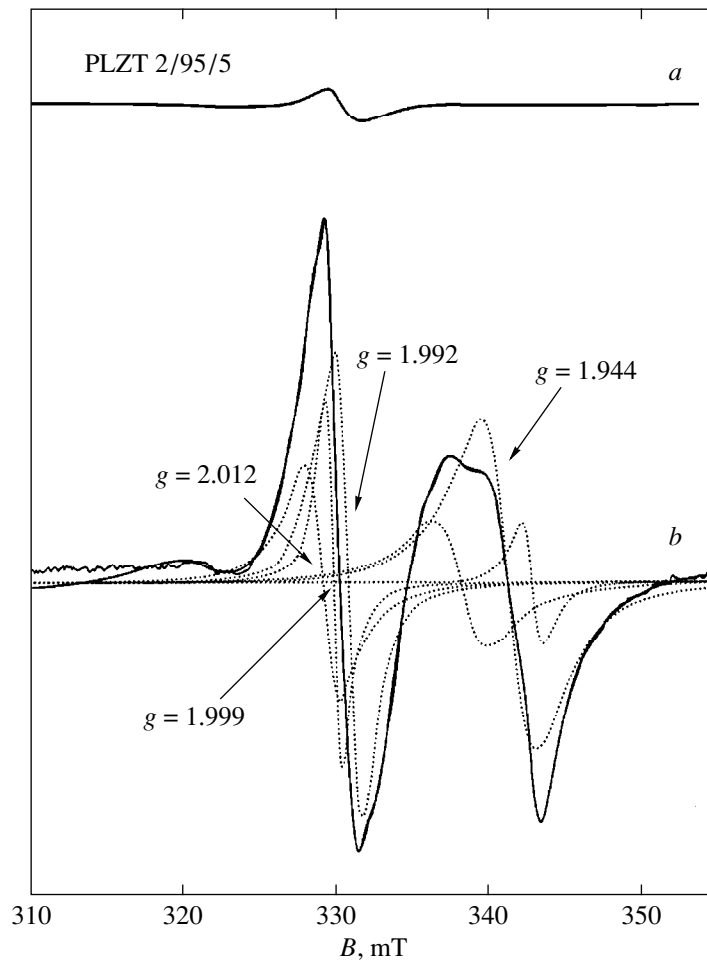
Fig. 1. EPR spectrum of the 2/95/5 PLZT ceramics at $T = 20$ K (*a*) before and (*b*) after UV irradiation (365 nm).

2. EXPERIMENTAL TECHNIQUE

The studies were performed on samples of optically transparent $Pb_{1-y}La_yZr_{1-x}Ti_xO_3$ ceramics ($y/1 - x/x$) of two compositions, 1.8/65/35 and 2/95/5, which were prepared by the standard two-stage hot-pressing method [6]. The samples were obtained in the form of platelets ($4 \times 2 \times 0.5$ mm in size) with carefully polished surfaces. The EPR spectra were recorded on an *X*-band spectrometer with an ESR-9 Oxford temperature-control attachment in the temperature range from 20 to 300 K. The samples were irradiated directly in a spectrometer cavity with a high-pressure mercury lamp at $T = 20$ or 290 K through narrow-passband color filters at wavelengths of 365, 405, 436, 579, 675, and 725 nm. When studying the effect of low-temperature annealing ($100 < T < 155$ K) on EPR spectra, the sample heated to a fixed temperature after irradiation at $T = 20$ K was allowed to stand for a preset time (usually, 1–40 min) and was cooled rapidly to the temperature $T = 20$ K at which the EPR spectrum was measured.

3. EXPERIMENTAL DATA

3.1. EPR spectra. Low-temperature ($T = 20$ K) EPR spectra of the 2/95/5 PLZT ceramics before optical irradiation revealed a very weak line with a *g*-factor close to that of a free electron ($g \approx 2$), whereas the 1.8/65/35 sample did not exhibit an EPR spectrum at all (Figs. 1a, 2a). At room temperature, no EPR spectra were observed for any of the samples studied.

After the irradiation has carried out at $T = 20$ K with UV light, whose energy is approximately equal to the band gap (3.4 eV), both samples exhibited photoinduced EPR spectra, which are displayed in Figs. 1b and 2b for the 2/95/5 and 1.8/65/35 compositions, respectively. The spectra were resolved into individual lines belonging to different paramagnetic centers by using the Peak Fit program. The curves thus obtained are indicated by dotted lines in Figs. 1b and 2b. This deconvolution of the spectra into its components was accomplished with the use of their temperature dependences, because different centers were stable within different temperature ranges. Computer processing yielded exact values of the *g*-factors of the individual lines.
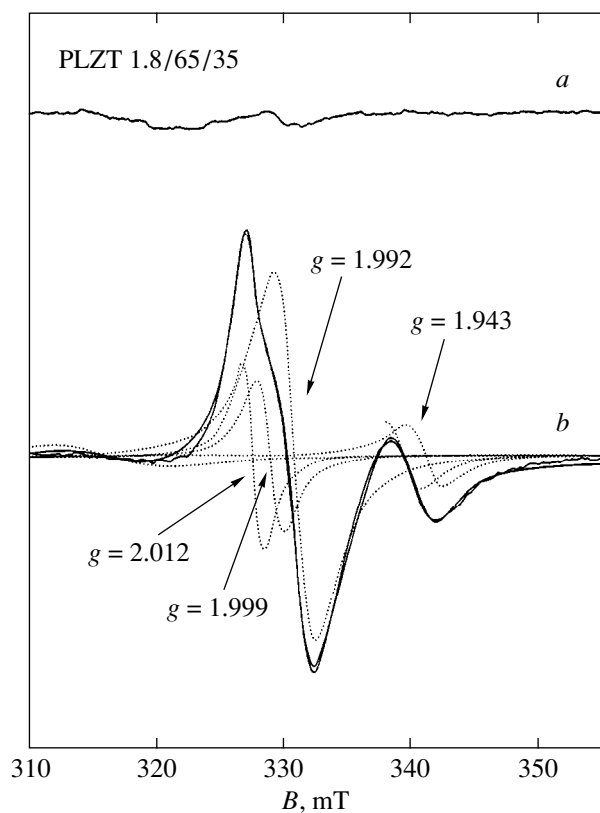
Fig. 2. EPR spectrum of the 1.8/65/35 PLZT ceramics at $T = 20$ K (*a*) before and (*b*) after UV irradiation (365 nm).
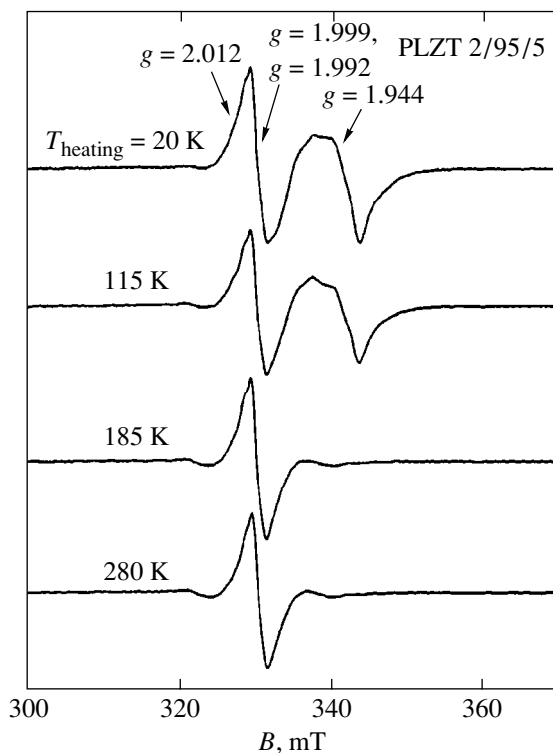

Fig. 3. Temperature dependence of photoinduced EPR spectra of the 2/95/5 PLZT ceramics.

As follows from the analysis, the spectra of both ceramic compositions consist of two groups of lines with approximately equal *g*-factors, $g \approx 2$ and 1.94. The EPR line with an average *g*-factor of 1.934 was observed earlier in both the PLZT and PZT ceramics and assigned to the titanium ion Ti^{3+} $(3d^1)$ [3, 4]. The spectrum with an average *g*-factor of 1.94 can also be attributed to the titanium ion, and its complex shape is due to the *g*-factor anisotropy. Besides the titanium spectrum, the 1.8/65/35 PLZT ceramics exhibited an EPR line with a *g*-factor of 2.015. This line was assigned to an *F*-center [5]. For both ceramic compositions, our analysis also revealed a line with a similar *g*-factor of 2.012, but its intensity in the 1.8/65/35 ferroelectric ceramics is about ten times higher than that in the 2/95/5 antiferroelectric sample. In this study, we identified it as belonging to the Ni^{3+} ion $(3d^7)$.

We believe the spectral lines lying close to $g = 2.00$ to be of the greatest interest. One of them can be assigned to the Pb^{3+} center with $g = 1.995$ described in [3, 4], and the slight difference in the magnitudes of the *g*-factor can be accounted for by a more precise calculation resulting from line separation. The second line ($g = 1.992$) isolated by the EPR spectrum deconvolution is observed for the first time in the PLZT ceramics and can be attributed to the thermally more stable Pb^+ center, because it was observed up to room temperature.

As is seen from Figs. 1 and 2, the intensities of the spectral lines with the same *g*-factors observed in different ceramic compositions differ substantially. For the 1.8/65/35 sample, the strongest lines are those with $g = 2.012$ and 1.992. The Ti^{3+} line ($g = 1.94$) is the weakest for this ceramics. For the 2/95/5 sample, the strongest lines are the Ti^{3+} spectrum and the line with $g = 1.992$.

3.2. Effect of the annealing temperature on the photoinduced spectra. The effect of the annealing temperature on the light-induced EPR spectra were studied in the temperature range from 20 to 280 K. The results obtained are presented in Figs. 3 and 4 for the 2/95/5 and 1.8/65/35 ceramic compositions, respectively. It is seen that the Ti^{3+} spectral intensity ($g = 1.94$) is maximum at low temperatures (20–70 K) for both ceramics. As the temperature increases, the intensity decreases, and the spectrum becomes practically unobservable above $T = 180$ K.

The line with $g = 2.012$ is observed up to $T \sim 190$ K for both ceramics. However, as can be seen from the temperature dependence (Fig. 4), its intensity first increases with an increase in temperature, reaches a maximum at $T \approx 130$ K, and then decreases very strongly as the temperature increases. For instance, even an increase in the temperature to 160 K results in a decrease in the intensity of this line to about one-fourth its level at $T = 130$ K.

The photoinduced centers belonging to lead ions, $g = 1.999$ and 1.992, whose spectra were observed up to room temperature, $T \sim 290$ K, are the most thermally stable centers. However, keeping the samples for a few days at 300 K brings about the "erasure" of all EPR spectra induced by UV light.

3.3. Effect of incident photon energy. The effect of the incident photon energy on the behavior of the EPR spectra was studied in two ways. In the first case, the samples were irradiated directly in the spectrometer cavity at $T = 20$ or 290 K with color filters transmitting at different wavelengths. In the second case, the samples were irradiated successively at $T = 20$ or 290 K by UV light (365 nm) and light of a preset wavelength. At both temperatures, an increase in the light wavelength resulted in a decrease in the intensity of all photoinduced spectra. Irradiation with red light at a wavelength of 546–579 nm after UV exposure completely eliminated all the spectra induced by the UV light.

Figures 5 and 6 illustrate the results obtained by successively illuminating (at $T = 20$ K by UV light and light at a wavelength of 405–725 nm) the 2/95/5 and 1.8/65/35 ceramic compositions, respectively. It is seen that an increase in the wavelength to 405 nm reduces the intensity of all EPR lines for both ceramics. A further increase in the wavelength to 546 nm brings about the total disappearance of the photoinduced spectra to leave only a weak single line with $g \approx 2$. However, illumination with UV and light with $\lambda = 675$ nm induces new intense EPR spectra in both samples. As the wavelength increases still more to 725 nm, the intensity of these EPR lines increases. The spectra induced in both ceramic samples closely resemble one another. They consist of two strong lines with similar g-factors of ≈ 1.99, two hyperfine lines, about four times weaker, and a high-field line (546 mT, $g = 1.23$). One should also point out that the separation between the hyperfine lines in the 1.8/65/35 PLZT sample is larger than that between the same lines in the 2/95/5 PLZT composition, which can be due to the difference in the crystal structure of the different-type ceramics. These lines are also present in the complex spectra displayed in Figs. 1 and 2. As was already mentioned, one of them ($g = 1.999$) most likely belongs to the Pb^{3+} center. Indeed, the observation of a hyperfine transition in the ^{207}Pb isotope in high fields ($B = 546$ mT) confirms the nature of this center. We believe that the second spectrum ($g = 1.992$) and the two satellite lines should be assigned to the Pb^+ ($6p^1$) center. A good resolution of the hyperfine lines permits a fairly accurate calculation of their relative integrated intensity, which amounts to 22% of the total spectral intensity and, thus, confirms that they belong to the ^{207}Pb isotope ($I = 1/2$; natural abundance, 22.8%). The observed negative deviation of the g-factor ($g - g_e < 0$) is in agreement with the crystal-field theory prediction for the $6p^1$ configuration. In this
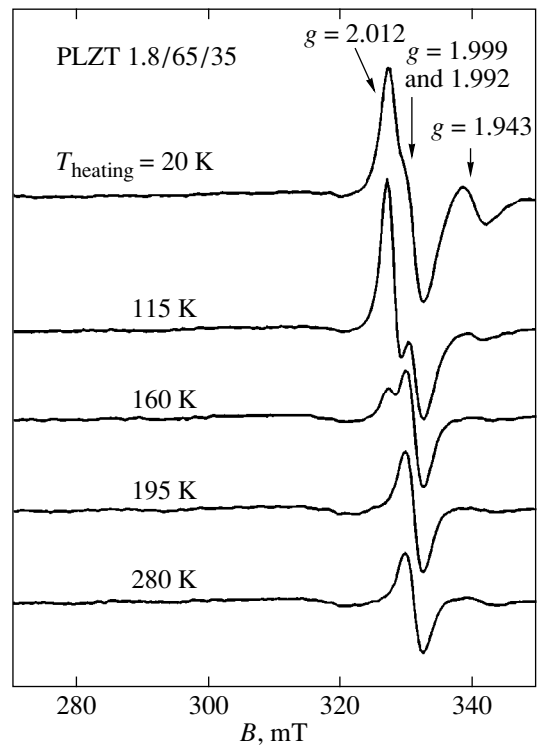

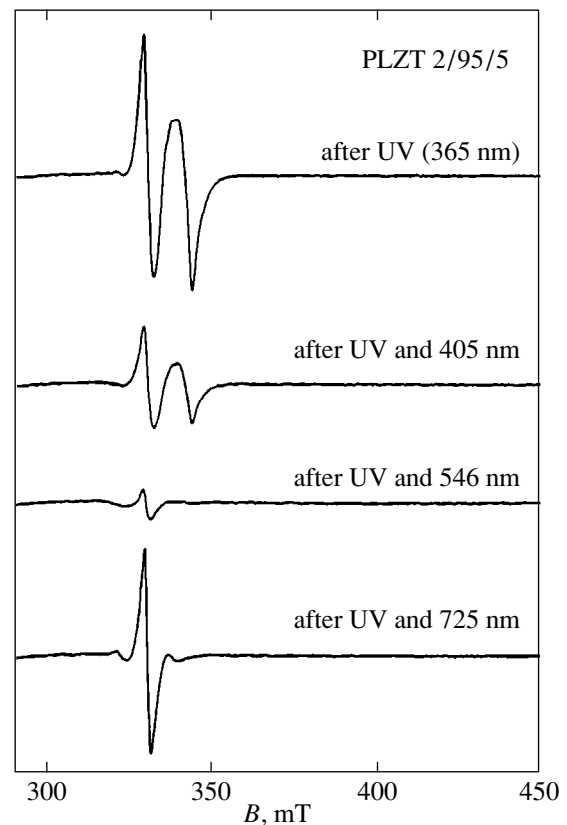**Fig. 4.** Temperature dependence of the photoinduced EPR spectra of the 1.8/65/35 PLZT ceramics.

Fig. 5. Effect of the incident photon energy on the EPR spectra of the 2/95/5 PLZT ceramics.
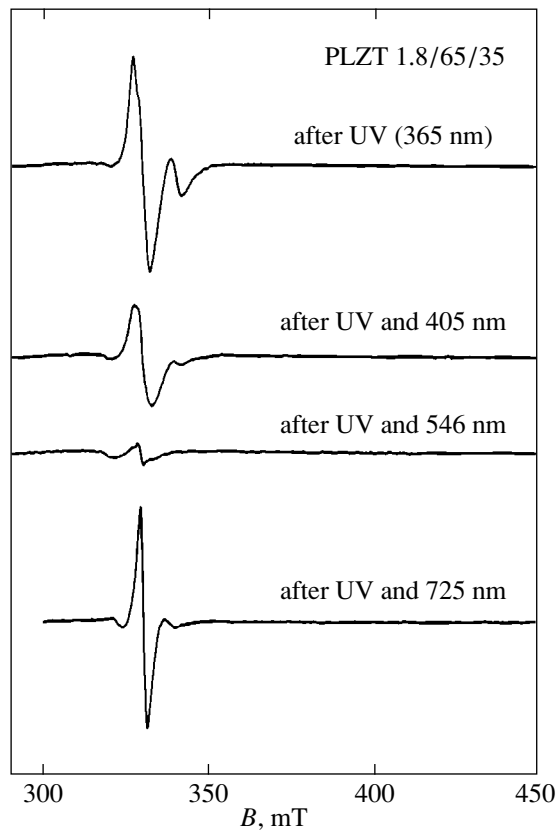
Fig. 6. Effect of the incident photon energy on the EPR spectra of the 1.8/65/35 PLZT ceramics.
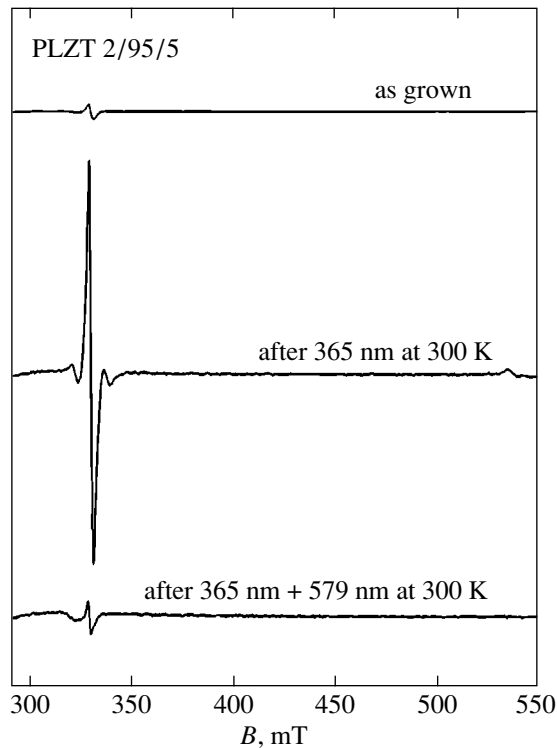

Fig. 7. Photoinduced EPR spectra of the 2/95/5 PLZT ceramics at room temperature.

approximation, the components of the g-factor can be written as [7]

$$g_\parallel = g_e; \quad g_\perp = g_e - 2\lambda/\delta,$$

where λ is the spin–orbit coupling constant, δ is the crystal-field splitting of energy levels of the ion, and g_e is the g-factor of a free electron. Hence, for a polycrystal, one can expect $g < g_e$. The average hyperfine splitting ($A = 0.018$ cm^{-1}) likewise lies within the range characteristic of the Pb$^+$ ion in other materials (see, e.g., [8]).

3.4. Optical illumination at $T = 290$ K. Before illumination at room temperature, no EPR spectra were observed on either of the samples. After UV irradiation at room temperature, the samples were held at this temperature for approximately 10–15 min, cooled to $T = 20$ K, and the EPR spectra were then measured. It was found that UV irradiation at $T = 290$ K induces an EPR spectrum only in the 2/95/5 PLZT sample (Fig. 7). It is readily seen that this spectrum is identical to that obtained under successive illumination by UV and red light at $T = 20$ K. Subsequent illumination by red light with $\lambda = 579$ nm at room temperature completely eliminates the EPR spectrum (Fig. 7).

4. IONIZATION ENERGY OF PHOTOINDUCED CENTERS IN PLZT

In order to determine the thermal ionization energies of the centers, we studied the effects of temperature and annealing time on the EPR spectra of the 1.8/65/35 ceramics. The measurements were carried out within the temperature range 96–155 K; the spectral intensities therein varied the most strongly. After illumination at $T = 20$ K, the sample was heated to a fixed temperature (T_i), allowed to stand at this temperature for 1–50 min, and cooled rapidly to $T = 20$ K, at which the EPR signal intensity (I) was measured. Within the temperature range in which thermal ionization of the centers started, the EPR signal intensity varied approximately exponentially:

$$I(T_i, t) = I_0 \exp(-P(T_i)t), \qquad (1)$$

where t is the heating time and $P(T)$ is the center ionization probability.

Relation (1) is valid for a simple ionization event of a local level, where carrier retrapping from the band can be neglected [9]. Such a behavior was characteristic of the Ti^{3+} center throughout the temperature range covered. The intensity of the other spectral lines varied nonmonotonically with an increase in the temperature and heating time. For instance, the signal intensity of the center with $g = 2.012$ first increased upon heating to $T \approx 130$ K and began to fall off exponentially with an increase in the heating time and temperature for $T > 130$ K. This behavior suggests that the electrons ionized from Ti^{3+}, rather than annihilating with holes, are

retrapped by deeper electron-type centers, namely, Pb^+ and the center with $g = 2.012$, thus increasing their concentration.

The numerical values of the ionization energies were derived from the expression relating the trap ionization probability to temperature [9]:

$$P(T) = N_e SV \exp(-E_a/kT), \qquad (2)$$

where E_a is the ionization energy; N_e is the effective density of states in the conduction or valence band; and V and S are the carrier thermal velocity and trapping cross-section, respectively. Neglecting the temperature dependence of S, the $N_e SV$ product can be approximately estimated as being proportional to T^2. Therefore, the temperature dependence of the ionization probability $P(T)$ is primarily governed by the exponent in Eq. (2); hence, E_a can be readily determined from the slope of the $\ln P$ vs. $1/T$ plot.

The ionization energies calculated in this way for the 1.8/65/35 PLZT ceramics are given in the table. No similar measurements of the center ionization energies were performed for the 2/95/5 PLZT ceramics. However, it should be noted that, since the latter ceramic composition has a larger band gap ($E_g \approx 4$ eV), the E_a values should be, accordingly, larger. In fact, the lead centers (Pb^{3+} and Pb^+) in the 2/95/5 PLZT ceramics are thermally stable at room temperature as well.

5. DISCUSSION

Irradiation of the PLZT ceramics with light whose photon energy is approximately equal to the band gap creates, in the conduction and valence bands, a large number of electrons and holes, part of which can be trapped into local levels formed by various defects and impurities. Among these lattice defects can be included centers located near the La^{3+} impurity. A positively charged La^{3+} impurity (La^{3+} substitutes for Pb^{2+}) can be considered exclusively as a source of lattice strain rather than as a donor, because there is no indication that the electronic level of this ion can be localized in the band gap. Nevertheless, by displacing the neighboring ions in the lattice, such a defect acts as a local potential well for free electrons, which transfer to one of the free $3d^1$ orbitals of the nearest Ti^{3+} or to $6p^1$ Pb^+; this process is energetically favorable because of the possible Jahn–Teller pseudoeffect [10, 11]. This mechanism of electron localization is realized also in La^{3+}- and Y^{3+}-doped $PbWO_4$ crystals, where the W^{5+}–La^{3+} and W^{5+}–Y^{3+} centers were convincingly identified from the observation of hyperfine lines due to the ^{139}La and ^{89}Y isotopes [11].

The second electron-type center identified by us, Pb^+, is deeper and more thermally stable than Ti^{3+}. It is this defect that should play an important part in photoinduced phenomena in the PLZT ceramics close to

EPR parameters and ionization energies of photoinduced defects in the 1.8/65/35 PLZT ceramics

Center	g-factor	E, eV
Ti^{3+}	1.934	0.047(9)
Pb^{3+}	1.999	0.117(6)
Pb^+	1.992	0.262(9)
$Ni^{3+}(?)$	2.011	0.078(9)

room temperatures. The mechanism of electron localization on the Pb^{3+} ion is apparently similar to that considered above for the Ti^{4+} site. It is well known [12] that the $6p$ lead states in lead-containing oxides, together with the nd states of a B-type ion, form the conduction band bottom; therefore, in such lattice-defect sites, a photoelectron can become localized also on the $6p^1$ lead-ion orbital to form the Pb^+ paramagnetic center.

In contrast to the Pb^+ and Ti^{3+} centers, Pb^{3+} ($6s$) is an acceptor center. Its local electronic level lies above the valence band top by approximately 0.12 eV. The localization of holes at lead ions can be associated with La^{3+} ions occupying the Ti^{4+} sites. This La^{3+} substitution appears fully probable already at impurity concentrations above 1%, so that the lead vacancies alone would not be able to compensate the excess positive charge introduced by a trivalent ion into the lattice.

Obviously, the Pb^{3+} and Pb^+ pair of centers plays a considerably larger part in the PLZT ceramics than could be expected from the Pb^{3+} and Ti^{3+} centers. Remaining thermally stable up to room temperature, both lead centers should appreciably affect the formation of a locally uncompensated space charge created in the ceramic under UV irradiation. The observed effect of optical annihilation of the Pb^+ and Pb^{3+} centers under illumination with red light that we discovered favors the disappearance of the space charge. The same effect is observed in samples heated above room temperature when thermal ionization of carriers from the Pb^{3+} and Pb^+ centers becomes intense.

Thus, the conditions in which lead centers form and are destroyed are similar in many respects to those under which, in particular, the recording and erasure of optical (holographic) information in PLZT take place. We hope that the photoinduced phenomena, observed and studied by us, will provide new insight into the complex physical processes underlying practical application of the optically transparent PLZT ceramics.

REFERENCES

1. Qi Tan and D. Viehland, Phys. Rev. B **53**, 14 103 (1996).
2. M. El. Marssi, R. Farhi, J.-L. Dellis, *et al.*, J. Appl. Phys. **83**, 5371 (1998).

3. W. L. Warren, C. H. Seager, D. Dimos, and E. J. Friebele, Appl. Phys. Lett. **61**, 2530 (1992).

4. W. L. Warren, B. A. Tuttle, P. J. McWhorter, *et al.*, Appl. Phys. Lett. **62**, 482 (1993).

5. Yu. L. Maksimenko, M. D. Glinchuk, and I. P. Bykov, Fiz. Tverd. Tela (St. Petersburg) **39**, 1833 (1997) [Phys. Solid State **39**, 1638 (1997)].

6. V. I. Dimza, A. A. Sprogich, A. E. Kapenleks, *et al.*, Ferroelectrics **90**, 45 (1989).

7. J. E. Wertz and J. R. Bolton, *Electronic Spin Resonance: Elementary Theory and Practical Applications* (McGraw-Hill, New York, 1972; Mir, Moscow, 1975).

8. I. Heynderickx, E. Goovaerts, S. V. Nistor, and D. Schoemaker, Phys. Status Solidi B **136**, 69 (1986).

9. R. Bude, *Photoconductivity of Solids* (Wiley, New York, 1960).

10. M. D. Glinchuk, R. O. Kuzian, V. V. Laguta, and I. P. Bykov, in *Defects and Surface-Induced Effects in Advanced Perovskites*, Ed. by G. Borstel *et al.* (Kluwer, Dordrecht, 2000), p. 367.

11. A. Hofstraetter, H. Alves, M. Bhom, *et al.*, Radiat. Eff. Defects Solids (2000) (in press).

12. Y. Zhang, N. A. W. Holzwarth, and R. T. Williams, Phys. Rev. B **57**, 12738 (1998).

Translated by G. Skrebtsov

LATTICE DYNAMICS
AND PHASE TRANSITIONS

Isotopic Effect in Brillouin Light-Scattering Spectra of a $Cs_5H_3(SO_4)_4 \cdot xH_2O$ Crystal

S. G. Lushnikov*, A. I. Fedoseev*, and L. A. Shuvalov**

* Ioffe Physicotechnical Institute, Russian Academy of Sciences, Politekhnicheskaya ul. 26, St. Petersburg, 194021 Russia
** Shubnikov Institute of Crystallography, Russian Academy of Sciences, Leninskiĭ pr. 59, Moscow, 117333 Russia
e-mail: Sergey.Lushnikov@shuvpop.ioffe.rssi.ru
Received March 29, 2000

Abstract—A Brillouin scattering study of the behavior of hypersonic longitudinal acoustic phonons in crystalline pentacesium trihydrogen tetrasulfate $Cs_5H_3(SO_4)_4 \cdot xH_2O$ (PCHS) and its deuterated analog $Cs_5D_3(SO_4)_4 \cdot xD_2O$ (DPCHS) at temperatures ranging from 420 to 120 K is reported. The effect of deuteration on the crystal lattice dynamics is investigated. The differences in the behavior of hypersonic acoustic phonons in the PCHS and DPCHS crystals suggest the existence of a hydrogen isotope effect in both the high- and low-temperature phases. A possible model of the isotopic effect in the high-temperature phase is discussed. An analysis is made of the acoustic response of the PCHS and DPCHS crystals in the region of the transition to the glasslike phase. © 2000 MAIK "Nauka/Interperiodica".

1. INTRODUCTION

$Cs_5H_3(SO_4)_4 \cdot xH_2O$ (PCHS) crystals belong to a new class of compounds of the general formula $Me_zH_y(AO_4)_{(z+y)/2} \cdot H_2O$, where Me = Cs, Rb, and NH_4 and A = S and Se [1]. The high-temperature phase of these crystals is characterized by a dynamically disordered hydrogen-bond network, which provides a high protonic conductivity called superprotonic conductivity [2, 3]. Experiments have demonstrated that protons play a dominant role in the crystal lattice dynamics of these compounds. The strong hydrogen isotope effect observed in a number of compounds of the $Me HAO_4$ or $Me_3H(AO_4)_2$ type manifests itself in the form of additional phases and structural phase transitions and has been studied extensively using various methods (see, e.g., [4–6]).

The effect of deuteration on the lattice dynamics of PCHS crystals above room temperature was discussed in [7]. These studies were later extended to the low-temperature range by using elastic and inelastic neutron scattering techniques [8]. At room temperature, the PCHS crystals have a hexagonal structure with the space symmetry $P6_3/mmc$ ($a = 6.2455$ Å, $c = 29.690$ Å, $V = 1003$ Å^3, and $Z = 2$) [9]. Extremely interesting structural changes occur in the vicinity of $T_{c1} = 414$ K and $T_{c2} = 360$ K. At T_{c1}, a superprotonic phase transition involving a change in symmetry, $P6/mmm \longleftrightarrow P6_3/mmc$, takes place [9–11], and at T_{c2}, an isostructural phase transition associated with a change in the local symmetry of the SO_4 tetrahedral complexes is observed [10, 12]. A decrease in temperature results in the hydrogen-bond network transferring from a dynamic to a

static disorder (both orientational and positional), and in the vicinity of $T_g = 260$ K, a transition to the proton-glass phase is realized [13]. The crystal symmetry remains unchanged down to liquid-helium temperatures [9]. Neutron diffraction measurements showed that the hexagonal-cell parameters of the deuterated compound $Cs_5D_3(SO_4)_4 \cdot xD_2O$ (DPCHS) differ slightly from those of the protonated species ($a_h = 6.2412(9)$ Å, $c_h = 29.6561(8)$ Å, $V = 1000.5$ Å^3, and $Z = 2$ [7]). Investigations of compounds differing in isotope composition, such as the diamond crystals ^{12}C and ^{13}C [14], have revealed a sensitivity of the elastic properties to these substitutions and the efficiency of using, in these cases, the Brillouin light scattering (BS).

This paper reports an BS study of the effect of deuteration on lattice dynamics of the PCHS crystal.

2. EXPERIMENTAL TECHNIQUE

Colorless PCHS and DPCHS single crystals were grown by slow evaporation from a supersaturated aqueous solution at room temperature. The DPCHS crystals underwent double recrystallization in heavy water. This resulted in a ~60% deuteration of the samples used in our experiments. The samples thus obtained were plate-shaped crystals with their face coinciding with the basal plane and with characteristic hexagonal faceting. A number of rectangular parallelepipeds with one face perpendicular to the hexagonal axis c_h were cut from the plates belonging to the same growth lot. The normals to the other two faces were arbitrarily oriented in the basal plane. The parallelepipeds polished to optical

quality measured $5 \times 5 \times 3.5$ mm. The crystals were oriented with a polarizing microscope.

We studied the temperature behavior of longitudinal hypersonic (LA) phonons in PCHS and DPCHS crystals with $\mathbf{q}_{ph} \parallel \mathbf{c}_h$ and $\mathbf{q}_{ph} \perp \mathbf{c}_h$ ($\mathbf{q}_{ph}$ is the wavevector of the acoustic phonon). The scattering spectra were excited by a Spectra Physics single-mode argon laser operating at wavelength $\lambda = 488$ nm. The radiation power did not exceed 50 mW. Check experiments carried out at a lower power showed that laser-beam heating of the crystal can be neglected. Scattering was studied in a 180° geometry. The scattered light was analyzed by a three-pass piezoscanning Fabry–Perot interferometer with a Burleigh DAS-1 system providing automatic signal accumulation and adjustment of the interferometer plane-mirror parallelism, thus permitting one to maintain the instrument finesse at the level $C = 50$. To improve the accuracy of measuring the shift of the BS components (ν) and their half-width (δ is the half-width at half-maximum), the interferometer free spectral range was varied from 11 to 14 GHz. This made it possible to observe the BS components in PCHS and DPCHS in the second order with respect to the undisplaced Rayleigh line, which substantially reduced the experimental error. In order to decrease the noticeable contribution of light scattering at the unshifted frequency to the BS spectra, the Rayleigh line was cut out for the time of scanning by a system of color filters. Conversely, in order to increase the intensity of the signal with the DAS-1 system, the period of scanning the channels corresponding to the BS components was increased by 99 times.

It should be noted that the study of the temperature behavior of hypersound in the PCHS crystal has an upper limit at $T_{c2} = 360$ K, because the acoustic phonon attenuation drastically increased as this temperature was approached. At the same time, the background due to the increasing contribution of quasi-elastic light scattering to the BS spectrum substantially increased in intensity, which was observed in [10, 11]. In this connection, in order to improve the accuracy of measurements on the PCHS crystal, studies above room temperature were performed on a Burleigh five-pass piezoscanning Fabry–Perot interferometer. This permitted us to closely approach the T_{c2} temperature.

The starting point in all the temperature measurements was room temperature ($T_r = 294$ K). Each temperature cycle was run on a new crystal sample, thus ensuring an identical prehistory for all the single crystals used in our experiments.

Measurements in the low-temperature range (294–120 K) were performed with an optical cryostat in which the sample was cooled by a nitrogen vapor flow. The temperature decreased slowly and continuously. Between the measurements, the cooling rate was 0.5 K min⁻¹. In the course of measurement, its value

did not exceed 0.05 K min⁻¹. The sample temperature was monitored to within ±0.1 K by two copper–constantan thermocouples attached to the sample. Thus, the error in the determination of the measurement temperature was no more than 0.5 K. An optical furnace fabricated at the laboratory was used in the measurements performed at 294–420 K. The temperature control system employed provided slow and uninterrupted sample heating. Between the measurements, the heating rate was 0.5 K min⁻¹. During the measurements, its value was 0.05 K min⁻¹ and decreased near the phase transitions to 0.02 K min⁻¹. The temperature was monitored to within ±0.1 K by a chromel–coppel thermocouple attached to the sample. The error in the determination of the measurement temperature did not exceed 0.5 K.

The velocity (V) and attenuation (α) of the longitudinal hypersonic phonons in a 180° scattering geometry were determined from the expressions

$$V = \nu\lambda/(2n), \qquad (1)$$

$$\alpha = 4\pi n\delta/(\nu\lambda), \qquad (2)$$

where n is the refractive index of the crystal. The value used in all calculations was $n = 1.51$ [15].

The experimental BS spectra were treated by the least-squares procedure. The Rayleigh component was approximated in the calculations by a Gaussian function, and the BS component, by a Voigt function. The Voigt function is actually a convolution of the Gaussian and Lorentz functions, which allows instrumental broadening to be adequately taken into account. In this way, one could bring the error in determination of the shift and of the spectral width of the BS component profile to a minimum. The results of the calculations exemplified in Fig. 1 demonstrate good agreement with the experiment throughout the temperature range covered.

In the analysis of our data, we found it convenient to use relative changes in the hypersound velocity. From Eq. (1), we obtain

$$\Delta V/V_0 = (V(T) - V_0)/V_0 \approx (\nu(T) - \nu_0)/\nu_0, \qquad (3)$$

where V_0 and ν_0 are the velocity and frequency shifts of the hypersonic phonon at $T_r = 294$ K, respectively. This temperature was chosen as the reference for matching the data, because, first, it was the starting point in all the measurements and, second, it is appropriately equally distant from both the low-temperature glasslike transition and the high-temperature phase transitions at $T_{c2} = 360$ K and $T_{c1} = 414$ K. The sign of the approximate equality in relationship (3) means that we did not include the possible temperature dependence of the refractive index in our calculations. In this case, the error in the measurements is fully determined by the experimental error in measuring the frequency shift of the BS components. In our experiments, it did not
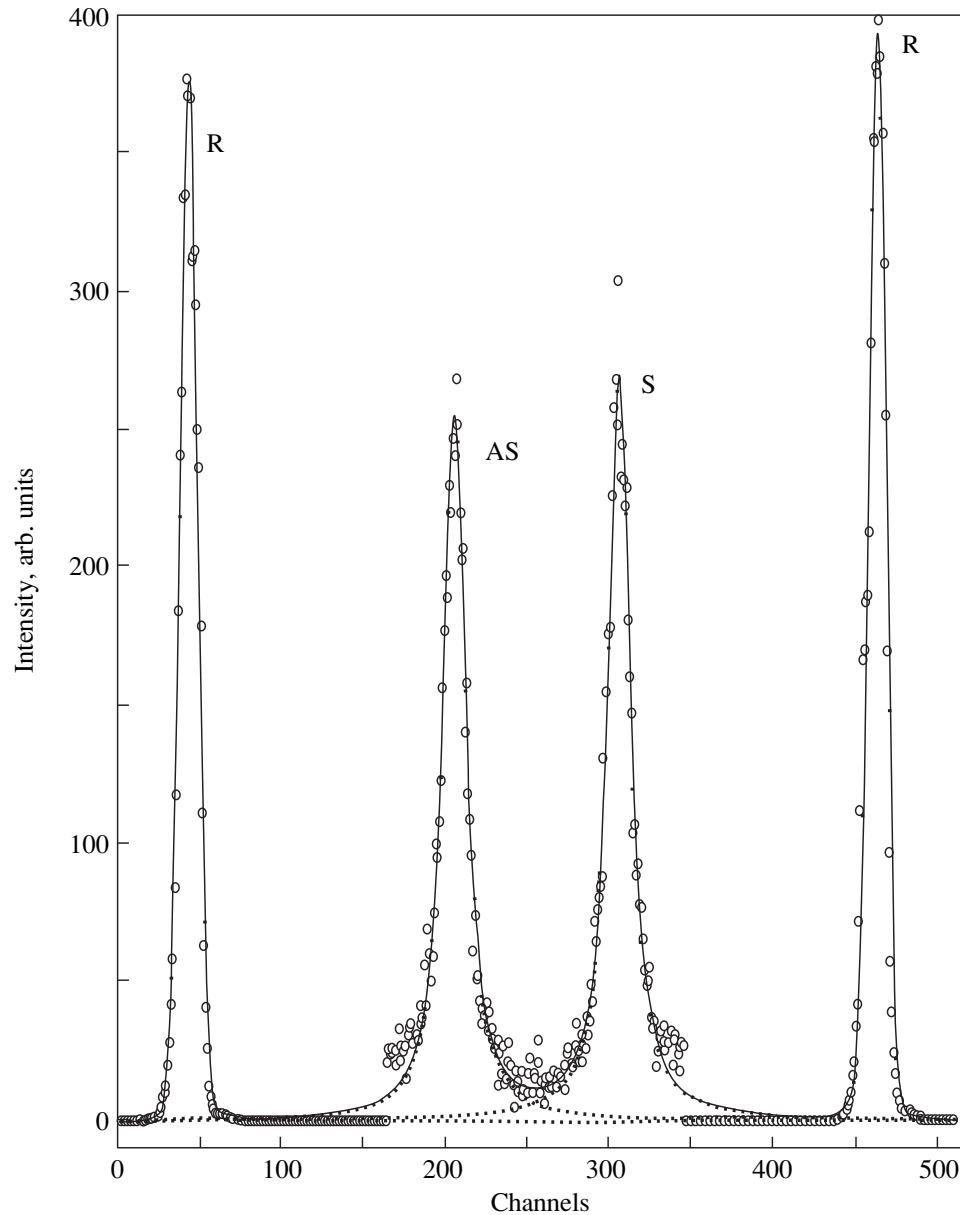
Fig. 1. BS from LA phonons with $\mathbf{q}_{ph} \parallel$ (001) in a PCHS crystal. Interferometer free spectral range, 12.375 GHz, $T = 299$ K. R is the Rayleigh component of the spectrum and AS and S are the anti-Stokes and Stokes scattering components, respectively. Open circles identify the experimental points, dotted lines display deconvolution of the experimental spectrum using the extrapolation functions discussed in the text, and the solid line is the result of fitting.

exceed 0.5%. The true half-width of the BS components (δ) was calculated as the difference between the experimentally observed half-widths of the BS components (δ_M) and the Rayleigh line (δ_0): $\delta_M - \delta_0$. In this case, the error in determining the attenuation α in Eq. (2) is primarily governed by the error in determining δ_M, which, in our experiments, did not exceed 10%. The magnitude of this quantity is ~0.04 GHz at room temperature and increases to 0.13 GHz in the vicinity of the high-temperature phase transitions as the hypersound attenuation increases.

3. RESULTS AND DISCUSSION

The velocity of longitudinal acoustic phonons propagating along a sixfold axis in a crystal of hexagonal symmetry (measured in a 180° scattering geometry) is given by the relationship $\rho V^2 = C_{33}$. In the basal plane, all directions of the propagation of the longitudinal acoustic phonons are equivalent and the velocity is determined by the expression $\rho V^2 = C_{11}$ [16]. In these expressions, C_{11} and C_{33} are the components of the elastic modulus and $\rho = 3.51 \times 10^3$ kg m^{-3} is the density
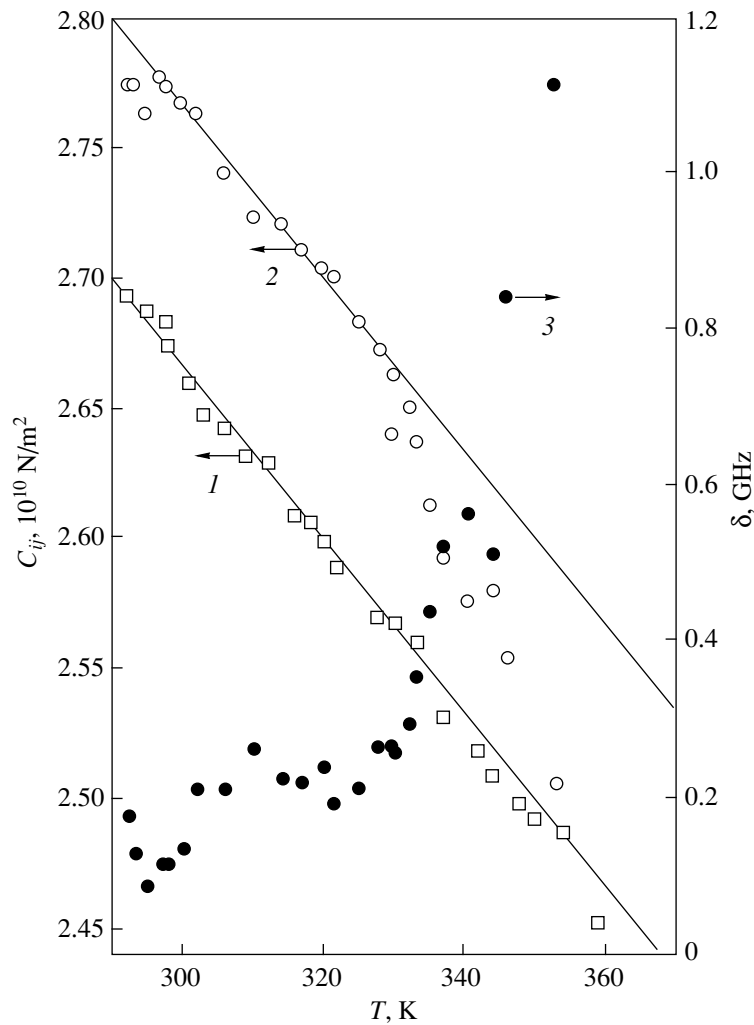
Fig. 2. Temperature evolution of the elastic moduli (*1*) C_{33} and (*2*) C_{11} and (*3*) the corresponding change in the attenuation of the hypersonic LA phonon with $\mathbf{q}_{ph} \parallel (100)$.

of the crystal taken from [9]. Thus, the temperature dependences of the shift of the BS components obtained in the experiment are directly and unambiguously correlated with those of the corresponding elastic moduli of the crystals under study (Fig. 2). The values of C_{11} and C_{33} for the DPCHS and PCHS crystals are different, which implies the existence of an isotopic effect. However, our major goal was to elucidate how deuteration affects the PCHS lattice dynamics, rather than to determine the magnitude of the elastic moduli in the deuterated and protonated compounds. Therefore, our attention was focused primarily on the relative variations in the velocity and the attenuation of hypersonic acoustic phonons.

Figures 3a and 4a present relative changes in the velocity of the hypersonic LA phonons with $\mathbf{q}_{ph} \perp \mathbf{c}_h$ and $\mathbf{q}_{ph} \parallel \mathbf{c}_h$. It is readily seen that while matching at room temperature, these quantities diverge in both the

high- and low-temperature phases. This prompted us to study these portions of the temperature dependence of the hypersound velocity in greater detail.

3.1. Acoustic Anomalies in the Vicinity of the Isostructural Phase Transition

As is evident from Fig. 2, within the temperature range from 294 to 330 K, the temperature dependences of C_{11} and C_{33} exhibit the same behavior, which can be satisfactorily fitted by a linear function. As the temperature increases, the elastic moduli follow different courses. In fact, C_{11} abruptly decreases ("softens") and deviates from the linear dependence, whereas C_{33} departs from its previous direction of variation insignificantly (and likewise decreases). The "softening" of C_{11} is observed up to $T \approx 355$ K, where $C_{11} \approx C_{33}$. From the standpoint of crystal acoustics, the decrease in C_{11} to a
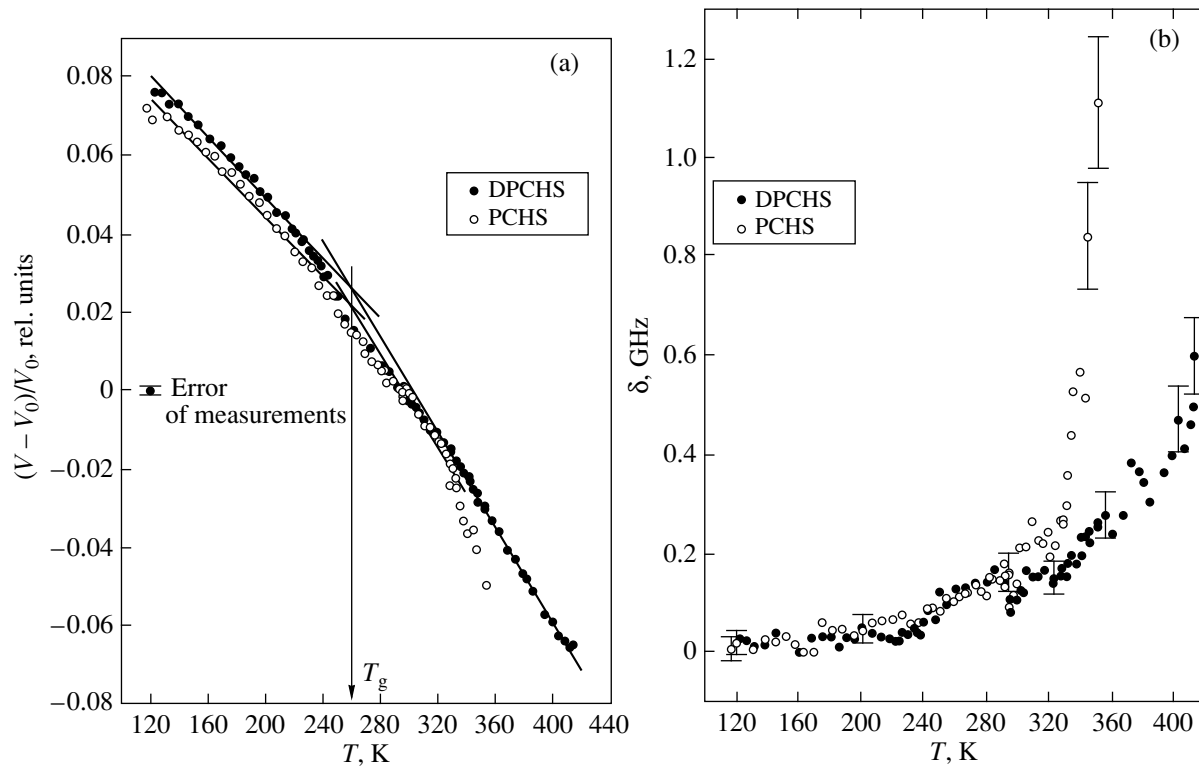
Fig. 3. (a) Temperature dependence of the relative variation in the velocity of the hypersonic LA phonon with $\mathbf{q}_{ph} \parallel (100)$ in the DPCHS and PCHS crystals. Straight lines show the fit of experimental data to a linear function. (b) Temperature dependences of the relative variation in the attenuation of the hypersonic LA phonon with $\mathbf{q}_{ph} \parallel (100)$ in the DPCHS and PCHS crystals. Note the considerable increase in the error of attenuation measurement in the protonated sample as the temperature approaches 360 K, which corresponds to an increase in the quasi-elastic scattering contribution to the BS spectra and a decrease in the accuracy of measurements (the same as in Fig. 4b).

value of C_{33} implies a change in the acoustic symmetry from hexagonal to "pseudocubic" [16]. This behavior of the elastic modulus C_{11} near T_{c2} is connected with a sharp increase in the attenuation of the hypersonic acoustic phonon propagating in the basal plane. The magnitude of this attenuation changes by a factor 2.5 at 355 K relative to its room-temperature value (Fig. 2) [17]. A comprehensive analysis of our results and the available data was performed in [12]. This analysis shows that an isostructural phase transition takes place in the PCHS crystal at T_{c2} within the $P6_3/mmc$ symmetry.

Similar BS experiments performed on a DPCHS crystal revealed no softening of the elastic modulus C_{11} in the vicinity of T_{c2}. This is clearly seen from Fig. 3a, where the relative changes in the velocity of the hypersonic phonons propagating in the basal plane differ for deuterated and protonated crystals in the high-temperature region. Note that longitudinal hypersonic phonons in the DPCHS crystal were clearly observed down to the superprotonic phase transition. The temperature behavior of the attenuation of the corresponding phonons near 360 K is likewise different (Fig. 3b). Unlike the PCHS crystals, the increase in the attenuation of the hypersonic LA phonons in the DPCHS crys-

tals is not accompanied by anomalies near 360 K. These results indicate that deuteration of the PCHS crystals leads to either suppression of the isostructural transition at T_{c2} or its shift to higher temperatures, i.e., to a substantial hydrogen isotope effect.

A possible explanation for the observed isotopic effect can be provided by the following model of the interaction of the transverse acoustic phonon with the pseudospin mode. Experiments on inelastic neutron scattering in the DPCHS crystal revealed a softening of the transverse acoustic (TA) phonon at the Brillouin zone edge with an increase in the temperature from 200 to 325 K [18]. The existence of a pseudospin mode in systems with hydrogen bonds is widely used in constructing different models of phase transitions [19]. It is possibly this mode that we observed in the neutron inelastic scattering experiments in DPCHS crystals on a triaxial spectrometer installed on the reactor at the Institute of Solid-State Physics in Budapest, Academy of Sciences of Hungary. Unfortunately, the resolution of the spectrometer employed was not sufficiently high and the dispersionless excitation at 0.8 meV was recorded without confidence. An excitation with similar parameters (and likewise not sufficiently reliable) was observed on a PRISMA inelastic scattering spec-
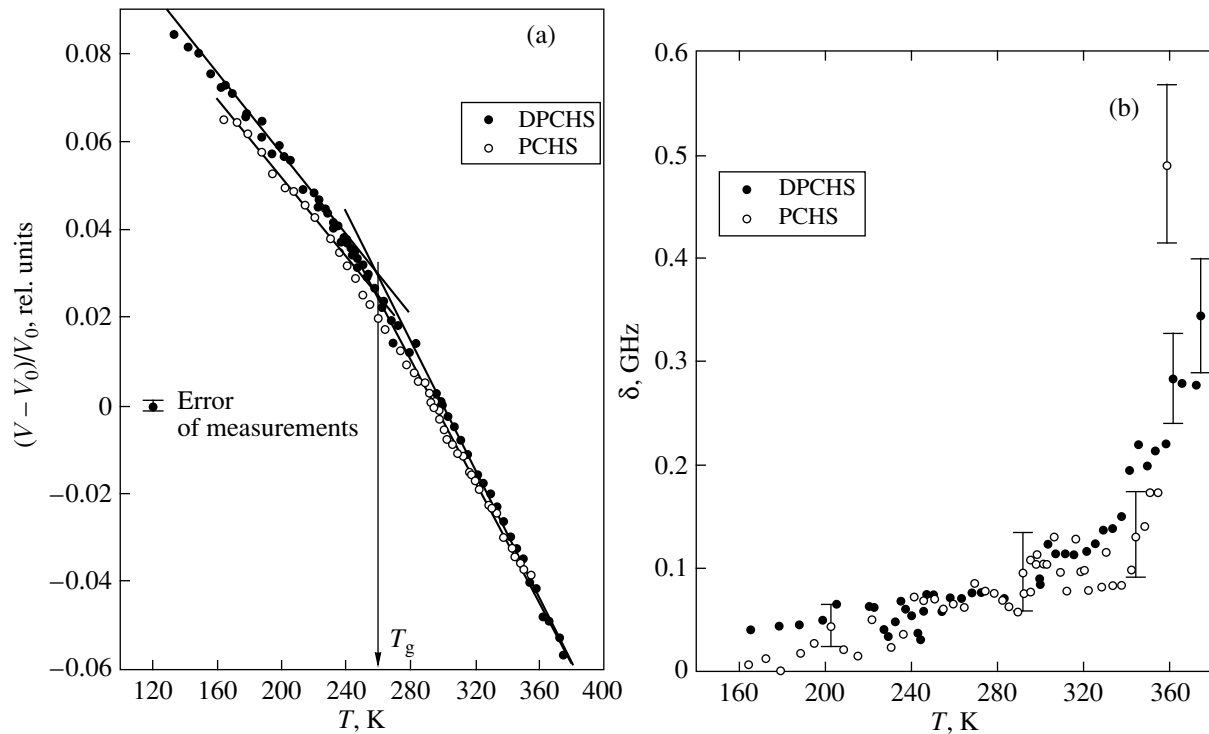
Fig. 4. (a) Temperature dependence of the relative variation in the velocity of the hypersonic LA phonon with $\mathbf{q}_{ph} \parallel (001)$ in the DPCHS and PCHS crystals. Straight lines show the fit of experimental data to a linear function. (b) Temperature dependences of the relative variation in the attenuation of the hypersonic LA phonon with $\mathbf{q}_{ph} \parallel (001)$ in the DPCHS and PCHS crystals.

trometer at the RAL (England). Nevertheless, we will assume a pseudospin mode exists (we are going to continue experimental studies in this direction). Thus, the pseudospin mode of the proton subsystem of the PCHS crystal at room temperature lies at a frequency of approximately 1.12 meV and does not interact with the TA phonon at the Brillouin zone edge whose frequency is 0.9 meV [18]. In these conditions, the PCHS crystal at approximately 360 K undergoes a phase transition induced by a softening of the TA phonon at the Brillouin zone edge. The situation changes in the case of the deuterated crystal: the pseudospin mode frequency decreases to 0.8 meV, and this turns out to be enough for the TA phonon to interact with the pseudospin mode at the Brillouin zone edge. As a result, no phase transition takes place at 360 K in the deuterated crystal DPCHS. This model should only be considered one of many possible explanations and it requires additional study.

3. 2. Transition to the Proton Glass Phase

A discussion of the behavior of hypersonic LA phonons in the PCHS and DPCHS crystals near the transition to the proton glass phase should be started from above room temperature. As is evident from Figs. 3a and 4a, within the range 330–290 K, the temperature behavior of the hypersound velocity in the crystals under study can be fitted by a linear function.

The temperature dependence starts to deviate from a straight line below 280 K, and a weak dispersion anomaly in the velocity appears near the transition to the glasslike state ($T_g = 260$ K). This anomaly is characteristic of phase transitions to a glasslike phase [20] and is more pronounced in the DPCHS crystal. As the temperature decreases still more, the experimental data can again be described by a linear temperature dependence, but with a smaller slope. It should be pointed out that the hypersound velocity recovers its linear behavior in PCHS at $T \approx 235$ K and in DPCHS at 215 K (Fig. 3a). Thus, the temperature range within which the velocity of the LA phonon propagating in the basal plane of the deuterated crystal exhibits an anomaly is 20 K greater than that of a pure protonated sample. A similar pattern is observed for the LA phonon with $\mathbf{q}_{ph} \parallel \mathbf{c}_h$ (Fig. 4a). Below 240 K, there is a difference between the corresponding relative changes in the hypersound velocity which is outside the limits of experimental error (Figs. 3a, 4a). Thus, in low-temperature measurements, at $T < T_g$, the BS spectra of the PCHS and DPCHS crystals also exhibit the isotopic effect.

As was already mentioned, the relative changes in the hypersound velocity can be approximated by a linear function, but different portions of the linear temperature dependence will have different slopes. If we extrapolate the linear approximation in the high- and low-temperature phases to the range of the transition to

the proton glass state, these conjectured temperature dependences of the hypersound velocity will intersect at $T \sim 260$ K (Figs. 3a, 4a). Note that this temperature point is the same for the protonated and the deuterated samples. It is quite possible that, upon thermal cycling, a broad anomaly in the hypersound velocity transforms into a kink in the linear temperature dependence. It is this effect that was observed in x-ray diffraction experiments: as a result of thermal cycling, the plateau in the temperature dependence of the cell parameters degenerated into a kink near the transition to the glasslike phase of the PCHS crystal [21]. The part played by the structural water should be mentioned. Baranov *et al.* [22, 23] particularly emphasized that its role in lattice dynamics should be taken into account. Thermal cycling apparently brings about the "evaporation" of the structural water and the formation of an orthorhombic phase below 220 K [21]. However, crystalline PCHS samples subjected to one thermal cycle revealed no noticeable changes in the phase composition either in x-ray diffraction measurements [21] or in neutron scattering experiments [8].

In studies of phase transitions to the structural glass phase, the maximum in attenuation is usually identified with the phase transition temperature (in doing this, one should not forget the strong frequency dependence of T_g). In our case, no substantial anomalies in the attenuation of the longitudinal hypersonic phonons under study were observed at $T < T_r$ (Figs. 3b, 4b). This is at variance with the results of ultrasonic measurements on PCHS, which revealed a broad anomaly in the attenuation with a maximum at $T \approx 240$ K [23–25]. Analysis of ultrasonic and dielectric data revealed a correlation between the attenuation anomaly and the high-frequency β relaxation at frequencies of the order of 10 MHz [23]. According to our calculations for the relaxation mechanism of acoustic phonon attenuation at hypersonic frequencies, the maximum shifts to a temperature of ~600 K. This is the reason why the maximum in the attenuation was not observed in our measurements.

Note that the acoustic anomalies exhibited a relaxation character in transitions to the superionic phase of some crystals, for instance, fluorites (PbF_2, SrF_2, etc.) [26], superionic glasses of the $(AgI)_x$–$(AG_2O–2B_2O_3)_{1-x}$ type [27], at glass transition temperatures in a number of polymers [28], and in transitions to the orientational glass state in the $K_xNa_{1-x}CN$ crystals [20]. The nature of these anomalies is the subject of considerable discussion in the literature: whether it stems from the distribution of the relaxation times or the distribution of the activation energies is of topical interest. We will return to this problem in greater detail in our next work dealing with the frequency dependence of the observed acoustic anomalies in crystals.

Thus, our studies of the Brillouin scattering in $Cs_5H_3(SO_4)_4 \cdot xH_2O$ and in its deuterated analog have shown that the behavior of the velocity of longitudinal hypersonic acoustic phonons depends substantially on deuteration.

The hydrogen isotope effect manifests itself in the high-temperature phase upon displacement or suppression of the isostructural phase transition near 360 K, as well as in the low-temperature range in the form of different temperature dependences of the hypersonic acoustic phonon velocity. The latter is apparently connected with the formation of a new phase of the $Cs_5H_3(SO_4)_4 \cdot xH_2O$ crystal at low temperatures, as reported in the paper dealing with neutron scattering in the above compounds [8].

REFERENCES

1. A. I. Baranov, O. A. Kabanov, B. V. Merinov, and L. A. Shuvalov, Ferroelectrics **127**, 257 (1992).

2. B. V. Merinov, A. I. Baranov, L. A. Shuvalov, and B. A. Maksimov, Kristallografiya **32** (1), 86 (1987) [Sov. Phys. Crystallogr. **32**, 47 (1987)].

3. D. Abramic, J. Dolinsek, R. Blinc, and L. A. Shuvalov, Phys. Rev. B **42** (1), 442 (1990).

4. T. Fukami and R. H. Chen, Phys. Status Solidi B **214**, 219 (1999).

5. M. Sumita, T. Osaka, and Y. Makita, J. Phys. Soc. Jpn. **51** (5), 1343 (1982).

6. M. H. Kuok, S. C. Ng, and D. J. Lockwood, Phys. Rev. B **51** (13), 8005 (1995).

7. S. G. Lushnikov, A. V. Belushkin, A. I. Beskrovnyi, *et al.*, Solid State Ionics **125**, 119 (1999).

8. S. G. Lushnikov, A. V. Belushkin, S. N. Gvassaliya, *et al.*, Physica B (Amsterdam) **276–278**, 483 (2000).

9. B. V. Merinov, A. I. Baranov, L. A. Shuvalov, *et al.*, Solid State Ionics **74**, 53 (1994).

10. Yu. I. Yuzyuk, V. P. Dmitriev, V. V. Loshkarev, *et al.*, Kristallografiya **39** (1), 70 (1994) [Crystallogr. Rep. **39**, 61 (1994)].

11. Yu. I. Yuzyuk, V. P. Dmitriev, V. V. Loshkarev, *et al.*, Ferroelectrics **167**, 53 (1995).

12. S. G. Lushnikov and L. A. Shuvalov, Kristallografiya **44** (4), 662 (1999) [Crystallogr. Rep. **44**, 615 (1999)].

13. A. I. Baranov, O. A. Kabanov, and L. A. Shuvalov, Pis'ma Zh. Éksp. Teor. Fiz. **58** (7), 542 (1993) [JETP Lett. **58**, 548 (1993)].

14. R. Vogelgesang, A. K. Ramdas, S. Rodríguez, *et al.*, Phys. Rev. B **54** (6), 3989 (1996).

15. F. Kadlec, Y. Yuzyuk, P. Simon, *et al.*, Ferroelectrics **176**, 179 (1996).

16. A. I. Fedorov, *The Theory of Elastic Waves in Anisotropic Media* (Nauka, Moscow, 1971).

17. S. G. Lushnikov, V. H. Schmidt, L. A. Shuvalov, and V. V. Dolbinina, Solid State Commun. **113**, 639 (2000).

18. A. V. Belushkin, M. Bull, C. Carlile, *et al.*, Physica B (Amsterdam) **241–243**, 484 (1997).

19. R. Blinc and B. Žekš, *Soft Modes in Ferroelectrics and Antiferroelectrics* (North-Holland, Amsterdam, 1974; Mir, Moscow, 1975).

20. Z. Hu, A. Wells, and C. W. Garland, Phys. Rev. B **44** (13), 6731 (1991).

21. B. V. Merinov, R. Melzer, R. E. Lechner, *et al.*, Solid State Ionics **97**, 161 (1997).

22. A. I. Baranov, V. V. Sinitsyn, V. Yu. Vinnichenko, *et al.*, Solid State Ionics **97**, 153 (1997).

23. A. I. Baranov, E. D. Yakuchkin, D. J. Jones, and J. Roziere, Solid State Ionics **125**, 99 (1999).

24. E. D. Yakushkin and A. I. Baranov, Fiz. Tverd. Tela (St. Petersburg) **39** (1), 89 (1997) [Phys. Solid State **39**, 77 (1997)].

25. R. Mizaras, V. Valevicius, V. Samulionis, *et al.*, Ferroelectrics **155**, 201 (1994).

26. C. R. A. Catlow, R. T. Harley, and W. Hayes, in *Lattice Dynamics*, Ed. by M. Balkanski (Flammarion Sciences, Paris, 1978), p. 547.

27. L. Borjesson, Phys. Rev. B **36** (9), 4600 (1987).

28. L. Comeiz, D. Fioretto, L. Verdin, and P. R. Rolla, J. Phys.: Condens. Matter **9**, 3973 (1997).

Translated by G. Skrebtsov

LATTICE DYNAMICS
AND PHASE TRANSITIONS

On the Theory of Phase Transformations
with a Nonuniform Nucleation Rate

N. V. Alekseechkin

Kharkov Institute of Physics and Technology, Ukrainian Scientific Center, Akademicheskaya ul. 1, Kharkov, 310108 Ukraine
e-mail: n.alex@kipt.kharkov.ua
Received April 3, 2000

Abstract—An expression for the phase volume fraction in a system with a nonuniform nucleation rate is derived by using the geometrical–probabilistic approach. Examples of such systems considered here are (1) a plane layer (with nucleation in the midplane) and random planes in space, (2) an infinitely long cylinder (with nucleation on the axis) and random lines in space, and (3) a sphere (with nucleation at the center) and nucleation at random points. In each case, an expression for the phase volume fraction is derived for the time-dependent rates of nucleation and growth. The equivalence of homogeneous nucleation and nucleation at points is established. © 2000 MAIK "Nauka/Interperiodica".

The kinetics of a phase transformation in an unbounded medium for the coordinate-independent nucleation rate $I(t)$ is described by the Kolmogorov expression [1] or the Johnson–Mehl–Avrami (JMA) formula [2, 3]

$$X(t) = 1 - \exp\left[-\int_0^t I(t')V(t', t)dt'\right], \quad (1)$$

where $V(t', t) = 4\pi/3R^3(t', t)$, $R(t', t) = \int_{t'}^t u(\tau)d\tau$, $u(t)$ is the nucleus growth rate, $R(t', t)$ is the radius at instant t of a nucleus appearing at the instant t', and $V(t', t)$ is its volume.

In this paper, expression (1) is generalized to the case when the nucleation rate depends on the position variable. For this purpose, the critical-region method used earlier by the author for calculating the volume fraction of competing phases [4] is employed. It should be noted that the concept of a critical region was introduced by Kolmogorov in [1], although no special term was used for this region [$V(t', t)$ is the volume of this region]. The result obtained by using Kolmogorov's approach can be formulated as follows: the probability that a random point O' of the system at instant t is in the untransformed volume is

$$Q(t) = \exp[-Y(t)], \quad Y(t) = \int_0^t I(t')V(t', t)dt'. \quad (2)$$

In other words, this is the probability that no center of the new phase appears in the critical region for point O'. For the sake of simplicity, we assume that nuclei have a spherical shape. Accordingly, the critical region is a sphere of radius $R(t', t)$ with the center at point O'. A generalization to other region shapes admissible in Kol-

mogorov's model presents no difficulty. In the case of a coordinate-dependent nucleation rate, expression (2) must be replaced by

$$Q(\mathbf{r}_0, t) = \exp[-Y(\mathbf{r}_0, t)], \quad (3)$$

where $\mathbf{r}_0$ is the radius vector of point O'.

The functions $Y(t)$ and $Y(\mathbf{r}_0, t)$, when calculated by the algorithm proposed in [1], can generally be expressed in terms of an integral over the critical region. For example, in the problem considered here, the function $Y(\mathbf{r}_0, t)$ must have the form

$$Y(\mathbf{r}_0, t) = \int_{t_0}^t dt' \int_{V(t', t)} I_{\mathbf{r}_0}(\mathbf{r}, t')d\mathbf{r}. \quad (4)$$

In the case of several competing phases [4], for the kth phase we have

$$Y_k(t) = \int_0^t dt' \int_0^{R_k(t', t)} I_k(t')q^{(k-1)}(t', r)(4\pi r^2)dr, \quad (5)$$

where $q^{(k-1)}(t', r)$ is the untransformed part of the critical region of the k phase [4].

In this sense, the form (2) of the function $Y(t)$ can be regarded as the simplest. Thus, Kolmogorov's method is a "differential" method with respect to the time variable, but an "integral" method with respect to the space coordinate. It is during the derivation of Eqs. (1)–(3) that a finite quantity, viz., the volume $V(t', t)$, is used from the very beginning.

The proposed method differs from the Kolmogorov approach in that it is a "differential" method in both the time and the space variables: the volume fraction is obtained by using the differential of the volume $V(t', t)$. As a result, the solution can be presented in the form of
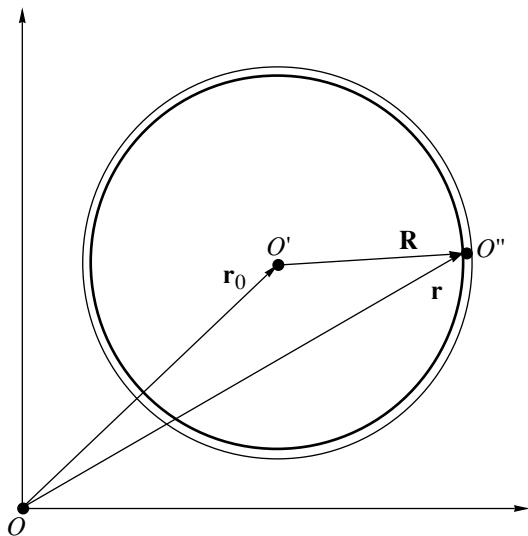
For the derivation of an expression for the volume fraction in the case of a coordinate-dependent nucleation rate.

an integral with respect to the time variables only, which is convenient for analysis of the dependences obtained [4]. Consequently, this approach is more effective in some cases. In particular, this advantage is manifested in the problem under consideration: in the case of a nonuniform nucleation rate, we must naturally operate with dV rather than with V.

In problems for which the difference between the two approaches is insignificant and the probabilistic analysis is similar to that in [1], the application of the result (3) obtained by using Kolmogorov's approach immediately leads to the solution (see Section 2).

The following two special cases of systems with a nonuniform nucleation rate are important for applications: (1) nucleation at various i-dimensional objects ($i < 3$), such as surfaces, lines, and points (the nucleation rate can be presented as a δ function of the coordinates), and (2) nucleation in a bounded volume G. The nucleation rate at a point $A(\mathbf{r})$ of the space has the form of a step function:

$$I(\mathbf{r}, t) = \begin{cases} I_0(\mathbf{r}_0, t), & A(\mathbf{r}) \in G \\ 0, & A(\mathbf{r}) \notin G, \end{cases}$$

the problem being simpler when I_0 is independent of $\mathbf{r}$.

The second case will be considered in a separate publication. In this paper, we analyze nucleation at the simplest i-dimensional objects, viz., planes, straight lines, and points. The article has the following structure. In Section 1, a general expression for the volume fraction is derived for a nonuniform nucleation rate. Expressions for the volume fractions of an infinitely large plane layer with nucleation at the midplane, of an infinite cylinder with nucleation at its axis, and of a sphere with nucleation at its center are derived in Sec-

tion 2. In Section 3, the problem of the calculation of the volume fraction is considered for nucleation at random planes, straight lines, and points distributed in an unbounded medium. The results obtained are discussed in Section 4.

1. THE VOLUME FRACTION OF A TRANSFORMED SUBSTANCE IN THE CASE OF A NONUNIFORM NUCLEATION RATE

We introduce a reference frame with the origin at point O (see figure). Let us determine the probability $dX(t)$ of a point $O'(\mathbf{r}_0)$ (randomly chosen in the system) being absorbed by the growing phase in the time interval $(t, t + dt)$. For this event to occur, it is necessary and sufficient that the following two conditions be met: (i) point O' must not be absorbed before the instant t and (ii) a center of the new phase that can absorb point O' during the time $(t, t + dt)$ (the critical center) appears at an instant t', $0 \le t' \le t$. Let $Q(\mathbf{r}_0, t)$ and $dY(\mathbf{r}_0, t)$ denote the probabilities of the first and second events, respectively. We consider the space–time diagram of the realization of the process in which both events occur.

We specify the spherical region of radius $R(t', t)$ with the center at point O' (the critical region). At the instant t', the boundary of the region moves to its center at a velocity $u(t')$ such that its radius decreases from the maximum value $R(0, t) \equiv R_m(t)$ to $R(t, t) = 0$. The fulfillment of condition (i) indicates that the emergence of centers of the new phase in the critical region is ruled out in the entire time interval $0 \le t' \le t$. In Kolmogorov's approach, the function $Q(t)$ is calculated directly from this condition. In the approach proposed here, condition (ii) is used for calculating this function.

The critical center emerging at the instant t' must be within the layer of thickness $dR(t', t) = (\partial R(t', t)/\partial t)dt$ at the distance $R(t', t)$ from the point O'. Let us suppose that it appears in the volume element $dV(\mathbf{r})$ in the vicinity of a certain point $O''(\mathbf{r})$ (see figure). This nucleation process is not of the Poisson type with respect to both t and $\mathbf{r}$ since the nucleation rate is a function of these variables; i.e., the steady-state condition is not satisfied [5]. However, we assume that the remaining two conditions of the Poisson process are satisfied: (a) the probability of the emergence of one center in a four-dimensional volume element $dt'dV(\mathbf{r})$ is equal to $I(\mathbf{r}, t')dt'dV(\mathbf{r})$, while the probability of the emergence of more than one center is an infinitely small quantity as compared to the former probability, and (b) the numbers of centers emerging in two nonintersecting volumes are independent random quantities. So, the probability of the emergence of a center in the neighborhood of point O'' is $I(\mathbf{r}, t')dt'dV(\mathbf{r})$, and in order to obtain the probability $dP(t', t)$ of the emergence of a critical center at instant t', we must integrate this expression over the boundary of the critical region. For this purpose, we introduce a spherical reference frame

with the origin at point O'. In this frame, point O'' has the coordinates $R(t', t)$, θ, ϕ, where $R(t', t) = |\mathbf{r} - \mathbf{r}_0|$). The volume element $dV(\mathbf{r})$ is equal to $dV(t', t)d\Omega/4\pi$, where $dV(t', t) = 4\pi R^2(t', t)dR(t', t)$ and $d\Omega = \sin\theta\, d\theta d\phi$ is a solid angle element. The nucleation rate in this reference frame has the form $I(\mathbf{r}, t') \equiv I_{\mathbf{r}_0}(\mathbf{R}, t') = I_{\mathbf{r}_0}(R(t', t), \theta, \phi; t')$ (the dependence of quantities on $\mathbf{r}_0$ is indicated by the corresponding subscript). We introduce the following notation:

$$J_{\mathbf{r}_0}(t', t) = \frac{1}{4\pi}\int_\Omega d\Omega I_{\mathbf{r}_0}(R(t', t), \theta, \phi; t'), \qquad (6)$$

where the integral is taken over the solid angle of the entire space. In this case, we obtain the following expression for the sought probability $dP(t', t)$:

$$dP_{\mathbf{r}_0}(t', t) = J_{\mathbf{r}_0}(t', t)dt'dV(t', t). \qquad (7)$$

The probability $dY_{\mathbf{r}_0}(t)$ of the emergence of a critical center in the interval $0 \leq t' \leq t$ is the integral of expression (7) with respect to t':

$$dY_{\mathbf{r}_0}(t) = \left\{\int_0^t dt' J_{\mathbf{r}_0}(t', t)\frac{\partial V(t', t)}{\partial t}\right\}dt. \qquad (8)$$

Thus, the simultaneous fulfillment of conditions (i) and (ii) leads to the following relation for $dX_{\mathbf{r}_0}(t)$:

$$dX_{\mathbf{r}_0}(t) = Q_{\mathbf{r}_0}(t)dY_{\mathbf{r}_0}(t). \qquad (9)$$

Since $X_{\mathbf{r}_0}(t) = 1 - Q_{\mathbf{r}_0}(t)$, expression (9) can be treated as a differential equation for $X_{\mathbf{r}_0}(t)$. Its solution for the initial condition $X_{\mathbf{r}_0}(t_0) = 0$ has the form

$$X_{\mathbf{r}_0}(t) = 1 - \exp[-Y_{\mathbf{r}_0}(t)],$$
$$Y_{\mathbf{r}_0}(t) = \int_{t_0}^t d\tau \int_0^\tau dt' J_{\mathbf{r}_0}(t', \tau)\frac{\partial V(t', \tau)}{\partial \tau}. \qquad (10)$$

The function $X_{\mathbf{r}_0}(t)$ is the probability that point O' will be absorbed by the growing phase by the instant t provided that it is located in the volume element $d\mathbf{r}_0$. The probability of the latter event is $d\mathbf{r}_0/V_0$, where V_0 is the volume of the system. The probability $X(t)$ that point O' at instant t is in the transformed part of the system is given by

$$X(t) = \frac{1}{V_0}\int_{V_0} X_{\mathbf{r}_0}(t)d\mathbf{r}_0, \qquad (11)$$

where the integral is taken over the system volume.

Expression (11) is the required volume fraction of the transformed substance in accordance with the geometrical definition of probability [5]. If the system is unbounded, expression (11) is treated as the limit for $V_0 \longrightarrow \infty$. However, it is significant that bounded systems are naturally covered by the definition (11) of the phase volume fraction. Thus, the expressions derived above can also be regarded as a generalization of formula (1) for the case of bounded systems. Even if the nucleation rate in such a system is independent of $\mathbf{r}$, the function $X_{\mathbf{r}_0}(t)$ is nevertheless a function of $\mathbf{r}_0$. The reason for this is that only a part of the critical region for point O' lies in the system in the general case. The size of this part depends on $\mathbf{r}_0$.

2. NUCLEATION ON A PLANE, STRAIGHT LINE, AND AT A POINT

We will use the indices s, l, and c for a plane, line, and point, respectively. Let the plane under investigation be the yz plane of the Cartesian system of coordinates, the straight line be the z axis, and the point be the origin (point O). The volume nucleation rate in each case can be presented in the form

$$I_v^{(i)}(\mathbf{r}, t) = \begin{cases} I_s(t)\delta(x), & i = s \\ I_l(t)\delta(x)\delta(y), & i = l \\ I_c(t)\delta(x)\delta(y)\delta(z), & i = c, \end{cases} \qquad (12)$$

where $I_i(t)$ ($i = s, l, c$) are the specific nucleation rates; I_s and I_l are the numbers of centers emerging per unit time per unit area and per unit length, respectively; and I_c is the probability of the emergence of a nucleating center at the point per unit time.

If the plane is at the middle of a layer of width $\varepsilon_s = 2L$, the straight line is the axis of a cylinder with the base area $\varepsilon_l = \pi L^2 \equiv s$, and the point is the center of a sphere of volume $\varepsilon_v = (4\pi/3)L^3 \equiv v$, then the average volume nucleation rate is

$$\bar{I}_v^{(i)}(t) = \varepsilon_i^{-1}\int_{\varepsilon_i} I_v^{(i)}(\mathbf{r}, t)d\varepsilon_i$$

or

$$\bar{I}_v^{(s)}(t) = \sigma I_s(t), \quad \bar{I}_v^{(l)}(t) = \lambda I_l(t),$$
$$\bar{I}_v^{(c)}(t) = n I_c(t), \qquad (13)$$

where $\sigma = (2L)^{-1}$ is the average area in a unit volume, $\lambda = s^{-1}$ is the average length in a unit volume, and $n = v^{-1}$ is the average number of points in a unit volume.

Without loss of generality, we take point O' on the x axis at a distance r_0 from the origin. For the angle θ in the spherical system of coordinates with the origin at point O', we take the angle formed by the vector $\mathbf{R}$ with the negative direction of the x axis. The angle ϕ lies in the yz plane. The components of the radius vector $\mathbf{r}$ in this system are as follows: $x = r_0 - R(t', t)\cos\theta$, $y = R(t', t)\sin\theta\sin\phi$, and $z = R(t', t)\sin\theta\cos\phi$. Substituting these values into Eq. (12) and following the computational algorithm described in Section 1, we obtain

the required result (see Appendix). However, we can obtain the result much more easily in this case by applying the critical-region method directly.

The critical region for point O' at instant t' is a sphere of radius $R(t', t)$. This sphere contains a part of the plane of area $S_{r_0}(t', t) = \pi[R^2(t', t) - r_0^2]$, or a part of the straight line of length $l_{r_0}(t', t) = 2[R^2(t', t) - r_0^2]^{1/2}$, or the point. We define the instant $t_m(t, r_0)$ through the equation

$$R(t_m, t) = r_0. \qquad (14)$$

For $t' > t_m$, the object under investigation is outside the critical region.

The necessary and sufficient condition for point O' to be in the untransformed region at instant t is that the center of the new phase does not appear in the time interval $0 \le t' \le t_m(t, r_0)$ on the area element $S_{r_0}(t', t)$, or on the segment of length $l_{r_0}(t', t)$, or at point O. The probability $Q_{r_0}^{(i)}(t)$ of this event can be calculated by the method developed in [1]; the result is obvious:

$$Q_{r_0}^{(i)}(t) = \exp\left[-\int_0^{t_m(t, r_0)} I_i(t')\zeta_{r_0}^{(i)}(t', t)dt'\right], \quad r_0 < R_m(t),$$

$$\zeta_{r_0}^{(i)}(t', t) = \begin{cases} S_{r_0}(t', t), & i = s \\ I_{r_0}(t', t), & i = l \\ 1, & i = c, \end{cases} \qquad (15)$$

$$Q_{r_0}^{(i)} = 1, \quad r_0 > R_m(t), \qquad (16)$$

since the object is not in the critical region for any time t' in this case (Eq. (14) has no solution).

Expression (3) has such a form in the given case. The advantage of this version of the critical-region method is manifested even more clearly in the case of nucleation on the surface (or a curve) of an arbitrary shape. The result is obviously analogous to Eq. (15):

$$Q_{\mathbf{r}_0}^{(i)}(t) = \begin{cases} \exp\left[-\int_0^{t_m(t, p)} I_s(t')S_{\mathbf{r}_0}(t', t)dt'\right], & i = s \\ \exp\left[-\int_0^{t_m(t, p)} I_l(t')l_{\mathbf{r}_0}(t', t)dt'\right], \\ i = l, \quad p < R_m(t), \end{cases} \qquad (17)$$

$$Q_{\mathbf{r}_0}^{(i)}(t) = 1, \quad p > R_m(t),$$

where $S_{\mathbf{r}_0}(t', t)$ is the area of a part of the surface ($l_{\mathbf{r}_0}(t', t)$ is the length of a segment of the curve) confined in the critical region at instant t' and p is the shortest distance from point O' to the object. For $t' > t_m(t, p)$, the object

remains outside the critical region. Naturally, the quantities depend in this case on all the coordinates of point O', which is signified by the subscript $\mathbf{r}_0$.

In order to obtain the fraction of the transformed substance in the layer, we integrate the function $X_{r_0}^{(s)}(t) = 1 - Q_{r_0}^{(s)}(t)$ with respect to r_0 in accordance with Eq. (11):

$$X^{(s)}(t) = 2\int_0^L X_{r_0}^{(s)}(t)\frac{dr_0}{2L}. \qquad (18)$$

We denote by t^* the instant of time at which a nucleus emerging at instant $t' = 0$ reaches the boundary of the layer $R_m(t^*) = L$. For $t < t^*$ [i.e., $R_m(t) < L$], this integral, in accordance with Eq. (16), can be reduced to

$$X_1^{(s)}(t) = 2\sigma\int_0^{R_m(t)} X_{r_0}^{(s)}(t)dr_0 = 2\sigma R_m(t)\int_0^1 X_\xi^{(s)}(t)d\xi,$$

$$\xi = r_0/R_m. \qquad (19)$$

For $t > t^*$, we use Eq. (18) itself for the volume fraction, which can be written in the form

$$X_2^{(s)}(t) = \int_0^1 X_\kappa^{(s)}(t)d\kappa, \quad \kappa = r_0/L. \qquad (20)$$

Finally, we obtain

$$X^{(s)}(t) = \eta(t^* - t)X_1^{(s)}(t) + \eta(t - t^*)X_2^{(s)}(t), \qquad (21)$$

where $\eta(x)$ is a symmetric unit function [6].

A similar expression also holds for volume fractions of a cylinder and a sphere. In the case of a cylinder, we have

$$X_1^{(l)}(t) = \int_0^{R_m(t)} X_{r_0}^{(l)}(t)\frac{2\pi r_0 dr_0}{s}$$

$$= 2\pi\lambda R_m^2(t)\int_0^1 X_\xi^{(l)}(t)\xi d\xi, \qquad (22)$$

$$X_2^{(l)}(t) = 2\int_0^1 X_\kappa^{(l)}(t)\kappa d\kappa, \qquad (23)$$

while for a sphere we obtain

$$X_1^{(c)}(t) = \int_0^{R_m(t)} X_{r_0}^{(c)}(t)\frac{4\pi r_0^2 dr_0}{v}$$

$$= 4\pi n R_m^3(t)\int_0^1 X_\xi^{(c)}(t)\xi^2 d\xi, \qquad (24)$$

$$X_2^{(c)}(t) = 3\int_0^1 X_\kappa^{(c)}(t)\kappa^2 d\kappa. \qquad (25)$$

For constant nucleation and growth rates, the integrals in the latter case can be evaluated, so the explicit dependence on time has the form

$$X_1^{(c)}(t) = \frac{6}{(I_c t^*)^3}\left\{\frac{(I_c t)^3}{6} - \frac{(I_c t)^2}{2} + I_c t - 1 + e^{-I_c t}\right\}, \quad (26)$$

$$X_2^{(c)}(t) = 1 - \frac{6e^{-I_c(t - t^*)}}{(I_c t^*)^3}\left\{\frac{(I_c t^*)^2}{2} - I_c t^* + 1 - e^{-I_c t^*}\right\},$$

$$t^* = L/u. \quad (27)$$

3. NUCLEATION AT RANDOM PLANES, STRAIGHT LINES, AND POINTS: ANOTHER DERIVATION OF KOLMOGOROV'S FORMULA

In view of the generality of the approach used here, we will consider the three cases simultaneously.

Let us suppose that planes, straight lines, or points are distributed at random in an unbounded medium. In order to obtain the volume fraction for nucleation at these objects, we will again use the critical-region method. We choose point O' at random and find the probability $Q^{(i)}(t)$ ($i = s, l, c$) that this point lies in the untransformed region at instant t. The critical region for point O' at instant $t' = 0$ is a sphere of radius $R_m(t)$. Let this region be intersected by N planes (or straight lines) or contain N points. We denote by r_k the distance between point O' and the kth object, $k = 1, \ldots, N$. The probability $q_N^{(i)}(\{r_k\}, t)$ of point O' being in the untransformed region at instant t for a given N and for a realization of the set $\{r_k\} = \{r_1, r_2, \ldots, r_N\}$ is the product of the probabilities in Eq. (15):

$$q_N^{(i)}(\{r_k\}, t) = \prod_{k=1}^{N} Q_{r_k}^{(i)}(t)$$

$$= \prod_{k=1}^{N} \exp\left[-\int_0^{t_m(t, r_k)} I_i(t')\zeta_{r_k}^{(i)}(t', t)dt'\right], \quad i = s, l, c. \quad (28)$$

The sought function $Q^{(i)}(t)$ will be obtained by averaging $q_N^{(i)}(\{r_k\}, t)$ over all the values of r_k and over N:

$$Q^{(i)}(t) = \sum_{N=0}^{\infty} P^{(i)}(N)$$

$$\times \int_0^{R_m(t)} \ldots \int_0^{R_m(t)} q_N^{(i)}(\{r_k\}, t)f^{(i)}(r_1, \ldots, r_N)dr_1, \ldots, dr_N, \quad (29)$$

where $f^{(i)}(\{r_k\})$ is the distribution function for the set $\{r_k\}$ and $P^{(i)}(N)$ is the probability of having the value N.

In order to obtain the function $f^{(i)}(\{r_k\})$, we first choose a parametric space for each class of objects. In the case of points, the parametric space coincides with the coordinate space itself: a point is defined by the coordinates (r, θ, ϕ), and a volume element is $dv = r^2\sin\theta\, dr\, d\theta\, d\phi$. We will assume that the points are distributed according to Poisson's law: the probability of a point being in the volume element dv is equal to $\alpha_c' dv$ and does not depend on the shape of this element or its position in space. We divide the volume $V_m(t) = (4\pi/3)R_m^3(t)$ of the critical region into layers of thickness dr, $dv(r) = 4\pi r^2 dr$, and use the following property of Poisson's process [5]: the probability of the kth point being in the volume element dv_k [provided that N points are in the entire volume $V_m(t)$] is dv_k/V_m (the distribution over the volume is uniform). Going over from v_k to r_k, we find that the probability that the kth point is in the interval $[r_k, r_k + dr_k]$ is $4\pi r_k^2 dr_k/V_m$. In addition, the distances r_k are independent random quantities. Consequently, we can write

$$f^{(c)}(\{r_k\}) = \prod_{k=1}^{N} f^{(c)}(r_k), \quad (30)$$

where $f^{(c)}(r_k) = 3r_k^2/R_m^3$.

The plane is defined unambiguously by two angles θ and ϕ and by the length of r_k, viz., the perpendicular to it dropped from the point O'. The element of the measure for planes in the parametric space (r, θ, ϕ) is $dE^{(s)} = \sin\theta\, dr\, d\theta\, d\phi$ [7]. For planes, we also assume that Poisson's distribution takes place; the probability that the plane is in the "volume" element $dE^{(s)}$ is $\alpha_s' dE^{(s)}$. Similarly, for the distribution of the set $\{r_k\}$, we obtain expression (30) with $f^{(s)}(r_k) = 1/R_m$.

We define the straight line by its direction θ, ϕ and by the polar coordinates r, β of the point of its intersection with the plane perpendicular to it and passing through the point O'. Thus, the measure element is $dE^{(l)} = r\, dr\, d\beta\, d\Omega$, and, for the Poisson distribution (with the parameter α_l'), the probability of the kth straight line being in the interval of distances $[r_k, r_k + dr_k]$ from point O' is $f^{(l)}(r_k)dr_k = 2r_k dr_k/R_m^2$.

Returning now to formula (29), we see that the N-dimensional integral is equal to $w_i^N(t)$, where

$$w_i(t) = \int_0^{R_m(t)} Q_r^{(i)}(t)f^{(i)}(r)dr. \quad (31)$$

Averaging with $P^{(i)}(N) = \alpha_i^N \exp(-\alpha_i)/N!$ gives

$$Q^{(i)}(t) = \sum_{N=0}^{\infty} \frac{\alpha_i^N}{N!}e^{-\alpha_i}w_i^N = e^{-\alpha_i(t)(1 - w_i(t))}. \quad (32)$$

Let us determine the Poisson parameter α_i for each class of objects. In the case of points, $\alpha_c = \bar{N} = V_m(t)n$. In the case of planes, we express α_s in terms of σ. The area S_r of the part of the plane confined inside the critical region is equal to $\pi(R_m^2 - r^2)$. Its mean value is

$$\bar{S}_r = \pi \int_0^{R_m(t)} (R_m^2 - r^2)\frac{dr}{R_m} = \frac{2}{3}\pi R_m^2.$$

The average area in a unit volume is $\sigma = \bar{S}_r \bar{N}/V_m = \bar{S}_r \alpha_s/V_m = \alpha_s/2R_m$, which gives

$$\alpha_s = 2\sigma R_m. \tag{33}$$

Similarly, for the straight lines we can easily find

$$\alpha_l = \pi\lambda R_m^2. \tag{34}$$

Substituting the expressions obtained for α_i into Eq. (32), we obtain the fraction of the transformed substance in each case:

$$X^{(i)} = 1 - \exp(-X_1^{(i)}(t)), \tag{35}$$

where $X_1^{(i)}(t)$ are given by formulas (19), (22), and (24).

Let us consider in greater detail the nucleation at points. Expression (35) in this case has the form

$$X^{(c)}(t) = 1$$
$$- \exp\left\{-4\pi n \int_0^{R_m(t)} \left[1 - \exp\left(-\int_0^{t_m(t,r)} I_c(t')dt'\right)\right]r^2 dr\right\}. \tag{36}$$

We introduce a function $\bar{I}_v(t)$ through the equality

$$\bar{I}_v(t) = nI_c(t)\exp\left(-\int_0^t I_c(t')dt'\right). \tag{37}$$

The integral of this function has the form

$$n_0(t) = \int_0^t \bar{I}_v(t')dt' = n\left\{1 - \exp\left(-\int_0^t I_c(t')dt'\right)\right\}. \tag{38}$$

It can easily be seen that expression (36) can be presented in terms of $\bar{I}_v(t)$ in the form

$$X^{(c)}(t) = 1 - \exp\left\{-4\pi \int_0^{R_m(t)} r^2 dr \int_0^{t_m(t,r)} \bar{I}_v(t')dt'\right\}. \tag{39}$$

Reversing the order of integration, we arrive at Kolmogorov's formula

$$X^{(c)}(t) = 1 - \exp\left\{-\int_0^t \bar{I}_v(t')V(t',t)dt'\right\}, \tag{40}$$

which shows that the function $\bar{I}_v(t)$ has the meaning of the average volume nucleation rate.

Indeed, in the case of nucleation at points, the volume nucleation rate can be presented in the form

$$I_v(\mathbf{r}, t) = I_c(t)\sum_{k=1}^{N_f(t)} \delta(\mathbf{r} - \mathbf{r}_k), \tag{41}$$

where $\mathbf{r}_k$ is the radius vector of the kth point in a certain reference frame and $N_f(t)$ is the number of "non-activated" points in the system (i.e., the points at which no nucleation took place by the instant t). We assume that the volume V_0 of the system is large enough, but finite, and contains N_0 points. The number $N_f(t)$ is a random quantity distributed according to the binomial law

$$P(N_f) = C_{N_0}^{N_f}\phi(t)^{N_f}[1 - \phi(t)]^{N_0 - N_f},$$

where $\phi(t) = \exp(-\int_0^t I_c(t')dt')$ is the probability of a point being "non-activated" by the instant t. This leads to $\bar{N}_f(t) = N_0\phi(t)$. Thus, the averaging of $I_v(\mathbf{r}, t)$ in Eq. (41) over N_f and over the volume for $V_0 \longrightarrow \infty$ gives $\bar{I}_v(t) = I_c(t)n\phi(t)$, i.e., expression (37).

In the limiting case of large values of $I_c(t)$, the function $\bar{I}_v(t)$ is δ-shaped, $\bar{I}_v(t) = n\delta_+(t)$, so that expression (40) describes the situation in this case when all the centers appear at $t' = 0$, i.e.,

$$X(t) = 1 - \exp[-nV_m(t)]. \tag{42}$$

Let us also consider the limiting cases for planes. If the exponent in $Q_{r_0}^{(s)}(t)$ in Eq. (15) is small (low nucleation and growth rates and small values of time), expression (19) is transformed to

$$X_1^{(s)}(t) = 2\pi\sigma \int_0^{R_m(t)} dr_0 \int_0^{t_m(t,r_0)} dt' I_s(t')[R^2(t', t) - r_0^2]. \tag{43}$$

Reversing the order of integration, we obtain

$$X_1^{(s)}(t) = \int_0^t dt' \bar{I}_v(t')V(t', t), \quad \bar{I}_v(t') = \sigma I_s(t'). \tag{44}$$

In the case of a large exponent, we obtain

$$X_1^{(s)}(t) = 2\sigma R_m(t). \tag{45}$$

The corresponding limiting cases for a system of planes can be obtain by substituting Eqs. (44) and (45) into Eq. (35). In this case, the expression $X^{(s)}(t) = 1 - \exp(-2\sigma R_m(t))$ can be interpreted as the volume fraction of infinite planar "nuclei" formed at $t' = 0$.

4. DISCUSSION OF RESULTS

It can be seen from the above considerations that the geometrical–probabilistic approach in the form of the critical-region method is quite efficient for solving various problems associated with the computation of volume fractions. In addition, the apparent advantage of this approach is its mathematical rigor. By way of an example of the inhomogeneity, we consider here the nucleation at various i-dimensional objects. The expressions for volume fractions of a plane layer, cylinder, and sphere are derived. Several remarks should be made concerning expressions (26) and (27) for the last quantities.

First, expression (21) combined with Eqs. (26) and (27) is the average volume fraction of a sphere at instant t. The true volume fraction $X_{tr}^{(c)}(t) = V(t', t)/v$ is a random quantity since the instant t' of the emergence of a nucleating center is random. The volume fraction in Eq. (21) can be obtained by averaging $X_{tr}^{(c)}(t)$ with the function $I_c \exp(-I_c t')$, which is the distribution function for the time of the emergence of a nucleating center. Thus, we can write

$$X_1^{(c)}(t) = \int_0^t V(t', t) I_v(t')(dt'), \quad t < t^*,$$

$$X_2^{(c)}(t) = \int_0^{t-t^*} v I_v(t') dt' + \int_{t-t^*}^t V(t', t) I_v(t') dt', \quad t > t',$$

(46)

where $I_v(t') = n I_c \exp(-I_c t')$. We can easily find that these expressions lead to Eqs. (26) and (27).

Second, the transformation time t_f is infinitely long in this simple bounded system. This fact is an obvious consequence of the random nature of the instant of the emergence of a nucleating center. The average transformation time is $\bar{t}_f = I_c^{-1} + t^*$. In the limiting case $I_c \longrightarrow \infty$, the time t_f is finite and equal to t^*.

In connection with the expression for the volume fraction in the case of nucleation on a plane, attention should be paid to the fact associated with the one-dimensional asymptotic form in Eq. (45), which takes place in the case of competing nucleation of two (or more) different phases on the plane. Let us suppose that two phases with the nucleation and growth rates $I_{s,k}(t)$ and $u_k(t)$, $k = 1, 2$, $u_2(t) > u_1(t)$ are formed. It was proved earlier [4] that, in order to calculate the volume fraction of each phase, the independent-phase approximation

can be used in this case. Thus, we obtain

$$Q_{r_0}^{(s)}(t) = \exp(- Y_{r_0, 1}(t) - Y_{r_0, 2}(t)),$$

$$Y_{r_0, k}(t) = \begin{cases} \displaystyle\int_0^{t_{m,k}(t, r_0)} I_{s, k}(t') S_{r_0, k}(t', t) dt', & r_0 < R_{m, k}(t) \\ 0 & r_0 > R_{m, k}(t) \end{cases}$$

(47)

The total fraction of the transformed substance $X^{(s)}(t)$ can be obtained by integrating the expression $1 - Q_{r_0}^{(s)}(t)$ with respect to r_0:

$$X^{(s)}(t) = 2\sigma R_{m, 1}(t) \left\{ \int_0^1 [1 - e^{-Y_{\xi, 1}(t) - Y_{\xi, 2}(t)}] d\xi \right.$$

$$\left. \int_1^{R_{m, 2}/R_{m, 1}} [1 - e^{-Y_{\xi, 2}(t)}] d\xi \right\},$$

(48)

where $\xi \equiv r_0/R_{m, 1}$ and $t < t^*$, with t^* being determined by the equation $R_{m, 2}(t^*) = L$.

In the limiting case of large values of $Y_{\xi, 2}(t)$, we have

$$X^{(s)}(t) = 2\sigma R_{m, 2}(t).$$

(49)

Thus, the process of phase transformation is determined by the second (rapidly growing) phase. The grains of the first phase turn out to be "immured" in the layer of the second phase and make no contribution to the increase in the transformed volume.

The expressions obtained from an analysis of nucleation at unit i-dimensional objects are used for calculating the volume fractions in unbounded systems in which these objects are distributed at random. Nucleation at pointlike objects was first considered by Avrami [3], who believed that the phase transformation in general follows such a scenario. Nucleation at random planes and straight lines was considered by Cahn [8] as applied to an analysis of the nucleation processes at the boundaries and edges of the grains. The analysis was carried out by using the JMA approach and led to expressions for volume fractions at constant nucleation and growth rates.

However, the JMA approach, which is also referred to as the mean-field approximation, is intuitive rather than a mathematically rigorous method. It may lead to an exact or approximate result. Kolmogorov's formula, which can also be obtained by using the JMA approach, is an example of the former result. An example of the latter result is the volume fractions of competing phases [4]: the JMA approach gives approximate expressions for them. These considerations inspire the revision of these expressions [8]. The derivation of these expressions carried out in this paper confirms the results obtained by Cahn [8]; expressions (35) for constant nucleation and growth rates are transformed into those

derived by Cahn. The fact that the mean field approximation leads to the exact result in the given problem, which follows from the theory presented in Section 3, is a consequence of the Poisson law of the distribution of objects. This form of distribution is the most widespread in physical systems. However, cases of the nonuniform distribution of objects are also possible. For example, pointlike objects (impurity particles at which nucleation takes place) can be distributed nonuniformly over volume for some reason. Such cases can also be analyzed in the framework of the theory developed in Sections 1 and 3 with appropriate modifications. For example, the function $Q^{(i)}(t)$, which can be evaluated with the help of the algorithm described in Section 3, will now be a function of the radius vector $\mathbf{r}_0$ of point O', and hence formula (11) should be used for evaluating the volume fraction. A detailed analysis of these cases is beyond the scope of this article.

In conclusion, let us analyze Eq. (40) in greater detail. It shows that the nucleation at points can be regarded as a process of homogeneous nucleation with the corresponding rate given by Eq. (37). The converse statement is also valid: the process of homogeneous nucleation at a rate $I_v(t)$ can be presented as nucleation at points. The corresponding specific nucleation rate $I_c(t)$ can be determined easily from Eq. (37):

$$I_c(t) = \frac{I_v(t)}{n - \int_0^t I_v(t')dt'} = \frac{I_v(t)}{n - n_0(t)}. \quad (50)$$

The parameter n remains arbitrary except for the condition $n > n_0(t)$. Thus, the inverse representation is ambiguous: expression (50) describes a family of curves corresponding to various values of n. In this case, two different situations are possible: $n_0(t)$ is finite or infinite for $t \longrightarrow \infty$.

Let us consider the latter situation by using the simple example when $I_v = \text{const} = a$. In this case, we have

$$I_c(t) = \frac{a}{n - at}. \quad (51)$$

The number of centers emerging by the instant t, $n_0(t) = at$ increases indefinitely with time. Consequently, the parameter n must also be infinitely large. However, there is no contradiction here. The number $n_0(t)$ can be presented as the sum $n_0(t) = n_0^{(r)}(t) + n_0^{(f)}(t)$, where

$$n_0^{(r)}(t) = \int_0^t I_v(t')Q(t')dt', \quad n_0^{(f)}(t) = \int_0^t I_v(t')X(t')dt', \quad (52)$$

$n_0^{(r)}(t)$ is the number of real centers, i.e., those emerging in the untransformed volume, and $n_0^{(f)}(t)$ is the number of centers emerging in the transformed volume. The latter are just fictitious centers, or "phantoms" in

the JMA approach. In the case of a constant nucleation rate, their number increases indefinitely with time ($n_0^{(r)}(t)$ is always finite). The divergence is associated with the fact that the transformation time t_f is formally infinite. In fact, it can always be chosen as finite and defined by the condition $Q(t_f) = Q_{\min}$, where $Q_{\min}$ is the minimum experimentally observed value of the volume fraction. In this case, the process is considered on the interval $0 < t < t_f$, and for n in Eq. (51) we can take any value $n > at_f$.

The established equivalence of homogeneous nucleation and nucleation at points indicates that the Avrami and Johnson–Mehl approaches are not alternatives [9], but can be reduced to each other through relations (37) and (50), respectively.

APPENDIX

In the case of nucleation on a plane, expression (6) has the form

$$J_{r_0}^{(s)}(t', t) = \frac{1}{4\pi} \int_0^{2\pi} d\phi \int_0^\pi d\theta \sin\theta I_s(t') \quad (A.1)$$
$$\times \delta(r_0 - R(t', t)\cos\theta).$$

In order to integrate over θ, we make use of the following property of the δ-function:

$$\delta(x(\theta)) = \frac{1}{|dx/d\theta|}\bigg|_{\theta = \theta_0} \delta(\theta - \theta_0),$$

where θ_0 is the root of the equation

$$r_0 - R(t', t)\cos\theta = 0. \quad (A.2)$$

This equation is valid only for $R(t', t) \geq r_0$. Hence, the maximum value of t' denoted by $t_m(t, r_0)$ is determined by Eq. (14). For $t_m < t' < t$, we have $J_{r_0}(t', t) = 0$. We shall take into account this fact with the help of the asymmetric unit function $\eta_-(x)$ [6].

The integration of Eq. (A.1) gives

$$J_{r_0}^{(s)}(t', t) = \frac{I_s(t')\eta_-(R(t', t) - r_0)}{2R(t', t)}. \quad (A.3)$$

For nucleation on a straight line or at a point, we have, respectively,

$$J_{r_0}^{(l)}(t', t) = \frac{1}{4\pi} \int_0^{2\pi} d\phi \int_0^\pi d\theta \sin\theta I_l(t')\delta(r_0 - R(t', t)\cos\theta)$$
$$\times \delta(R\sin\theta\sin\phi) = \frac{I_l(t')\eta_-(R(t', t) - r_0)}{2\pi R^2(t', t)\sin\theta_0}, \quad (A.4)$$

$$
\begin{aligned}
J_{r_0}^{(c)}(t', t) \; = \; & \frac{1}{4\pi} \int\limits_{0}^{2\pi} d\phi \int\limits_{0}^{\pi} d\theta \sin\theta \, I_c(t') \delta(r_0 - R(t', t)\cos\theta) \\
& \times \delta(R \sin\theta \sin\phi) \delta(R \sin\theta \cos\phi) \\
& \times \frac{2 I_c(t') \eta_-(R(t', t) - r_0) \delta(R \sin\theta_0)}{4\pi R^2(t', t) \sin\theta_0}.
\end{aligned}
\tag{A.5}
$$

Substituting $\sin\theta_0 = \sqrt{R^2 - r_0^2}/R$ into Eq. (A.5), we obtain

$$
\begin{aligned}
\frac{2\delta(R \sin\theta_0)}{\sin\theta_0} \; &= \; 2\delta(R - r_0)\eta_-(R - r_0) dR \\
&= \; \delta_+(R - r_0) dR \; = \; d\eta_+(R - r_0).
\end{aligned}
$$

The substitution of $J_{r_0}^{(i)}$ into Eq. (7) gives

$$
dP_i(t', t) \; = \; I_i(t') \eta - (R(t', t) - r_0) dt' d\zeta_{r_0}^{(i)}(t', t), \tag{A.6}
$$

where $\zeta_{r_0}^{(i)}(t', t)$ is given by formulas (15); in the case of points, we put

$$
\zeta_{r_0}^{(c)}(t', t) = \eta_+(R(t', t) - r_0).
$$

Thus, we obtain the following equation for $Y_{r_0}(t)$:

$$
Y_{r_0}^{(i)}(t) \; = \; \int\limits_{t_0}^{t} d\tau \int\limits_{0}^{t_m(\tau, r_0)} dt' I_i(t') \frac{\partial \zeta_{r_0}^{(i)}(t', \tau)}{d\tau}. \tag{A.7}
$$

Reversing the order of integration, we finally get

$$
Y_{r_0}^{(i)}(t) \; = \;
\begin{cases}
\displaystyle\int\limits_{0}^{t_m(t, r_0)} dt' I_i(t') \zeta_{r_0}^{(i)}(t', t), & r_0 < R_m(t) \\[4mm]
0, & r_0 > R_m(t).
\end{cases}
\tag{A.8}
$$

ACKNOWLEDGMENTS

REFERENCES

1. A. N. Kolmogorov, Izv. Akad. Nauk SSSR, Ser. Mat. **3**, 355 (1937).
2. W. A. Johnson and R. F. Mehl, Trans. AIME **135**, 416 (1939).
3. M. Avrami, J. Chem. Phys. **7**, 1103 (1939); **8**, 212 (1939); **9**, 177 (1941).
4. N. V. Alekseechkin, Fiz. Tverd. Tela (St. Petersburg) **42** (7), 1316 (2000) [Phys. Solid State **42**, 1354 (2000)].
5. B. V. Gnedenko, *Theory of Probability* (Fizmatgiz, Moscow, 1961; Central Books, London, 1970).
6. G. A. Korn and T. M. Korn, *Mathematical Handbook for Scientists and Engineers* (McGraw-Hill, New York, 1968; Nauka, Moscow, 1984).
7. M. G. Kendall and P. A. Moran, *Geometric Probability* (Hafner, New York, 1963; Nauka, Moscow, 1972).
8. J. W. Cahn, Acta Metall. **4** (5), 449 (1956).
9. V. Z. Belen'kiĭ, *Geometric–Probabilistic Models of Crystallization* (Nauka, Moscow, 1980).

Translated by N. Wadhwa

LATTICE DYNAMICS
AND PHASE TRANSITIONS

Theoretical Pressure–Temperature Phase Diagram for [N(CH₃)₄]₂CuCl₄

$$\text{Theoretical Pressure–Temperature Phase Diagram for } [N(CH_3)_4]_2CuCl_4$$

D. G. Sannikov

Shubnikov Institute of Crystallography, Russian Academy of Sciences, Leninskiĭ pr. 59, Moscow, 117333 Russia
e-mail: el-mech@orc.ru
Received May 4, 2000

Abstract—The pressure–temperature phase diagram for a $[N(CH_3)_4]_2CuCl_4$ crystal has been theoretically constructed using the phenomenological approach developed earlier. The relationships for the thermodynamic potentials of different phases and the boundaries between these phases are derived. The theoretical and experimental diagrams are in reasonable agreement. The approximations and assumptions made in the construction of the diagrams are discussed. © *2000 MAIK "Nauka/Interperiodica"*.

1. INTRODUCTION

The $[N(CH_3)_4]_2CuCl_4$ (TMATC-Cu) crystal belongs to a large family of well-investigated tetramethylammonium tetrahalogenmetal compounds $[N(CH_3)_4]_2MX_4$ (where M is a bivalent metal and X is a halogen) [1–3]. The theoretical approach to the construction of the pressure–temperature (P–T) phase diagram for the TMATC-M crystals, specifically for the TMATC-Zn crystal, was proposed in [4]. This approach was based on the assumption that the phase diagram involves a triple point that was termed the Lifshitz-type point (LT point). This point was theoretically introduced by Aslanyan and Levanyuk [5] and is somewhat similar to the Lifshitz point (L point) [6]. Three lines of the transitions between the incommensurate (IC) phase, initial (C) phase, and commensurate ($C_{0/1}$) phase (equitranslational with the C phase) converge to the LT point, as to the L point (the classification and features of the triple points were described in [7]). The presence of the LT point in the phase diagram is associated with the characteristic feature in the dispersion of a soft optical branch in the normal vibration spectrum of the crystal, which is responsible for the phase transition. In a certain range of parameters, this branch exhibits two minima: one minimum is observed in the center of the Brillouin zone, and the other minimum, at an arbitrary point of this zone.

The soft branch of the TMATC-Cu crystal differs in symmetry from that of the related TMATC-M (where M = Zn, Fe, and Mn) crystals. The LT point is not observed in the P–T diagram, because it lies at negative pressures. However, the technique proposed in [4] is also applicable to this crystal. Figure 1 schematically represents the experimental P–T phase diagram obtained using x-ray diffraction analysis [8]. Figure 2 schematically shows the P–T phase diagram derived by dielectric measurements in other ranges of temperatures and pressures [9]. These diagrams are combined

in Fig. 3, which also shows the boundary between the $C_{0/1}$ and $C_{1/3}$ phases [10] (see also the experimental P–T phase diagrams obtained from measurements of optical birefringence and elastic properties in [11]).

The aim of this work was to construct the theoretical P–T phase diagram for the TMATC-Cu crystal with the use of the technique proposed in [4]. First, we will construct the phase diagram on a plane of the dimensionless variables D_0 and A, which are combinations of the thermodynamic potential coefficients (see below). Then, under the assumption that D_0 and A linearly depend on P and T, we will construct the P–T diagram and compare it with the experimental diagrams (Figs. 1–3).

2. PHASE SYMMETRY

The initial C phase of the crystal has the space group D_{2h}^{16} in the standard *bca–Pmcn* setting. The wavevector
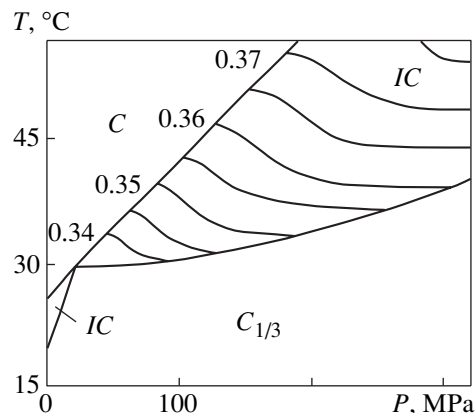

Fig. 1. Experimental P–T phase diagram for TMATC-Cu [8]. Phase designations are the same as in the text.

of the incommensurate phase *IC* is $k_z = qc^*$. The space groups of the commensurate phases $C_{m/l}$ are $P112_1/n$ ($C_{0/1}$ phase) and $P12_1/c1$ ($C_{1/3}$ phase) (see [8–10] and references therein).

It is reasonable to assume that all the phases observed in the *P*–*T* diagrams are associated with the same soft optical branch in the normal vibration spectrum of the initial phase in the crystal (the terminology of crystal lattice dynamics is convenient to use irrespective of whether we consider phase transitions of the displacement type or the order–disorder type). This assumption is consistent with the space groups of the $C_{m/l}$ phases (table). The symmetry of the soft branch is uniquely determined by the space group $P112_1/n$ (C_{2h}^5) of the $C_{0/1}$ phase in the chosen setting of the group *Pmcn* (D_{2h}^{16}) of the *C* phase and the direction of the wavevector of the *IC* phase along the *z* axis.

The space groups of all the possible $C_{m/l}$ phases that correspond to this branch are given in the table, which is cited from the tables presented in [12]. The first column of this table contains the representation of the point group *mmm* (D_{2h}), according to which the transition from the *C* phase to the $C_{0/1}$ phase occurs, the lowest-rank tensor component (that transforms via this representation) in parentheses, and the space group of the $C_{0/1}$ phase. The next three columns list the space groups of three possible phases c_1, c_2, and c_3 for each $C_{m/l}$ phase for all $q_{m/l} = m/l$ (m_+, m_- are even numbers and m_-, l_- are odd numbers) and also the lowest-rank tensor components that have spontaneous values in the c_1 and c_2 phases (for more detail, see [12]).

3. THERMODYNAMIC POTENTIALS: THE SOFT BRANCH

Let us use the relationships derived in [4] for the thermodynamic potentials of phases and add the term proportional to ρ^6 (which is necessary, as will be seen from further consideration). The potential of the $C_{m/l}$ phases with $q_{m/l} = m/l$ (except for $q_{0/1} = 0/1$) has the form

$$\Phi_{m/l} = \alpha(q_{m/l})\rho^2 + \beta\rho^4 + \gamma\rho^6 - \alpha'_{2l}\rho^{2l}\cos 2l\varphi, \quad (1)$$

where ρ and φ are the amplitude and the phase of the two-component order parameter [the soft branch is doubly degenerate; i.e., $\alpha(q) = \alpha(-q)$], respectively. It is assumed that $\beta > 0$ and $\gamma > 0$. The potential of the *IC* incommensurate phase is given by

$$\Phi_{IC} = \alpha(q)\rho^2 + \beta\rho^4 + \gamma\rho^6. \quad (2)$$

Note that the anisotropic term with the α'_{2l} coefficient in formula (1) for arbitrary incommensurate *q* does not satisfy the translational symmetry of the crystal and,
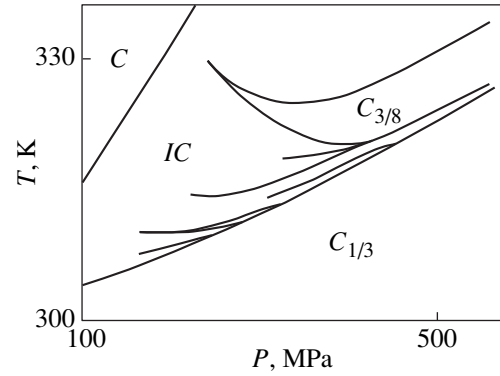

Fig. 2. Experimental *P*–*T* phase diagram for TMATC-Cu [9]. Phase designations are the same as in the text.
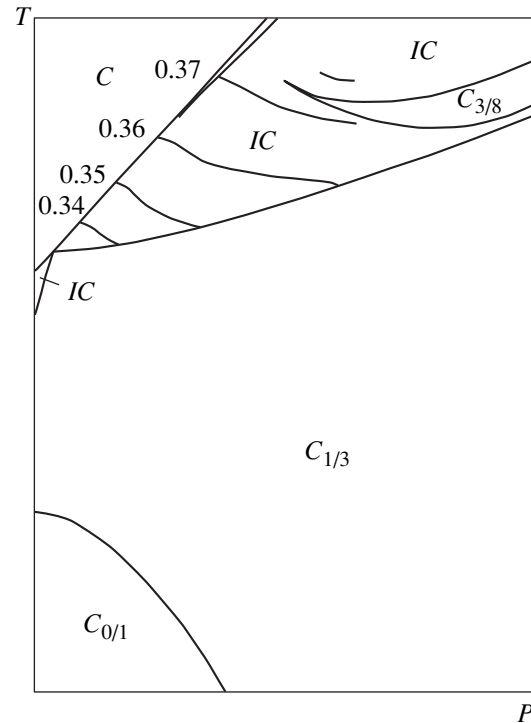

Fig. 3. Experimental *P*–*T* phase diagram for TMATC-Cu (constructed from Figs. 1, 2 and the data taken from [10]), reduced to the same scale.

hence, is not an invariant. The potential of the *C* initial and $C_{0/1}$ commensurate phases is defined as

$$\Phi_{0/1} = \alpha\zeta^2 + \frac{2}{3}\beta\zeta^4 + \frac{2}{5}\gamma\zeta^6. \quad (3)$$

The soft optical branch or, more exactly, the dependence of the coefficient of elasticity $\alpha(q)$ [see formulas (1) and (2)] on the wave number *q* is described by the expression [5]

$$\alpha(q) = \alpha - \delta q^2 - \kappa q^4 + \tau q^6, \quad (4)$$

Space groups of all possible commensurate phases corresponding to the soft branch with the wavevector $k_z = qc*$ in the normal vibration spectrum of the initial phase $Pmcn$ (D_{2h}^{16}) in TMATC-Cu crystal

$\dfrac{m}{l}$	$\dfrac{0}{1}$	$\dfrac{m_-}{l_-}$		$\dfrac{m_+}{l_-}$		$\dfrac{m_-}{l_+}$	
		$c_1\ P2_1cn$	$C_{2v}^9\ x$	$P112_1/n$	$C_{2h}^5\ xy$	$Pc2_1n$	$C_{2v}^9\ y$
$B_{1g}(xy)$	$P112_1/n\ C_{2h}^5$	$c_2\ P12_1/c1$	$C_{2h}^5\ zx$	$P2_12_12_1$	$D_2^4\ xyz$	$P2_1/c11$	$C_{2h}^5\ yz$
		$c_3\ P1c1$	C_s^2	$P112_1$	C_2^2	$Pc11$	C_s^2

where κ and τ are assumed to be more than 0.

Relationship (4) can be rewritten as

$$\alpha(q) = a + \Delta(q),$$

$$\Delta(q) = \tau(b^2 - q^2)^2 \left[2(b^2 - q_L^2) + q^2\right],$$

$$a = \alpha - \Delta_0, \quad \Delta_0 = \Delta(0) = 2\tau b^4(b^2 - q_L^2), \tag{5}$$

$$\delta = \tau b^2(3b^2 - 4q_L^2), \quad q_L^2 = \kappa/2\tau.$$

Here, we introduced the quantities a, b, and q_L, which will be used in subsequent descriptions. Their physical meaning is as follows: a and b are the coefficients of the minimum in the soft branch at an arbitrary point of the Brillouin zone

$$q = b, \quad \alpha(b) = a. \tag{6}$$

This minimum is observed at $\delta > -\kappa^2/3\tau$ or $b^2 > 2q_L^2/3$. The minimum in the center of the Brillouin zone

$$q = 0, \quad \alpha(0) = \alpha \tag{7}$$

can be observed at $\delta < 0$ or $b^2 < 4q_L^2/3$. Therefore, in the range $-\kappa^2/3\tau < \delta < 0$ or $2q_L^2 < b^2 < 4q_L^2/3$, the soft branch exhibits two minima. The LT point is determined from the condition that these minima are equal to each other and simultaneously become zero. The coordinates of the LT point, depending on the plane in which they are determined, take the form

$$a = 0, \quad b^2 = q_L^2, \quad \delta = -\tau q_L^4, \quad \Delta_0 = 0. \tag{8}$$

Consequently, the q_L quantity corresponds to one of the coordinates of the LT point.

Expressions (1)–(3) for the potentials can be simplified by varying them with respect to the variables. As a result, at $\gamma = 0$, we have [4]

$$\Phi_C = 0, \quad \Phi_{IC} = -a^2/4\beta, \quad \Phi_{0/1} = -3\alpha^2/8\beta,$$

$$\Phi_{m/l} = -\frac{\alpha_{m/l}^2}{4\beta}\left[1 + \frac{|\alpha_{2l}'|}{\beta}\left(\frac{-\alpha_{m/l}}{2\beta}\right)^{l-2}\right], \tag{9}$$

$$\alpha_{m/l} \equiv \alpha(q_{m/l}), \quad \Delta_{m/l} = \Delta(q_{m/l}).$$

The last relationship for $\Phi_{m/l}$ is obtained providing that the anisotropic (i.e., dependent on the phase φ) invariant in formula (1) is small compared to the isotropic invariant [4]

$$\frac{|\alpha_{2l}'|\rho^{2l}}{2\beta\rho^4} = \frac{|\alpha_{2l}'|}{2\beta}\left(\frac{-\alpha_{m/l}}{2\beta}\right)^{l-2} \ll 1. \tag{10}$$

It should be emphasized that the neglect of the $\gamma\rho^6$ term in the thermodynamic potentials (9) (see [4]) is not justified for $\Phi_{1/3}$. Actually, at $\gamma = 0$, the minimum of the $\Phi_{1/3}$ potential described by formula (1) at finite values of ρ^2 disappears rather rapidly with an increase in $\alpha(q_{1/3})$ even at small values of $|\alpha_6'|$. In order to avoid this situation, it is necessary to include the $\gamma\rho^6$ term and to set $\gamma \geq |\alpha_6'|$. It is clear that the $\gamma\rho^6$ term should be also included in all the potentials (rather than only in $\Phi_{1/3}$). By minimizing relationships (1)–(3) with respect to their variables, we obtain the expressions for the thermodynamic potentials [more complex than formulas (9)]

$$\Phi_{IC} = -\frac{2\beta^3}{27\gamma^2}\left\{\left[1 - \frac{3\gamma a}{\beta^2}\right]^{3/2} - \left[1 - \frac{9\gamma a}{2\beta^2}\right]\right\},$$

$$\Phi_{0/1} = -\frac{50}{27}\frac{2\beta^3}{27\gamma^2}\left\{\left[1 - \frac{9}{10}\frac{3\gamma a}{\beta^2}\right]^{3/2} - \left[1 - \frac{9}{10}\frac{9\gamma a}{2\beta^2}\right]\right\},$$

$$\Phi_{1/3} = -\frac{2\beta^3}{27(\gamma - |\alpha_6'|)^2}\left\{\left[1 - \frac{3(\gamma - |\alpha_6'|)\alpha_{1/3}}{\beta^2}\right]^{3/2}\right.$$
$$\left. - \left[1 - \frac{9(\gamma - |\alpha_6'|)\alpha_{1/3}}{\beta^2}\right]\right\}, \tag{11}$$

$$\Phi_{m/l} = -\frac{2\beta^3}{27\gamma^2}\left\{\left[1 - \frac{3\gamma\alpha_{m/l}}{\beta^2}\right]^{3/2} - \left[1 - \frac{9\gamma\alpha_{m/l}}{2\beta^2}\right]\right\}$$
$$- \frac{|\alpha_{2l}'|}{\beta}\left[\frac{\beta}{3\gamma}\left(\left[1 - \frac{3\gamma\alpha_{m/l}}{\beta^2}\right]^{1/2} - 1\right)\right]^l.$$

The last relationship for $\Phi_{m/l}$ is derived under the condition of a weak anisotropy. Now, this condition takes the form

$$\frac{|\alpha'_{2l}|\rho^{2l}}{2\beta}\left[\frac{\beta}{3\gamma}\left[1 - \frac{3\gamma\alpha_{m/l}}{\beta^2}\right]^{1/2} - 1\right]^{l-2} \ll 1, \qquad (12)$$

which coincides with condition (10) at $3\gamma(-\alpha_{m/l})/\beta^2 \ll 1$.

4. INTERPHASE BOUNDARIES

The following variables and parameters will be used below:

$$A = -\frac{a}{\tau Q^6}, \quad D_0 = \frac{\Delta_0}{\tau Q^6}, \quad D_{m/l} = \frac{\Delta_{m/l}}{\tau Q^6},$$

$$B = \frac{b}{a}, \quad Q_L = \frac{q_L}{Q}, \quad Q_{m/l} = \frac{q_{m/l}}{Q}, \quad D = \frac{\delta}{\tau Q^4}, \quad (13)$$

$$\epsilon_{2l} = \frac{\tau Q^6}{2\beta}\left(\frac{|\alpha'_{2l}|}{\tau Q^6}\right)^{1/(l-1)}, \quad \epsilon_\gamma = \frac{\tau Q^6}{2\beta}\left(\frac{\gamma}{\tau Q^6}\right)^{1/2}.$$

For convenience (see the D_0–A phase diagram in Fig. 4), the sign of A is taken opposite to the sign of a. Each $C_{m/l}$ phase is characterized by only one dimensionless parameter ϵ_{2l}, which is determined by the α'_{2l} coefficient. There is also the parameter ϵ_γ that is common for all the phases. Since the α, δ, κ, and τ coefficients themselves are dimensionless quantities, Q is the number and is introduced into relationships (13) for the convenience of choosing numerical values of different quantities in the construction of the phase diagrams.

The phase diagram should be constructed on the plane of two thermodynamic potential coefficients which are small and, therefore, considerably depend on P and T. The remaining coefficients are assumed to be independent of P and T. This is justified, because these coefficients, in general, are not small. The coefficients δ (and, hence, D) and α (and, hence, A) are small. Thus, the phase diagram in [4] was constructed on the D–A plane. However, analysis shows that it is more convenient to construct the phase diagram on the D_0–A plane under the assumption that these variables linearly depend on P and T and the remaining quantities Q_L, ϵ_γ, and ϵ_{2l} are constant. Therefore, the κ, τ, β, γ, and α'_{2l} coefficients of the potential are also constant.

By equating the potentials described by relationships (11), we obtain the expressions for the boundaries between the corresponding phases. We will restrict our consideration to the boundaries that are observed in the experimental phase diagrams. The C–IC and C–$C_{0/1}$ boundaries with the initial phase C are given respectively by

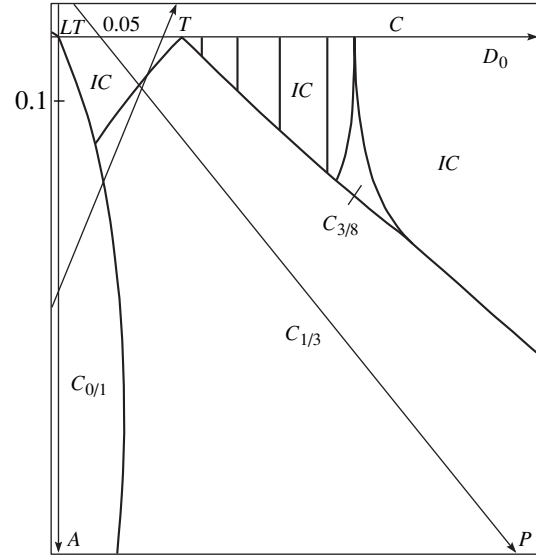$$A = 0, \quad A = D_0. \qquad (14)$$

Fig. 4. D_0–A phase diagram with the LT point.

The IC–$C_{0/1}$, IC–$C_{1/3}$, and $C_{0/1}$–$C_{1/3}$ boundaries are represented respectively as follows:

$$[1 + 12\epsilon_\gamma^2 A]^{3/2} - [1 + 18\epsilon_\gamma^2 A]$$

$$= \frac{50}{27}\left\{\left[1 + \frac{9}{10}12\epsilon_\gamma^2(A - D_0)\right]^{3/2}\right.$$

$$\left. - \left[1 + \frac{9}{10}18\epsilon_\gamma^2(A - D_0)\right]\right\},$$

$$\frac{1}{\epsilon_\gamma^4}\{[1 + 12\epsilon_\gamma^2 A]^{3/2} - [1 + 18\epsilon_\gamma^2 A]\} = \frac{1}{(\epsilon_\gamma^2 - \epsilon_6^2)^2}$$

$$\times\{[1 + 12(\epsilon_\gamma^2 - \epsilon_6^2)(A - D_{1/3})]^{3/2}$$

$$- [1 + 18(\epsilon_\gamma^2 - \epsilon_6^2)(A - D_{1/3})]\}, \qquad (15)$$

$$\frac{50}{27}\frac{1}{\epsilon_\gamma^4}\left\{\left[1 + \frac{9}{10}12\epsilon_\gamma^2(A - D_0)\right]^{3/2}\right.$$

$$\left. - \left[1 + \frac{9}{10}18\epsilon_\gamma^2(A - D_0)\right]\right\} = \frac{1}{(\epsilon_\gamma^2 - \epsilon_6^2)^2}$$

$$\times\{[1 + 12(\epsilon_\gamma^2 - \epsilon_6^2)(A - D_{1/3})]^{3/2}$$

$$- [1 + 18(\epsilon_\gamma^2 - \epsilon_6^2)(A - D_{1/3})]\}.$$

Three boundaries C–IC and C–$C_{0/1}$ [relationships (14)] and IC–$C_{0/1}$ [relationship (15)] converge to one
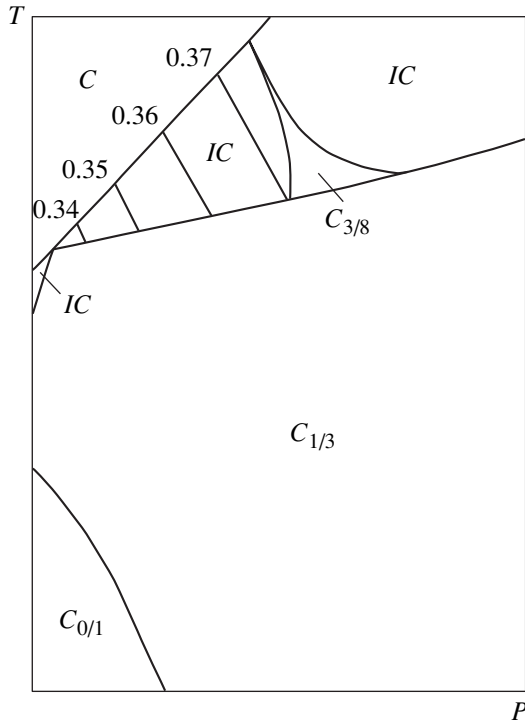
Fig. 5. Theoretical P–T phase diagram for TMATC-Cu, obtained from Fig. 4.

point, namely, the LT point. Its coordinates on the D_0–A and D–A planes are respectively as follows:

$$D_0 = 0, \quad A = 0; \quad D = -Q_L^4, \quad A = 0 \qquad (16)$$

[in this point, $B^2 = Q_L^2$, see relationships (8)].

As follows from expression (12), the IC–$C_{m/l}$ boundary has the form

$$A = \frac{1}{\epsilon_{2l}} D_{m/l}^{1/(l-1)} \left[1 + 3\epsilon_\gamma^2 \frac{1}{\epsilon_{2l}} D_{m/l}^{1/(l-1)} \right]. \qquad (17)$$

This expression is obtained under the condition $D_{m/l} \ll A$, which virtually coincides with condition (12) of weak anisotropy that in designations (13) takes the form

$$\epsilon_{2l} \left[\frac{\epsilon_{2l}}{6\epsilon_\gamma^2} ([1 + 12\epsilon_\gamma^2 A]^{1/2} - 1) \right]^{l-2} \ll 1. \qquad (18)$$

The $C_{m/l}$–$C_{1/3}$ boundary only slightly differs from the IC–$C_{1/3}$ boundary, and this difference most frequently can be ignored, which is done in Fig. 4.

The $D_{m/l}$, D_0, and D quantities in relationships (13) are expressed in terms of B^2 according to formulas (5) in the following way:

$$
\begin{aligned}
D_{m/l} &= (B^2 - Q_{m/l}^2)^2 [2(B^2 - Q_L^2) + Q_{m/l}^2], \\
D_0 &= 2B^4(B^2 - Q_L^2), \quad D = B^2(3B^2 - 4Q_L^2).
\end{aligned}
\qquad (19)
$$

Setting the value of B^2, we determine the value of A from relationships (14)–(17) and the value of D_0 from expressions (19), which allows us to construct the boundaries in the D_0–A diagram.

The minimum in the branch of the spectrum at the arbitrary point of the Brillouin zone disappears below $B^2 = (2/3)Q_L^2$. In this case, the a and b (A and B) quantities lose their meaning. Consequently, the plot in the D_0–A or D–A plane has meaning only at $D_0 \geq (-8/27)Q_L^6$ or $D \geq (-4/3)Q_L^4$.

5. THEORETICAL PHASE DIAGRAMS

In order to construct the D_0–A phase diagram for the TMATC-Cu crystal, it is necessary to choose the values of the Q_L, ϵ_γ, and ϵ_{2l} parameters for each $C_{m/l}$ phase, in our case, at $m/l = 1/3$ and $3/8$. The choice is based on the best fitting of the theoretical P–T phase diagram obtained from the D_0–A diagram to the experimental P–T phase diagram depicted in Figs. 1–3. The parameters chosen are as follows:

$$Q_L^2 = 0.2, \quad \epsilon_\gamma = \epsilon_6 = 0.6, \quad \epsilon_{16} = 1.5, \quad Q = 0.5. \quad (20)$$

These parameters are taken to be virtually accurate to the first decimal place. The simplifying assumption that $\epsilon_\gamma = \epsilon_6$ is used. Figure 4 displays the D_0–A phase diagram obtained from relationships (14)–(20). The LT point with coordinates (16) is designated by the letters LT.

The P–T phase diagram is constructed from the D_0–A diagram (Fig. 4) by assuming the simplest linear dependences of D_0 and A on P and T. Then, the P and T axes in Fig. 4 are straight lines. Their location, orientation, and scale are determined from the best fit to the experimental P–T diagram (Figs. 1–3). Let $\cot \widehat{TD_0} = 0.4$ and $\cot \widehat{PD_0} = 0.8$. These values are obtained with due regard for the scale on the D_0 and A axes. Note that the values of these cotangents in Fig. 4 (without regard for the scale) are larger by a factor of two (0.8 and 1.6).

It should be remarked that A and D_0 are related by the expression $\alpha/\tau Q^6 = -A + D_6$ [see relationships (5) and (13)]. It is usually assumed that the coefficients α of the potential linearly depend on P and T. From the assumption that A linearly depends on P and T, it directly follows that D_0 also linearly depends on P and T. This mutual correspondence does not occur for the A and D variables, and they cannot simultaneously depend in a linear manner on P and T [see relationships (5) and (13)].

Figure 5 depicts the theoretical P–T phase diagram constructed from Fig. 4 with the P and T axes shown in the latter figure. A comparison of Figs. 5 and 3 shows that the theoretical and experimental diagrams are in reasonable agreement. This agreement can be some-

what improved by a more adequate choice of the Q_L, ϵ_γ, and ϵ_{2l} parameters and the orientation of the P and T axes in the D_0–A diagram. A strong nonlinear dependence of $q_{m/l}$ on P and T is seen in Figs. 1–3. The nonlinearity of the $C_{3/8}$ commensurate phase in Figs. 2 and 3 is so strong, especially in the region close to the $C_{1/3}$ phase, that the boundary between these phases is not observed. At the same time, no such features are revealed in the theoretical phase diagram (Fig. 5).

In summary, let us list the approximations and assumptions that were made in the construction of the theoretical D_0–A and P–T phase diagrams. It was assumed that the triple LT point theoretically introduced in [5] resides in the phase diagram (and the L point is absent [6]). Note that the LT point in the P–T diagram lies in the range of negative pressures (approximately at $P = -100$ MPa).

The one-harmonic approximation was applied to the IC phase. This leads to errors (even though not large) in the determination of the boundaries between the IC phase and the $C_{m/l}$ phases. The weak anisotropy condition was used for the $C_{m/l}$ phases ($m/l \neq 1/3$), which made it possible to derive the explicit relationships for the potentials of the $C_{m/l}$ phases and, hence, for the boundaries with these phases. This condition is sufficiently well met over the entire region of the D_0–A and P–T phase diagrams (Figs. 4, 5).

It was assumed that only two small quantities D_0 and A depend on P and T. The remaining quantities Q_L, ϵ_γ, and ϵ_{2l} (or κ, τ, β, γ, and α'_{2l}) were taken to be constant, i.e., independent of P and T. The assumption that D_0 and A linearly depend on P and T is a simplification, which obviously is not quite in agreement with the experimental data (cf. Figs. 5 and 3). The diagram was constructed using the numerical parameters taken to be accurate to the first decimal place. The approximation that $\epsilon_\gamma = \epsilon_6$ was employed. The dispersion (i.e., the dependence on q) of the β, γ, and α'_{2l} coefficients was ignored.

The above approximations and assumptions did not interfere in reaching a satisfactory agreement between the theoretical and experimental P–T phase diagrams for the TMATC-Cu crystal. This was achieved in spite of the fact that the phenomenological model under consideration contains a small number of parameters: the Q_L parameter that determines the coordinate of the LT point, ϵ_γ, and ϵ_{2l} (one parameter for each $C_{m/l}$ phase) that determines the q range (around $q_{m/l}$) occupied by the $C_{m/l}$ phase (at a specified value of A).

Thus, the results obtained demonstrated that the phenomenological approach to the structural phase transitions, which usually works well, adequately describes the experimental data in the special case of the complex phase diagram which involves the specific triple point, the incommensurate phase, and a large number of commensurate phases.

ACKNOWLEDGMENTS

REFERENCES

1. J. D. Axe, M. Iizumi, and G. Shirane, in *Incommensurate Phases in Dielectrics*, Vol. 2: *Materials*, Ed. by R. Blinc and A. P. Levanyuk (North-Holland, Amsterdam, 1985), Chap. 10.
2. K. Gesi, Ferroelectrics **66**, 269 (1986).
3. H. Z. Cummins, Phys. Rep. **185** (5–6), 211 (1990).
4. D. G. Sannikov, G. A. Kessenikh, and H. Mashiyama, J. Phys. Soc. Jpn. **69** (1), 130 (2000).
5. T. A. Aslanyan and A. P. Levanyuk, Fiz. Tverd. Tela (Leningrad) **20** (3), 804 (1978) [Sov. Phys. Solid State **20**, 466 (1978)].
6. R. M. Hornreich, M. Luban, and S. Strikman, Phys. Rev. Lett. **35** (25), 1678 (1975).
7. D. G. Sannikov, Kristallografiya **41** (1), 5 (1996) [Crystallogr. Rep. **41**, 1 (1996)].
8. S. Shimomura, H. Tarauchi, N. Hamaya, and Y. Fujii, Phys. Rev. B **54** (10), 6915 (1996).
9. K. Gesi, J. Phys. Soc. Jpn. **65** (7), 1963 (1996).
10. K. Gesi, Kristallografiya **44** (1), 89 (1999) [Crystallogr. Rep. **44**, 84 (1999)].
11. O. G. Vlokh, A. V. Kityk, V. G. Gribik, and O. M. Mokryĭ, Fiz. Tverd. Tela (Leningrad) **30** (8), 2554 (1988) [Sov. Phys. Solid State **30**, 1472 (1988)].
12. D. G. Sannikov, Kristallografiya **36** (4), 813 (1991) [Sov. Phys. Crystallogr. **36**, 455 (1991)].

Translated by O. Borovik-Romanova

LATTICE DYNAMICS
AND PHASE TRANSITIONS

Independent Anharmonic Oscillator Approximation in the Theory of Structural Phase Transitions in Crystals

M. B. Smirnov* and J. Hlinka**

* Grebenshchikov Institute of Silicate Chemistry, Russian Academy of Sciences, ul. Odoevskogo 24/2, St. Petersburg, 199155 Russia
** Institute of Physics, Czech Academy of Sciences, CZ-18221, Prague, Czech Republic
e-mail: mike@isc.nw.ru
Received March 21, 2000; in final form, May 10, 2000

Abstract—A new method in the microscopic theory of anharmonic crystal lattice dynamics—the independent anharmonic oscillator (IAO) approximation—is discussed. The method is compared with traditional approaches (such as the mean-field and renormalized self-consistent phonon methods) from the standpoint of the analysis of the main approximations. Different methods are applied to the description of the structural phase transition in a monoatomic anharmonic crystal, the results obtained are analyzed, and the numerical accuracy of different approximations is estimated. It is demonstrated that, for this model in the displacement-type instability range, the new method, unlike the self-consistent phonon method, adequately describes the phase transition as a second-order transition. The phase transition temperature calculated in the displacement limit monotonically tends to the exact value in contrast with the temperature obtained within the mean field approximation. © 2000 MAIK "Nauka/Interperiodica".

1. INTRODUCTION

A correct physical theory should, on the one hand, take into account the main factors that affect the phenomenon under consideration and, on the other hand, be simple enough to ensure quantitatively significant results for real objects. In most cases, the simultaneous fulfillment of these requirements is a complicated problem. Such is indeed the case in the microscopic theory of structural phase transitions in crystals. Crystals that undergo structural phase transitions are of considerable interest owing to the attendant anomalies in their different physical characteristics. As a rule, these crystals have complex structures with a low symmetry and a large number of atoms in the unit cell. The dynamics of their crystal lattices at low temperatures is rather simply described within the quasi-harmonic approximation (QHA). However, this approximation is inapplicable in the range of structural phase transitions when the role of anharmonic contributions increases and some modes become harmonically unstable. The available theoretical methods for the microscopic description of the dynamics of strongly anharmonic crystals are too complicated to be applied to complex polyatomic crystals. The development of new methods in the theory of anharmonic crystal lattice dynamics, which should be sufficiently precise and applicable to the study of complex low-symmetry structures, remains a topical problem of solid state physics.

Boyer and Hardy [1] considered the lattice dynamics and structural phase transitions in a $RbCaF_3$ crystal and proposed a method for providing the applicability of the quasi-harmonic approximation (without loss of its conceptual simplicity) even in the range of thermodynamic conditions at which normal lattice vibrations become harmonically unstable, i.e., when they are characterized by imaginary frequencies. To accomplish this, it was sufficient to include anharmonic corrections for each oscillator (under conditions of their independence) in the calculations of their contributions to the entropy. Hence, this approach can be referred to as the independent anharmonic oscillator (IAO) approximation. In a recent work [2], this method was applied to the study of structural phase transitions in quartz, which made it possible to describe an anomalous thermal expansion in this material. Moreover, the theoretical estimates obtained in [1, 2] for the structural phase transition temperatures turned out to be very close to temperatures observed in the experiment. However, neither the rigorous justification of the assumptions underlying the IAO approximation nor its comparison with other (traditional) methods has been made up to now. The purpose of the present work was to fill this gap.

2. THEORETICAL JUSTIFICATION: ANALYSIS OF THE MAIN APPROXIMATIONS

Calculation of the free energy in the classical approximation involves the computation of the statistical integral

$$Z = \iiint\limits_{x_1 \dots x_n} e^{\frac{-U(x_1, \dots, x_n)}{T}} dx_1 \dots dx_n, \qquad (1)$$

where T is the temperature, x_n are the atomic coordinates, and U is the potential energy. The integration over all atomic coordinates in an infinite crystal is a complex mathematical problem, which cannot be solved without simplifying approximations. As a rule, the potential function is represented as the sum of single-particle functions

$$U(x_1, \ldots, x_n) = \sum_i \phi_i(x_i). \tag{2}$$

In this case, the statistical integral is split into the product of the simple integrals

$$Z_i = \int e^{\frac{-\phi_i(x)}{T}} dx. \tag{3}$$

The most universally used method that leads to expansion (2) is based on the mean field concept. In this concept, the variation in the potential function along a particular coordinate is analyzed under the assumption that the instantaneous values of the other coordinates are equal to their thermodynamic means. The mean field concept is realized in the independent-site approximation (ISA) [3], according to which it is assumed that each atom in the lattice independently moves in a specific mean field defined by the single-particle potential

$$\phi(x) = U(\bar{x}_1, \ldots, x, \ldots, \bar{x}_n). \tag{4}$$

Within this approximation, no constraints are imposed on a specific form of the potential function. This universality of the ISA method leads to considerable difficulties in the calculation of the corresponding statistical integrals (3). The calculations are substantially simplified in the case when the mean field approach is applied not to the potential function itself, but to its expansion into a power series in the vicinity of the point $x = \bar{x}$. If, then, we change over to the normal lattice coordinates $q(\mathbf{k})$, the quadratic part of the expansion takes a diagonal form. In the simplest variant of the quasi-harmonic approximation, this expansion is truncated at quadratic terms. In this case, the coordinates are immediately separated, the single-mode potentials have the simple form

$$\phi(q_i(\mathbf{k})) = \frac{1}{2}\lambda_i(\mathbf{k})|q_i(\mathbf{k})|^2, \tag{5}$$

and integrals (3) are easily calculated on the condition that all the eigenvalues of the dynamic matrix $\lambda(\mathbf{k})$ are positive. This condition is not met in the range of structural phase transitions in which the higher-order terms of the expansion should be taken into account. To accomplish this and, in doing so, to retain the separation of the contributions from different modes, the products $q_i(\mathbf{k})q_i(-\mathbf{k})$ are separated out, and the expressions for the coefficients of these terms are replaced by their mean values. This operation results in the single-mode potentials

$$\phi(q_i(\mathbf{k})) = \frac{1}{2}(\lambda_i(\mathbf{k}) + \Delta_i(\mathbf{k}))|q_i(\mathbf{k})|^2. \tag{6}$$

The quantities $\Delta_i(\mathbf{k})$ depend on the anharmonic coefficients of the expansion and also on the mean values $\langle q_i(\mathbf{k})q_i(-\mathbf{k})\rangle$. The stabilizing anharmonic correction $\Delta_i(\mathbf{k})$ increases with a rise in the temperature, and the sum $\lambda + \Delta$ remains positive even in the range of structural phase transitions. In [3], this approach was termed the independent-mode approximation (IMA). It should be noted that this approximation is more frequently referred to as the renormalized (or self-consistent) phonon approximation. The formalism of this method in the general form was described, for example, in the review [4]. In the next section, this approach will be considered in more detail as applied to the case of a single-mode crystal.

The independent anharmonic oscillator approximation under consideration uses the same mean field concept as the independent-site approach. By using the technique of determining single-particle potentials (4) for the expansion of the potential function in the space of normal coordinates and taking into account that the mean value of $q_i(\mathbf{k})$ is equal to zero, we obtain the expansion in which the cross terms (that correspond to the interaction between different modes) are absent but the single-mode potentials contain the anharmonic contributions

$$\phi(q_i(\mathbf{k})) = \frac{1}{2}\lambda_i(\mathbf{k})|q_i(\mathbf{k})|^2 + \frac{1}{24}\mu_i(\mathbf{k})|q_i(\mathbf{k})|^4 + \ldots . \tag{7}$$

Similarly to the independent-site approximation, the IAO approximation remains physically meaningful in the case when certain $\lambda < 0$, because it accounts for the stabilizing effect of anharmonic contributions. The appropriate integrals (3) can easily be calculated with the special function $G(p)$ (see [2] and Appendix).

3. PHASE TRANSITION IN THE 2–4 MODEL SYSTEM

It is hardly probable that the question of the applicability or advantages of a particular approximation in the theory of structural phase transitions can be conclusively solved reasoning only from general considerations by analyzing and comparing the assumptions underlying these approaches. It is of special interest to compare the numerical results obtained within different approximations for a model system in which the character of the structural phase transitions can vary from the displacement type to the order–disorder type. A relatively simple, well-studied model, namely, the 2–4 model, can serve as this system. The 2–4 model system represents a monoatomic cubic lattice in which each atom resides in a local double-well potential of the type $v(x) = -\frac{1}{2}\alpha x^2 + \frac{1}{4}\beta x^4$ and interacts with the six nearest neighbors through harmonic forces whose
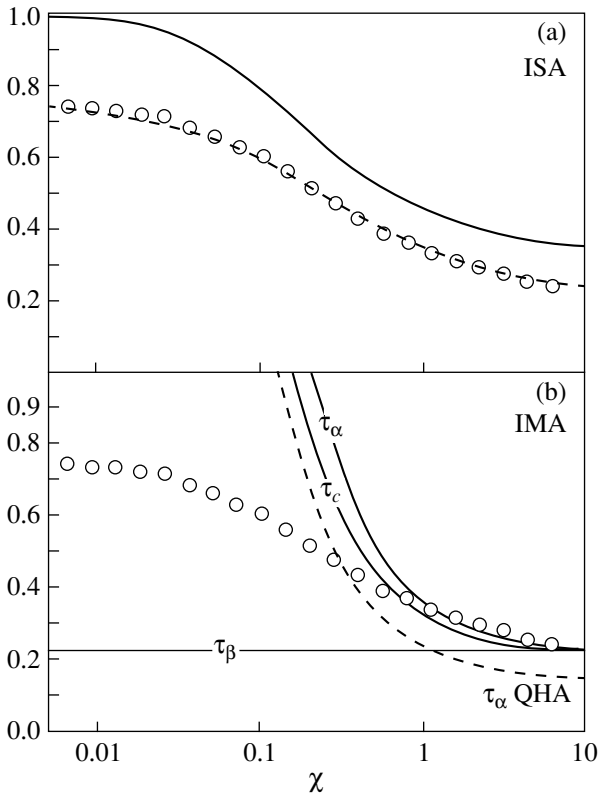
Fig. 1. (a) Dependences $\tau_c(\chi)$ obtained by the Monte Carlo method [5] (circles), by extrapolation with the heuristic formula [6] (dashed line), and within the independent-site approximation (solid line). (b) Dependences $\tau_c(\chi)$, $\tau_\alpha(\chi)$, and $\tau_\beta(\chi)$ calculated by the IMA method. The dashed line represents the dependence $\tau_\alpha(\chi)$ calculated within the quasi-harmonic approximation.

potential has the form $\frac{1}{2}\gamma(x_i - x_j)^2$. In order to simplify our analysis, a one-dimensional motion is treated under the assumption that the harmonic forces between the neighboring atoms are isotropic. This system serves as the simplest model of the sublattice, which is active upon the phase transition and whose interaction with all the other sublattices is replaced by the potential field of an inert medium.

Now, we change over to dimensionless quantities by taking $(\alpha/\beta)^{1/2}$ and α^2/β as the unit length and the unit energy, respectively. Then, the potential function has the form

$$U(x) = \sum_i \left(\nu(x_i) + \frac{1}{2}\kappa \sum_j (x_i - x_j)^2 \right), \qquad (8)$$

where $\nu(x) = -\frac{1}{2}x^2 + \frac{1}{4}x^4$ and $\kappa = \frac{\gamma}{\alpha}$ is the sole parameter of the model. In what follows, we will use the more convenient quantity $\chi = 6\kappa$. Moreover, the atomic mass is taken equal to unity.

At any χ parameter, the system under consideration is statically stable at $x = \pm 1$. This corresponds to the low-temperature low-symmetry α-phase. As the temperature increases, the statically unstable high-symmetry β-phase that corresponds to $x = 0$ becomes thermodynamically preferable. At a certain temperature T_c, the system undergoes a second-order phase transition. The character of this transition depends on the value of χ: it is the displacement-type phase transition at $x \gg 1$ and the order–disorder transition at $\chi \ll 1$ [3]. The T_c temperature turns out to be almost proportional to the χ parameter, and, hence, the ratio $\tau_c = T_c/\chi$, rather than T_c, will be used in the subsequent discussion of the numerical results.

Rubtsov *et al.* [5] performed the Monte Carlo calculations for the $\bar{x}$ values at different temperatures and different χ parameters. The results obtained were used to determine the dependence of τ_c on χ (Fig. 1a). Hereafter, this dependence will be treated as the exact solution of the problem. Hlinka *et al.* [6] proposed the simple approximation of this dependence

$$\tau_c = 0.76 - 0.49 \tanh\chi, \qquad (9)$$

which is also depicted in Fig. 1a. Now, we analyze how this dependence is reproduced in each of the above approximations.

3.1. Independent-site approximation. According to definition (4), the single-particle potential can be determined as $\varphi(x, \bar{x}) = -\frac{1}{2}(\chi - 1)x^2 + \frac{1}{4}x^4 - \chi x \bar{x} + \frac{1}{2}\chi\bar{x}^2$.

The value of $\bar{x}(T)$, which determines the crystal structure at a specified temperature, can be found from the minimum condition for the free energy $F = -T\ln Z$. It is known that, in this model, the ISA method correctly describes the structural phase transition as a second-order transition [3]. Then, the T_c temperature can be obtained from the condition $d^2F/dx^2|_{x=0} = 0$, which, in our case, leads to the equation

$$\tau_c = \frac{\int x^2 \exp(-\varphi(x, 0)/T_c)dx}{\int \exp(-\varphi(x, 0)/T_c)dx}. \qquad (10)$$

The integrals that enter into relationship (10) can be expressed in terms of the $G(p)$ function and its derivative (this function and the computational details are discussed in the Appendix). The curve $\tau_c(\chi)$ calculated by the ISA method is also displayed in Fig. 1a.

In order to analyze the other approximations, it is necessary to change over to the normal lattice coordinates, which are related to the atomic coordinates by the formula

$$x_n = \bar{x} + \sum_{\mathbf{k}} e^{i\mathbf{kn}}q(\mathbf{k}). \qquad (11)$$

Here, $\mathbf{n}$ is the vector with integer-valued components which numbers the cells and $\mathbf{k} = (k_1, k_2, k_3)$ is the wave

vector, each component of which varies in the range from $-\pi$ to π. The substitution of expression (11) into relationship (8) with due regard for the normalization of the harmonic functions

$$\frac{1}{N}\sum_{\mathbf{n}} e^{i\mathbf{kn}} = \Delta(\mathbf{k})$$

gives the expression for the energy density

$$u(\bar{x}, q) = \frac{U}{N} = v(\bar{x}) + v'(\bar{x})q(0)$$

$$+ \frac{1}{2}\sum_{\mathbf{k}} (v''(\bar{x}) + f(\mathbf{k}))q(\mathbf{k})q(-\mathbf{k})$$

$$+ \frac{v'''(\bar{x})}{6} \sum_{\mathbf{k}_1, \mathbf{k}_2, \mathbf{k}_3} q(\mathbf{k}_1)q(\mathbf{k}_2)q(\mathbf{k}_3)\Delta(\mathbf{k}_1 + \mathbf{k}_2 + \mathbf{k}_3) \quad (12)$$

$$+ \frac{v''''}{24} \sum_{\mathbf{k}_1, \mathbf{k}_2, \mathbf{k}_3, \mathbf{k}_4} q(\mathbf{k}_1)q(\mathbf{k}_2)q(\mathbf{k}_3)q(\mathbf{k}_4)$$

$$\times \Delta(\mathbf{k}_1 + \mathbf{k}_2 + \mathbf{k}_3 + \mathbf{k}_4).$$

The coefficient $f(\mathbf{k})$ accounts for the dispersion relationship for the harmonic interaction between the nearest neighbors in a monoatomic cubic lattice and has the simple form

$$f(\mathbf{k}) = \chi\left(1 - \frac{1}{3}(\cos k_1 + \cos k_2 + \cos k_3)\right). \quad (13)$$

In what follows, we will ignore the contributions from the normal coordinate $q(0)$ to expansion (12), because the integration over this coordinate is not required in the calculation of the partial free energy and, in essence, this coordinate and $\bar{x}$ describe the same degrees of freedom.

3.2. Quasi-harmonic approximation. Prior to analyzing the results obtained by the IMA and IAO methods, it is expedient to discuss the benefits of applying the quasi-harmonic approximation to our problem. If the third- and fourth-order terms are neglected in expansion (12), the potential function corresponds to a system of independent harmonic oscillators whose frequencies squared are defined by the dispersion relationship

$$\lambda(\mathbf{k}) = \lambda_0(\bar{x}) + f(\mathbf{k}), \quad (14)$$

where $\lambda_0 = v'' = -1 + 3\bar{x}^2$. The dispersion branches along the directions that connect the singular points in the Brillouin zone are displayed in Fig. 2a. The corresponding density of states $g(\lambda)$ is shown in Fig. 2b.

Within the quasi-harmonic approximation, the free energy is expressed by the simple relationship

$$F(\bar{x}) = v(\bar{x}) + \frac{T}{2}\frac{1}{N}\sum_{\mathbf{k}} \ln\lambda(\mathbf{k}). \quad (15)$$
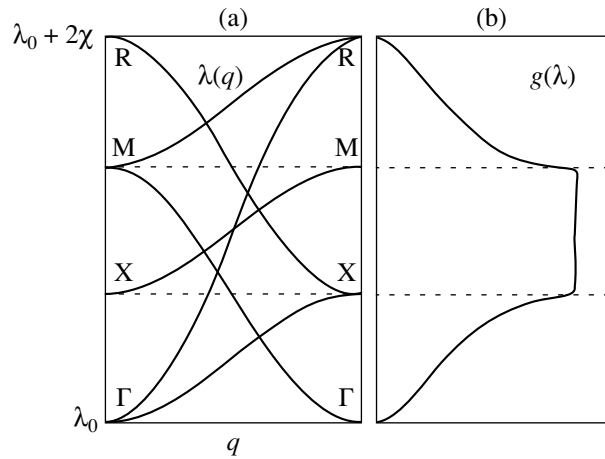

Fig. 2. (a) Dispersion of the square of the phonon frequency between singular points in the Brillouin zone and (b) the density of states for the 2–4 model system.

Note that the dependence of λ on $\bar{x}$ in the model under consideration is determined only by the first term in the dispersion relationship (14) and, hence,

$$\frac{d\lambda(\mathbf{k})}{d\bar{x}} = v''' = 6\bar{x}. \quad (16)$$

With this formula, we obtain the equilibrium condition

$$F'(\bar{x}) = v'(\bar{x}) + \frac{3\bar{x}T}{N}\sum_{\mathbf{k}}\frac{1}{\lambda(\mathbf{k})} = 0. \quad (17)$$

The solution of this equation gives $\bar{x}(T, \chi)$. By gradually increasing the temperature, we find the temperature T_α above which Eq. (16) does not possess solutions, except for the trivial solution $\bar{x} = 0$. The corresponding dependence $\tau_\alpha(\chi)$ is shown by the dashed line in Fig. 1b. The T_α temperatures thus determined correspond to the temperature below which the low-symmetry phase exhibits a local minimum (i.e., this phase is metastable). Recall that the quasi-harmonic approximation, in principle, is inapplicable to the high-symmetry phase for which $\lambda_0 < 0$. Consequently, the T_α value determined within this approach gives only an upper estimate of the phase transition temperature. As follows from Fig. 1b, this temperature is strongly overestimated at $\chi < 1$ and underestimated at $\chi > 1$. At large χ, the limiting value of τ_α within the quasi-harmonic approximation is equal to 2/3 of the exact value.

3.3. Independent-mode approximation. If only the terms containing the $q(\mathbf{k})q(-\mathbf{k})$ products are retained in expansion (12) and the linear terms are retained in the expansion into a power series of the deviations
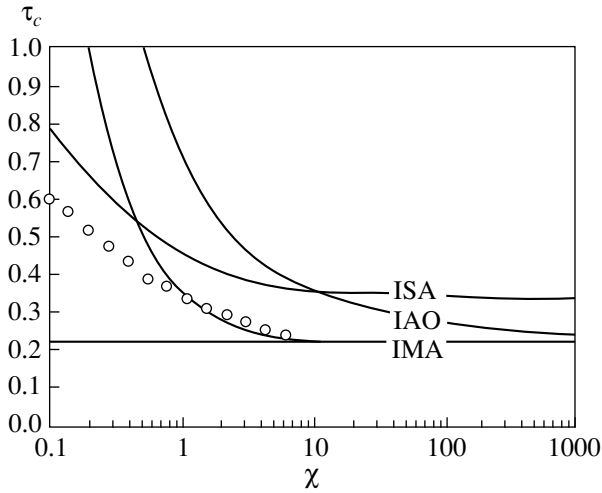
Fig. 3. Dependences $\tau_c(\chi)$ calculated within different approximations. Circles represent the results obtained by the Monte Carlo method [5]. Dependences $\tau_\alpha(\chi)$ and $\tau_\beta(\chi)$ are calculated in the independent-mode approximation.
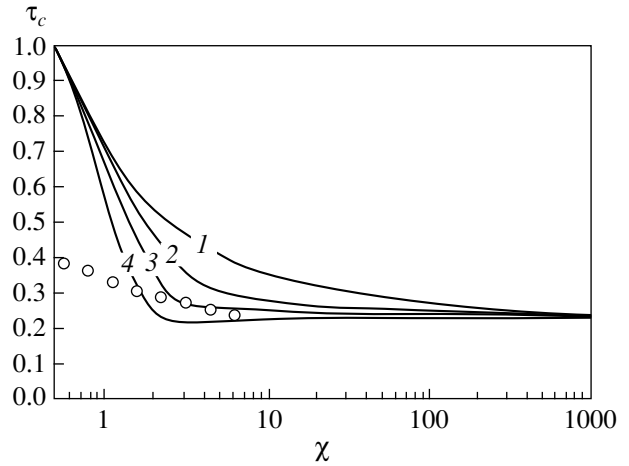

Fig. 4. Dependences $\tau_c(\chi)$ calculated within the IAO approximation for the cut-off of the coefficients $\mu = 1/4\exp(-\lambda^2/g^2)$ at $\lambda > 0$: (*1*) $g = \infty$, (*2*) $g = 1$, (*3*) $g = 0.5$, and (*4*) $g = 0.25$. Circles represent the results obtained by the Monte Carlo method [5].

$q(\mathbf{k})q(-\mathbf{k}) - \langle q(\mathbf{k})q(-\mathbf{k})\rangle$, we obtain the representation of the potential function at the IMA level

$$u(\bar{x}, q) = \nu(\bar{x}) + \frac{1}{2}\sum_{\mathbf{k}}(\lambda(\mathbf{k}) + 3I)|q(\mathbf{k})|^2 - \frac{3}{4}I^2, \quad (18)$$

where

$$I = \sum_{\mathbf{k}}\langle q(\mathbf{k})q(-\mathbf{k})\rangle = \frac{T}{N}\sum_{\mathbf{k}}\frac{1}{\lambda(\mathbf{k}) + 3I}. \quad (19)$$

Then, we can write the expression for the free energy

$$F = \nu(\bar{x}) + \frac{T}{2N}\sum_{\mathbf{k}}\ln(\lambda(\mathbf{k}) + 3I) - \frac{3}{4}I^2 \quad (20)$$

and the equilibrium condition

$$F' = \nu'(\bar{x}) + 3\bar{x}I = 0. \quad (21)$$

It should be noted that the relationship for the derivative F' can be obtained either by treating I as a function of x and differentiating expression (20) with respect to x (with due regard for this dependence) or by treating F as a function of two independent parameters x and I. In the latter case, the partial derivative with respect to x gives Eq. (21), and the condition for the minimum of F with respect to I leads to relationship (19). The possibility of treating I as an independent parameter of the free energy provides the basis for the variation approach to the formulation of the self-consistent phonon method [4].

By solving Eqs. (19) and (21), we obtain $\bar{x}(T, \chi)$ and, then, the critical temperatures T_α and T_β, which are defined in the following way: the local minimum of $F(\bar{x})$ in the low-symmetry phase takes place at $0 < T <$

T_α, and the local minimum in the high-symmetry phase exists at $T > T_\beta$. Upon the second-order phase transition, $T_\alpha = T_\beta = T_c$. Upon the first-order phase transition, $T_\alpha > T_\beta$. In the latter case, the phase transition temperature T_c lies in the range between T_α and T_β and can be determined from the equality of the free energies for two local minima. In the independent-mode approximation, the temperatures T_α and T_β appear to be different, and, hence, this method erroneously describes the structural phase transition as a first-order transition [3]. Figure 1b displays the dependences of τ_α, τ_β, and τ_c on χ, which were calculated within the independent-mode approximation. At large χ, $\tau_\beta \approx \tau_c \approx \tau_\alpha \approx 0.22$, which corresponds to the exact limit at $\chi \longrightarrow \infty$. At small χ, the values of τ_α and τ_c calculated by the IMA method substantially exceed the exact values of τ_c and turn out to be even larger than τ_α calculated within the quasi-harmonic approximation.

3.4. Independent anharmonic oscillator approximation. Expansion (10) for our model involves two terms

$$\Phi(q(\mathbf{k})) = \frac{1}{2}\lambda(\mathbf{k})|q(\mathbf{k})|^2 + \frac{3}{4}|q(\mathbf{k})|^4. \quad (22)$$

It is evident that the anharmonic corrections in our model are identical for all modes in the phonon spectrum. The calculation of integral (3) with this potential is discussed in the Appendix. By using the functions $G(p)$ and $H(p)$, which are determined in the Appendix, we obtain the relationship for the free energy

$$F = \nu(\bar{x}) - \frac{T}{N}\sum_{\mathbf{k}}\ln G\left(\frac{\lambda(\mathbf{k})}{2(3T)^{\frac{1}{2}}}\right) \quad (23)$$

and the equilibrium equation

$$F' = v'(\bar{x}) + \frac{\bar{x}(3T)^{\frac{1}{2}}}{N} \sum_{\mathbf{k}} H\left(\frac{\lambda(\mathbf{k})}{2(3T)^{\frac{1}{2}}}\right) = 0. \quad (24)$$

By solving Eq. (24), we obtain the temperatures T_α and T_β. It turns out that the equality $T_\beta = T_\alpha$ is rigorously fulfilled in the range of the displacement-type structural phase transition (at $\chi \geq \chi_0 \approx 0.5$). This implies that the IAO approximation, unlike the IMA method, adequately describes the phase transition as a second-order transition in the model under consideration. Figure 3 shows the dependence of τ_c on χ, which was calculated within the IAO approximation. It should be that, in the displacement limit, i.e., at $\chi \longrightarrow \infty$, the τ_c value calculated in the IAO approximation monotonically tends to the exact limit $\tau_c \approx 0.22$, unlike the limiting value $\tau_c = \frac{1}{3}$ obtained by the ISA method [3].

In the instability range of the order–disorder type (at $\chi < 0.5$), the IAO approximation results in the substantially overestimated temperature T_c. Note that, in this range, the T_α and T_β temperatures calculated within the IAO approximation differ insignificantly. Thus, it can be concluded that, similar to the IMA method, the IAO approximation is inapplicable to the systems undergoing a structural phase transition of the order–disorder type.

The application of the IAO approximation to the investigation of the lattice dynamics in complex polyatomic crystals requires the determination of the quasi-harmonic frequencies $\lambda_i(\mathbf{k}) = \omega_i^2(\mathbf{k})$ and the fourth-order parameters $\mu_i(\mathbf{k})$ for each geometry studied. The quasi-harmonic frequencies are determined by the standard methods for the construction and diagonalization of the dynamic matrix, whereas the determination of the numerical parameters $\mu_i(\mathbf{k})$ demands certain efforts. In [1, 2], these parameters were numerically determined from the dependence $\phi(q)$ for specific harmonically unstable modes. It was found that the $\mu_i(\mathbf{k})$ values are almost identical for all modes $\lambda_i(\mathbf{k}) < 0$. Earlier [2], we proposed to use the same μ value for all modes of the phonon spectrum (this case is realized in the above model). Boyer and Hardy [1] employed the conventional quasi-harmonic approximation for all the harmonically stable modes; i.e., they assumed that $\mu_i(\mathbf{k}) = 0$. It is of interest to analyze variations in the calculated values of τ_c under this assumption. In order to exclude numerical instabilities and to ensure the continuity of all the functions, we introduce the following "cut-off" of the μ coefficients into the aforementioned model: $\mu = 3/4$ at $\lambda \leq 0$ and $\mu = \frac{3}{4} \exp(-\lambda^2/g^2)$ at $\lambda > 0$. The dependences $\tau_c(\chi)$ calculated for different parameters g are displayed
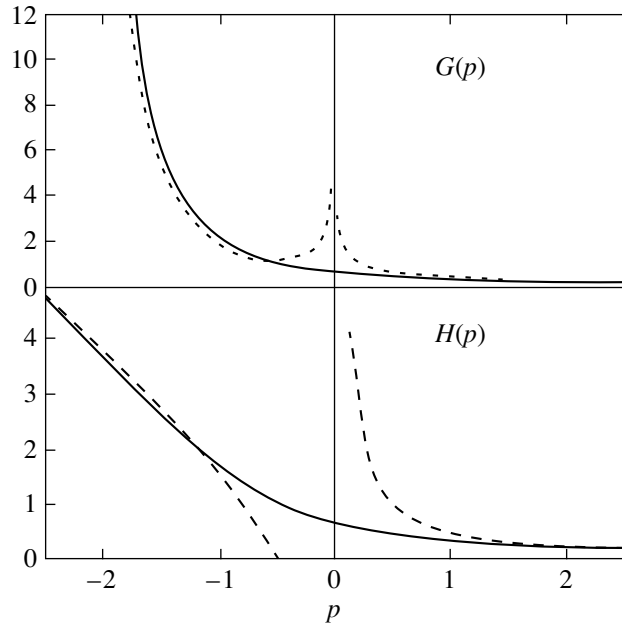

Fig. 5. Functions $G(p)$ and $H(p)$ (solid lines) and their asymptotics (dashed lines).

in Fig. 4. These results allow us to reach the conclusion that the elimination of anharmonic corrections for all the harmonically stable modes brings about a certain decrease in τ_c but changes neither the type of the structural phase transition nor the value of τ_c in the displacement limit. Moreover, this correction of the μ parameters leads to numerical results which are in better agreement with the exact solution.

4. DISCUSSION

The concepts underlying the IAO approximation are similar to the initial assumptions of the ISA and IMA methods. In the strict sense, the IAO approximation is the approximation obtained in the case when the mean field approach (the replacement of the instantaneous coordinate values by their means) is formally applied to the expansion of the potential function of the lattice into a series in terms of its normal coordinates.

The numerical calculations in the framework of the IAO approximation are only slightly complicated as compared to those within the quasi-harmonic approximation. A certain complication of the calculations due to the inclusion of the fourth-order term in the statistical integral can be readily overcome using the table of the special functions $G(p)$ and $H(p)$.

For the 2–4 model system in the displacement-type instability range, the IAO approximation permits a correct description of the structural phase transition as a second-order transition. The T_c temperature calculated within this approximation tends to the exact solution in the displacement limit, even if somewhat exceeds its exact value. The elimination of anharmonic corrections

for harmonically stable modes leads to a decrease in the T_c temperature and improves the numerical accuracy of the approximation.

5. CONCLUSION

The results presented in this work and the data obtained earlier by the IAO method, as applied to investigations of structural transformations in complex crystals [1, 2], give grounds to treat this approximation as an efficient and promising method in the microscopic theory of structural phase transitions.

APPENDIX

The statistical integral (3) with the potential $\varphi(x) = \lambda/2x^2 + \mu/4x^4$ can be represented as

$$Z = \int \exp\left(-\frac{\varphi(x)}{T}\right)dx = \sqrt{2}\left(\frac{T}{\mu}\right)^{1/4} G\left(\frac{\lambda}{2\mu^{1/2}T^{1/2}}\right), \text{ (A.1)}$$

where

$$G(p) = e^{p^2} f(p) \text{ and } f(p) = \int \exp[-(x^2 + p)^2]dx.$$

The integral $f(p)$ can be calculated by the Gauss–Christoffel method (see, for example, [7]). The properties and the plot of this function are presented in [2].

The problem of minimizing the free energy involves the calculation of the function $H = -\dfrac{G'}{G}$. The functions $G(p)$ and $H(p)$ are shown in Fig. 5. Let us consider their specific properties.

At $\lambda > 0$, the $G(p)$ function gives the value of integral (A.1) for the oscillator with the quartic anharmonic correction. Note that, at $\lambda \gg \mu$, we have the limiting case of a harmonic oscillator and

$$G(p) \approx \frac{1}{2\sqrt{p}}, \quad H(p) \approx \frac{1}{2p}, \quad p \longrightarrow \infty.$$

At $\lambda < 0$, the $G(p)$ function allows one to calculate integral (A.1) for the 2–4 system with the double-well potential. In this case, $p^2 = \varepsilon/T$ (where ε is the potential well depth) and

$$G(p) = \frac{e^{p^2}}{\sqrt{-2p}}, \quad H(p) \approx -2p + \frac{1}{2p}, \quad p \longrightarrow -\infty.$$

At $\lambda = 0$, we have a quartic oscillator and $G(0) = (1/2\sqrt{2\pi})\Gamma(1/4)$.

It should be also noted that the functions $G(p)$ and $H(p)$ are the solutions of the following differential equations:

$$G'' = G + 2pG',$$

$$H' = H^2 + 2pH - 1,$$

which enable one to obtain easily the formulas for the higher derivatives.

In particular, the $H(p)$ function makes it possible to calculate the T_c temperature within the ISA method. Relationship (12) can be rewritten as

$$\frac{T_c^{1/2}}{\chi} = H(z), \quad z = \frac{\chi - 1}{2T_c^{1/2}}.$$

From these expressions, we obtain

$$\chi = \frac{1}{1 - 2zH(z)}, \quad \frac{T_c}{\chi} = \frac{H^2(z)}{1 - 2zH(z)},$$

which determines the dependence $\tau_c(\chi)$ in the parametric form.

ACKNOWLEDGMENTS

REFERENCES

1. L. L. Boyer and J. R. Hardy, Phys. Rev. B **24** (5), 2577 (1981).

2. M. B. Smirnov, Phys. Rev. B **59** (6), 4036 (1999).

3. A. D. Bruce and R. A. Cowley, *Structural Phase Transitions* (Taylor and Francis, London, 1981).

4. V. L. Aksenov, N. M. Plakida, and S. Stamenkovič, *Neutron Scattering by Ferroelectrics* (Énergoatomizdat, Moscow, 1983; World Scientific, Singapore, 1990).

5. A. N. Rubtsov, J. Hlinka, and T. Janssen, Phys. Rev. E **61** (1), 126 (2000).

6. J. Hlinka, T. Janssen, and V. Dvořák, J. Phys.: Condens. Matter **11** (16), 3209 (1999).

7. N. N. Kalitkin, *Numerical Methods* (Nauka, Moscow, 1978), p. 94.

Translated by O. Borovik-Romanova

<center>

**LOW-DIMENSIONAL SYSTEMS
AND SURFACE PHYSICS**

</center>

Contact Phenomena in 2D Electronic Systems
with an Integer Filling Factor

V. B. Shikin and Yu. V. Shikina

Institute of Solid-State Physics, Russian Academy of Sciences, Chernogolovka, Moscow oblast, 142432 Russia
e-mail: shikin@issp.ac.ru
Received January 12, 2000

Abstract—An interpretation of the available experimental data on the linear electrooptical effect in two-dimensional (2D) electronic systems in quantized magnetic fields has been proposed. The self-consistent treatment of the data obtained for the Corbino and Hall samples in both equilibrium and transport-current-carrying states is performed with due regard for the contact phenomena observed during sample preparation. The limiting cases of small and large contact-potential differences as compared to the cyclotron energy are analyzed. © *2000 MAIK "Nauka/Interperiodica"*.

1. INTRODUCTION

Earlier [1], we discussed the possibility of measuring "incompressible" regions in inhomogeneous two-dimensional (2D) electronic systems with integer filling factors with the use of capacitance methods. It was assumed that the inhomogeneities stem from contact phenomena occurring, with a high probability, in the systems under consideration. In the present work, we treated the local characteristics of different 2D systems in a magnetic field, which can be measured using the linear electrooptical effect (see [2–4]). Analysis of the data obtained in [3, 4] revealed that the spatial homogeneity of the electron density is disturbed in electrooptical experiments. This disturbance is most likely caused by contact phenomena.

2. EQUILIBRIUM CONDITIONS

2.1. Figure 1 demonstrates the characteristic distributions of the electric potential $\varphi(x)$ over the cross-section of the rectangular and Corbino geometry samples in the normal and integer states in the absence of a transport current. The normal part of this distribution is depicted schematically (Fig. 1, line *A*). Line *B* (Fig. 1), which is conventionally termed anomalous, represents the data obtained by Knott *et al.* [3, Fig. 9] for one of the cross-sections of a Hall sample. A qualitatively similar distribution was also observed in the Corbino geometry [4, Fig. 2].

The difference between the normal and anomalous behavior of $\varphi(x)$ can easily be explained for the Corbino geometry samples. Actually, since the filling factor is integer, the 2D electronic system acquires the dielectric properties. Hence, the electric potential $\varphi(x)$ should monotonically decrease from a fixed value equal to the contact-potential difference across the exterior electrodes to its minimum value in the center of the 2D system, as is the case in the experiment.

For a rectangular geometry, a similar interpretation is inapplicable. Indeed, a two-dimensional sample ($2l \times 2w$, $l \gg w$) has ohmic contacts along its short sides of length $2w$ and has no contacts along the other two sides of length $2l$. In these conditions, when the 2D system acquires the dielectric properties, the expected inhomogeneities of $\varphi(y)$ can be realized only along the direction between the short sides of the rectangular sample with the characteristic dependence $\varphi(y) \propto y/l$ but not in
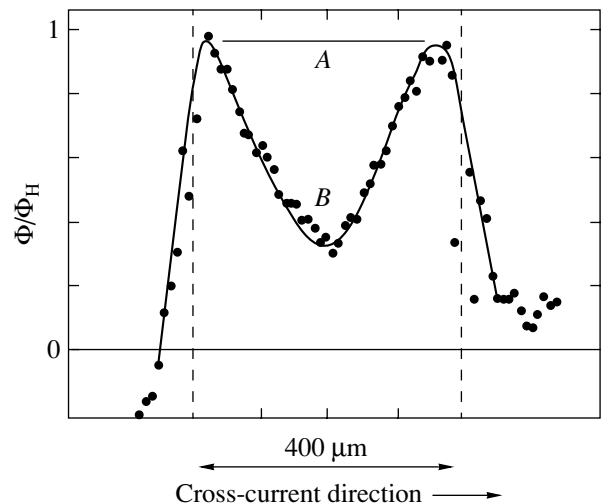

Fig. 1. Normal and anomalous behavior of the electric potential over the cross-section of the Hall sample. Line *A* corresponds (schematically) to the normal behavior of $\varphi(x)$ when the overall 2D system is in the high-conductivity state. The smooth behavior of $\varphi(x)$ at the edges of the 2D system is associated with the finiteness of the laser beam radius. Line *B* and the experimental points along this line represent the data taken from [3] for the Hall sample.

the "Hall" cross-sections of the rectangle $-w \leq x \leq +w$. This contradicts the data obtained in [3] (see Fig. 1, line *B*), for which the $\varphi(x)$ inhomogeneity similar to that observed in the Corbino configuration [4] is clearly seen in the Hall cross-sections (i.e., $\varphi(x) \propto x/w$). Therefore, the assumption about the homogeneity of the dielectric 2D state in experiments performed on a rectangular configuration [3] seems untenable.

Let us assume that the 2D system is inhomogeneous along the *x* direction. In this case, if the central part of the rectangle acquires the dielectric properties, its perimeter (including the free sides) remains in the well-conducting state. The situation becomes similar to that realized in the Corbino geometry sample, and the x/w-type inhomogeneity of $\varphi(x)$ is easily explained. It remains to demonstrate that the contact-potential difference at the short sides of the rectangular sample gives rise to an inhomogeneity of the electron density in the section $-w \leq x \leq +w$.

The electrostatic part of the problem is formulated as follows:

$$e\varphi(x, y) = \frac{2e^2}{\kappa} \int_{-l}^{2+l} d\sigma \int_{-w}^{+w} ds \frac{\delta n(s, \sigma)}{\sqrt{(x-s)^2 + (y-\sigma)^2}}$$

$$= \text{const} = W,$$ (1)

$$-w \leq x \leq +w, \quad -l \leq y \leq +l;$$

$$\varphi(x, y) = 0, \quad -w \leq x \leq +w,$$

$$-\infty \leq y \leq -l \quad \text{or} \quad +l \leq y \leq +\infty.$$ (2)

Here, $\delta n(x, y, t)$ is the deviation of the electron density from the equilibrium value in the absence of the contact energy W and κ is the dielectric constant. For simplicity, the potentials of the metallic contacts are assumed to be identical (and equal to zero).

In expressions (1) and (2), we change over to the Fourier components with respect to the variable *y* and obtain

$$\delta n(x, y) \propto \delta n(x, q) \exp(iqy),$$
$$\varphi(x, y) \propto \varphi(x, q) \exp(iqy),$$ (3)

$$\varphi(x, q) = \text{const} = \frac{2e}{\kappa} \int_{-w}^{+w} \delta n(s, q) K_0(q|x-s|) ds,$$ (4)

$$0 \leq |q| \leq 2\pi/l.$$

Here, $K_0(x)$ is the modified Bessel function.

In the range of small arguments, the $K_0(x)$ function has a logarithmic singularity. Hence, in the central part of the 2D rectangle, the solution of the integral equation (4) for $\delta n(x, q)$ has a form similar to the solution of the problem for an infinite charged strip of width $2w$, that is,

$$e\varphi(x) = \frac{2e^2}{\kappa} \int_{-w}^{+w} \delta n(s) \ln|x-s| ds = \text{const}.$$ (5)

The solution of problem (5) for $\delta n(x)$ yields the relationship

$$\delta n(x) \propto \frac{\text{const}}{\sqrt{w^2 - x^2}}.$$ (6)

Therefore, in our case,

$$\delta n(x, q)_{q \to 0} \propto \frac{\text{const}}{\sqrt{w^2 - x^2}}.$$ (7)

The limit $q \longrightarrow 0$ implies that the inequality $w \ll l$ is met and the cross-section of the 2D rectangle is chosen in the vicinity of its middle. Near the short sides of the sample, the electron density distribution should deviate from asymptotics (7).

Thus, the electron density inhomogeneity is observed in all the Hall cross-sections of the rectangular 2D samples, which are in ohmic contact with metallic control electrodes only at certain portions of their perimeter. Evidently, the specific details of the dependence $\delta n(x)$ for the Corbino and rectangular configurations are different. Recall that, in the presence of contact phenomena in the Corbino disk, the dependence $\delta n(x)$ is represented as

$$\delta n(x) \propto \frac{\text{const}}{(w^2 - x^2)},$$ (8)

which is valid in the quasi-one-dimensional case at $(R_1 - R_2)/(R_1 + R_2) \ll 1$, where R_1 and R_2 are the outer and inner radii of the 2D Corbino disk. A qualitative similarity between the disturbances defined by expressions (7) and (8) is obvious. It is also clear that, in a magnetic field, the sample with the density inhomogeneity described by relationship (7) or (8) cannot have an integer filling factor throughout its surface. This is confirmed by the data obtained in [3, 4], which are qualitatively represented in Fig. 1 (line *B*).

2.2. Now, we turn to the discussion of the inhomogeneity scale in the 2D samples. Unfortunately, the available equilibrium electrooptical data [2–4] and, in particular, the results presented in Fig. 1 (line *B*) give no absolute values of the potential $\varphi(x)$. This is essential for the solution of the problem as a whole and also for a detailed description of this potential, which depends on the ratio between the energies $\hbar\omega_c$ and W (where ω_c is the cyclotron frequency). For $\hbar\omega_c \leq W$, the central part of the 2D channel is predominantly occupied by one incompressible strip of width $2a \leq 2w$ with a particular distribution $\varphi(x)$. In the case when $\hbar\omega_c \ll W$, the 2D channel is filled by a large number of incompressible strips, so that the averaged distribution $\varphi(x)$ appears to be different. In the absence of absolute data on the potential $\varphi(x)$, the probable difference in its behavior can be useful in analyzing 2D systems.

The solution of the problem of an isolated symmetrical incompressible channel, which, in the general form, was considered by Chklovskiĭ *et al.* [5] (for more

details of this problem in the presence of contact phenomena, see also [1]), results in the following relationship for $\varphi(x)$:

$$\varphi(x) \propto (a^2 - x^2)^{3/2}, \quad -a \leq x < +a, \qquad (9)$$

where $2a < 2w$ is the width of the incompressible strip. The maximum width at the electron density described by expression (8) is determined by the formula

$$(a_{max}/w)^3 = \frac{3\pi\hbar\omega_c}{2W}. \qquad (10)$$

Note that the strip width is rather sensitive to a magnetic field. As the magnetic field strength increases, the width of the strip varies from zero at the instant of its formation to the critical size [formula (10)] when the maximum value of potential (9) in the center of the channel reaches the value of $\hbar\omega_c$, after which the strip studied breaks into two strips (for more details, see [5]).

In the case when $\hbar\omega_c \ll W$, the formation of a large number of incompressible strips becomes possible and expressions (9) and (10) lose their meaning. Hence, it is necessary to use a formalism accounting for a large number of strips and their interaction with each other. One way to accomplish this is to take into account the potential difference $\hbar\omega_c$ across the edges of each strip. Then, the local electric potential in the problem with a large number of strips can be written as

$$e\varphi(x) \simeq \hbar\omega_c\nu(x), \quad \nu(x) = \pi l_H^2 n(x), \qquad (11)$$

where $\nu(x)$ is the local filling factor.

According to relationships (11), in the limit $\hbar\omega_c \ll W$, the electric potential, on the average, reproduces the local behavior of the electron density.

2.3. Let us treat the available experimental data [3, 4] on the equilibrium distribution of $\varphi(x)$ in the Corbino and rectangular samples according to relationships (7)–(11).

The most interesting qualitative results obtained in [3] are displayed in Fig. 1 (line B), according to which the electron density distribution in the Hall sample is inhomogeneous. Unfortunately, a number of uncertainties in these data make their interpretation more difficult. In particular, a pronounced asymmetry can be due to the effect of adjacent channels. Moreover, the cross-section position chosen by the authors for the convenience of measurements is close to the short side of the 2D system and is poorly determined, which complicates the detailed description of $\varphi(x)$.

The results obtained for the Corbino disk are more readily interpreted. The experimental data obtained in [4] are compared with the multichannel [relationship (11)] and single-channel [relationship (9)] distributions of $\varphi(x)$ in Figs. 2 and 3, respectively. The calculated
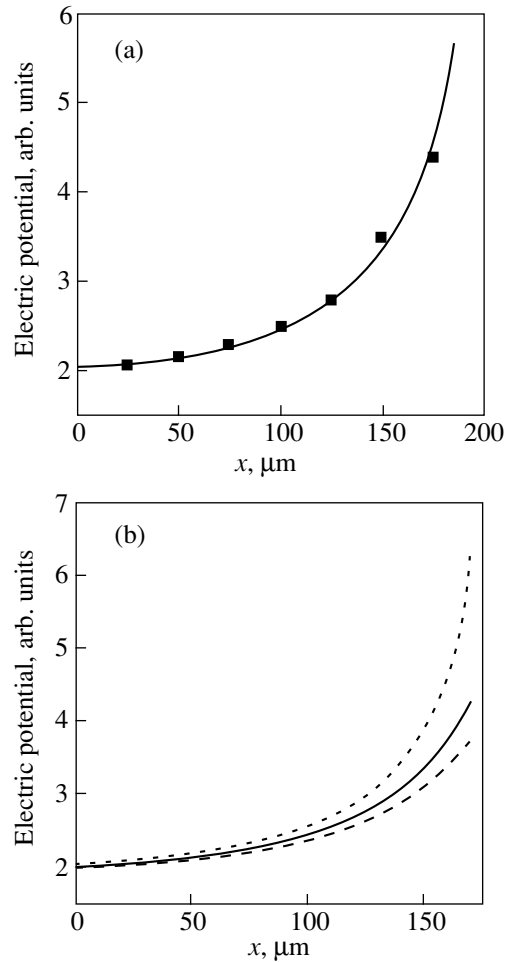

Fig. 2. (a) Coordinate dependences of the potentials defined by relationships (12), (11), and (8). The solid line corresponds to the parameters $R = 50$ μm and $\omega = 250$ μm. Points are the experimental data taken from [4]. (b) Evolution of the potentials [relationships (12), (11), and (8)] with a variation in radius R (μm): 75 (points), 50 (solid line), and 5 (dashed line).
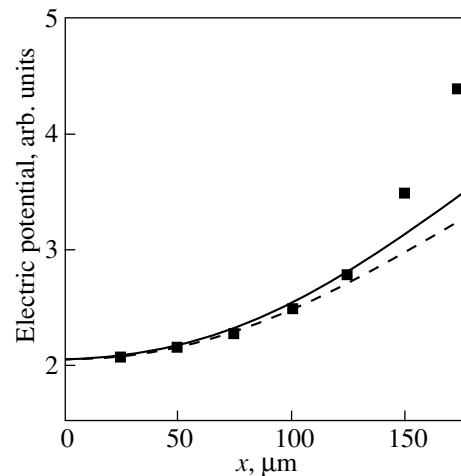

Fig. 3. Dependences $\varphi(x)$ defined by relationships (12) and (9) at $R = 50$ μm and different parameters a (μm): 230 (solid line) and 250 (dashed line).

curves $\phi(x)$ were constructed with the use of the expression

$$\phi(x) = \frac{1}{2R} \int_{x-R}^{x+R} \varphi(s)ds. \qquad (12)$$

Here, R is the radius of a laser beam used in the experiments [3, 4]. The curves were located with reference to the minimum $\phi(0)$ and were then fitted to the experimental points by varying R and the geometric parameters that enter into relationships (11) and (9). The solid line in Fig. 2a corresponds to $R = 50\,\mu m$ and $w = 250\,\mu m$. Figure 2b illustrates how the radius of the laser beam affects the behavior of $\phi(x)$. The $\varphi(x)$ dependence calculated from relationship (9) with two different a values and $R = 50\,\mu m$ is fitted to the same experimental points in Fig. 3.

It should be noted that the experimental points displayed in Figs. 2 and 3 were obtained by scanning Figs. 1 and 2, taken from [4]. Then, using Fig. 9 from [3], which is identical to Fig. 1 in [4], the data obtained by scanning Fig. 2 taken from [4] were recalculated in terms of $\phi(x)$.

Summing up, we can state that the best agreement between the data obtained in [4] and the calculated dependence $\varphi(x)$ is achieved with relationship (11) (Fig. 2). However, more reliable inferences regarding variants of the $\varphi(x)$ distributions require a knowledge of the anomaly scale, which hitherto has not been determined in experiments performed under equilibrium conditions.

3. MEASUREMENTS IN A TRANSPORT REGIME

The anomaly scale we are interested in (for example, the magnitude of the electrostatic "dip" in Fig. 1) can be estimated from experiments with a transport current. In this case, the problem includes an additional energy parameter—the driving voltage V. This offers new possibilities for further analysis, specifically for the Corbino disk.

The electrical part of the problem in the presence of a transport current needs special comments. There are several approximate schemes of these calculations.

For $\sigma_{xx} \neq 0$, the calculations are based on the condition $\mathrm{div}\mathbf{j} = 0$, which, according to the Ohm law, can be reduced to the equation for $\varphi(x, y)$ with boundary conditions that allow joining the potentials in normal and integer ranges. In this formulation, the problem is as yet unsolved.

If $\sigma_{xx} = 0$, which is quite reasonable for the quantum Hall effect, the condition $\mathrm{div}\mathbf{j} = 0$ degenerates. In this case, it is necessary to search for other relationships between $\varphi(x, y)$ and $\delta n(x)$, which, together with the Poisson equation, would provide closure of the electrostatic problem. An example of this solution independent of σ_{xx} is given in [6]. In the present work, the formulated problem is solved within the contact approxi-

mation, which is a simple extension of the approach proposed in [1]. The case in point is the electron density distribution over the cross section of the 2D system in contact with supplying electrodes, which accounts for the effect of the contact-potential difference and the driving voltage. With this distribution, we can readily obtain the distribution of $\varphi(x)$ with the use of relationship (11), providing that $eV \gg \hbar\omega_c$. By definition,

$$\delta n(x) = \frac{1}{4\pi e^2}\left(\left.\frac{\partial u}{\partial z}\right|_{+0} - \left.\frac{\partial u}{\partial z}\right|_{-0} \right), \qquad (13)$$

$$u(x, z)|_{z \to 0} = \begin{cases} 0, & -\infty \leq x \leq -w \\ W, & -w \leq x \leq +w \\ eV, & +w \leq x \leq +\infty. \end{cases} \qquad (14)$$

Using the known solution of the Dirichlet problem (14), we calculate the required derivatives [formula (13)] and obtain the relationship for $\delta n(x)$, that is,

$$\delta n(x) = \frac{w(2W - eV) - eVx}{2\pi^2 e^2(w^2 - x^2)}. \qquad (15)$$

In the limit $V \longrightarrow 0$, expression (15) transforms into relationship (8).

The distribution described by formula (15) exhibits a characteristic maximum at the point x_m

$$\frac{|x_m|}{w} = \left(\left(\frac{2W}{|eV|} - 1\right) - \sqrt{\left(\frac{2W}{|eV|} - 1\right)^2 - 1} \right). \qquad (16)$$

The maximum in the $\varphi(x)$ distribution is observed in the experiment. According to [3], $x_m/w \simeq 0.8$ at $eV \simeq 0.3$ eV. In this case, from relationship (16), we have $W \simeq 0.73$ eV. The value of $\hbar\omega_c$ is of the order of 100 K; i.e., the condition $W \gg \hbar\omega_c$, which allows us to use expression (11) relating the density (15) to the observed electrostatic potential, is rigorously fulfilled.

4. CONCLUSION

In this work, we proposed a scheme for describing the inhomogeneous 2D electronic systems, which contain a large number of integer channels in a magnetic field. The average description of the channel system leads to the conclusion that the observed electrostatic potential is proportional to the inhomogeneous electron density of the sample [see relationship (11)]. For a transport current, the model explains the observed location of the electrostatic maximum within the 2D sample.

ACKNOWLEDGMENTS

REFERENCES

1. V. B. Shikin and Yu. V. Shikina, Fiz. Tverd. Tela (St. Petersburg) **41**, 1103 (1999) [Phys. Solid State **41**, 1005 (1999)].

2. P. F. Fontein, P. Hendriks, F. A. Bloom, *et al.*, Surf. Sci. **263**, 91 (1992).

3. R. Knott, W. Dietsche, K. von Klitzing, *et al.*, Semicond. Sci. Technol. **10**, 117 (1995).

4. W. Dietsche, K. von Klitzing, and K. Ploog, Surf. Sci. **361/362**, 289 (1996).

5. D. B. Chklovskii, B. I. Shklovskii, and L. I. Glazman, Phys. Rev. B **46** (7), 4026 (1992); D. B. Chklovskii, K. F. Matveev, and B. I. Shklovskii, Phys. Rev. B **47** (18), 12605 (1993).

6. A. H. MacDonald, T. M. Rice, and W. F. Brinkman, Phys. Rev. B **28**, 3648 (1983).

Translated by O. Borovik-Romanova

LOW-DIMENSIONAL SYSTEMS
AND SURFACE PHYSICS

Change in the Shape of a Symmetric Light Pulse Passing through a Quantum Well

L. I. Korovin[1], I. G. Lang[1], D. A. Contreras-Solorio[2], and S. T. Pavlov[2, 3]

[1] *Ioffe Physicotechnical Institute, Russian Academy of Sciences, ul. Politekhnicheskaya 26, St. Petersburg, 194021 Russia*

e-mail: ilang@dor.ioffe.rssi.ru

[2] *Escuela de Física de la UAZ, Apartado Postal c-580, Zacatecas, 98060 México*

e-mail: pavlov@ahobon.reduaz.mx

[3] *Lebedev Institute of Physics, Russian Academy of Sciences, Leninskiĭ pr. 53, Moscow, 117924 Russia*

Received April 14, 2000

Abstract—A theory for the response of a $2D$ two-level system to irradiation by a symmetric light pulse is developed. Under certain conditions, such an electron system approximates an ideal solitary quantum well in a zero field or a strong magnetic field **H** perpendicular to the plane of the well. One of the energy levels is the ground state of the system, while the other is a discrete excited state with energy $\hbar\omega_0$, which may be an exciton level for **H** = 0 or any level in a strong magnetic field. It is assumed that the effect of other energy levels and the interaction of light with the lattice can be ignored. General formulas are derived for the time dependence of the dimensionless "coefficients" of the reflection $\mathcal{R}(t)$, absorption $\mathcal{A}(t)$, and transmission $\mathcal{T}(t)$ for a symmetric light pulse. It is shown that the $\mathcal{R}(t)$, $\mathcal{A}(t)$, and $\mathcal{T}(t)$ time dependences have singular points of three types. At points t_0 of the first type, $\mathcal{A}(t_0) = \mathcal{T}(t_0) = 0$ and total reflection takes place. It is shown that for $\gamma_r \gg \gamma$, where γ_r and γ are the radiative and nonradiative reciprocal lifetimes, respectively, for the upper energy level of the two-level system, the amplitude and shape of the transmitted pulse can change significantly under the resonance $\omega_l = \omega_0$. In the case of a long pulse, when $\gamma_l < \gamma_r$, the pulse is reflected almost completely. (The quantity γ_l characterizes the duration of the exciting pulse.) In the case of an intermediate pulse duration $\gamma_l \simeq \gamma_r$, the reflection, absorption, and transmission are comparable in value and the shape of the transmitted pulse differs considerably from the shape of the exciting pulse: the transmitted pulse has two peaks due to the existence of the point t_0 of total reflection, at which the transmission is zero. If the carrier frequency ω_l of light differs from the resonance frequency ω_0, the oscillating $\mathcal{R}(t)$, $\mathcal{A}(t)$, and $\mathcal{T}(t)$ time dependences are observed at the frequency $\Delta\omega = \omega_l - \omega_0$. Oscillations can be observed most conveniently for $\Delta\omega \simeq \gamma_l$. The position of the singular points of total absorption, reflection, and transparency is studied for the case when ω_l differs from the resonance frequency. © 2000 MAIK "Nauka/Interperiodica".

A strong change in the shape of a strongly asymmetric light pulse with a steep front passing through a quantum well and a large intensity of the reflected pulse were predicted by Lang and Belitsky [1]. They assumed that the carrier frequency ω_l of the exciting pulse is close to the electron excitation energy ω_0 measured from the ground-state energy. These phenomena can take place under the condition

$$\gamma_r \gg \gamma, \qquad (1)$$

where γ_r and γ are the reciprocal radiative and nonradiative lifetimes of the electron excitation, respectively. It is well known that in the opposite case, when

$$\gamma_r \ll \gamma, \qquad (2)$$

the shape of the pulse transmitted through the well changes insignificantly and the reflected and absorbed pulses are weaker than the exciting pulse.

The radiative broadening of energy levels takes place for quasi-two-dimensional systems as a result of breaking of the translational symmetry in a direction perpendicular to the plane of the well [2, 3]. For high-quality wells, the radiative broadening γ_r can be comparable with the contributions from other relaxation mechanisms and can even exceed them. This new physical situation requires an adequate theoretical description in which higher order terms in the interaction between electrons and the electromagnetic field must be taken into account [1–14]. The reciprocal radiative lifetime γ_r for the exciton energy level in a quantum well was calculated in [2] for zero magnetic field, in [11, 12] for a strong magnetic field, and in [12] for a magnetic polaron in a quantum well.

Here, we consider a two-level system having the ground state and an excited state. We assume that the influence of other energy levels can be ignored. The

role of the electron excitation can be played by an exciton in a quantum well in a zero or a strong magnetic field. Since it is difficult to obtain a light pulse with one steep front, we consider, in contrast to [1], a symmetric pulse.

1. ELECTRIC FIELDS TO THE RIGHT AND LEFT OF A QUANTUM WELL UNDER PULSED IRRADIATION

Let us suppose that an exciting light pulse falls on a solitary quantum well from the left (where $z < 0$) and that the electric field corresponding to it has the form

$$\mathbf{E}_0(z, t) = E_0\mathbf{e}_l\exp(-i\omega_l p)\{\Theta(p)\exp(-\gamma_{l1}p/2)$$
$$+ [1 - \Theta(p)]\exp(-\gamma_{l1}p/2)\} + \text{c.c.,} \quad (3)$$

where E_0 is the real-valued amplitude, $\mathbf{e}_l$ is the polarization vector; $p = t - zn/c$, n is the refractive index of the medium outside the well; $\Theta(p)$ is a step function; and γ_{l1} and γ_{l2} define the attenuation and build-up of the symmetric pulse, respectively. The pulse in Eq. (3) corresponds to the Poynting vector

$$\mathbf{S}(p) = \mathbf{S}_0 P(p),$$
$$\mathbf{S}_0 = \mathbf{e}_z c E_0^2/(2\pi n), \quad (4)$$

$$P(p) = \Theta(p)\exp(-\gamma_{l1}p/2)$$
$$+ [1 - \Theta(p)]\exp(-\gamma_{l2}p/2), \quad (5)$$

where $\mathbf{e}_z$ is a unit vector along the z axis.

We carry out the Fourier transformation of expression (3) written in the form

$$\mathbf{E}_0(z, t) = E_0\mathbf{e}_l\int_{-\infty}^{\infty} d\omega e^{-i\omega p}\mathcal{D}_0(\omega) + \text{c.c.,} \quad (6)$$

where

$$\mathcal{D}_0(\omega) = \frac{i}{2\pi}$$
$$\times [(\omega - \omega_l + i\gamma_{l1}/2)^{-1} - (\omega - \omega_l - i\gamma_{l2}/2)^{-1}]. \quad (7)$$

In [1, 10, 11], a strongly asymmetric pulse with a steep front was used, for which $\gamma_{l2} \longrightarrow \infty$ and the second term in Eq. (5), as well as the second term in the brackets in Eq. (7), vanishes. For

$$\gamma_{l1} = \gamma_{l2} = \gamma_l, \quad (8)$$

the pulse in Eq. (3) is symmetric. For $\gamma_l \longrightarrow 0$, the symmetric pulse is transformed into a monochromatic wave of frequency ω_l and the function $\mathcal{D}_0(\omega)$ is transformed into $\delta(\omega - \omega_l)$. The pulse of the form of Eq. (3) is convenient for computations. Its drawback is the discontinuity of the derivative at the point $t - zn/c$ [see Eq. (5)], but all the qualitative conclusions that will be drawn below remain valid after a transition to pulses with a smoothed shape. Some results for a symmetric pulse proportional to $[\cosh(\gamma_l p)]^{-1}$ are given in [1].

Let us consider quantum wells whose width d is much smaller than the wavelength $c/(n\omega_l)$ of a light wave. In this case, the electric fields $\mathbf{E}_{l(r)}(z, t)$ on the left (right) of the quantum well are given by [1]

$$\mathbf{E}_{l(r)}(z, t) = \mathbf{E}_0(z, t) + \Delta\mathbf{E}_{l(r)}(z, t), \quad (9)$$

$$\Delta\mathbf{E}_{l(r)}(z, t) = E_0\mathbf{e}_l\int_{-\infty}^{\infty} d\omega e^{-i\omega(t \pm zn/c)}\mathcal{D}(\omega) + \text{c.c.,} \quad (10)$$

where the upper (lower) sign corresponds to the subscript l (r). In accordance with Eq. (10), the polarization of the induced electric field coincides with the polarization of the exciting field. Result (10) presumes that the incident waves have a circular polarization

$$\mathbf{e}_l = 2^{-1/2}(\mathbf{e}_x \pm i\mathbf{e}_y), \quad (11)$$

where $\mathbf{e}_x$ and $\mathbf{e}_y$ are unit vectors along the x and y axes, respectively. It is also assumed that each of the two circular polarizations corresponds to the excitation (from the ground state) of one of the two types of electron–hole pairs (EHP) with the same energy (see [12, 15]).

The frequency dependence of $\mathcal{D}(\omega)$ has the form

$$\mathcal{D}(\omega) = -\frac{4\pi\chi(\omega)\mathcal{D}_0(\omega)}{1 + 4\pi\chi(\omega)}, \quad (12)$$

$$\chi(\omega) = (i/4\pi)\sum_{\rho}(\gamma_{r\rho}/2)$$
$$\times [(\omega - \omega_\rho + i\gamma_\rho/2)^{-1} + (\omega + \omega_\rho + i\gamma_\rho/2)^{-1}], \quad (13)$$

where ρ is the index of the excited state; $\hbar\omega_\rho$ is the energy of the excited state measured from the ground state; and $\gamma_{r\rho}$ and γ_ρ are the radiative and nonradiative reciprocal lifetimes of the excited state with the index ρ, respectively. The second term in the brackets in Eq. (13) is a nonresonant term, which will henceforth be disregarded. We assume that the reflection and absorption of light by the quantum well are due only to electron transitions from the valence band to the conduction band. The interaction of light with the lattice and deep electron levels is disregarded.

It was mentioned above that in the sum in Eq. (13) we take into account the only excited level; i.e., we consider a two-level system in which the first level corresponds to the ground state, and the second, to the excited state. The index ρ assumes only one value, and hence the following notation will be used:

$$\omega_\rho = \omega_0, \quad \gamma_{r\rho} = \gamma_r, \quad \gamma_\rho = \gamma, \quad \Gamma = \gamma_r + \gamma. \quad (14)$$

Using formulas (7)–(13), we obtain the following result for the field induced on the left of the well under

irradiation by a symmetric pulse:

$$\Delta \mathbf{E}_l(z, t) = -iE_0 \mathbf{e}_l(\gamma_r/2)$$

$$\times \left\{ \mathscr{E} \Theta(s) + \frac{(1 - \Theta(s)) \exp(-i\omega_0 s - \Gamma s/2)}{\Delta\omega + i(\Gamma + \gamma_l)/2} \right\} + \text{c.c.},$$

$$\mathscr{E} = \frac{\exp(-i\omega_l s - \gamma_l s/2)}{\Delta\omega + i(\Gamma - \gamma_l)/2} - \exp(-i\omega_0 s - \Gamma s/2)$$

$$\times \left[\frac{1}{\Delta\omega + i(\Gamma - \gamma_l)/2} - \frac{1}{\Delta\omega + i(\Gamma + \gamma_l)/2} \right], \quad (15)$$

where $s = t + zn/c$ and $\Delta\omega = \omega_l - \omega_0$. The expression for $\Delta \mathbf{E}_r(z, t)$ differs from Eq. (15) only in the substitution of the variable $p = t - zn/c$ for s. Since expression (15) is valid for $|z| \gg d$, we will henceforth ignore the width of the quantum well, assuming that it lies in the plane $z = 0$.

2. CALCULATION OF TRANSMITTED, REFLECTED, AND ABSORBED ENERGY FLUXES

For the sake of brevity, we will refer to the Poynting vector as the energy flux. The transmitted flux, i.e., the flux on the right of the well, is given by

$$\mathbf{S}_r(z, t) = (\mathbf{e}_z/4\pi)(c/n)(\mathbf{E}_r(p))^2, \quad (16)$$

while the flux on the left of the well is

$$\mathbf{S}_l(z, t) = \mathbf{S}(p) + \mathbf{S}_{\text{ref}}(s), \quad (17)$$

where $\mathbf{S}_{(p)}$ is the flux of the exciting light pulse defined by Eq. (4) and $\mathbf{S}_{\text{ref}}(s)$ is the reflected flux, which is given by

$$\mathbf{S}_{\text{ref}}(s) = -(\mathbf{e}_z/4\pi)(c/n)(\Delta \mathbf{E}_l(s))^2. \quad (18)$$

The absorbed energy flux is defined as

$$\mathbf{S}_{\text{abs}}(t) = \mathbf{S}_l(z = 0, t) - \mathbf{S}_r(z = 0, t) \quad (19)$$

and is equal to

$$\mathbf{S}_{\text{abs}}(t) = -(\mathbf{e}_z/2\pi)(c/n)\mathbf{E}_r(z = 0, t)\Delta\mathbf{E}(t), \quad (20)$$

where

$$\Delta\mathbf{E}(t) = \Delta\mathbf{E}_l(z = 0, t) = \Delta\mathbf{E}_r(z = 0, t). \quad (21)$$

We introduce the dimensionless "coefficients" of the transmission $\mathscr{T}(x)$, reflection $\mathscr{R}(x)$, and absorption $\mathscr{A}(x)$, defining them as

$$\mathbf{S}_r(z, t) = \mathbf{S}_0 \mathscr{T}(p), \quad \mathbf{S}_{\text{ref}}(z, t) = -\mathbf{S}_0 \mathscr{R}(s),$$
$$\mathbf{S}_{\text{abs}}(t) = \mathbf{S}_0 \mathscr{A}(t) \quad (22)$$

It follows from Eq. (19) that the equality

$$\mathscr{T}(x) + \mathscr{R}(x) + \mathscr{A}(x) = P(x) \quad (23)$$

always holds. The quantities $P(x)$, $\mathscr{T}(x)$, and $\mathscr{R}(x)$ are always positive, while absorption can be positive or

negative. Negative absorption at a certain instant t indicates that the electron system of the quantum well gives away the energy accumulated during previous time intervals. Instead of the notation x for the variable, we will henceforth use the notation t, bearing in mind the definitions in Eq. (22). The variable t corresponds to real time for $z = 0$.

3. TIME POINTS OF ZERO ABSORPTION, TOTAL REFLECTION, AND COMPLETE TRANSMISSION

This section is based on an analysis of the formulas from Section 2, which is carried out without specifying the expression for the induced field $\Delta\mathbf{E}(z, t)$. For this reason, the results obtained below are valid for any number of excited energy levels in the quantum well (see, for example, [10–14]) rather than only in the case of a single energy level for which formula (15) is applicable.

In the figures presenting the $\mathscr{A}(t)$, $\mathscr{T}(t)$, and $\mathscr{R}(t)$ curves, we can see the points of zero absorption $\mathscr{A}(t) = 0$, total reflection $\mathscr{R}(t) = P(t)$, and complete transmission $\mathscr{T}(t) = P(t)$. We will refer to these time points as singular points. It follows from formulas (16), (18), and (20) that these points can be of three types. For the first two types, they correspond to the disappearance of the electric fields or their combinations. For singular points of the first type, the fields $\mathbf{E}_r(z = 0, t)$ or $\Delta\mathbf{E}_l(x = 0, t)$ are equal to zero. For the case of $\mathbf{E}_r(z = 0, t_0) = 0$, we have

$$\mathscr{A}(t_0) = 0, \quad \mathscr{T}(t_0) = 0, \quad \mathscr{R}(t_0) = P(t_0), \quad (24)$$

and the point t_0 is referred to as the point of total reflection of the first type. For the case of $\Delta\mathbf{E}_l(z = 0, t_x) = 0$, we have

$$\mathscr{A}(t_x) = 0, \quad \mathscr{R}(t_x) = 0, \quad \mathscr{T}(t_x) = P(t_x), \quad (25)$$

and the point t_x is referred to as the point of complete transmission of the first type. Thus, the absorption $\mathscr{A}(t) = 0$ at singular points of total reflection and complete transmission of the first type.

The equality $P(t) - \mathscr{R}(t) = 0$ can be written in the form

$$(\mathbf{E}_0)^2 - (\Delta\mathbf{E})^2 = 0, \quad (\mathbf{E}_0 + \Delta\mathbf{E})(\mathbf{E}_0 - \Delta\mathbf{E}) = 0,$$
$$\mathbf{E}_r(\mathbf{E}_0 - \Delta\mathbf{E}) = 0, \quad (26)$$

while the equality $P(t) - \mathscr{T}(t) = 0$ can be written as

$$(\mathbf{E}_0)^2 - (\Delta\mathbf{E}_r)^2 = 0, \quad (\mathbf{E}_0 - \mathbf{E}_r)(\mathbf{E}_0 + \mathbf{E}_r) = 0,$$
$$\Delta\mathbf{E}(\mathbf{E}_0 + \mathbf{E}_r) = 0. \quad (27)$$

Consequently, the condition $\mathbf{E}_0 - \Delta\mathbf{E} = 0$ corresponds to the point of total reflection, while the condition $\mathbf{E}_0 + \mathbf{E}_r = 0$ corresponds to the point of complete transmission. At these points, the absorption $\mathscr{A}(t)$ generally differs from zero. We will refer to these points as the points of total reflection and complete transmission of the second type. Finally, expressions (20), (26), and

(27) indicate that the special points $\mathscr{A} = 0$, $\mathscr{R} = P$, and $\mathscr{T} = P$ can appear when the vector $\mathbf{E}_r$ is perpendicular to $\Delta\mathbf{E}$, $\mathbf{E}_r$ is perpendicular to $\mathbf{E}_0 - \Delta\mathbf{E}$, and $\Delta\mathbf{E}$ is perpendicular to $\mathbf{E}_0 + \mathbf{E}_r$, respectively. These singular points will be referred to as singular points of the third type.

In experiments, the singular points can be observed as follows. We will measure the transmission as a function of time t in the plane $z = z_0$, while the reflection will be measured in the plane $z = -z_0$, i.e., on the left of the quantum well. Let t_0 be the point of total reflection of the first type. Taking into account expression (22), we find that at the instant $t = t_0 + z_0 n/c$, the transmission is equal to zero, while the reflection is total. The absorption $\mathscr{A}$ cannot be measured directly, but, having defined it as $\mathscr{A} = P - \mathscr{R} - \mathscr{T}$ at the instant $t = t_0 + z_0 n/c$, we find that $\mathscr{A} = 0$ for a singular point of the first type. This means that, in such an experiment, the absorption is measured with a delay by the time interval $\Delta t = z_0 n/c$.

4. ENERGY FLUXES IN THE CASE OF EXACT RESONANCE FOR ARBITRARY RELATIONS BETWEEN RECIPROCAL LIFETIMES

Using the results obtained in Section 2 and expressions (3), (8), (9), and (15) for electric fields, we can determine the transmitted, reflected, and absorbed energy fluxes for any values of the parameters ω_l and γ_l characterizing the exciting pulse and of the parameters ω_0, γ_r, and γ characterizing the energy level in the quantum well.

For $\gamma_l = 0$, which corresponds to monochromatic irradiation, we obtain the expressions

$$\mathscr{T} = \frac{(\Delta\omega)^2 + \gamma^2/4}{(\Delta\omega)^2 + \Gamma^2/4}, \quad \mathscr{R} = \frac{\gamma^2/4}{(\Delta\omega)^2 + \Gamma^2/4},$$

$$\mathscr{A} = \frac{\gamma\gamma_r/2}{(\Delta\omega)^2 + \Gamma/4}, \tag{28}$$

which were derived earlier in [2–5, 8].

In the case of exact resonance

$$\omega_l = \omega_0, \tag{29}$$

we obtain the following results for the quantities characterizing the energy fluxes:

$$\mathscr{T}(p) = \Theta(p)[\mathscr{F}_T(p)]^2 + [1 - \Theta(p)]$$

$$\times \exp(\gamma_l p)(\gamma + \gamma_l)^2/(\Gamma + \gamma_l)^2,$$

$$\mathscr{F}_T(p) = \exp(-\gamma_l p/2)(\gamma - \gamma_l)/(\Gamma - \gamma_l) \tag{30}$$

$$+ \exp(-\Gamma p/2)\gamma_r G,$$

$$\mathscr{R}(s) = \gamma_r^2\{\Theta(s)[\mathscr{F}_R(s)]^2$$

$$+ [1 - \Theta(s)]\exp(\gamma_l s)(\Gamma + \gamma_l)^{-2}\},$$

$$\mathscr{F}_R(s) = (\exp(-\gamma_l s/2) - \exp(-\Gamma s/2))/(\Gamma - \gamma_l) \tag{31}$$

$$+ \exp(-\Gamma s/2)/(\Gamma + \gamma_l),$$

$$\mathscr{A}(t) = 2\gamma_r\{\Theta(t)\mathscr{F}_A(t)$$

$$+ [1 - \Theta(t)]\exp(\gamma_l t)(\gamma + \gamma_l)/(\Gamma + \gamma_l)^2\},$$

$$\mathscr{F}_A(t) = \exp(-\gamma_l t)\frac{\gamma - \gamma_l}{(\Gamma - \gamma_l)^2} - \gamma_r G^2 \exp(-\Gamma t)$$

$$+ G\exp(-(\Gamma + \gamma_l)t/2)\frac{\gamma_r - \gamma + \gamma_l}{\Gamma - \gamma_l}. \tag{32}$$

In formulas (30) and (32), we have introduced the notation $G = (\Gamma - \gamma_l)^{-1} - (\Gamma + \gamma_l)^{-1}$. Expressions (9) and (15) for $\omega_l = \omega_0$ imply that the position of the point t_0 of total reflection of the first type is determined by the condition $t > 0$ and the equation

$$\exp(-\gamma_l t/2)\frac{\Gamma - \gamma_l - \gamma_r}{\Gamma - \gamma_l}$$

$$+ \exp(-\Gamma t/2)\frac{2\gamma_r\gamma_l}{\Gamma^2 - \gamma_l^2} = 0. \tag{33}$$

Solving this equation, we obtain

$$t_0 = \frac{2}{\Gamma - \gamma_l}\ln\frac{2\gamma_r\gamma_l}{(\gamma_l - \gamma)(\Gamma + \gamma_l)}, \quad \gamma_l > \gamma, \tag{34}$$

so that the point of total reflection always exists for a short pulse. This means that, for larger values of time, the absorption of energy by the quantum well is replaced by energy generation since $\mathscr{A}(t_0) = 0$ and is negative for $t > t_0$.

The position of the point t_t of complete transmission of the second type, at which $\mathbf{E}_r + \mathbf{E}_0 = 0$, is determined by the conditions

$$t > 0,$$

$$\exp(-\gamma_l t/2)\left(2 - \frac{\gamma_r}{\Gamma - \gamma_l}\right) + \exp(-\Gamma t/2)\frac{2\gamma_r\gamma_l}{\Gamma^2 - \gamma_l^2} = 0, \tag{35}$$

which lead to

$$t_t = \frac{2}{\Gamma - \gamma_l}\ln\frac{2\gamma_r\gamma_l}{(\Gamma + \gamma_l)(2\gamma_l - \Gamma - \gamma)}, \tag{36}$$

$$\gamma_l > \gamma + \gamma_r/2.$$

It follows from Eq. (36) that the point t_t exists for short pulses. Note that the condition $\gamma_l > \gamma + \gamma_r/2$ is more stringent than the requirement $\gamma_l > \gamma$ from Eq. (34).

In the case of only one excited level in question, under the condition of exact resonance $\omega_l = \omega_0$, the conditions $\Delta\mathbf{E} = 0$ and $\mathbf{E}_0 - \Delta\mathbf{E} = 0$ cannot be met and, hence, the points of complete transmission of the first
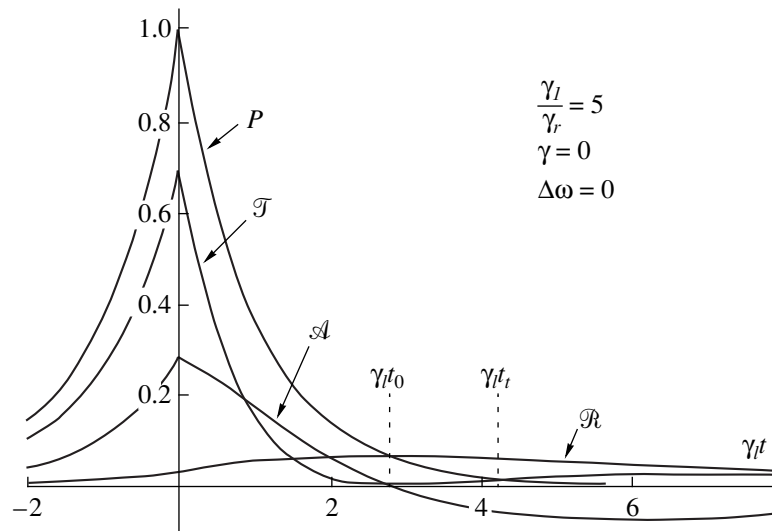
Fig. 1. Dimensionless "coefficients" of the reflection $\mathcal{R}(t)$, absorption $\mathcal{A}(t)$, and transmission $\mathcal{T}(t)$ for a symmetric light pulse and a two-level system in the case of exact resonance $\Delta\omega = \omega_l - \omega_0 = 0$ and a short pulse. Here, t_0 is a total-reflection point of the first type; t_t is a complete-transmission point of the second type; γ_r and γ are the radiative and nonradiative reciprocal lifetimes of the excited level, respectively; γ_l determines the duration of the chosen symmetric pulse; ω_l is the carrier frequency; and ω_0 is the resonance transition frequency.

type and of total reflection of the second type do not exist, which is reflected in Figs. 1–3.

Singular temporal points of the third type in the case of exact resonance do not exist either. Indeed, the vectors $\mathbf{E}_0$, $\mathbf{E}_r$, and $\Delta\mathbf{E}$ are parallel at all instants. This can easily be verified with the help of Eqs. (3), (9), and (15) for $\Delta\omega = 0$. For the vectors $\mathbf{E}_0(z = 0, t)$, $\mathbf{E}_r(z = 0, t)$, and $\Delta\mathbf{E}(z = 0, t)$, as well as for their combinations $\mathbf{E}_0 - \Delta\mathbf{E}$ and $\mathbf{E}_0 + \mathbf{E}_r$, we obtain expressions of the type

$$\mathbf{E}_i(z = 0, t) = E_0 F_i(t)\mathbf{e}_l^{\pm}(t), \tag{37}$$

where

$$\mathbf{e}_l^{\pm}(t) = \mathbf{e}_l\exp(-i\omega_l t) + \mathbf{e}_l^*\exp(i\omega_l t)$$
$$= \sqrt{2}(\mathbf{e}_x\cos\omega_l t \pm \mathbf{e}_y\sin\omega_l t), \tag{38}$$

the signs + (–) correspond to the right (left) circular polarization, and $F_i(t)$ are dimensionless real-valued functions. Equation (37) just indicates that all three vectors are parallel. The singular points of the second and third types correspond to the equalities $F_i(t) = 0$ for $t > 0$.

For short pulses, for $\gamma_l > \Gamma$ and $p \gg \gamma_l^{-1}$, the following situation takes place. The exciting field containing the factor $\exp(-\gamma_l p/2)$ becomes negligibly small and, hence,

$$\mathbf{E}_r(z, t) \simeq \Delta\mathbf{E}_r(z, t). \tag{39}$$

In this case, for $t \gg \gamma_l^{-1}$, we find that

$$\mathcal{R}(t) \simeq \mathcal{T}(t), \quad \mathcal{A}(t) \simeq -2\mathcal{R}(t). \tag{40}$$

This means that only the induced fields $\Delta\mathbf{E}_{l(r)}$ symmetric relative to the plane of the well persist. The electron system of the well gives away the energy accumulated in it, emitting this energy symmetrically in the form of two flows propagating to the right and to the left. The fulfillment of relations (40) for $\gamma_l t \gg 1$ is illustrated in Fig. 1.

5. ENERGY FLUXES FOR EXACT RESONANCE UNDER THE CONDITION $\gamma_r \gg \gamma$

In the case when $\gamma_r \ll \gamma$, the perturbation theory is applicable and it is sufficient to take into account only the lowest order terms in the interaction of electrons with the electromagnetic field, which is equivalent to discarding the term $4\pi\chi(\omega)$ in the denominator of formula (12).[1] For $\gamma_r \ll \gamma$, the fields $\Delta\mathbf{E}_{l(r)}$ induced on the left (right) of the well are smaller than the exciting field in Eq. (3) for $p = 0$; i.e., the dimensionless reflection $\mathcal{R}$ and absorption $\mathcal{A}$ are smaller than unity. The shape of the transmitted pulse differs insignificantly from that of the exciting pulse. Interesting results are also obtained in this case: "pulling" of a short pulse is observed in the transmitted light for times of the order of γ^{-1}, while sinusoidal beats are observed in the case of two closely spaced energy levels at a frequency $\Delta E/\hbar$, where ΔE is

---

[1] In the case of pulsed irradiation of a quantum well, the lowest order approximation in the perturbation theory for $\gamma_r \ll \gamma$ is applicable only for times $t \ll \gamma_l^{-1}$ since the intensity of the transmitted and reflected light for $t \ge \gamma_r^{-1}$ attenuates according to the law $\exp(-\gamma_r t)$.
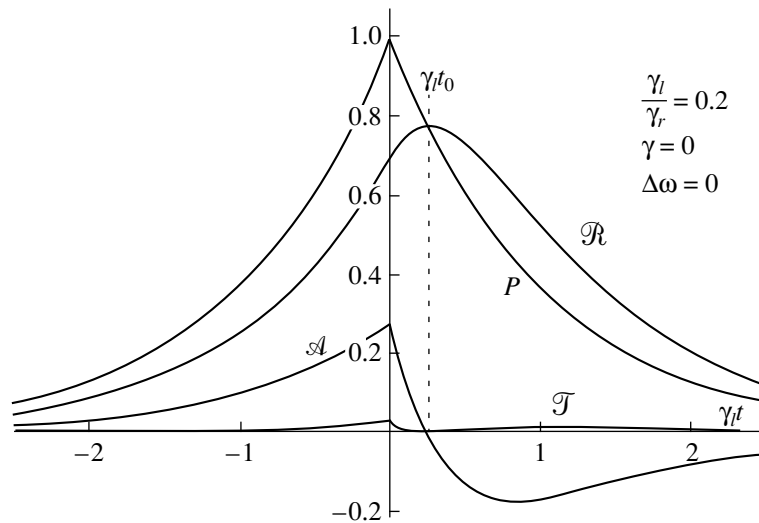
Fig. 2. The same as in Fig. 1 for a long pulse. The complete-transmission point is absent.
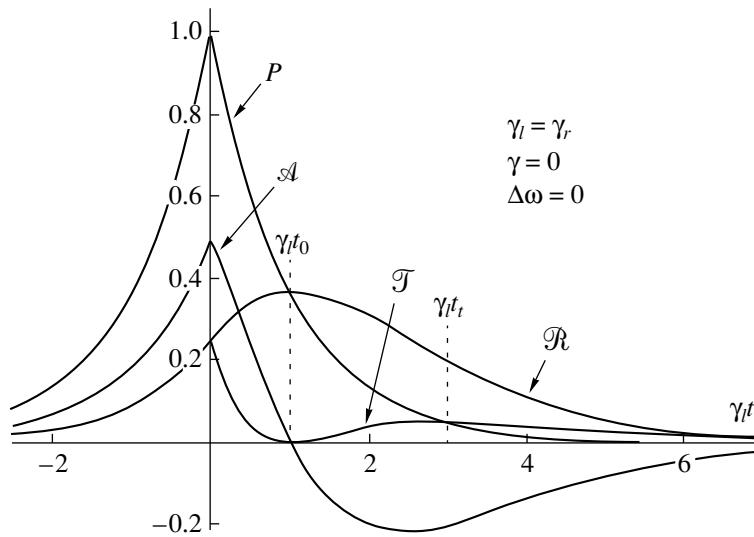

Fig. 3. The same as in Fig. 1 for an intermediate pulse.

the energy spacing between the levels (see, for example, [16]).

In the opposite case $\gamma_r \gg \gamma$, the induced fields are comparable to the exciting fields in magnitude and the shape of the transmitted pulse might change significantly. Lang and Belitsky [1] proved this for a strongly asymmetric pulse and presented the results of numerical calculations for a symmetric pulse proportional to $[\cosh(\gamma_l p)]^{-1}$. The analytical expressions for the dimensionless quantities $\mathcal{T}$, $\mathcal{R}$, and $\mathcal{A}$ for the symmetric pulse in Eq. (3) were presented above [see Eqs. (30)–(32)].

Let us consider the case when $\gamma = 0$, in which the condition $\gamma_r \gg \gamma$ always holds. Figures 1–3 show the curves calculated by using formulas (30)–(32) (in which we

have put $\gamma = 0$) for short ($\gamma_l \gg \gamma_r$), long ($\gamma_l \ll \gamma_r$), and intermediate ($\gamma_l = \gamma_r$) pulses. In these figures, we can see the point t_0 of total reflection of the first type, which always exists for $\gamma = 0$ and is defined by the expression

$$t_0 = \frac{2}{\gamma_r - \gamma_l} \ln \frac{2\gamma_r}{\gamma_r + \gamma_l}. \tag{41}$$

For this reason, the curve $\mathcal{T}(t)$ has two peaks, which can be seen especially clearly in Fig. 3. Figures 1 and 3 also show the point of complete transmission t_t of the second type, which exists for $\gamma_l > \gamma_r/2$ in the case when $\gamma = 0$ and is given by

$$t_t = \frac{2}{\gamma_r - \gamma_l} \ln \frac{2\gamma_r \gamma_l}{(\gamma_r + \gamma_l)(2\gamma_l - \gamma_r)}. \tag{42}$$

This point is not observed in Fig. 2 since the condition $\gamma_l > \gamma_r/2$ is violated for long pulses.

It can be seen from formulas (30)–(32) and from Fig. 1 that in the case of a short pulse, the transmitted pulse differs from the exciting pulse insignificantly. The reflected pulse is very weak since formula (31) contains a small factor $\sim(\gamma_r/\gamma_l)^2$. The absorbed power is also small as compared to that of the exciting pulse, but is greater than the reflected power since it contains the factor $\sim(\gamma_r/\gamma_l)$.

In the case of a long pulse, the situation is completely different, which is illustrated in Fig. 2. The pulse is reflected almost completely; i.e., the reflected pulse almost coincides with the exciting pulse. The transmitted pulse is very weak and contains the factor $\sim(\gamma_r/\gamma_l)^2$. The absorption is larger than the transmission since it contains the factor $\sim(\gamma_r/\gamma_l)$.

Figure 3 corresponds to the case when $\gamma_l = \gamma_r$. Substituting $\gamma_l = \gamma_r$ and $\gamma = 0$ into Eqs. (30)–(32), we find that

$$\mathscr{T}(t) = [\Theta(t)e^{-\gamma_l t}(1 - \gamma_l t)^2 + (1 - \Theta(t))e^{\gamma_l t}]/4,$$

$$\mathscr{R}(t) = [\Theta(t)\exp(-\gamma_l t)(1 + \gamma_l t)^2$$
$$+ (1 - \Theta(t))\exp(\gamma_l t)]/4, \tag{43}$$

$$\mathscr{A}(t) = [\Theta(t)\exp(-\gamma_l t)(1 - (\gamma_l t)^2)$$
$$+ (1 - \Theta(t))\exp(\gamma_l t)]/2.$$

Obviously, the points t_0 of total reflection of the first type and t_t of complete transmission of the second type are given by

$$t_0 = \gamma_l^{-1}, \quad t_t = 3\gamma_l^{-1}. \tag{44}$$

The exciting, transmitted, and reflected pulses are of the same order of magnitude, but the transmitted pulse differs significantly in shape from the excited pulse, which is illustrated in Fig. 3. The transmitted pulse has a minimum at the point $t_0 = \gamma_l^{-1}$ and then a second peak; i.e., it has two humps.

6. INTEGRATED ENERGY FLUXES IN THE CASE OF EXACT RESONANCE $\omega_l = \omega_0$

The total amount of the energy absorbed per unit area in the case of pulsed irradiation is given by

$$\mathscr{E}_{\mathscr{A}} = 2|S_0|\mathscr{K}_{\mathscr{A}}/\gamma_l, \tag{45}$$

where we have introduced the dimensionless quantity

$$\mathscr{K}_{\mathscr{A}} = (\gamma_l/2)\int_{-\infty}^{\infty} \mathscr{A}(t)dt. \tag{46}$$

The total amount of exciting, transmitted, and reflected

energy per unit area is given, respectively, by

$$\mathscr{E}_P = 2|S_0|\mathscr{K}_P/\gamma_l, \quad \mathscr{E}_{\mathscr{T}} = 2|S_0|\mathscr{K}_{\mathscr{T}}/\gamma_l,$$
$$\mathscr{E}_{\mathscr{R}} = 2|S_0|\mathscr{K}_{\mathscr{R}}/\gamma_l, \tag{47}$$

where

$$\mathscr{K}_P = \frac{\gamma_l}{2}\int_{-\infty}^{\infty} P(t)dt, \quad \mathscr{K}_{\mathscr{T}} = \frac{\gamma_l}{2}\int_{-\infty}^{\infty} \mathscr{T}(t)dt,$$

$$\mathscr{K}_{\mathscr{R}} = \frac{\gamma_l}{2}\int_{-\infty}^{\infty} \mathscr{R}(t)dt, \tag{48}$$

so that

$$\mathscr{K}_{\mathscr{T}} + \mathscr{K}_{\mathscr{R}} + \mathscr{K}_{\mathscr{A}} = \mathscr{K}_P. \tag{49}$$

Using Eqs. (30)–(32), we obtain

$$\mathscr{K}_{\mathscr{T}} = \frac{\gamma^2(\Gamma + 2\gamma_l) + \gamma_l^2\Gamma}{\Gamma(\Gamma + \gamma_l)^2}, \tag{50}$$

$$\mathscr{K}_{\mathscr{R}} = \frac{\gamma_r^2(\Gamma + 2\gamma_l)}{\Gamma(\Gamma + \gamma_l)^2}, \tag{51}$$

$$\mathscr{K}_{\mathscr{A}} = \frac{2\gamma_r\gamma(\Gamma + 2\gamma_l)}{\Gamma(\Gamma + \gamma_l)^2}. \tag{52}$$

Similar expressions for an asymmetric pulse with a steep front were given in [1]. It follows from Eq. (52) that the total amount of absorbed energy is equal to zero for $\gamma = 0$. This is obvious from the physical point of view since electron excitations in a quantum well transmit their energy to other excitations (e.g., phonons) only for $\gamma \neq 0$. If $\gamma = 0$, the entire energy of the electron excitations is ultimately transformed into the luminous energy and the total absorption is zero. For $\gamma = 0$ and $\gamma_r = \gamma_l$, formulas (50) and (51) show that three-fourths of the energy of the exciting pulse is reflected and one-fourth is transmitted through the well.

7. REFLECTION AND ABSORPTION OF A LIGHT PULSE FOR A CARRIER FREQUENCY DEVIATING FROM THE RESONANCE VALUE

Expressions for the dimensionless absorption $\mathscr{A}(t)$, reflection $\mathscr{R}(t)$, and transmission $\mathscr{T}(t)$ for a departure from resonance have the form

$$\mathscr{A}(t) = \frac{\Theta(t)}{(\Delta\omega)^2 + (\gamma_l - \Gamma)^2/4}$$

$$\times \left\{ \frac{1}{2}\exp(-\gamma_l t)\gamma_r(\gamma - \gamma_l) - \frac{\exp(-\Gamma t)\gamma_r^2\gamma_l^2}{2[(\Delta\omega)^2 + (\gamma_l + \Gamma)^2/4]} \right.$$

$$\left. - \gamma_r\gamma_l\sqrt{\frac{(\Delta\omega)^2 + (\gamma_l + \gamma_r - \gamma)^2/4}{(\Delta\omega)^2 + (\gamma_l + \Gamma)^2/4}} \right. \tag{53}$$

$$\times \exp(-(\gamma_l + \Gamma)t/2)\cos(\Delta\omega t + \chi)\Big\}$$

$$+ [1 - \Theta(t)]\frac{\exp(\gamma_l t)\gamma_r(\gamma_l + \gamma)}{(\Delta\omega)^2 + (\gamma_l + \Gamma)^2/4},$$

$$\mathcal{R}(t) = \frac{\gamma_r^2}{4}\Bigg\{\frac{\Theta(t)}{(\Delta\omega)^2 + (\gamma_l - \Gamma)^2/4}$$

$$\times [a_{\mathcal{R}}^2(t) + b_{\mathcal{R}}^2(t) + 2a_{\mathcal{R}}(t)b_{\mathcal{R}}(t)\cos(\Delta\omega t - \zeta)]$$

$$+ \frac{[1 - \Theta(t)]\exp(\gamma_l t)}{(\Delta\omega)^2 + (\gamma_l + \Gamma)^2/4}\Bigg\}, \tag{54}$$

$$\mathcal{T}(t) = \frac{\Theta(t)[a_{\mathcal{T}}^2 + b_{\mathcal{T}}^2 + 2a_{\mathcal{T}}b_{\mathcal{T}}\cos(\Delta\omega t + \kappa)]}{(\Delta\omega)^2 + (\Gamma - \gamma_l)^2/4}$$

$$+ \frac{(1 - \Theta(t))\exp(\gamma_l t)[(\Delta\omega)^2 + (\gamma + \gamma_l)^2/4]}{(\Delta\omega)^2 + (\Gamma + \gamma_l)^2/4}, \tag{55}$$

where the following notation has been introduced:

$$a_{\mathcal{R}} = \exp(-\gamma_l t/2),$$

$$b_{\mathcal{R}} = \frac{\gamma_l \exp(-\Gamma t/2)}{\sqrt{(\Delta\omega)^2 + (\gamma_l - \gamma)^2/4}}, \tag{56}$$

$$a_{\mathcal{T}} = \sqrt{(\Delta\omega)^2 + (\gamma_l - \gamma)^2/4}\exp(-\gamma_l t/2),$$

$$b_{\mathcal{T}} = \gamma_r\gamma_l/[2\sqrt{(\Delta\omega)^2 + (\Gamma + \gamma_l)^2/4}]\exp(-\Gamma t/2), \tag{57}$$

and the angles χ, ζ, and κ are defined through the relations

$$\cos\chi$$
$$= -\frac{(\Delta\omega)^2 + (\gamma_l + \Gamma)(\gamma_l + \gamma_r - \gamma)/4}{\sqrt{[(\Delta\omega)^2 + (\gamma_l + \Gamma)^2/4][(\Delta\omega)^2 + (\gamma_l + \gamma_r - \gamma)^2/4]}},$$

$$\sin\chi$$
$$= \frac{\Delta\omega\gamma}{\sqrt{[(\Delta\omega)^2 + (\gamma_l + \Gamma)^2/4][(\Delta\omega)^2 + (\gamma_l + \gamma_r - \gamma)^2/4]}}, \tag{58}$$

$$\cos\zeta = -\frac{\gamma_l + \Gamma}{2\sqrt{[(\Delta\omega)^2 + (\gamma_l + \Gamma)^2/4]}},$$

$$\sin\zeta = -\frac{\Delta\omega}{\sqrt{[(\Delta\omega)^2 + (\gamma_l + \Gamma)^2/4]}}, \tag{59}$$

$$\cos\kappa$$
$$= -\frac{(\Delta\omega)^2 + (\gamma_l - \gamma)(\gamma_l + \Gamma)/4}{\sqrt{[(\Delta\omega)^2 + (\gamma_l + \Gamma)^2/4][(\Delta\omega)^2 + (\gamma_l - \gamma)^2/4]}},$$

$$\sin\kappa$$
$$= \frac{\Delta\omega(\Gamma + \gamma)/2}{\sqrt{[(\Delta\omega)^2 + (\gamma_l + \Gamma)^2/4][(\Delta\omega)^2 + (\gamma_l - \gamma)^2/4]}}. \tag{60}$$

In all three dependences, oscillations are observed at the frequency $\Delta\omega$ with different phase shifts.

8. SINGULAR POINTS FOR A CARRIER FREQUENCY DEVIATING FROM THE RESONANCE VALUE

Let us prove that singular temporal points of the first and second types generally do not exist for $\Delta\omega \neq 0$. Indeed, expressions (9), (10), and (15) imply that the fields $\Delta\mathbf{E}(z = 0, t)$ and $\mathbf{E}_r(z = 0, t)$ can be written in the form

$$\mathbf{E}(z = 0, t) = E_0\mathbf{e}_l\{\Theta(t)[A\exp(-\gamma_l t/2 - i(\omega_l t + \xi))$$
$$+ B\exp(-\Gamma t/2 - i(\omega_0 t + \varphi))]$$
$$+ [1 - \Theta(t)]C\exp(\gamma_l t/2 - i(\omega_l t + \zeta))\} + c.c., \tag{61}$$

where A, B, and C are real-valued coefficients independent of time and ξ, φ, and ζ are phase shifts. Using the circular polarization defined in Eq. (11), we transform Eq. (61) to

$$\mathbf{E}(z = 0, t)$$
$$= E_0\{\Theta(t)[A\sqrt{2}\exp(-\gamma_l t/2)(\mathbf{e}_x\cos(\omega_l t + \xi)$$
$$\pm \mathbf{e}_y\sin(\omega_l t + \xi))] + B\sqrt{2}\exp(-\Gamma t/2)$$
$$\times (\mathbf{e}_x\cos(\omega_0 t + \varphi) \pm \mathbf{e}_y\sin(\omega_0 t + \varphi))$$
$$+ [1 - \Theta(t)]C\sqrt{2}\exp(\gamma_l t/2)$$
$$\times (\mathbf{e}_x\cos(\omega_0 t + \zeta) \pm \mathbf{e}_y\sin(\omega_0 t + \zeta))\}, \tag{62}$$

where the $+$ ($-$) sign corresponds to the right (left) circular polarization of the exciting light. Thus, in the case of the deviation from resonance for $t > 0$, the transmitted, as well as reflected, pulse contains two circularly polarized waves with different carrier frequencies ω_l and ω_0 and different phase shifts relative to $\mathbf{E}_0(z = 0, t)$. In this case, the resultant vector $\mathbf{E}(z = 0, t)$ does not vanish in the general case. Setting the vector $\mathbf{E}(z = 0, t)$ equal to zero, we obtain two equations for the same unknown t, which have no solutions. The same applies to the combinations of vectors $\mathbf{E}_0 - \Delta\mathbf{E}$ and $\mathbf{E}_0 + \mathbf{E}_r$. Thus, the singular points of the first and second type are absent in the case of a deviation from resonance. On the other hand, singular points of the third type are possible and do exist since some of the vectors $\Delta\mathbf{E}$, $\mathbf{E}_r$, $\mathbf{E}_0 - \Delta\mathbf{E}$,
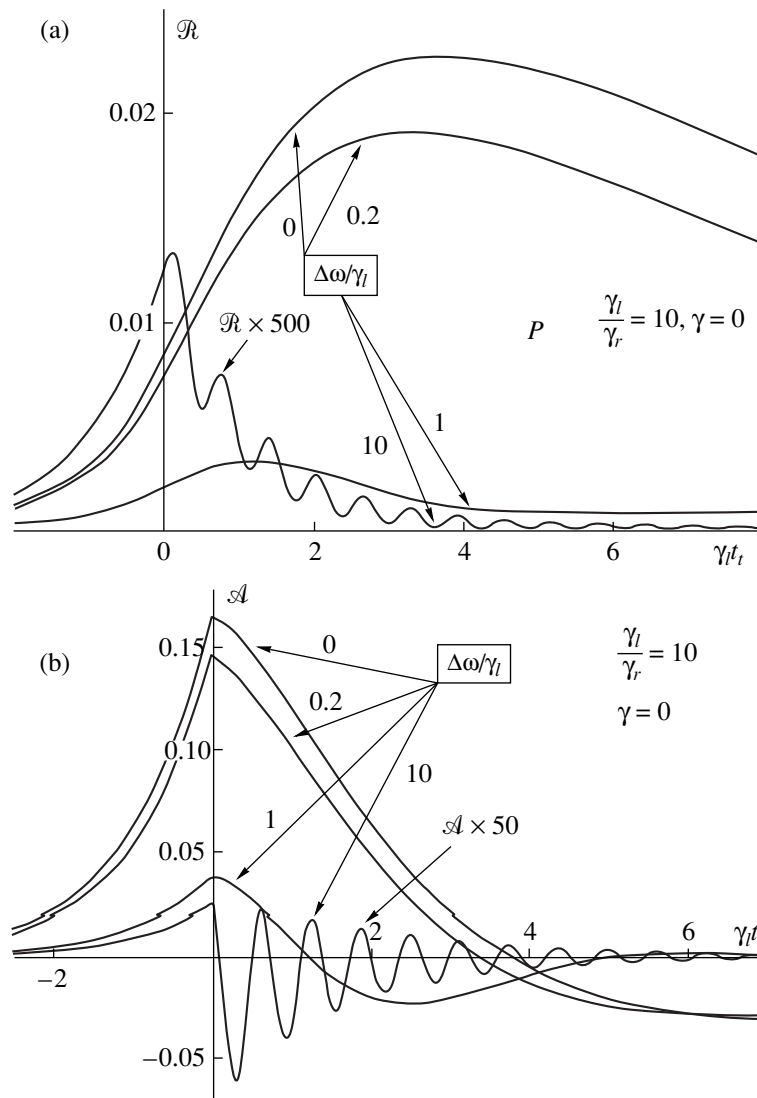
Fig. 4. (a) $\mathcal{R}(t)$ and (b) $\mathcal{A}(t)$ curves for a very short pulse for various values of deviation $\Delta\omega$ of the carrier frequency of the pulse from resonance.

and $\mathbf{E}_0 + \mathbf{E}_r$ can be perpendicular to each other at certain instants.

It is more convenient to analyze the conditions for the existence of a point of zero absorption, total reflection, or complete transmission of the third type by using expressions (53)–(55). We will confine our subsequent analysis to the most interesting case of $\gamma_r \gg \gamma$, setting $\gamma = 0$. In this case, the condition $\int_{-\infty}^{\infty} \mathcal{A}_{\gamma=0}(t)dt = 0$ holds and at least one point of zero absorption must obviously exist. An analysis of expression (53) for $\gamma = 0$ shows that a finite odd number of zero-absorption points exists for $\gamma_l \neq \gamma_r$. This means that for large values of time, the quantity $\mathcal{A}_{\gamma=0}(t)$ becomes negative. The number of points for which $\mathcal{A}_{\gamma=0}(t) = 0$ depends on the ratio $q = \Delta\omega/\gamma_l$, i.e., on the deviation from resonance. In

the case of a short pulse, when $\gamma_l \gg \gamma_r$, there exists only one zero-absorption point for $q \ll \pi$, while several points of this kind exist for $q \gg \pi$. In the case of a long pulse, when $\gamma_l \ll \gamma_r$, there is one zero-absorption point for $q \ll \pi\gamma_r/\gamma_l$ and many such points exist for $q \gg \pi\gamma_r/\gamma_l$.

For $\gamma_l = \gamma_r$, the number of zero-absorption points is infinitely large. However, the number of total-reflection points is determined by the parameter q. The number of total-reflection points is infinitely large for $q < q_b$ and is equal to zero for $q > q_b$. The value of q_b is determined by the equation $(2q_b - 1)\sqrt{1 + q_b^2} - 1 = 0$ and is equal to 0.876. It should also be noted that the number of complete-transmission points for $\gamma_l = \gamma_r$ is infinitely large for any q.
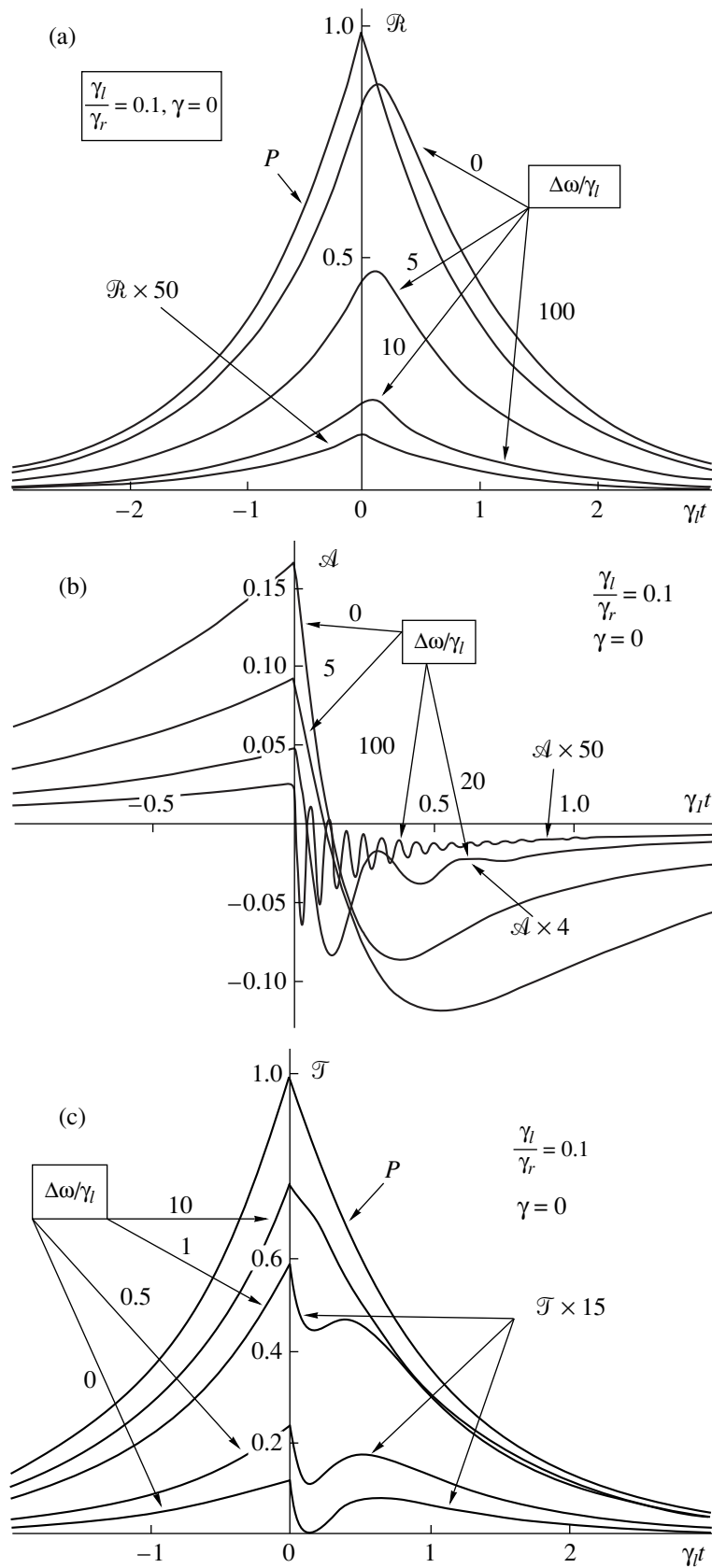
Fig. 5. (a) $\mathcal{R}(t)$, (b) $\mathcal{A}(t)$, and (c) $\mathcal{T}(t)$ curves for a very long pulse for various values of $\Delta\omega$.
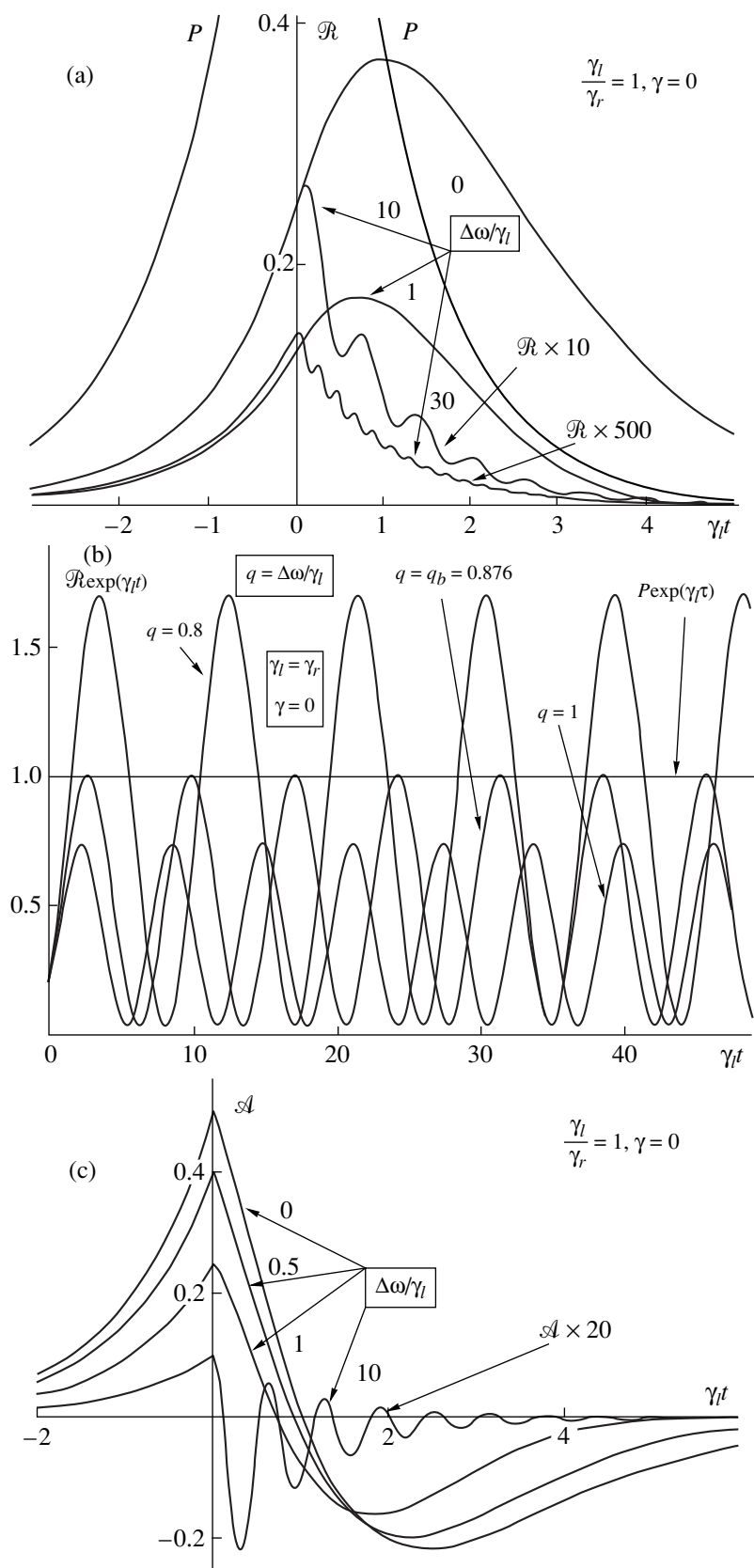
Fig. 6. $\mathcal{R}(t)$, $\mathcal{A}(t)$, and $\mathcal{T}(t)$ curves for an intermediate pulse for various values of $\Delta\omega$: (a) $\mathcal{R}(t)$; (b) $\mathcal{R}(t)\exp(\gamma_l t)$ curves for $q < q_b$, $q = q_b$, and $q > q_b$; (c) $\mathcal{A}(t)$; (d) $\mathcal{T}(t)$; and (e) $\mathcal{R}(t)\exp(\gamma_l t)$, $\mathcal{A}(t)\exp(\gamma_l t)$, and $\mathcal{T}(t)\exp(\gamma_l t)$ curves for $q = 0.7$.
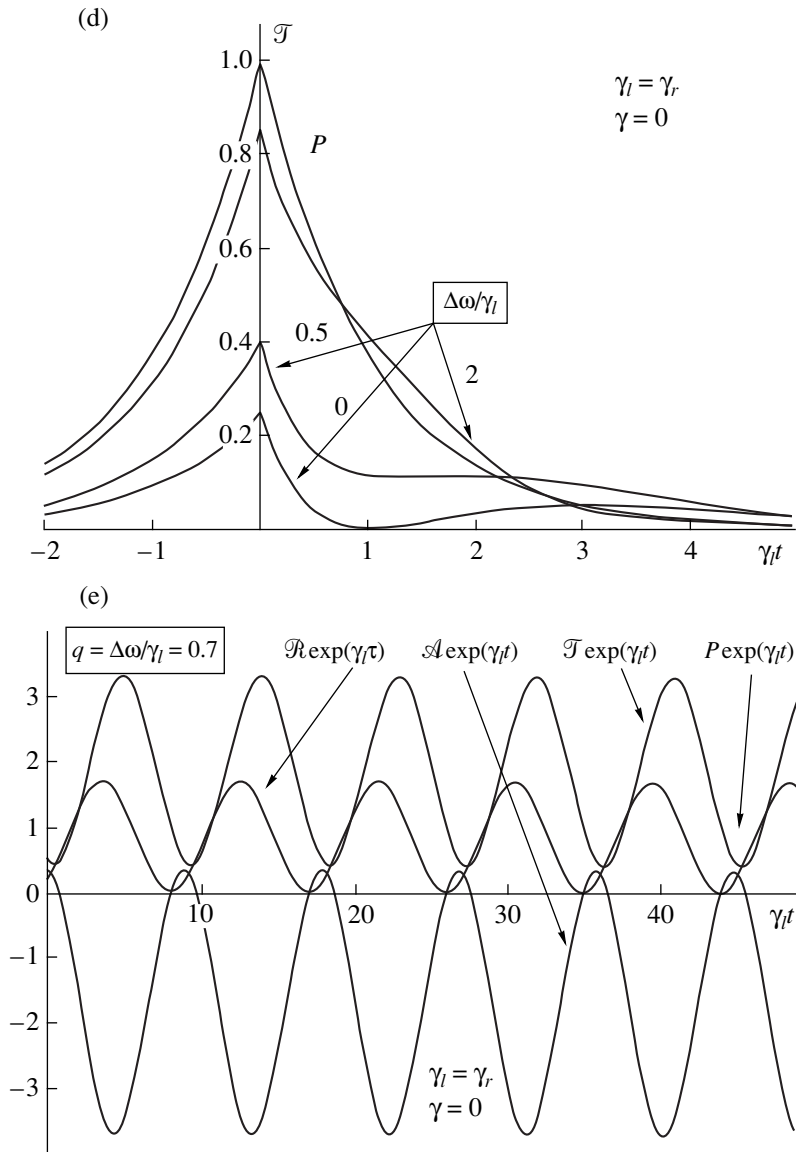
Fig. 6. (Contd.)

9. DISCUSSION OF RESULTS FOR THE CASE OF A FREQUENCY DIFFERING FROM ITS RESONANCE VALUE

Figures 4–6 depict the functions $\mathcal{R}(t)$, $\mathcal{A}(t)$, and $\mathcal{T}(t)$ for $\gamma = 0$ and for various relations between the parameters γ_r, γ_l, and $\Delta\omega$. Figure 4 corresponds to short pulses for which $\gamma_l \gg \gamma_r$, while Fig. 5 corresponds to long pulses ($\gamma_l \ll \gamma_r$). Figure 6 corresponds to intermediate pulses for which $\gamma_l/\gamma_r = 1$.

Figure 4 depicts the dependences of reflection $\mathcal{R}(t)$ and absorption $\mathcal{A}(t)$ on the dimensionless quantity $\gamma_l t$ for $\gamma_l/\gamma_r = 10$ and for various values of the parameter $q = \Delta\omega/\gamma_l$ characterizing the departure from resonance. The transmission $\mathcal{T}(t)$ curves for short pulses are not presented since they are close to $P(t)$ for values of q varying from 1 to 10; i.e., the transmission is always

significant. It can be seen from Fig. 4 that the values of $\mathcal{R}$ and $\mathcal{A}$ are much smaller than unity for $\Delta\omega = 0$ and attenuate rapidly with an increasing deviation from resonance. The oscillating contribution to $\mathcal{R}$ and $\mathcal{A}$ attenuates according to the law $\exp[-(\gamma_l + \gamma_r)t/2]$. The attenuation parameter is defined as $\Pi = 2/(1 + \gamma_r/\gamma_l)$ ($\Pi = 1.9$ in Fig. 4). The period of oscillations is $T = 2\pi/q$. On the $\mathcal{R}(t)$ and $\mathcal{A}(t)$ curves, oscillations cannot be seen since $T \gg \Pi$ for $q = 0.2$. However, oscillations can be seen clearly on the curves for $q = 1$ and 10. With an increasing deviation from resonance, the period of oscillations, as well as their amplitude, becomes smaller. Figure 4a contains total-reflection points of the third type, while Fig. 4b contains zero-absorption points of the third type (see Section 8).

Figure 5 shows the $\mathcal{R}$, $\mathcal{A}$, and $\mathcal{T}$ curves for $\gamma_l/\gamma_r = 0.1$. The oscillations cannot be seen on the $\mathcal{R}$ curves in

Fig. 5a for any value of q since their amplitude is much smaller than the nonoscillating contribution. For $q = 0$, the $\mathcal{R}(t)$ curve is close to the $P(t)$ curve; i.e., the pulse is reflected almost completely, while with increasing q the reflection decreases, attaining small values for $q = 100$. It can be seen from Fig. 5b that absorption also decreases rapidly when parameter q increases. Oscillations on the $\mathcal{A}(t)$ curves can be clearly seen for $q = 20$ and 100. The number of zero-absorption points differs from unity only for $q = 100$, which agrees with the results obtained in Section 8. The transmission $\mathcal{T}$ (Fig. 5c) is small for $q = 0$; it increases with q and approaches $P(t)$ for $q > 10$. Oscillations cannot be seen. For $q = 0$, there exists a point of total reflection of the first type (Fig. 5a), which corresponds to the zero-absorption point in Fig. 5b and the zero-transmission point in Fig. 5c. With increasing q, the zero-transmission point is transformed into a minimal-transmission point, while the total-reflection point is transformed into the maximal-reflection point.

Finally, Fig. 6 shows the $\mathcal{R}(t)$, $\mathcal{A}(t)$, and $\mathcal{T}(t)$ curves for an intermediate pulse for $\gamma_l = \gamma_r$. Figure 6a depicts the $\mathcal{R}(t)$ curves for $q = 0$, 1, 10, and 30. While the reflection is comparable with $P(t)$ for $q = 0$, it becomes extremely small as compared to unity already for $q = 10$. Oscillations can be observed on the curves for $q = 10$ and 30. A total-reflection point of the first type can be seen on the curve for $q = 0$, while on the remaining curves such points are absent. This is in accord with the results obtained in Section 8 for $q > q_b$. Figure 6b shows the $\mathcal{R}\exp(\gamma_l t)$ curves for which attenuation is ruled out, and hence an infinitely large number of oscillations is observed. In accordance with Section 8, there exists an infinitely large number of total-reflection points of the third type for $q < q_b$, while no point of this type is observed for $q > q_b$. For $q = q_b$, the $\mathcal{R}\exp(\gamma_l t)$ curve touches the $P(t)\exp(\gamma_l t)$ straight line corresponding to an excited pulse. Figure 6c depicts the $\mathcal{A}(t)$ curves for an intermediate pulse. When the parameter q increases, the absorption decreases, and we can clearly see oscillations and a large number of zero-absorption points for $q = 10$. It should be recalled that, for $\gamma_l = \gamma_r$, the number of zero-absorption points is infinitely large. Figure 6d shows the $\mathcal{T}(t)$ curves for an intermediate pulse. The transmission increases with q and becomes close to the $P(t)$ curve even for $q = 2$. The number of complete-transmission points must be infinitely large for any value of $q \geq 0$. However, only one such point can be seen for $q = 0.5$ and two points for $q = 2$ in view of the rapid attenuation of the curves. In order to demonstrate the large number of complete-transmission, total-reflection, and zero-absorption points, Fig. 6e depicts the $\mathcal{R}\exp(\gamma_l t)$, $\mathcal{A}(t)\exp(\gamma_l t)$, and $\mathcal{T}\exp(\gamma_l t)$ curves corresponding to $q = 0.7$ as well as the $P\exp(\gamma_l t)$ straight line for $t > 0$. It can be seen that all three oscillating curves are different in phase. It should be emphasized that the $\mathcal{R}(t)$ curve in Figs. 6b and 6e does not assume the zero value, as it might appear, but assumes very small positive values at the points of the minima.

Thus, we can draw the following qualitative conclusions obtained under the condition $\gamma \ll \gamma_r$. (For the sake of simplicity, we assume that $\gamma = 0$.) For exact resonance, when $\omega_l = \omega_0$, in the case of a very short pulse for which $\gamma_l \gg \gamma_r$, the pulse passes through the well almost without changing its shape. The reflection and absorption are small, the reflection being much smaller than the absorption. In the case of a long pulse for which $\gamma_l \ll \gamma_r$, the pulse is reflected almost completely and the transmission is much smaller than the absorption. Since the integrated absorption is zero for $\gamma = 0$, for any relation between γ_l and γ_r there exists a zero-absorption point at which the luminous-energy absorption is replaced by emission. At the point of zero absorption, total reflection takes place and the transmission is equal to zero (a singular point of the first type).

The case when $\omega_l = \omega_0$ and $\gamma_l \simeq \gamma_r$, in which the reflection, absorption, and transmission have comparable values, is of special interest. The shape of the transmitted pulse differs significantly from the shape of the exciting pulse. The transmitted pulse has two peaks, i.e., a two-humped shape due to the presence of a singular point of the first type.

When the frequency deviates from the resonance value, i.e., when $\Delta\omega = \omega_l - \omega_0 \neq 0$, the reflection and absorption decrease with an increasing deviation $\Delta\omega$, while the intensity and shape of the transmitted pulse become similar to those of the exciting pulse. For $\Delta\omega \gg \gamma_l$, the pulse passes through the well, remaining almost unchanged. All the $\mathcal{R}(t)$, $\mathcal{A}(t)$, and $\mathcal{T}(t)$ curves display oscillations at the frequency $\Delta\omega$. However, these oscillations cannot be observed on all the curves in Figs. 4–6 which correspond to the departure from resonance. For $\Delta\omega \ll \gamma_l$, the period of oscillations is much longer than the time period over which the values of $\mathcal{R}(t)$, $\mathcal{A}(t)$, and $\mathcal{T}(t)$ attenuate. For $\Delta\omega \gg \gamma_l$, the period of oscillations is small, but their amplitude is also small. For this reason, oscillations can be seen best of all for $\Delta\omega \simeq \gamma_l$.

In the case of a deviation from resonance, the points of total reflection, complete transmission, and zero absorption do not coincide. Such singular points were called the points of the third type. For a more detailed analysis of these points in the most interesting case when $\gamma_r \simeq \gamma_l$, we use Figs. 6b and 6e in which attenuation of the curves is ruled out since the quantities $\mathcal{R}(t)$, $\mathcal{A}(t)$, and $\mathcal{T}(t)$ multiplied by $\exp(\gamma_l t)$ are laid on the ordinate axis. It is shown that, in the case of the exact equality $\gamma_r = \gamma_l$, the number of zero-absorption and complete-transmission points is always infinitely large for $\Delta\omega \neq 0$, while the number of total-reflection points is infinitely large for $\Delta\omega/\gamma_l < q_b$, where $q_b = 0.876$. The infinitely large number of zero-absorption points indicates that the energy is transferred from the electron system to light waves and back an infinite number of

times, but it should be borne in mind that these oscillations attenuate according to the law $\exp(-\gamma_l t)$. When the exact equality $\gamma_r = \gamma_l$ is violated, the number of singular points of the third type is always finite. In particular, the number of zero-absorption points is odd since absorption is always negative for large values of time; i.e., the system emits the luminous energy accumulated earlier.

ACKNOWLEDGMENTS

REFERENCES

1. I. G. Lang and V. I. Belitsky, Solid State Commun. **107** (10), 577 (1998).
2. L. C. Andreani, F. Tassone, and F. Bassani, Solid State Commun. **77** (9), 641 (1991).
3. L. C. Andreani, in *Confined Electrons and Photons*, Ed. by E. Burstein and C. Weisbuch (Plenum, New York, 1995), p. 57.
4. E. L. Ivchenko, Fiz. Tverd. Tela (Leningrad) **33** (8), 2388 (1991) [Sov. Phys. Solid State **33**, 1344 (1991)].
5. F. Tassone, F. Bassani, and L. C. Andreani, Phys. Rev. B **45** (11), 6023 (1992).
6. T. Strouken, A. Knorr, C. Anthony, *et al.*, Phys. Rev. Lett. **74** (9), 2391 (1995).
7. T. Strouken, A. Knorr, P. Thomas, and S. W. Koch, Phys. Rev. B **53** (4), 2026 (1996).
8. L. C. Andreani, G. Panzarini, A. V. Kavokin, and M. V. Vladimirova, Phys. Rev. B **57** (8), 4670 (1998).
9. M. Hübner, J. Kuhl, S. Haas, *et al.*, Solid State Commun. **105** (2), 105 (1998).
10. I. G. Lang, V. I. Belitsky, and M. Gardona, Phys. Status Solidi A **164** (1), 307 (1997).
11. I. G. Lang and V. I. Belitsky, Phys. Lett. A **245** (4), 329 (1998).
12. I. G. Lang, L. I. Korovin, D. A. Contreras-Solorio, and S. T. Pavlov, cond–mat/0001248; Phys. Rev. B (in press).
13. D. A. Contreras-Solorio, S. T. Pavlov, L. I. Korovin, and I. G. Lang, cond–mat/0002229; Phys. Rev. B (in press).
14. I. G. Lang, L. I. Korovin, D. A. Contreras-Solorio, and S. T. Pavlov, cond–mat/0004178.
15. H. Stolz, *Time Resolved Light Scattering from Excitons* (Springer-Verlag, Berlin, 1994).
16. L. I. Korovin, I. G. Lang, and S. T. Pavlov, Zh. Éksp. Teor. Fiz. **116**, 1419 (1999) [JETP **89**, 764 (1999)].

Translated by N. Wadhwa

LOW-DIMENSIONAL SYSTEMS AND SURFACE PHYSICS

Self-Organization in the Formation of a Nanoporous Carbon Material

S. K. Gordeev*, S. A. Kukushkin**, A. V. Osipov**, and Yu. V. Pavlov**

* Central Research Institute of Materials, St. Petersburg, 191014 Russia
**Institute of Problems of Mechanical Engineering, Russian Academy of Sciences,
Bol'shoǐ pr. 61, Vasil'evskiǐ ostrov, St. Petersburg, 199178 Russia
e-mail: ksa@math.ipme.ru
Received March 6, 2000; in final form, April 27, 2000

Abstract—A new mechanism of nanopore formation in carbon materials produced by the interaction of carbides with chlorine is proposed. In essence, this method is the following. A series of nonlinear chemical reactions proceed in the course of a chemical interaction between chlorine and a carbide. If the external parameters, the component fluxes, and the diffusion rates satisfy certain relations, the self-organization process can occur. This process results in the creation of a periodic nanoporous structure in the carbon material formed. A mathematical model is proposed, the main characteristics of the process are calculated, and the restrictions on the parameters at which the formation of the porous structure becomes possible are found. © 2000 MAIK "Nauka/Interperiodica".

1. INTRODUCTION

Earlier [1–4], it was shown that carbon materials with unique properties can be obtained by chlorine treatment of carbon-containing compounds (B_4C, SiC, TiC, Mo_2C, etc.). In particular, it was established [2–6] that nanopores 0.8–2 nm in size are formed in carbides treated with chlorine [2, 3, 5, 6]. The action of chlorine on carbides leads to a substantial transformation of the carbon sublattice of the carbides, and the carbon atoms are displaced by a distance of 1–2 Å.

Fedorov *et al.* [2, 3] revealed that the pore size in the carbon material prepared from SiC is equal to 0.8 nm. It turned out that all the pores have almost the same size, with a distribution half-width of 0.02 nm.

At present, the theory of pore formation in solids is quite well developed [7]. According to the concepts developed in these models, the main reasons for pore formation are as follows:

(i) The pores are formed from a supersaturated solution of vacancies, which arise either upon heat generation or under exposure of the solid to ionizing radiation with a sufficient energy (the so-called vacancy porosity).

(ii) The pores arise under mechanical action on solids (deformation pores).

(iii) The pores can also be formed during the growth of crystals and films upon the sorption of gases, microshrinkage, nonuniform deposition, etc. [7].

In all the above cases, the pore formation is due to physical transformations in the structure and is not accompanied by a chemical transformation of the material. In the case under study, the reason for the pore formation is quite different. It concerns the chemical reaction proceeding in the course of the chlorine treatment of carbides, that is,

$$MeC_\mu + \frac{\nu}{2}Cl_2 \longrightarrow MeCl_\nu + \mu C. \qquad (1)$$

Here, *Me* is the general designation of the carbide-forming element and μ and ν are the stoichiometric coefficients. In the process of the chemical reaction, chlorine "eats away" atoms of the carbide-forming metal and leaves behind the carbon atoms and voids.

As a rule, this process is accompanied by the formation of a homogeneous-in-size spatially periodic porous structure in which the positions of carbon atoms are displaced with respect to their initial positions [2, 3]. To our knowledge, this phenomenon has not been explained in the literature thus far. In this connection, the objective of this work was to develop a model of the formation of the nanoporous structure in carbon materials obtained by the chlorination of carbides.

Such a model is important both for understanding the processes occurring in the course of the preparation of nanoporous materials according to reaction (1) and for controlling the structure of the materials produced [8].

2. PHYSICAL PRINCIPLES AND THE MODEL OF NANOPORE FORMATION

In this work, we investigated the formation of nanopores in silicon carbide. Let us dwell on this specific example.

The chemical reaction in this case proceeds according to scheme (1), where Me = Si, μ = 1, and ν = 4. Apparently, this reaction involves several stages. Indeed, the chlorine molecules should first dissociate into atoms, which then diffuse into the bulk of the silicon carbide and combine with silicon. It is evident that the active radicals are thus generated and can catalyze this reaction until the stable gas $SiCl_4$ is formed, which is then removed from the sample.

The generation of intermediate radicals leads to the emergence of a nonlinear feedback; i.e., the reaction product $SiCl_4$ (radicals) will itself activate its appearance and, correspondingly, the formation of carbon. At a low flux of chlorine, the substance is virtually homogeneously distributed in the system, because the diffusion has had time to compensate for the existing heterogeneities. However, in the case when the chlorine flux density is high enough, the system is in principle unable to receive and process such a quantity of the substance in a uniform way. It will be forced to reorganize itself for the nonlinear chemical reaction to proceed more rapidly.

One possible reorganization is the formation of a periodic spatial distribution of the substance. For the system under study, this means that the sample should consist of periodically arranged pores (the $SiCl_4$ gas is removed) and carbon atoms. Such a process is referred to as self-organization [9, 10]. Let us consider it in a quantitative manner.

We designate the concentrations of chloride $[Me\text{Cl}] = A$, chlorine $[\text{Cl}] = B$, carbon $[C] = C$, and carbide $[Me\text{C}] = D$.

In order to describe the kinetics of the chemical reaction, we use the following reactions:

$$\frac{\partial A}{\partial \tau} = F_A \Delta A + k A^m B^n D - \frac{A}{T_0},$$

$$\frac{\partial B}{\partial \tau} = F_B \Delta B + J + k A^m B^n D,$$

$$\frac{\partial D}{\partial \tau} = -k A^m B^n D,$$

$$\frac{\partial C}{\partial \tau} = k A^m B^n D,$$

(2)

where $\Delta = \partial^2/\partial X^2$ is the Laplacian; X is the spatial coordinate; τ is the time; F_A and F_B are the diffusion coefficients of the substances A and B, respectively; T_0 is the characteristic time of the outflow of the reaction product (chloride A) from the system; J is the rate of the chlorine inflow into the system; and k is a constant.

The derivatives $\partial A/\partial \tau$, $\partial B/\partial \tau$, and the others in the left-hand sides of the equations of set (2) are the rates of change in the concentrations of the corresponding substances. The summands $F_A \Delta A$ and $F_B \Delta B$ in the righthand sides of these equations account for the dif-

fusion processes of chloride and chlorine, respectively. The summand $k A^m B^n D$ corresponds to the chemical equation, but, as mentioned above, $m > 1$ owing to the catalytic role of the A chloride. The chloride outflow from the system is allowed for by the term $-A/T_0$ in the first equation, and the inflow of chlorine into the system is taken into account by the term $+J$ in the second equation.

Let us study the possibility of forming a periodic structure of the distribution of the reaction product, i.e., of the C quantity. In the case of a steady time-independent flux $J \neq 0$ no stationary periodic structures are formed, since it follows from the set of Eqs. (2) that $A^m B^n D \longrightarrow 0$. According to the second equation of set (2), the latter result leads to $B \longrightarrow \infty$.

In the case when the flux J vanishes at a certain instant of time τ_0, the B quantity can decrease with time according to the second equation of set (2) and the A quantity can decrease according to the first equation of this set. Hence, it can be assumed that $A^m B^n D \longrightarrow 0$ and, as a consequence of the fourth equation, the resulting structure of the reaction product C is stabilized.

In order to investigate the formation of quasi-stationary periodic structures under the assumption of a slow change in d, it is sufficient to consider the self-organization in the case described by only the first two equations of set (2).

We introduce the dimensionless variables and constants which are convenient for the mathematical analysis of the behavior of the system, that is,

$$t = \frac{\tau}{T_0}, \quad z = \frac{X}{\sqrt{D_A T_0}}, \quad j = J T_0 \sqrt[p]{k T_0}, \quad \alpha = \frac{F_B}{F_A},$$

$$a = A \sqrt[p]{k T_0}, \quad b = B \sqrt[p]{k T_0}, \quad d = D \sqrt[p]{k T_0},$$

$$c = C \sqrt[p]{k T_0}, \quad x = a - j, \quad y = -b - (d j^{m-1})^{-1/n},$$

(3)

where $p = m + n$.

Linearizing the first two equations of set (2) with respect to x and y, we obtain

$$\frac{\partial x}{\partial t} = \Delta x + (m-1)x + n d^{1/n} j^{(m+n-1)/n} y,$$

$$\frac{\partial y}{\partial t} = \alpha \Delta y - mx - n d^{1/n} j^{(m+n-1)/n} y.$$

(4)

This set of equations has a homogeneous solution $x = 0$, $y = 0$. However, it might become unstable at certain parameters j, α, and d; i.e., any arbitrarily small deviations from this solution will increase with time. The expansion of the possible deviations into a Fourier

GORDEEV *et al.*
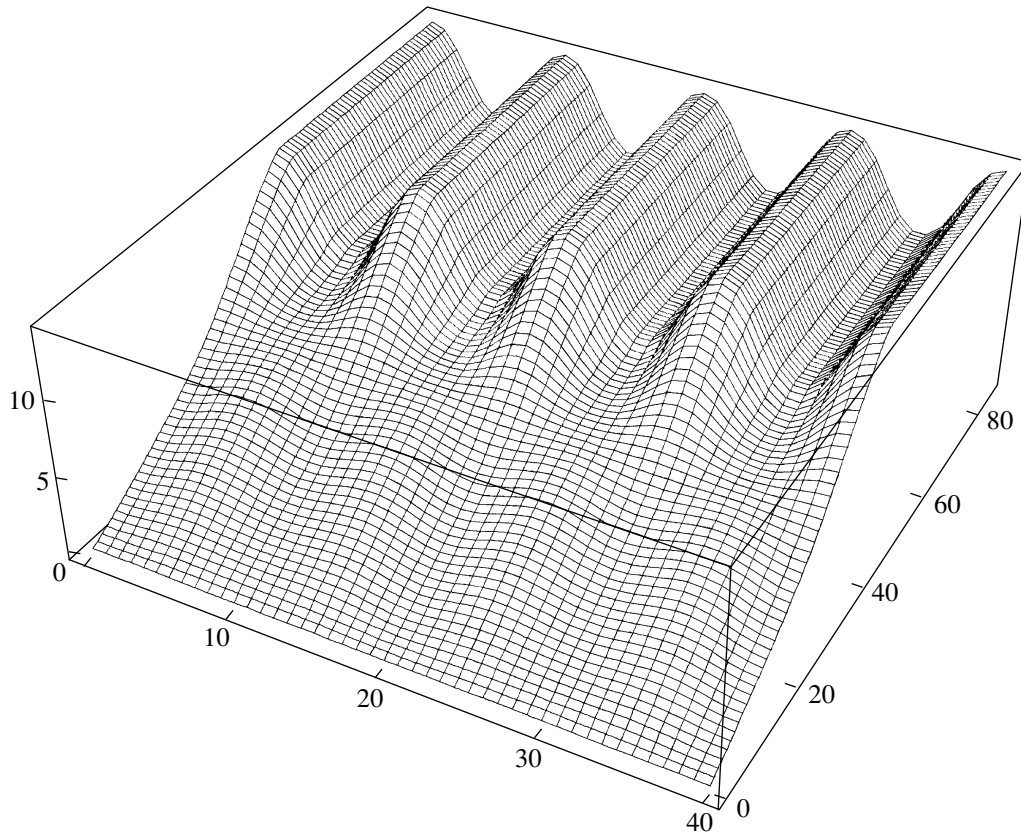
The dependence $c(t, z)$ for $\alpha = 10$, $d(0, z) = 24$, $j = 0.25$ at $t < 45$, and $j = 0$ at $t > 45$.

series with respect to the spatial coordinate z (the 1D case) gives

$$x(z, t) = \sum_n x_n(t) \cos \omega_n z,$$

$$y(z, t) = \sum_n y_n(t) \cos \omega_n z. \tag{5}$$

The factors $x_n(t)$ and $y_n(t)$ must satisfy the set of equations

$$\begin{pmatrix} x'_n(t) \\ y'_n(t) \end{pmatrix} = A \begin{pmatrix} x_n(t) \\ y_n(t) \end{pmatrix} \tag{6}$$

with the matrix

$$A = \begin{pmatrix} m - 1 - \omega_n^2 & n d^{1/n} j^{(m+n-1)/n} \\ -m & -n d^{1/n} j^{(m+n-1)/n} - \alpha \omega_n^2 \end{pmatrix}. \tag{7}$$

The condition for an increase in $x_n(t)$ and $y_n(t)$ with time is equivalent to the condition that the A matrix has the eigenvalues with positive real parts. This takes place at

$\omega < \sqrt{m-1}$ under the condition

$$m > 1, \quad n > 0. \tag{8}$$

Thus, the substance A, which is the product of the reaction, should serve as a catalyst for this reaction in conformity with $m > 1$, as was assumed above.

Otherwise, in the case when

$$\alpha > \frac{\sqrt{m}+1}{\sqrt{m}-1},$$

$$\left(\frac{m-1}{n}\right)^n \frac{1}{j^{m+n-1}} < d < \left(\frac{\alpha(\sqrt{m}-1)^2}{n}\right)^n \frac{1}{j^{m+n-1}}, \tag{9}$$

the increase in perturbations is selective with respect to ω (i.e., a certain type of self-organization occurs). Only those perturbations increase for which ω satisfies the inequality

$$\sqrt{\frac{m-1}{2\alpha}\left(\alpha - 1 - \sqrt{(\alpha-1)^2 - \frac{4\alpha}{m-1}}\right)} < \omega$$

$$< \sqrt{\frac{m-1}{2\alpha}\left(\alpha - 1 + \sqrt{(\alpha-1)^2 - \frac{4\alpha}{m-1}}\right)}. \tag{10}$$

The initial set of Eqs. (2) is nonlinear. As a result, the increase in perturbations can cease. Thus, if conditions (8) and (9) are met, the self-organization in the set of Eqs. (2) and the formation of a stationary periodic structure with the period $\Pi = 2\pi/\omega$, where ω obeys inequality (10), become possible.

The plot for the numerical solution $c(t, z)$ of the set of Eqs. (2) at $m = 2$, $n = 1$, and $\alpha = 10$ is shown in the figure.

It can be seen from the figure that a periodic porous structure (alternating valleys) is formed in the carbon distribution. Upon termination of the inflow of chlorine into the system, the growth of the pores ceases and the resulting structure is stabilized. In the case when the inflow of chlorine molecules into the system continues, further growth of the pores is observed.

3. DISCUSSION

By applying the results obtained to the characteristic case when at least one intermediate stage of the chemical reaction exists (i.e., $m = 2$, $n = 1$), we obtain the following necessary conditions for the formation of the porous structure:

$$\frac{F_B}{F_A} > \frac{\sqrt{2}+1}{\sqrt{2}-1}, \quad \frac{1}{J^2} < kT_0^3 D < (\sqrt{2}-1)^2 \frac{F_B}{F_A} \frac{1}{J^2}. \quad (11)$$

Thus, if relation (11) is valid, self-organization in the system is possible, i.e., as the emergence of periodically alternating voids and carbon.

If one takes the ratio of the diffusion coefficients, $F_A > F_B$, to be equal to ten because of the different molecular masses of the reaction products and the initial substance (chlorine) and $T_0 = 10$ s, then it follows from inequality (10) that the size of the pores falls within the range from 0.7 to 1.7 nm. This agrees with the experimental data.

When the ratio of the diffusion coefficients does not meet condition (11), self-organization is impossible.

Hence, heterogeneous chemical reactions occur, and no ordered porous structures arise.

On the contrary, if the experimental situation allows a choice of different initial conditions, the self-organization is possible. Generally speaking, this is true for arbitrary fluxes, but the parameters must satisfy condition (11).

REFERENCES

1. G. F. Kirillova, G. A. Meerson, and A. N. Zelikman, Izv. Vyssh. Uchebn. Zaved., Tsvetn. Metall. **3**, 90 (1960).
2. N. F. Fedorov, Ross. Khim. Zh. **39** (6), 37 (1995).
3. N. F. Fedorov, G. K. Shikhnyuk, and D. N. Gavrilov, Zh. Prikl. Khim. (Leningrad) **54** (2), 272 (1982).
4. S. K. Gordeev and A. V. Vartanova, Zh. Prikl. Khim. (St. Petersburg) **67** (7), 1080 (1995).
5. A. E. Kravchik, A. S. Osmakov, and R. G. Avarbé, Zh. Prikl. Khim. (Leningrad) **61** (11), 2430 (1989).
6. R. N. Kyutt, É. A. Smorgonskaya, S. K. Gordeev, *et al.*, Fiz. Tverd. Tela (St. Petersburg) **41** (8), 1484 (1999) [Phys. Solid State **41**, 1359 (1999)].
7. P. G. Cheremskoǐ, V. V. Slezov, and V. I. Betekhtin, *Pores in Solids* (Énergoatomizdat, Moscow, 1990).
8. R. G. Avarbé, S. K. Gordeev, A. V. Vartanova, *et al.*, RF Patent No. 2,084,036, MKl6NO169/00, Byul. No. 19 (1997).
9. G. Nicolis and I. Prigogine, *Self-Organization in Non-Equilibrium Systems* (Wiley, New York, 1977; Mir, Moscow, 1979).
10. S. A. Kukushkin and A. V. Osipov, Fiz. Tverd. Tela (St. Petersburg) **36** (5), 1258 (1994) [Phys. Solid State **36**, 687 (1994)].

Translated by M. Lebedkin

═══════════════ **ERRATA** ═══════════════

Erratum: "Effect of Electric Field on NMR Spectra in Centroantisymmetric Antiferromagnets" [*Phys. Solid State* 42 (5), 903 (2000)]

V. V. Leskovets and E. A. Turov

On page 906, Eq. (17) should have the form

$$\Omega^2_{1,4} = AL_{y'}[(AL_{y'} - 2M_{y'}) + 2(-\lambda_{123} \pm \lambda_{113})L_{y'}E_z],$$
$$\Omega^2_{2,3} = AL_{y'}[(AL_{y'} + 2M_{y'}) + 2(\lambda_{123} \pm \lambda_{113})L_{y'}E_z]. \tag{17}$$

In the next paragraph, λ_{123} should be replaced by λ_{113}.